博士論文

論文題目 **Studies of equilibrium states with magnetic field and meridional flow in astrophysics**

(天体物理学における磁場や子午面流を伴った平衡状態の研究)

氏 名：藤澤 幸太郎

It is better to create than to learn! Creating is the essence of life.
— Gaius Julius Caesar —

Contents

Alea iacta est.
The die is cast.
(Gaius Julius Caesar)

Abstract

We have considered and calculated equilibrium states with magnetic field and meridional flow in astrophysics under the assumptions of stationary and axisymmetric barotropes. We have obtained many equilibrium states across the widely astrophysical areas in order to understand equilibrium configurations deeply.

In our present formulation, arbitrary functions of the magnetic flux function appear in the expression for the current density in case of magnetic field configurations. By appropriately choosing the functional form for one of the arbitrary functions that corresponds to the distribution of the non force-free toroidal current density, we have obtained magnetized equilibrium states with extremely strong but highly localized poloidal magnetic fields in the second chapter. The absolute values of the central magnetic fields are stronger than those of the surface region by two orders of magnitude. By applying our results to magnetars, the internal magnetic poloidal fields could be 10^{17} G, although the surface magnetic fields are about 10^{15} G in the case of magnetars. For white dwarfs, the internal magnetic poloidal fields could be 10^{12} G, when the surface magnetic fields are 10^{9-10} G. If the star has such extremely strong but localized poloidal magnetic field deep inside, the contributions from higher order magnetic multipole moment to the outer fields around the star cannot be neglected.

We have showed the importance of coexistence of oppositely flowing φ currents for magnetized stars to sustain strong toroidal magnetic fields within the stars by analysing stationary states of magnetized stars with surface currents which flow in the opposite direction with respect to the bulk currents within the stars in the third chapter. If the stars could have the toroidal surface currents which flow in the opposite directions to the internal toroidal currents, the positively flowing internal toroidal currents can become stronger than the upper limit value of the current for configurations without surface toroidal currents. Thus, the energies for the toroidal magnetic fields can become much larger than those for the magnetized stars without surface toroidal currents.

The physical meaning of the oppositely flowing toroidal current density has been discussed in the fourth chapter. We have showed a sufficient condition for magnetized star with large toroidal magnetic fields in stationary and axisymmetric system. As we have seen in the third chapter, the magnetized star with large toroidal magnetic field has oppositely flowing non force-free toroidal current density, and such oppositely flowing toroidal current density changes the stellar shape prolate. These results mean that the large toroidal magnetic fields result in and result from the prolate stellar deformation and oppositely flowing non force-free toroidal current

density. A condition that a star has oppositely flowing non force-free toroidal current density and its shape is prolate is sufficient for large toroidal magnetic fields inside the star.

We have succeeded in obtaining magnetic field configurations with both poloidal and toroidal components throughout magnetized stellar interior and exterior in the fifth chapter. We have divided the magnetized star into a hydromagnetic equilibrium core, a Hall equilibrium crust and a twisted force-free magnetosphere. We have calculated these regions under various boundary conditions simultaneously and systematically using the Green function relaxation method and found four interesting characteristics of numerical results. First, the core toroidal magnetic fields and the twisted magnetosphere make the size of the crustal toroidal magnetic field region large in Hall equilibrium. Second, the current sheet on the core-crust boundary affects both internal and external magnetic field configurations. Especially, the negative and positive current sheets make the core magnetic field energy ratio $\mathcal{M}co/\mathcal{M}$ large and small respectively. Finally, the twisted magnetosphere makes a cross-point of magnetic field lines such as X-point geometry in the magnetosphere. The X-point geometry appears and disappears according to the strength of the twisted field in the magnetosphere or the core-crust boundary conditions. Our results mean that both Hall MHD secular evolution and magnetospheric dynamical evolution would be deeply affected by conditions of another region and core-crust stress of magnetars.

We have obtained the general forms for the current density and the vorticity from the integrability conditions of the basic equations which govern the stationary states of axisymmetric magnetized self-gravitating barotropic objects with meridional flows under the ideal magnetohydrodynamics (MHD) approximation in the sixth chapter. As seen from the stationary condition equations for such bodies, the presence of the meridional flows and that of the poloidal magnetic fields act oppositely on the internal structures. The different actions of these two physical quantities, the meridional flows and the poloidal magnetic fields, could be clearly seen through stationary structures of the toroidal gaseous configurations around central point masses in the framework of Newtonian gravity because the effects of the two physical quantities can be seen in an amplified way for toroidal systems compared to those for spheroidal stars. The meridional flows make the structures more compact, i.e. the widths of toroids thinner, while the poloidal magnetic fields are apt to elongate the density contours in a certain direction depending on the situation. Therefore, the simultaneous presence of the internal flows and the magnetic fields would work as if there were no such different actions within and around the stationary gaseous objects such as axisymmetric magnetized toroids with internal motions around central compact objects under the ideal MHD approximation, although these two quantities might exist in real systems.

We have evaluated the stellar deformation by the meridional flows in the seventh chapter. We have shown analytically that shapes of incompressible stars could be prolate if appropriate meridional flows exist. Although this result is strictly valid only if either the meridional flow or the rotation is absent and the vorticity is associated uniformly with meridional flow, this implies that perpendicular forces against centrifugal and/or magnetic forces might play important roles within stars. A consequence of the presence of meridional flows might be to decrease stellar

oblateness due to centrifugal and/or magnetic fields.

Omnia mala exempla ex rebus bonis orta sunt.
All bad precedents begin as justifiable measures.
(Gaius Julius Caesar)

1 Introduction

The main theme of this thesis is the investigation of equilibrium states with magnetic field and meridional flow in astrophysics. The physical origin and mechanism of magnetic field and meridional flow in the stellar interior are different from each other. They are often considered as different physics in different aspects of the astrophysics, but the mathematical formalism and treatment of them are very similar in many respects. Magnetic fields offer us important hints for meridional flows, and vice versa.

The structures of the magnetic fields and meridional flows are interesting themselves. The structures are important for various astrophysical phenomena in a wide ranging scale, because they affect both dynamical events and secular evolutions of stellar objects. Magnetic field and meridional flow change the stellar structure and shape by the Lorentz force and ram pressure, respectively. Although I have focused on the magnetic fields and developed the method for magnetized equilibrium states mainly in this thesis, I also consider the meridional flows using the method and results. We go back and forth between magnetic fields and meridional flow in order to solve problems and gain an new insight for astrophysics.

1.1 Various stellar magnetic fields among the stars

Magnetic fields play very important roles in many fields of astrophysics, the Sun, stars and compact objects such as white dwarfs and neutron stars. The magnetic fields have influence on both dynamical events and secular evolutions significantly. They are important energy sources of active astrophysical events such as jets, flares and bursts. They also affect the angular momentum transport of the stellar rotation and thermal evolution within the interior of compact stars on secular timescale.

Those stars have detectable magnetic fields. The magnitude of the magnetic field ranges from a few hundred G to over a few billion G. The typical values of their magnetic fields on their surface are $\sim 10^3$G (the sunspots), $\sim 10^3$ G (strongly magnetized O stars), $\sim 10^3 - 10^4$ G (strong magnetized Ap stars and Bp stars), $10^6 - 10^9$ G (strongly magnetized white dwarfs) and $10^9 - 10^{12}$ G (neutron stars). Above all things, Anomalous X-ray Pulsars (AXPs) and Soft Gamma-ray Repeaters (SGRs) have extremely strong magnetic fields whose dipole magnetic field strength reach 10^{14-15}G at their surfaces (Harding & Lai 2006). They are considered as strongly magnetized neutron stars, magnetars (Thompson & Duncan 1995). They have the strongest magnetic fields among the stars in the universe. They show intense high-energy emissions, bursts and flares by releasing their strong magnetic field energy. Recently, however, we have found low magnetic field SGRs (Rea et al. 2010; Rea et al. 2012). They exhibit the observational characteristics of typical SGRs, but their dipole magnetic field strength ($\sim 10^{12-13}$ G) is much weaker than those of typical dipole magnetic fields of SGR. They would have strong internal magnetic fields in order to show the typical activity of SGR, but we can not observe the internal magnetic fields directly. Therefore, we need to calculate them theoretically in order to obtain the magnetic field configurations. We consider and calculate magnetized star with extremely strong poloidal magnetic field in chapter 2.

The origin of the magnetic fields inside the star is not still understood well. According to the recent progresses of the theoretical researches, there are two possibilities for the mechanism to generate and sustain magnetic fields, i.e. 1) the dynamo theory and 2) the fossil field theory (see Moss 1994). Stars which have convective regions regenerate and sustain the magnetic fields by the dynamo mechanism. On the other hand, A, B, O stars have a convective core where dynamo action develops (e.g. Brun et al. 2005). However, the timescale for the dynamo-generated field in this core to reach the surface is too long (Charbonneau & MacGregor 2001). Therefore the magnetic field observed at the stellar surface is supposed to be fossil field. Recent observations show the observed magnetic fields' properties confirm this hypothesis (see Wade et al. 2011). Consequently, it has long been considered that magnetic fields of such stars would come from fossil magnetic fields. According to the fossil field theory, the magnetic fields of such stars would be originated from magnetized interstellar media. If the magnetic fluxes would be conserved during star formation processes, the magnetic fields could be concentrated to smaller regions of the stars by the gravitational contraction and result in strong magnetic fields inside the stars. Since the electric conductivities of the stars are very large, those magnetic fields do not diffuse during their formation stages. As for neutron stars, the origin of their strong magnetic fields is much more uncertain. If the fossil field theory could be applied, the strong magnetic fields could be reached by the same mechanism as those mentioned above for stars without external convective regions. On the other hand, if we could adopt the dynamo theory, the strong magnetic fields would be formed by the dynamo due to the rapid differential rotations in the convective regions of the proto-neutron stars (Duncan & Thompson 1992). The differential rotation could wind up the initial poloidal magnetic fields to produce strong toroidal magnetic fields before the crusts would crystallize. In either case, the magnetic fields

of neutron stars would be present even at birth and survive on much longer timescales than the Alfvén timescale ($= \sqrt{4\pi\rho}r_s/B \sim 100$ s for typical neutron stars with magnetic fields of order of $B = 10^{12}$G). Here r_s is the radius of the stellar surface which is, for axisymmetric configurations, a function of θ of the polar coordinates (r, θ, φ), i.e. $r_s(\theta)$. In order to sustain these kinds of fossil magnetic fields for a long time, these magnetic fields must be stationary and stable. Thus, in order to understand the magnetic fields originated from the fossil fields, it would be useful and important to obtain stationary and stable configurations of magnetized stars.

On the other hand, the magnetized equilibria have been studied theoretically for over sixty years, which was long before the discovery of neutron stars. Babcock detected the evidence of the Zeeman splitting due to the stellar magnetic fields in the spectrum of Ap star (Babcock 1947). The observation showed that stars other than the sun have detectable magnetic fields for the first time. After this important discovery by Babcock, several classical works were published by Chandrasekhar and his colleagues. They calculated and considered the magnetic field configurations and its influence on the stellar structures.

1.2 Classical magnetized equilibrium studies

The basic ideas and methods for magnetized equilibrium states have already been investigated by the classical works (Chandrasekhar & Fermi 1953, Ferraro 1954, Prendergast 1956 and Woltjer 1959a,b, 1960). Chandrasekhar & Fermi (1953) considered several problems related to magnetized stars and estimated the maximum strength of magnetic fields in the stellar interior, but they did not calculate magnetic field configurations. Ferraro (1954) calculated a purely poloidal magnetic field configuration of incompressible star analytically and evaluated the small stellar deformation by the poloidal magnetic fields. Prendergast (1956) suggested that a stable stellar magnetic fields require both poloidal and toroidal magnetic fields and considered incompressible magnetized equilibria with both poloidal and toroidal magnetic fields (Chandrasekhar 1956b; Chandrasekhar & Prendergast 1956, Woltjer 1959a). Woltjer (1959b, 1960) calculated compressible star with both poloidal and toroidal magnetic fields (Wentzel 1961). Several recent works (Haskell et al. 2008; Broderick & Narayan 2008; Duez & Mathis 2010 in Newtonian framework and Ioka & Sasaki 2004 in General relativistic framework) are essentially same as these classical works. These studies, however, assumed that the magnetic fields are too weak to change the stellar structures. They fixed the background structure and did not calculated magnetic deformation self-consistently. Following these classical works, Miketinac (1973) calculated magnetized equilibria with purely toroidal magnetic fields and Miketinac (1975) calculated magnetized equilibria with purely poloidal magnetic fields.

However, only a few works had calculated magnetized equilibrium consistently under limited conditions. Ostriker & Hartwick (1968) obtained magnetized equilibria with both poloidal and toroidal magnetic fields consistently, but their boundary condition was special one. All magnetic field lines in the work are closed within the star. These studies have been extended to

general relativistic formulations such as purely poloidal magnetic fields self-consistent study (Bocquet et al. 1995) and purely toroidal magnetic fields self-consistent study (Kiuchi & Yoshida 2008).

On the other hand, stability analysis of the magnetic fields is also an important problem in order to keep the stellar magnetic fields for a long time. It was suggested by Prendergast (1956) that both poloidal and toroidal components are required for stable stellar magnetic fields. Markey & Tayler (1973) showed that purely poloidal magnetic fields in the star become unstable (see also Flowers & Ruderman 1977). Tayler (1973) showed that the purely toroidal magnetic fields becomes also unstable by kink instability. Stable magnetized stars should have both poloidal and toroidal magnetic fields. Moreover, the magnitudes of the toroidal fields must be comparable with those of the poloidal fields as Tayler (1980) suggested. However, the stability analysis for magnetized stars with both magnetic fields are too difficult to calculate systematically. Nobody have succeeded in showing the stability criteria for magnetized equilibria analytically and systematically.

1.3 Recent progress of the studies

Recent progress of numerical simulations have showed new insights about the magnetic field stability. Braithwaite & Spruit (2004) succeeded in obtaining the stable magnetic fields configurations numerically after a few Alfvén timescale computations. As Tayler (1980) described, their solution has both poloidal and toroidal magnetic fields. The toroidal magnetic field locates within the torus region in the stellar interior and poloidal magnetic field lines exist around the torus. They named this magnetic field configuration twisted-torus configurations (Braithwaite & Nordlund 2006). Braithwaite also studied stability of purely toroidal magnetic field configuration (Braithwaite 2006) and purely poloidal magnetic field configuration with rotation (Braithwaite 2007). These studies showed those purely magnetic field configurations become unstable within a few Alfvén timescale. The progress of these numerical simulations and observations of magnetars (e.g. Kouveliotou et al. 1998, 1999) are promoting magnetized equilibrium studies. We consider and obtain the stationary magnetic field configurations of magnetar throughout its interior to exterior in chapter 5.

Tomimura & Eriguchi (2005) succeeded in obtaining twisted-torus magnetized equilibrium states with both poloidal and toroidal magnetic fields self-consistently in Newtonian gravity. Their formulation and calculations were developed by Yoshida & Eriguchi (2006) and Yoshida et al. (2006). Yoshida & Eriguchi (2006) changed the functional form and obtained the solutions with locally strong toroidal magnetic field. Yoshida et al. (2006) calculated magnetized equilibria with differential rotation. Especially noted these twisted-torus magnetized equilibrium states are poloidal magnetic field dominated configurations (see also Lander & Jones 2009). We can see the same tendencies in general relativistic perturbative calculations by Ciolfi et al. (2009, 2010).

On the other hand, Braithwaite (2009) and Duez et al. (2010) have showed a stability criteria

of stellar magnetic fields as below:

$$a\frac{\mathcal{M}}{|W|} < \frac{\mathcal{M}_p}{\mathcal{M}} \leq 0.8, \tag{1.1}$$

where $\mathcal{M}/|W|$ is the ratio of the magnetic energy to the gravitational energy. $\mathcal{M}_p/\mathcal{M}$ is the ratio of the poloidal magnetic energy to the total magnetic energy and a is a certain dimensionless factor of order 10 for main-sequence stars and of order 10^3 for neutron stars. The value of $\mathcal{M}/|W|$ is about 10^{-5} even for magnetars and is expected to be $\mathcal{M}/|W| < 10^{-5}$ for other real stars. Thus the left hand side of this inequality could be less than about 10^{-3} even if the value of a might be ~ 1000. Therefore, this criterion means the configurations with the twisted-torus magnetic fields are stable even if the toroidal magnetic fields are much stronger than the poloidal magnetic fields. In contrast, the right hand side of this inequality means that the strong poloidal magnetic field configurations are unstable. As shown in dynamical simulations mentioned above, configurations with the strong poloidal magnetic fields are likely to become unstable within several Alfvén timescales. This criteria would not be applied to all situations because we might be able to consider various kinds of magnetic field configurations as the initial states and different choices of the initial conditions might influence on the evolutions of the magnetic fields. However, it seems to be the case that there is a tendency to become more unstable even for the twisted-torus magnetic field configurations with larger poloidal magnetic field energies. Therefore, it would be a natural consequence to consider that there would be stable magnetized stars with strong toroidal magnetic fields which satisfy the condition $\mathcal{M}_p/\mathcal{M} < 0.8$, i.e. $\mathcal{M}_t/\mathcal{M} > 0.2$ where $\mathcal{M}_t$ is the energy of the toroidal field.

Many magnetized equilibrium studies had failed to obtain the toroidal magnetic fields dominated solutions as I have described. In some of their solutions the toroidal magnetic fields are almost as strong as the poloidal magnetic fields only in the particular local regions inside the stars, but the total energies of the toroidal magnetic fields as a whole are much smaller than those of the total poloidal magnetic fields. In other words, the ratios of $\mathcal{M}_p/\mathcal{M}$ in their solutions are much bigger than 0.8.

By contrast this, some studies of magnetized stationary configurations (Glampedakis et al. 2012; Duez & Mathis 2010; Yoshida et al. 2012) have succeeded in obtaining the magnetized equilibria with strong toroidal magnetic fields by choosing very special boundary conditions for the poloidal magnetic fields. Their boundary conditions are different from those adopted by many other studies (e.g. Tomimura & Eriguchi 2005; Lander & Jones 2009; Ciolfi et al. 2009). However, they did not explain the reason why the magnetized stars can sustain such configurations with large toroidal magnetic energies under their special boundary conditions.

Therefore there are some important questions to be answered: how strong magnetic fields magnetized star sustain inside, and why these special configurations have large toroidal magnetic fields. These questions are addressed in chapters 2, 3 and 4 in this thesis.

1.4 Equilibrium studies with meridional flow

Meridional flow inside the stellar object is also interesting physical process. Since the first suggestion by Eddington (1925), meridional flow of rotating stars have been studied by many works. Roxburgh (1974) calculated the meridional flow structures inside the star under special boundary condition. The mathematical formulation and treatment of meridional flow is similar to magnetic field in stationary axisymmetric barotropic system. In this thesis, we give new expression for the current density and the vorticity inside the stationary and axisymmetric self-gravitating barotropes (chapter 6).

Such flows can change the stellar shape as magnetic fields do, because meridional flows have non-zero ram pressure inside the star. Eriguchi et al. (1986) investigated and calculated self-gravitating objects with meridional flow self-consistently. Recently, Birkl et al. (2011) extend the formulations of Eriguchi et al. (1986) and calculated general relativistic neutron star with arbitrary meridional flow self-consistently. These works showed that such meridional flow tends to make stellar shape prolate. We also evaluate the stellar deformation by the meridional flow using the method which have been developed for magnetized equilibrium studies in chapter 7.

1.5 Organization of the thesis

In this thesis, I consider and calculate equilibrium states with magnetic field and meridional flow in order to solve these problems. We calculate the magnetized equilibrium states with strong highly localized poloidal magnetic fields in chapter 2 [(a)]. We see that the oppositely flowing toroidal current density can sustain the strong toroidal magnetic fields energy within the star in chapter 3 [(b)]. We consider and find the physical meaning of the oppositely flowing toroidal current density in chapter 4 [(c)]. Using these results, we investigate stationary magnetic field configurations throughout magnetar interior to exterior as an astrophysical application in chapter 5 [(d)]. We formulate and calculate magnetized equilibrium states with meridional flow, which is the most general case in stationary and axisymmetric barotropes in chapter 6 [(e)]. We also find the influence of meridional flow on the equilibrium states in the chapter. We consider prolate stars due to meridional flows quantitatively in chapter 7 [(f)]. Finally, I summarise and conclude this thesis in chapter 8.

[(a)] Fujisawa et al. (2012).
[(b)] Fujisawa & Eriguchi (2013).
[(c)] Fujisawa & Eriguchi (submitted).
[(d)] Fujisawa & Kisaka (submitted).
[(e)] Fujisawa et al. (2013).
[(f)] Fujisawa & Eriguchi (2014).

As a rule, men worry more about what they can't see
than about what they can.
(Gaius Julius Caesar)

2

Magnetized stars with extremely strong poloidal fields

At first, we consider magnetized stars with strong poloidal magnetic fields. We choose an arbitrary functional form so as to achieve such magnetic field configurations. Since the arbitrary function relates to the Lorentz force of the magnetic fields inside the star, the distribution of the Lorentz force is affected by different choice of the functional form.

2.1 Introduction

The magnetic field inside a star is scarcely detectable by direct observations but has been considered to affect stellar evolutions and activities in many aspects. For instance, if strong magnetic fields are hidden inside degenerate stars such as white dwarfs or neutron stars, they may significantly affect the cooling process of the stars by providing an energy reservoir or by modifying heat conduction. Highly localized, anisotropic and relatively strong magnetic field configurations, on the other hand, may affect accretion modes onto degenerate stars in close binary systems by providing a well-focused channel of accretion to their magnetic poles. In order to know the possible distributions and strengths of the magnetic fields inside the stars, we have to rely on theoretical studies. Until very recently, however, theoretical investigations could give us few hints about the interior magnetic fields. The reason for that may be twofold: one is related to the difficulty of the evolutionary computations of stellar magnetic fields and the other is related to the lack of methods to obtain stationary configurations of the magnetized stars.

Concerning the evolution of the stellar magnetic fields, since it has been very difficult to pursue evolutionary computations of the global magnetic fields for both interiors and exteriors of stars, few results have been obtained. Recently, however, Braithwaite and his collabora-

tors have succeeded in following the evolution of global stellar magnetic fields (Braithwaite & Spruit 2004; Braithwaite & Nordlund 2006; Braithwaite & Spruit 2006; Braithwaite 2006; Braithwaite 2007; Braithwaite 2008; Braithwaite 2009; Duez et al. 2010). They found that the twisted-torus configurations of the magnetic fields inside stars seem to be stable across the dynamical timescale.

On the other hand, to investigate possible structures of the interior and exterior magnetic fields by imposing stationarity is a different theoretical approach. Concerning this problem, many attempts have been made but it has also been difficult to obtain stellar structures with both *poloidal* and *toroidal* non force-free magnetic fields self-consistently, not only in the Newtonian gravity but also in general relativity (see e.g. Chandrasekhar & Fermi 1953; Ferraro 1954; Chandrasekhar 1956b; Chandrasekhar & Prendergast 1956; Prendergast 1956; Woltjer 1959a; Woltjer 1959b; Woltjer 1960; Wentzel 1961; Ostriker & Hartwick 1968; Miketinac 1973; Miketinac 1975; Bocquet et al. 1995; Ioka & Sasaki 2004; Kiuchi & Yoshida 2008; Haskell et al. 2008 ; Duez & Mathis 2010). It is only recently that axisymmetric and stationary barotropic stellar structures have been successfully solved for configurations with both *poloidal* and *toroidal* magnetic components (Tomimura & Eriguchi 2005; Yoshida & Eriguchi 2006; Yoshida et al. 2006; Lander & Jones 2009; Otani et al. 2009) in a non-perturbative manner.

It should be noted that the twisted-torus magnetic configuration that appears during the evolutionary computations by Braithwaite & Spruit (2004) is qualitatively the same as one of the exact axisymmetric and stationary solutions obtained in Yoshida et al. (2006). Moreover, stable configurations of stellar magnetic fields must have a twisted-torus structure according to Braithwaite (2009). Concerning the stability analysis, this type of configurations is expected to be stable, while magnetic fields with purely *poloidal* configurations or purely *toroidal* configurations have been shown to be unstable (see e.g. Tayler 1973; Wright 1973; Markey & Tayler 1973; Flowers & Ruderman 1977).

In this chapter, we apply the formulation developed by Tomimura & Eriguchi (2005), Yoshida & Eriguchi (2006) and Yoshida et al. (2006) in order to find out how strong and localized *poloidal* magnetic fields can exist inside stars, as far as equilibrium configurations are concerned. In this formulation, the electric current density consists of several terms with different physical significances which contain arbitrary functionals of the magnetic flux function. These arbitrary functions correspond to the degrees of freedom in magnetized equilibria. One of the arbitrary functionals in the expression for the electric current density corresponds to the current in the *toroidal* direction. By choosing this functional form properly, we would be able to obtain equilibrium configurations of axisymmetric barotropic stars with highly localized and extremely strong *poloidal* magnetic fields.

2.2 Formulation and numerical method

Here we summarize the main scheme and formulation briefly. We describe the details of formulation in Appendix A.1 and numerical method in Appendix B.2.

2.2.1 Assumptions and basic equations

We make the following assumptions in this chapter. The system is in a stationary state and the configurations are axisymmetric. The systems are treated in the framework of Newtonian gravity. The rotation is rigid and we neglect meridional flows in this chapter. The conductivity of the stellar matter is infinite (ideal MHD). No electrical current is assumed in the vacuum region. The barotropic equation of state is assumed :

$$p = p(\rho) \ . \tag{2.1}$$

Here p and ρ are the pressure and the mass density, respectively. Assumptions of axisymmetric and equatorial symmetries as well as rigid rotation are adopted here in order to simplify our investigations.

Under these assumptions, the basic equations are written as follows. The continuity equation is expressed as

$$\nabla \cdot (\rho \boldsymbol{v}) = 0 \ , \tag{2.2}$$

where $\boldsymbol{v}$ is the fluid velocity. The equations of motion in the stationary state are written as:

$$\frac{1}{\rho}\nabla p = -\nabla \phi_g + R\Omega^2 \boldsymbol{e}_R + \frac{1}{\rho}\left(\frac{\boldsymbol{j}}{c} \times \boldsymbol{B}\right) , \tag{2.3}$$

where ϕ_g, Ω, $\boldsymbol{j}$, c and $\boldsymbol{B}$ are gravitational potential, angular velocity, electric current density, speed of light and magnetic field, respectively. Here we use the cylindrical coordinates (R, φ, z) and $\boldsymbol{e}_R$ is the unit vector in the R-direction. We also use the spherical coordinate (r, θ, φ) in this thesis. The gravitational potential satisfies Poisson equation:

$$\Delta \phi_g = 4\pi G \rho \ , \tag{2.4}$$

where G is the gravitational constant. Maxwell's equations are written as,

$$\nabla \cdot \boldsymbol{E} = 4\pi \rho_e \ , \tag{2.5}$$

$$\nabla \cdot \boldsymbol{B} = 0 \ , \tag{2.6}$$

$$\nabla \times \boldsymbol{E} = 0 \ , \tag{2.7}$$

$$\nabla \times \boldsymbol{B} = 4\pi \frac{\boldsymbol{j}}{c} \ , \tag{2.8}$$

where ρ_e and $\boldsymbol{E}$ are the electric charge density and the electric field, respectively. Notice that we neglect the displacement current term in Eq. (2.7) as is common in MHD approximation.

The ideal MHD condition, or the generalized Ohm's equation, can be expressed as:

$$\boldsymbol{E} = -\frac{\boldsymbol{v}}{c} \times \boldsymbol{B} \ . \tag{2.9}$$

We choose two kinds of barotropic equations of state. One is the polytropic equation of state:

$$p = K_0 \rho^{1+1/N} \ , \tag{2.10}$$

where N and K_0 are the polytropic index and the polytropic constant, respectively. The other is the degenerated Fermi gas at zero temperature, defined as

$$p = a[x(2x^2 - 3)\sqrt{x^2+1} + 3\ln(x + \sqrt{x^2+1})], \tag{2.11}$$

where

$$\rho = bx, \tag{2.12}$$

$$a = 6.00 \times 10^{22} \quad \mathrm{dyn/cm^2}, \tag{2.13}$$

$$b = 9.825 \times 10^5 \mu_e \quad \mathrm{g/cm^3}. \tag{2.14}$$

Here μ_e is the mean molecular weight. We fix $\mu_e = 2$ in all our computations here, which corresponds to a fully ionized pure hydrogen gas. This choice of parameters is same as that in Hachisu (1986a).

2.2.2 The form of the current density and the boundary condition

From the assumptions of axisymmetry and stationarity, we introduce magnetic flux function Ψ as follows:

$$B_r \equiv \frac{1}{r^2 \sin\theta} \frac{\partial \Psi}{\partial \theta}, \quad B_\theta \equiv -\frac{1}{r \sin\theta} \frac{\partial \Psi}{\partial r} \ , \tag{2.15}$$

where B_r and B_θ are magnetic field components in the r-direction and θ-direction, respectively. We assume this flux function is positive in the entire space. By introducing this magnetic flux function, Eq. (2.6) can be automatically satisfied. It should be noted that the magnetic flux function Ψ can be expressed as:

$$\Psi = r \sin\theta A_\varphi \ , \tag{2.16}$$

where A_φ is the φ-component of the vector potential defined by $\boldsymbol{B} \equiv \nabla \times \boldsymbol{A}$.

As shown in Tomimura & Eriguchi (2005), for axisymmetric and stationary barotropes with rigid rotation we can constrain the form of the electric current density by using an integrability

condition of the equations of motion, Eq. (2.3):

$$\frac{\boldsymbol{j}}{c} = \frac{1}{4\pi}\frac{d\kappa(\Psi)}{d\Psi}\boldsymbol{B} + r\sin\theta\rho\mu(\Psi)\boldsymbol{e}_{\varphi}\ , \tag{2.17}$$

where $\kappa(\Psi)$ and $\mu(\Psi)$ are arbitrary functions of the magnetic flux function Ψ. Notice, in particular, that the *toroidal* component of magnetic field is given as

$$B_{\varphi} = \frac{\kappa(\Psi)}{r\sin\theta} \tag{2.18}$$

which can be derived from Eqs. (2.3), (2.8) and (2.17). It should be noted that these two arbitrary functions are conserved along the *poloidal* magnetic field lines. Although the meanings of these two functions are described in previous works (see, e.g., Lovelace et al. 1986), in this chapter we will explain their meanings differently from our point of view.

Since we have assumed that there is no electric current in the vacuum region, in other words that there is no *toroidal* magnetic field outside the star (see Eq. 2.17), the form for κ needs to be a special one. The simplest form can be $\kappa =$ constant, but for this choice of κ the *toroidal* magnetic field would extend to the vacuum region. In order to avoid this possibility, we choose the functional form of κ as follows:

$$\kappa(\Psi) = \begin{cases} 0\ , & \text{for} \quad \Psi \le \Psi_{\max}\ , \\ \dfrac{\kappa_0}{k+1}(\Psi - \Psi_{\max})^{k+1}\ , & \text{for} \quad \Psi \ge \Psi_{\max}\ , \end{cases} \tag{2.19}$$

This choice of κ is the same as that in Yoshida & Eriguchi (2006) and Lander & Jones (2009). In this chapter we fix $k = 0.1$. Eqs. (2.18) and (2.19) ensure that the *toroidal* magnetic field vanishes smoothly at the stellar surface. Incidentally, using these functionals, we obtain the first integral of Eq. (2.3) as follows:

$$\int \frac{dp}{\rho} = -\phi_g + \frac{1}{2}(r\sin\theta)^2\Omega_0^2 + \int \mu(\Psi)\, d\Psi + C\ , \tag{2.20}$$

where C is an integration constant. The first term of the right-hand side is the gravitational potential. The second term on the right hand side is related to rotation. We can consider it as a rotational potential. Similarly, the third term means the potential of Lorentz force. We can regard this term as the magnetic force potential. Therefore, $\int \mu\, d\Psi$ is considered to be non-force-free contribution from the current density, as is seen in Eq. (2.17). Since the Lorentz force is given by the cross product $\boldsymbol{j}/c \times \boldsymbol{B}$, the first term of Eq. (2.17) has no effect on the equation of motion, i.e, it is force-free, and only the second term contributes to the Lorentz force, i.e., non force-free. The distribution of Lorentz force could be changed by adopting different functional forms for μ. All previous works (Tomimura & Eriguchi 2005, Yoshida & Eriguchi 2006, Yoshida et al. 2006, Lander & Jones 2009, Otani et al. 2009) fixed $\mu = \mu_0$

(constant). We choose a different functional form for μ in this chapter as follows:

$$\mu(\Psi) = \mu_0(\Psi+\epsilon)^m\,, \tag{2.21}$$

$$\int \mu(\Psi)\,d\Psi = \frac{\mu_0}{m+1}(\Psi+\epsilon)^{m+1}\,, \tag{2.22}$$

where m and ϵ are two constant parameters. In order to avoid singular behavior, we fix $\epsilon = 1.0\times10^{-6}$ in all calculations. As we shall see below, the parameter m determines a degree of localization of the interior *poloidal* magnetic field. We assume that *poloidal* magnetic fields extend throughout the whole space and that there are no discontinuities even at the stellar surface. The global magnetic field configurations of our models are nearly dipole-like because of the requirement of the functional form for κ at the stellar surface. These configurations contain closed *poloidal* magnetic field lines inside the star. The flux function Ψ attains its maximum at the central parts of these closed field lines and it takes its minimum on the symmetric axis and at infinity. The minimum value is zero because of $\Psi = r\sin\theta A_\varphi$ and the boundary condition for $A_\varphi = 0$ at infinity. The magnetic potential $\left(\int \mu d\Psi\right)$ changes its qualitative behavior in its spatial distribution when $m = -1$. If we adopt $m < -1$, as Ψ decreases from its maximum to zero on the axis of the star the value of the magnetic potential increases unboundedly if $\epsilon \to 0$. As a result, the *poloidal* magnetic field lines are concentrated near the axis in order to fulfill such magnetic potential distributions. On the other hand, if we choose $m > -1$, the value of the magnetic potential decreases as Ψ decreases from its maximum to zero, which is realized on the axis. Then the *poloidal* magnetic field lines are distributed more uniformly than those for configurations with $m < -1$. If we choose $m = 0$, we obtain $\mu =$ constant configurations. They are the same as those investigated by other authors.

It is remarkable that the only freedom that we can take in our formulation is related to the choices of functional forms and the values of the parameters which appear in those functions. It implies that degrees of freedom for choices for these functions and parameters correspond to degrees of freedom for many kinds of stationary axisymmetric magnetic field configurations. In fact, as we see from our results, different values for m result in qualitatively different distributions for the magnetic potentials and the *poloidal* magnetic fields. In other words, we can control the magnetic field distributions to a certain extent by adjusting the value for m. This is the reason why we use this functional form of μ in this chapter.

After we choose the functional form of the current density, by using Eq. (2.17) and the definition of the vector potential, we obtain the following partial differential equation of the elliptic type:

$$\Delta^*\Psi \equiv \frac{\partial^2\Psi}{\partial r^2} + \frac{\sin\theta}{r^2}\frac{\partial}{\partial\theta}\left(\frac{1}{\sin\theta}\frac{\partial\Psi}{\partial\theta}\right) = -4\pi r\sin\theta\frac{j_\varphi}{c}, \tag{2.23}$$

or

$$\Delta(A_\varphi\sin\varphi) = -4\pi\frac{j_\varphi}{c}\sin\varphi. \tag{2.24}$$

As we have seen in the previous paragraph, all the physical quantities related to the vector potential can be expressed solely by Ψ. Therefore we need not solve for A_r and A_θ. It implies that our present formulation does not depend on the gauge condition for the vector potential $\boldsymbol{A}$. Next we impose the boundary conditions for the gravitational potential and the vector potential, chosen as follows:

$$\phi_g \sim \mathcal{O}\left(\frac{1}{r}\right) , \quad (r \to \infty) , \tag{2.25}$$

$$A_\varphi \sim \mathcal{O}\left(\frac{1}{r}\right) , \quad (r \to \infty) . \tag{2.26}$$

This boundary condition for A_φ results in

$$B_p \sim \mathcal{O}\left(\frac{1}{r^2}\right) , \quad (r \to \infty) . \tag{2.27}$$

where B_p is the *poloidal* magnetic field. From these boundary conditions and using a proper Green's function for the Laplacian, we have the integral representations of Eqs. (2.4) and (2.24) as follows:

$$\phi_g(\boldsymbol{r}) = -G \int \frac{\rho(\boldsymbol{r}')}{|\boldsymbol{r} - \boldsymbol{r}'|} \, d^3\boldsymbol{r}' , \tag{2.28}$$

$$A_\varphi(\boldsymbol{r}) \sin\varphi = \frac{4\pi}{c} \int \frac{j_\varphi(\boldsymbol{r}') \sin\varphi'}{|\boldsymbol{r} - \boldsymbol{r}'|} \, d^3\boldsymbol{r}' . \tag{2.29}$$

Therefore, we can obtain smooth potentials, ϕ_g and A_φ by integrating these equations. Since we have chosen the functional form of the current density which decreases near the surface and vanishes at the stellar surface sufficiently smoothly, we obtain continuous *poloidal* magnetic fields from A_φ.

2.2.3 Global characteristics of equilibria

To see the global characteristic of magnetized equilibria, we define some integrated quantities as follows:

$$W \equiv \frac{1}{2} \int \phi_g \rho \, d^3\boldsymbol{r} , \tag{2.30}$$

$$T \equiv \frac{1}{2} \int \rho |\boldsymbol{v}|^2 \, d^3\boldsymbol{r} , \tag{2.31}$$

$$\Pi \equiv \int p \, d^3\boldsymbol{r} , \tag{2.32}$$

$$U \equiv N\Pi , \tag{2.33}$$

for polytropic models and

$$U \equiv \int g(x)\, d^3\boldsymbol{r}\ , \tag{2.34}$$

$$g(x) = a\{8x^3[(x^2+1)^{\frac{1}{2}} - 1]\} - p, \tag{2.35}$$

for the Fermi gas configurations (see. Chandrasekhar 1939),

$$\mathcal{M} \equiv \int r \cdot \left(\frac{\boldsymbol{j}}{c} \times \boldsymbol{B}\right)\, d^3\boldsymbol{r} = \frac{1}{8\pi}\int |\boldsymbol{B}|^2 d^3\boldsymbol{r}\ . \tag{2.36}$$

$$K = \int (\nabla \times \boldsymbol{A}) \cdot \boldsymbol{A}\, d^3\boldsymbol{r} = \int \boldsymbol{B} \cdot \boldsymbol{A}\, d^3\boldsymbol{r}\ , \tag{2.37}$$

where W, T, Π, U, $\mathcal{M}$ and K are the gravitational energy, rotational energy, total pressure, internal energy, magnetic field energy and magnetic helicity, respectively. In order to evaluate the structures of magnetic fields, we define some physical quantities related to the magnetic fields as follows:

$$B_{sur} = \frac{\int_0^{2\pi}\int_0^{\pi} r_s^2(\theta)\ \sin\theta |\boldsymbol{B}(r_s,\theta)|\, d\theta d\varphi}{S}\ , \tag{2.38}$$

where $r_s(\theta)$ and $|B_{sur}|$ are the stellar radius in the direction of θ and the surface magnetic field strength, respectively, and the surface area of the star is defined as:

$$S = \int_0^{2\pi}\int_0^{\pi} r_s^2(\theta)\sin\theta\, d\theta\, d\varphi. \tag{2.39}$$

The volume-averaged magnetic field strength in the central region of the star is defined as

$$B_{\rm c} = \frac{\int_0^{2\pi}\int_0^{\pi}\int_0^{r_c} r^2\sin\theta |\boldsymbol{B}(r,\theta)| dr d\theta d\varphi}{V}, \tag{2.40}$$

where we choose $r_c = 0.01 r_e$ and V is the volume of the central region with $r \le r_c$, defined as

$$V = \int_0^{2\pi}\int_0^{\pi}\int_0^{r_c} r^2\ \sin\theta dr\, d\theta d\varphi\ . \tag{2.41}$$

This central region seems to be very small, but we can resolve it sufficiently because we use non-uniform and centrally concentrated meshes in this chapter (see Fig. 2.1 and Eq. 2.49 in Appendix B). We have 77 meshes to resolve the region in actual numerical computations.

In order to know the contributions of the *poloidal* magnetic field and the *toroidal* magnetic field separately, we define the *poloidal* magnetic energy $\mathcal{M}_p$ and the *toroidal* magnetic energy

$\mathcal{M}_t$ as

$$\mathcal{M}_p = \frac{1}{8\pi}\int_0^{2\pi}\int_0^{\pi}\int_0^{\infty} r^2 \sin\theta \, |B_r^2 + B_\theta^2| dr d\theta d\varphi \, , \tag{2.42}$$

$$\mathcal{M}_t = \frac{1}{8\pi}\int_0^{2\pi}\int_0^{\pi}\int_0^{\infty} r^2 \sin\theta \, |B_\varphi^2| dr d\theta d\varphi \, , \tag{2.43}$$

As for the magnetic multipole moment seen outside a star, we compute each multipole component by solving the following equation in a vacuum:

$$\Delta \left(A_\varphi \sin\varphi \right) = 0 \, . \tag{2.44}$$

Considering the boundary conditions at infinity and the symmetry of the magnetized stars, the solution of the above equation can be expressed as

$$A_\varphi \sin\varphi \equiv \sum_{n=1}^{\infty} A_{\varphi,n} \sin\varphi = \sum_{n=1}^{\infty} b_{n,1} r^{-n-1} Y_{n,1}(\theta,\varphi) \, , \tag{2.45}$$

where $Y_{n,1}(\theta,\varphi)$ is the spherical harmonics of degree n and order $m = 1$. The coefficients $b_{n,1}$ correspond to the magnetic multipoles.

2.2.4 Setting for Numerical Computations

For numerical computations, the physical quantities are transformed into dimensionless ones using the maximum density $\rho_{\max}$, the maximum pressure $p_{\max}$ and the equatorial radius r_e as follows:

$$\hat{r} \equiv \frac{r}{r_e} = \frac{r}{\sqrt{\frac{1}{\beta}\frac{p_{\max}}{4\pi G \rho_{\max}^2}}} \, , \tag{2.46}$$

for polytropic configurations and

$$\hat{r} \equiv \frac{r}{r_e} = \frac{r}{\sqrt{\frac{1}{\beta}\frac{8a}{b}\frac{1}{4\pi G \rho_{\max}^2}}} \, , \tag{2.47}$$

for the Fermi gas models, and

$$\hat{\rho} \equiv \frac{\rho}{\rho_{\max}} \, . \tag{2.48}$$

Here β is introduced so as to make the distance from the center to the equatorial surface of the star to be unity. Arbitrary functions are also transformed into dimensionless ones. Quantities with $\hat{}$ are dimensionless. For example, the dimensionless length is $\hat{r}$ and the dimensionless arbitrary functions are $\hat{\mu}$ and $\hat{\kappa}$, respectively. Dimensionless forms of other quantities are collected in App. B.1.

The computational domain is defined as $0 \leq \theta \leq \frac{\pi}{2}$ in the angular direction and $0 \leq \hat{r} \leq 2$ in the radial direction. Since the equation of magnetohydrostationary equilibrium is defined only inside the star and the source terms of the elliptic equations for the gravitational potential and the magnetic flux function vanish outside the star, our computational domain covers a region of the space that is sufficient for obtaining equilibria. In order to resolve the region near the axis sufficiently, we use a special coordinate in actual numerical computations.

In the $\hat{r}$-direction, we divide the whole space into two distinct regions: $[0, 1.0]$ (region 1), and $[1.0, 2.0]$ (region 2). In each region, the following mesh points are defined:

$$\hat{r}_i = w_i^2 \begin{cases} w_i = (i-1)\Delta w_1 \ , & \Delta w_1 \equiv \dfrac{\sqrt{1}-\sqrt{0}}{n_1 - 1} \ , \quad \text{for} \quad 1 \leq i \leq n_1 \ , \\ w_i = 1.0 + (i - n_1)\Delta w_2, & \Delta w_2 \equiv \dfrac{\sqrt{2}-\sqrt{1}}{n_2 - 1}, \quad \text{for} \quad n_1 \leq i \ . \end{cases} \tag{2.49}$$

where n_1 and n_2 are the mesh numbers defined as follows:

$$n_1 \equiv \frac{3}{4}(n_r - 1) + 1 \ , \tag{2.50}$$

$$n_2 \equiv \frac{1}{4}(n_r - 1) + 1 \ . \tag{2.51}$$

Here n_r is the total mesh number in the r-direction. In practice, since we use a difference scheme of the second-order accuracy for the derivative and Simpson's integration formula, we divide each mesh interval defined above further into two equal size intervals in the r coordinate. We use $n_r = 513$ and thus the actual total number of the mesh points is $(2n_r - 1) = 1025$.

Concerning the θ-direction, we have to resolve the region near the axis, because for $m < 0$ values the magnetic fields seem to be highly localized to the axis region. In order to treat such magnetic fields near the axis region, we introduce the following mesh in the θ-direction:

$$\theta_j = \lambda_j^2 \ , \ \lambda_j = (j-1)\ \Delta\lambda \ , \ 1 \leq j \leq n_\theta \ , \ \Delta\lambda = \frac{\sqrt{\pi/2}}{n_\theta - 1} \ , \tag{2.52}$$

where n_θ is the total mesh number in the θ-direction. We also divide each mesh interval defined above further into two equal size intervals. Then, we use $n_\theta = 513$ and thus the actual total number of the mesh points is 1025. Fig. 2.1 shows the relations between the order of the grid points and the r- or θ-coordinate value.

2.2.5 Numerical method

We use the scheme of Tomimura & Eriguchi (2005). This scheme is based on the Hachisu Self-Consistent Field (HSCF) scheme (Hachisu 1986a,b), which is the method for obtaining equilibrium configurations of rotating stars. We define the ratio of the equatorial radius to the polar radius as the axis ratio q. This quantity q characterizes how distorted the stars are due to non-spherical forces. The stronger the non-spherical force becomes, the more distorted the stellar shape is. The non-spherical force can be the centrifugal force, the magnetic force or both

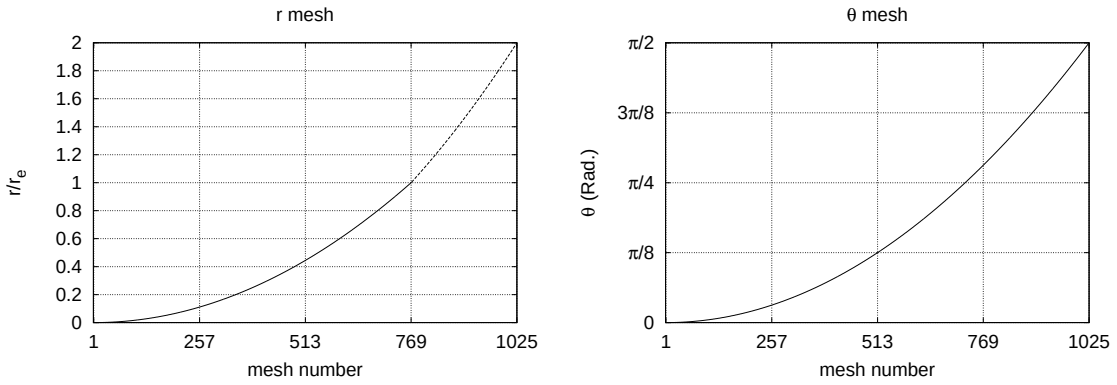

Figure 2.1: Left: the coordinate r/r_e is plotted as a function of the grid points. The solid curve shows the region 1 ($[0, 1]$) and the dashed curve shows the region 2 ($[1, 2]$). Right: the same as the left panel except for the θ coordinate.

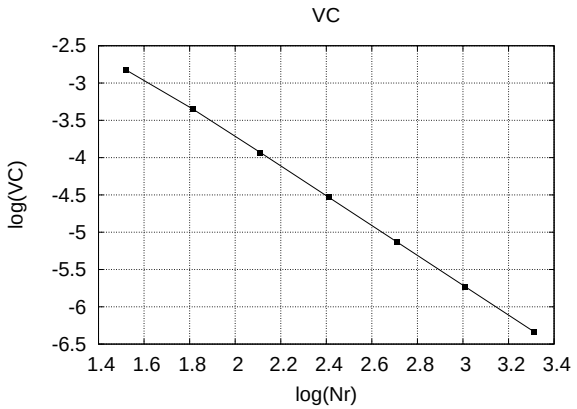

Figure 2.2: The virial quantity VC, plotted against the number of grid points in the r-direction.

of them. We fix the value of q in order to obtain the magnetized equilibria. We also fix one of $\hat{\mu}_0$ and $\hat{\Omega}_0$. If we fix $\hat{\mu}_0$, we will obtain the value of $\hat{\Omega}_0$ after the relaxation and iteration. If we fix $\hat{\Omega}_0$, we will obtain $\hat{\mu}_0$. Then, we will obtain one magnetized equilibrium state.

2.2.6 Numerical accuracy check

In order to check the accuracy of converged solutions, we compute a relative value of the virial relation as follows:

$$\mathrm{VC} \equiv \frac{|2T + W + 3\Pi + \mathcal{M}|}{|W|}. \tag{2.53}$$

Since this quantity VC must vanish for exact equilibrium configurations, we can check the global accuracies of the numerically obtained models as a whole (see e.g. Hachisu 1986a). Since the numerical results depend on mesh size, we have computed the same model by changing the number of grid points in the r-coordinate but fixing the number of grid points in the θ-direction as $n_\theta = 513$. Fig. 2.2 shows VC as a function of the number of grid points in the r-coordinate for polytropic models. Since we use schemes of second-order accuracy, VC

m	$1-q$	$B_c/B_{\rm sur}$	$\mathcal{M}_p/\mathcal{B}$	$\mathcal{M}/\lvert W\rvert$	$\Pi/\lvert W\rvert$	β	$\hat{\mu}_0$	$\hat{K}$	VC
				$N=1.0$					
-2.0	2.2E-2	1.03E+2	9.987E-1	3.74E-5	3.33E-1	5.07E-2	2.28E-9	7.76E-7	5.132E-8
-1.5	1.9E-3	4.44E+1	9.982E-1	3.02E-5	3.33E-1	5.07E-2	9.65E-8	8.27E-7	2.646E-6
-1.1	4.2E-4	2.19E+1	9.978E-1	2.60E-5	3.33E-1	5.07E-2	1.80E-6	8.33E-7	2.775E-6
-0.9	2.5E-4	1.62E+1	9.976E-1	2.45E-5	3.33E-1	5.07E-2	7.74E-6	8.35E-7	2.785E-6
-0.5	1.3E-4	1.02E+1	9.972E-1	2.21E-5	3.33E-1	5.07E-2	1.41E-4	8.35E-7	2.788E-6
0.0	8.8E-5	7.17E+0	9.968E-1	1.99E-5	3.33E-1	5.07E-2	5.25E-3	8.31E-7	2.789E-6
0.5	7.0E-5	5.69E+0	9.963E-1	1.83E-5	3.33E-1	5.07E-2	1.92E-1	8.23E-7	2.789E-6
1.0	6.1E-5	4.78E+0	9.959E-1	1.70E-5	3.33E-1	5.07E-2	6.90E+0	8.11E-7	2.789E-6

Table 2.1: Physical quantities for $\hat{\Omega}_0 = 0$, $\hat{\kappa}_0 = 10$ and $B_{sur} = 1.5 \times 10^{15}$G polytropes with different values of m.

decreases as the square inverse of the number of grid points (see also Lander & Jones 2009; Otani et al. 2009).

2.3 Numerical Results

We give a brief summary of our numerical results here. First we show the basic features for negative m models and the dependences of the magnetic field configurations on the values of m for barotropes. We also show rotating and magnetized polytropic models in order to examine the effect of rotation on magnetic fields. The influence of the equation of state on the interior magnetic field is also displayed. We have computed $N = 0.5, 1, 1.5$ polytropic models and four white dwarf models with $\rho_c = 1.0 \times 10^7, 1.0 \times 10^8$, 1.0×10^9, and $1.0 \times 10^{10}\mathrm{gcm}^{-3}$.

2.3.1 Effect of the distribution of the *toroidal* current density on the distribution of the magnetic field

We show the results for the distributions of the magnetic fields for different values of m. In particular, in order to examine the effect of magnetic fields alone, we consider configurations without rotation. The effect of stellar rotation is discussed in Sec. 2.3.2. Thus we set $\hat{\Omega}_0 = 0$ and compute $N = 1$ polytropic equilibrium models with different values of m and appropriate values of q so that the surface magnetic field becomes roughly $B_{sur} = 10^{15}$ G when $\rho_c = 1.0 \times 10^{15}\mathrm{gcm}^{-3}$ and mass $M = 1.4M_\odot$. By setting $N = 1$ and an appropriate choice of polytropic constant K of $p = K\rho^2$, we obtain models with $M = 1.4M_\odot$. It should be noted that these models have the typical mass and radius for neutron stars. We choose $N = 1$ as a simple approximation of neutron stars here. We searched and found the value of q by calculating many equilibrium states.

Physical quantities of these models are shown in Tab. 2.1. It can be seen that values of $\Pi/|W|$ and β are almost the same among these models. Although the strength of the averaged surface magnetic field is $B_{sur} = 1.5 \times 10^{15}$ G, the values of $\mathcal{M}/|W|$ are much smaller than those of $\Pi/|W|$. It implies that the effect of the magnetic fields in these configurations on their global structures is very small. On the other hand, values of B_c/B_{sur} and $\mathcal{M}/|W|$ vary rather considerably for different values of m. As the value of m is decreased, values of B_c/B_{sur} and

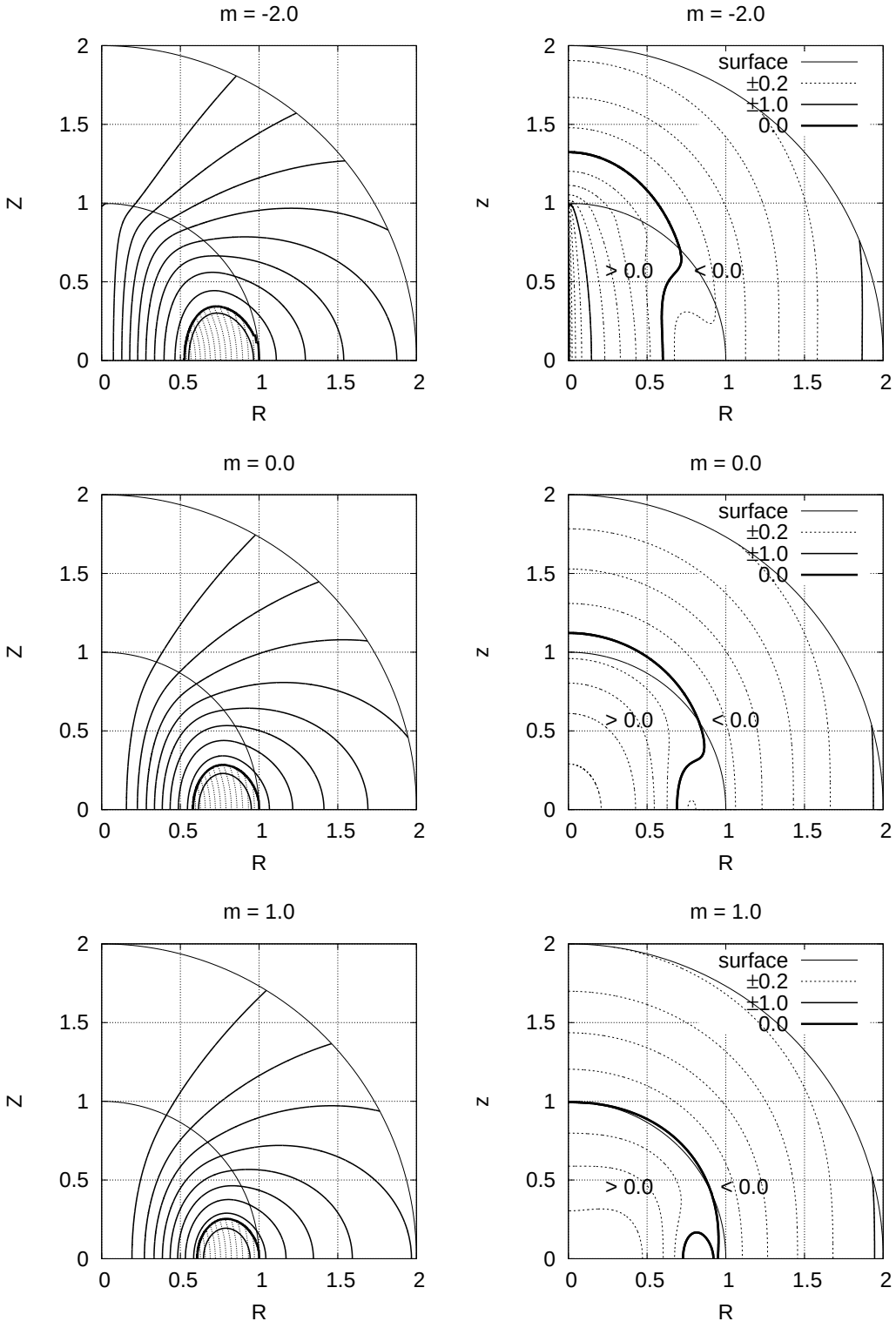

Figure 2.3: Contours for the magnetic flux function (left panels) and for the logarithm of the strength of the magnetic field normalized by the averaged surface magnetic field (right panels) are shown. The inner solid circle corresponds to the surface of the star and the outer solid circle denotes the boundary of our computational region. The flux difference between two adjacent contours of thick lines is 1/10 of the maximum value of $\hat{\Psi}$. In the left panels, the thick *poloidal* field line is the boundary of the *toroidal* magnetic field region. The *toroidal* magnetic field exists only inside the region. In the right panels, the distribution of the logarithm of the magnetic field normalized by the averaged surface magnetic field, $\log_{10}|\boldsymbol{B}/B_{sur}|$ contour, is shown. The thick solid curve corresponds to the curve with $\log_{10}|\boldsymbol{B}/B_{sur}| = 0$. Inside this curve $\log_{10}|\boldsymbol{B}/B_{sur}| > 0$ and outside this curve $\log_{10}|\boldsymbol{B}/B_{sur}| < 0$. The difference between two adjacent contours is 0.2.

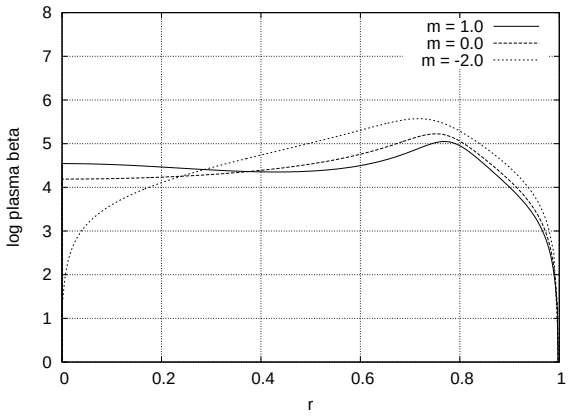

Figure 2.4: Profiles of $\log \beta_p$ at $\theta = \pi/2$, where β_p is the plasma β_p. Solid line represents the distribution for an $m = 1.0$ configuration, dashed line that for an $m = 0.0$ configuration and dotted line that for an $m = -2.0$ model, respectively.

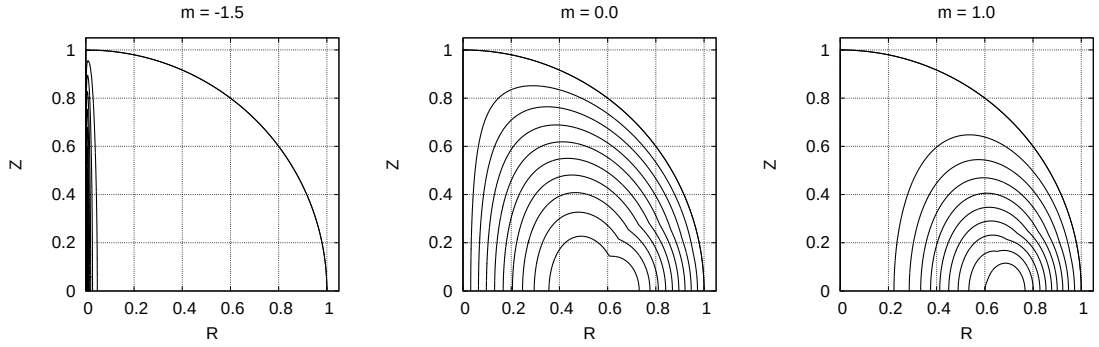

Figure 2.5: Isocontours of j_φ for different values of m. These panels show $N = 1$, $q = 0.99$ polytropic equilibrium models. The outermost curve denotes the stellar surface. The difference between two adjacent contours is 1/10 times the maximum of j_φ. The current is non-zero in the whole star except at the stellar surface and the symmetric axis (z-axis).

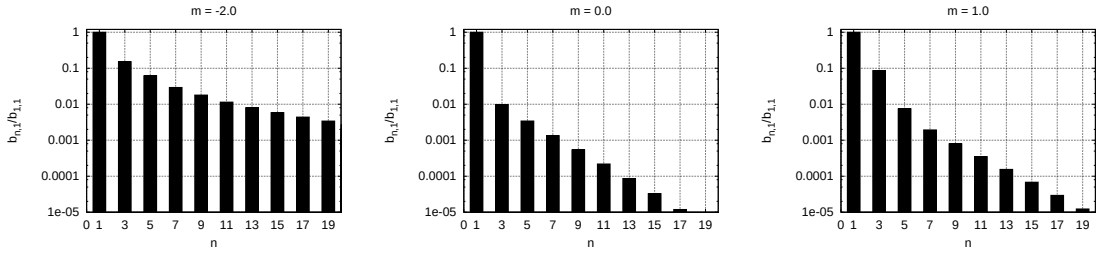

Figure 2.6: The ratio of the magnetic 2^n-pole moment coefficient to the magnetic dipole moment coefficient, $|b_{n,1}/b_{1,1}|$, is plotted against the multipole moment number n. Here $b_{n,1}$ is defined in Eq. (2.45).

$\mathcal{M}/|W|$ increase. In Fig. 2.3 the structure and strength of magnetic fields are shown for three different values of m, i.e. $m = -2.0$ (negative m model), $m = 0.0$ ($\hat{\mu}$ = constant model) and $m = 1.0$ (positive m model). The left-hand panels show the *poloidal* magnetic field lines and the regions where the *toroidal* magnetic field exists. The right-habd panels display the strength of the magnetic field $|\boldsymbol{B}|$ normalized by the averaged surface magnetic field B_{sur}.

As seen from these figures, there are no discontinuities of the magnetic fields at the stellar surfaces. Due to the choice of the functional form of the arbitrary function $\hat{\kappa}(\hat{\Psi})$ and the distribution of the magnetic flux function, *toroidal* magnetic fields appear only in the region that is bounded by the outermost closed *poloidal* magnetic field line inside the star (thick line). Thus the toroidal magnetic fields exist inside the torus region.

As the value of m is increased, i.e. from top panels to bottom panels, the ratio of B_c/B_{sur} decreases (see left panels in Fig. 2.3) because the *poloidal* magnetic field becomes weaker. This is also related to the fact that the interior *poloidal* magnetic field lines are much more localized near the axis for negative m models. The contours of magnetic field strength also display the same tendency. For the $m = 1.0$ model, the contour of $|\boldsymbol{B}| = B_{sur}$ (thick line) shows the stellar surface and the shapes of contours are nearly spherical. By contrast, the contours of the $m = -2.0$ model are highly distorted near the axis. The strength of the *poloidal* magnetic fields for the negative m models could exceed 10^{17}G near the central region. Fig. 2.4 shows the profiles of the plasma β_p on the $\theta = \pi/2$ plane, i.e. on the equatorial plane. Here, the plasma β_p is defined as follows:

$$\beta_p = 8\pi p/|\boldsymbol{B}|^2. \tag{2.54}$$

This quantity denotes the contribution of the gas pressure effect compared with the magnetic pressure effect. Fig. 2.4 shows profiles of β_p for models with $m = -2.0, 0.0, 1.0$. As seen from Fig. 2.4, the profiles of β_p are very similar to each other near the stellar surface regions. For the region around $\hat{r} \sim 0.6$, however, the value of β_p for the $m = -2.0$ model is larger than those for the $m = 0$ and $m = 1.0$ models. Since these models have almost the same mass density distributions, this difference means a difference of magnetic pressure distribution. In this region the magnetic field of the $m = -2.0$ configuration is weaker and thus the β_p becomes larger. However, *it should be noted that* these contours for the model with $m = -2.0$ are rather confined to the very narrow region near the central part. In other words, the gradient of the magnetic field distribution for the model with $m = -2$ is much steeper than the gradient of the gas pressure distribution compared with the models with $m = 1.0$ and $m = 0.0$. Thus the value of $\log \beta_p$ becomes dramatically small within the $\hat{r}[0 : 0.1]$ region and the minimum value of β_p can reach about ~ 20 in the central part. Therefore, in the central region of the model with $m = -2.0$ the influence of magnetic field on the local structure of the star is no longer negligible.

Here we explain the reason why this kind of highly localized *poloidal* magnetic field configuration can be realized. We need to note the distribution of the *toroidal* current density $\hat{j}_\varphi$ in order to analyse our models properly, because the current density is related to the magnetic

field closely by the two equations (Eqs. 2.8 and 2.17). In Fig. 2.5 we show the distributions of the *toroidal* current density for models with different values of m. As seen from Fig. 2.5, the distribution of the *toroidal* current density is concentrated toward the magnetic axis for the configuration with negative values of m. This is due to the dependence of $\hat{\mu}$ on the value of m. The current density distribution spreads over a large region inside the star as the value of m *increases* (from left panel to right panel). In other words, the distribution of the magnetic flux function becomes more and more concentrated toward the magnetic axis as the value of m *decreases*. It implies that the strengths of magnetic fields for models with negative values of m become very great near the magnetic axis. Our results show one possibility that a strong *poloidal* magnetic field can exist deep inside a star. If such a strong *poloidal* magnetic field is sustained deep inside a star, the contours of the magnetic field strength are no longer nearly spherical as in the bottom right panel of Fig. 2.3. Although this feature might be modified by dropping the assumption of the axisymmetry, it would give us one possibility for the presence of a strong *poloidal* magnetic field configuration deep inside a star.

Finally, to characterize the magnetic structure we show the magnetic multipole moments of magnetized stars. In Fig. 2.6 the values of $|b_{n,1}/b_{1,1}|$ (Eq. 2.45) are plotted. There appear to be only multipolar magnetic moments with odd degree ($n = 1, 3, 5$), because we have assumed the equatorial symmetry. As seen from these figures, in configurations with negative values of m the higher order magnetic multipole moments contribute ($|b_{n,1}/b_{1,1}|$) significantly to the total magnetic field, while in configurations with positive values of m the magnetic dipole moment is the dominant component of the total magnetic field. These figures show that the external magnetic field is nearly dipole when we adopt $m = 0$ but it is not simple dipole when $m > 0$ and $m < 0$. From the left panel, we see that the $n = 3$ (octupole) component reaches about a few tens of per cent of the dipole component when $m = -2.0$.

2.3.2 Effect of stellar rotation

We calculate two sequences with rotation for different values of m in order to examine the influence of rotation. We choose the value of $\hat{\mu}_0$ by obtaining a configuration with $\hat{\Omega}_0 = 0$ and $q = 0.99$ as a non-rotating limit of our equilibrium sequence. We choose $q = 0.99$ here for simplicity. The value of $q = 0.99$ corresponds to an equilibrium configuration with $B_{sur} \sim 10^{15}$ G when we consider a typical neutron star model with negative m. We have obtained sequences of stationary configurations by fixing the parameters m and $\hat{\mu}_0$ and changing the value of q. By changing the value of q for a fixed value of $\hat{\mu}_0$, we have equilibrium configurations with shapes that are deformed from spheres by rotational effect in addition to the magnetic force. Since we fix the magnetic potential parameter $\hat{\mu}_0$ and m along one sequence, the equilibrium sequence is the one with approximately constant magnetic effect. If the values of m and $\hat{\mu}_0$ are changed, we will be able to solve another stationary sequence. We have calculated two stationary sequences with negative m ($m = -1.5$) and with $m = 0.0$, i.e. $\hat{\mu} =$ constant .

Physical quantities of stationary configurations are tabulated in Table 2.2. As seen from this table, the quantities $|\hat{W}|$ and β or the ratio $\Pi/|W|$ and $T/|W|$ depend on the strength of the

q	$B_{\rm c}/B_{\rm sur}$	$\mathcal{M}_p/\mathcal{M}$	$\lvert\hat{W}\rvert$	$\mathcal{M}/\lvert W\rvert$	$\Pi/\lvert W\rvert$	$T/\lvert W\rvert$	β	$\hat{\Omega}_0^2$	$\hat{K}$	VC
				$m=-1.5$	$\hat{\mu}_0 =$ 5.070E-7					
0.99	4.75E+1	0.9979	9.71E-2	1.14E-4	3.33E-1	0.00E+0	5.06E-2	0.00E+0	3.33E-6	1.80E-6
0.9	4.54E+1	0.9972	8.00E-2	1.26E-4	3.19E-1	2.14E-2	4.51E-2	1.17E-2	3.61E-6	3.41E-5
0.8	4.36E+1	0.9960	6.16E-2	1.45E-4	3.02E-1	4.67E-2	3.87E-2	2.36E-2	3.95E-6	1.34E-5
0.7	4.19E+1	0.9940	4.40E-2	1.74E-4	2.85E-1	7.30E-2	3.22E-2	3.37E-2	4.32E-6	5.70E-6
				$m=0.0$	$\hat{\mu}_0 =$ 5.520E-2					
0.99	6.98E+0	0.9947	9.60E-2	2.31E-3	3.33E-1	0.00E+0	5.03E-2	0.00E+0	1.20E-4	1.85E-6
0.9	6.63E+0	0.9934	7.90E-2	2.35E-3	3.18E-1	2.14E-2	4.48E-2	1.16E-2	1.15E-4	1.24E-6
0.8	6.29E+0	0.9913	6.05E-2	2.39E-3	3.01E-1	4.73E-2	3.83E-2	2.37E-2	1.06E-4	1.36E-6
0.7	5.99E+0	0.9878	4.32E-2	2.39E-3	2.83E-1	7.40E-2	3.18E-2	3.37E-2	9.24E-5	1.51E-6

Table 2.2: Physical quantities of two sequences with $m = 0.0$ and $m = -1.5$.

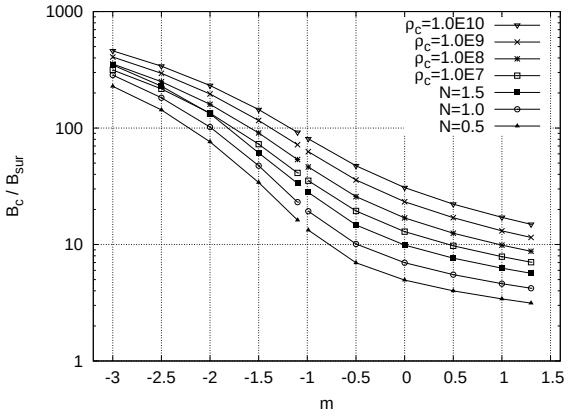

Figure 2.7: The value of $B_{\rm c}/B_{\rm sur}$ is plotted against the value of m for polytropes ($q = 0.99$) and white dwarfs ($q = 0.999$).

rotation. By contrast, magnetic quantities are almost unaffected by rotation. The dependence of the ratio B_c/B_{sur} on rotation is relatively small. The equilibrium configurations with highly localized magnetic fields that we have obtained in this chapter are almost unchanged even by rapid rotation. Therefore, we do not consider the effect of rotation any longer in this chapter.

2.3.3 Effect of equations of state

Thus far, we have discussed our magnetized configurations by showing the results for $N = 1$ polytropic models. The distribution of the *toroidal* current density, however, depends on the mass density profile through Eq. (2.17). Thus we show other polytropic models, i.e. $N = 0.5$ and $N = 1.5$ polytropes, as well as configurations for degenerate gases, i.e. white dwarf models, in order to examine the influence of equations of state on configurations with highly localized magnetic fields.

We set $q = 0.99$ for polytropes and $q = 0.999$ for degenerate gases. The degenerate model with $q = 0.999$ corresponds to a configuration with a $B_{sur} \sim 1.0 \times 10^9$G magnetized white dwarf with $m = -3.0$, the central density is $1.0 \times 10^8 {\rm gcm}^{-3}$. This central density results in a white dwarf of about $1.16 M_\odot$. Neither models rotates. We calculate 11 models with fixed values for q by setting $m = -3.0, -2.5, -2.0, -1.5, -1.1, -0.9, -0.5, 0.0, 0.5, 1.0, 1, 3$ and examine the dependence of B_c/B_{sur} on the equation of state.

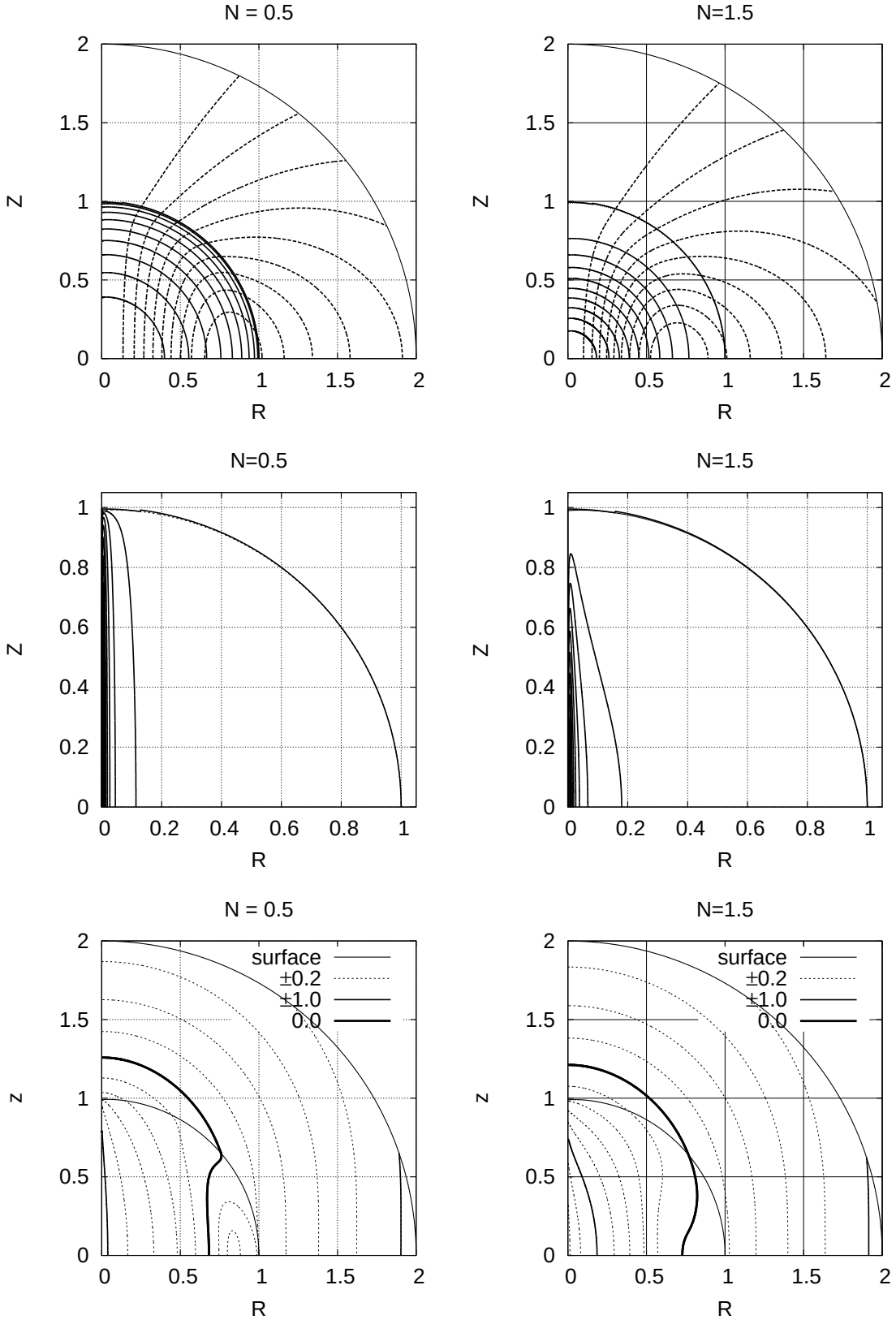

Figure 2.8: Isocontours for ρ and Ψ (top), j_φ (middle) and $\log[|\boldsymbol{B}|/|B_{sur}|]$ (bottom). These panels are for configurations with $m = -0.99$. The left panels are contours for the model of a $N = 0.5$ polytrope and the right panels are for a $N = 1.5$ polytrope. The difference between two adjacent contours is 1/10 times the maximum of the corresponding quantities.

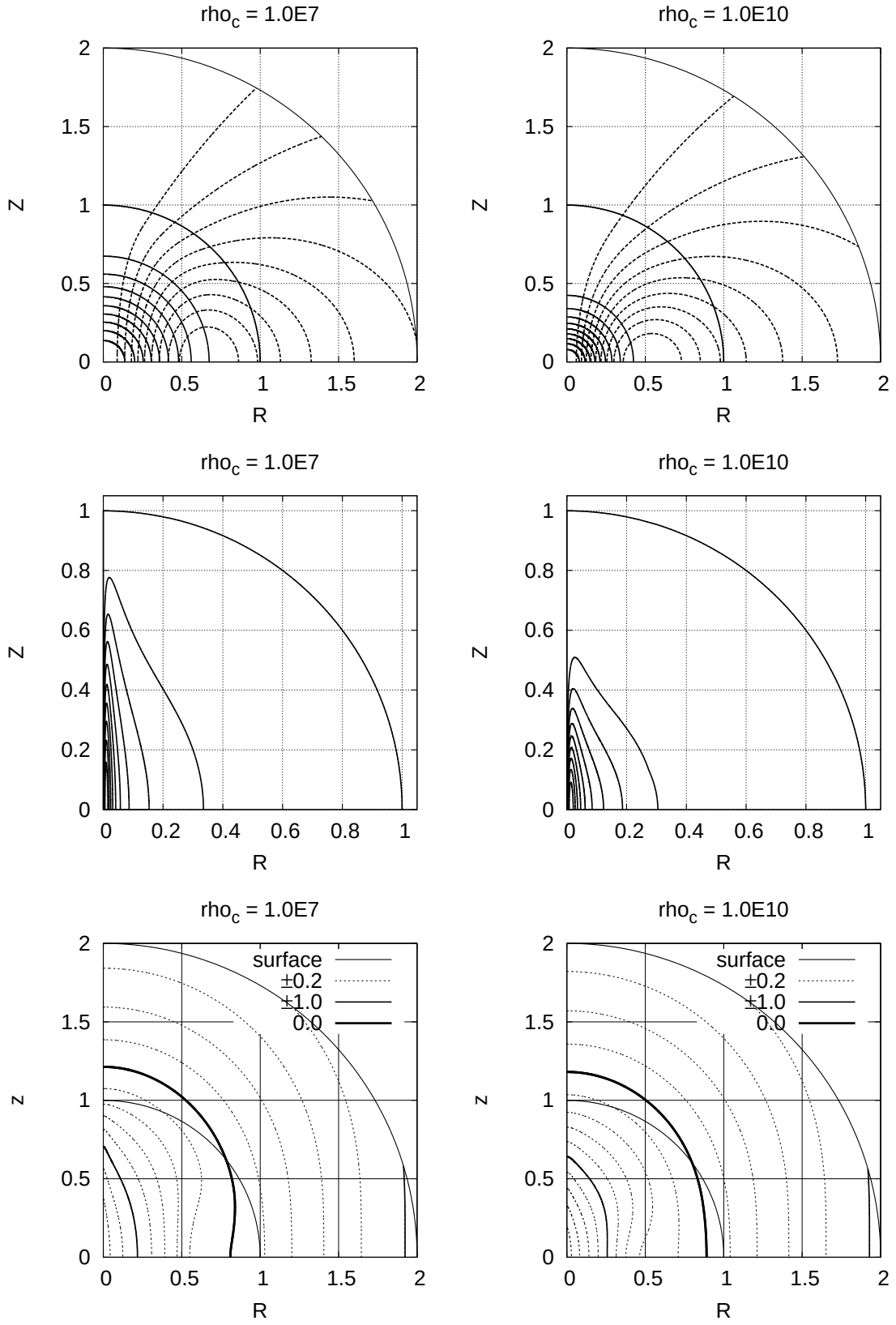

Figure 2.9: Same as Fig. 2.8 except for the equations of state. The left panels are for a white dwarf with $1.0 \times 10^7 \mathrm{gcm}^{-3}$ and the right panels are for a white dwarf with $1.0 \times 10^{10} \mathrm{gcm}^{-3}$.

Fig. 2.7 displays the ratio B_c/B_{sur} against the value of m for different equations of state. The dependency of this ratio on the value of m is qualitatively similar for these equations of state. Whichever equation of state we choose, we obtain configurations with highly localized magnetic fields, for which B_c/B_{sur} can exceed 100. The same is true for white dwarfs with highly localized magnetic fields. However, B_c/B_{sur} tends to become smaller for stiffer equations of state, as seen from Fig. 2.7.

Fig. 2.8 and Fig. 2.9 display the distribution of mass density, current density and the contour of $\log_{10}|\boldsymbol{B}|/B_{sur}$ of $m = -0.99$ configurations. Fig. 2.8 shows results for polytropes $N = 0.5$ and $N = 1.5$ (stiffest and softest equations of state among the polytropic models considered here) and Fig. 2.9 shows results for white dwarfs with $\rho_c = 1.0 \times 10^7 \mathrm{gcm}^{-3}$ and $\rho_c = 1.0 \times 10^{10} \mathrm{gcm}^{-3}$ (stiffest and softest among the white dwarf models considered here). As seen from top panels in each figure, the mass density distributions of the softer equation of state ($N = 1.5$ and $\rho_c = 1.0 \times 10^{10} \mathrm{gcm}^{-3}$) are more centrally concentrated than those of the stiffer equation of state ($N = 0.5$ and $\rho_c = 1.0 \times 10^7 \mathrm{gcm}^{-3}$). The current density distributions are also more centrally concentrated compared with the mass density distribution (middle panels). As a result, the *poloidal* magnetic fields become more highly localized for the softer equation of state (bottom panels). The mass of the white dwarf becomes higher for the higher central density. This implies that higher mass white dwarfs can have stronger interior magnetic fields deep inside if the magnetic field structure is fixed as in the present study.

2.4 Discussion and conclusions

In this chapter we have constructed axisymmetric and stationary magnetized barotropes that have extremely strong *poloidal* magnetic fields around the central region near the magnetic axis. The strength of the magnetic field in that region could be two orders of magnitude larger than that of the surface magnetic field. In the context of the neutron star physics, this would imply that there might be magnetars whose interior magnetic fields amounting to 10^{17} G if we assume the surface field to be order of 10^{15}G and that there might be magnetized white dwarfs with interior magnetic fields that reach 10^{12} G when the mass is nearly the Chandrasekhar limit and the surface field is of the order of 10^9 G.

Moreover, it should be noted that highly localized magnetized stars could have higher order magnetic multipole moments in addition to the dipole moment. Although in most astrophysical situations magnetic dipole fields have been assumed, we may need to consider configurations with contributions from higher multipole magnetic moments for some situations. In those cases, configurations with negative values of m might be used to analyze such systems.

2.4.1 Higher order magnetic multipole moments with even n

It should be noted that in the analysis of this chapter only higher magnetic multipole moments with odd $n = 2\ell+1$ where ℓ is an integer, i.e. $2^{2\ell+1}$ moments, appear and that there are no higher magnetic multipole moments with even $n = 2\ell$. This is due to the choice of the current density.

Our choice of the arbitrary function $\mu(\Psi)$ and the assumption of the symmetry of Ψ about the equator necessarily result in magnetic field distributions that are symmetric about the equator. It implies that the magnetic field should penetrate the equator and that $2^{2\ell}$ type distributions that are confined the upper or lower half of the space of the equator are excluded. In order to obtain closed magnetic field distributions in the half plane above or below the equator, the current density must be chosen so as to flow in opposite directions above and below the equatorial plane. It also implies that we need to set the current density on the equator in the φ-direction to vanish.

Concerning $2^{2\ell}$ multipole magnetic moments distributions, Ciolfi et al. (2009) have obtained such configurations. Their solutions correspond to the choice of the current density distributions that are antisymmetric about the equator.

2.4.2 Forms of arbitrary functions

One might think it curious that functions appear in the formulation and that there is no physical principle specifying how to choose those arbitrary functional forms. The same situation appears for the problem of calculating equilibrium structures or stationary structures of rotating and axisymmetric *barotropes*. For that problem, the three component equations of the equations of motion do not remain independent but come to depend on each other. This implies that one could not solve for all the three components of the flow velocity completely. Assumptions of the *stationarity* and *barotropy* reduce the problem to a degenerate problem concerning the components of the flow velocity. Although there are *three* component equations for the *three* components of the flow velocity, those three component equations are no more independent. They become dependent each other due to the *barotropic nature* of the assumption for the gas. Therefore, one needs to *specify* the *rotation law or corresponding relation* in order to find stationary or equlibrium configurations for axisymmetric barotropes. The form of the rotation law is *arbitrary*.

The only requirement for the functional form regarding the rotation law comes from the nature of the stability of the system. However, one needs to know the stability of the system beforehand. If one does not have any information about the system to be solved, one has no principle by which to choose the form of the rotation law.

The situation is the same for the *stationary* problem for axisymmetric magnetized *barotropes*. For the stationary states of axisymmetric magnetized barotropes, the situation is more complicated than that for rotating barotropes, because not only the flow velocity but also the magnetic field appears in the problem. That also leads to the appearance of a greater number of arbitrary functions in the problem. Thus it is very hard to specify the forms of arbitrary functions *physically meaningfully*. In such situations the only thing one can might be to explore many kinds of arbitrary functions to find out the general consequences of the resulting magnetic fields.

Of course, if one could obtain a lot of information of the magnetic characteristics about the equilibrium states at hand, one could constrain the arbitrary functions more appropriately and more physically meaningfully. One possibility is to rely on the stability nature of the

equilibrium, as in the rotating barotropic stars. Since there is no useful stability criterion for the field configuration with both *poloidal* and *toroidal* fields and linear stability analysis of the equilibrium is beyond our scope, we leave this issue of constraining the functional form for a future study.

2.4.3 Application to magnetars

The typical strength of the surface magnetic field of Anomalous X-ray Pulsar (AXP) and Short Gamma-ray Repeater (SGR) is considered to be $10^{14} - 10^{15}$G by assuming the magnetic dipole spin down (see e.g. Kouveliotou et al. 1998; Kouveliotou et al. 1999; Murakami et al. 1999; Esposito et al. 2009; Enoto et al. 2009; Enoto et al. 2010). According to recent observational evidences, some types of AXP and SGR are regarded as similar kinds of isolated neutron star and are categorized as magnetars, although they were first considered to belong to two different types of neutron star. (see e.g. Duncan & Thompson 1992; Duncan & Thompson 1996; Woods & Thompson 2006; Mereghetti 2008).

For neutron stars with a strong magnetic field, such as magnetars, the strength of the maximum *toroidal* magnetic field inside has been estimated to be 10^{17} G (see e.g. Thompson & Duncan 1995; Kluźniak & Ruderman 1998; Spruit 1999; Spruit 2009). Many authors have considered that only *toroidal* magnetic fields could become extremely strong and be hidden below the surfaces of the stars. Concerning *poloidal* magnetic fields, a very strong field is not considered because it would be observed as a strong surface field since it is dipole-dominated. However, as shown in this chapter, extremely strong *poloidal* magnetic fields can exist in the very central region at $r_c \sim 0.01 r_e$, as seen from Tables 2.1 and 2.2 and Fig. 2.7 and the definition of B_c, Eq. (2.40). If we apply our equilibrium models with negative values of m to magnetars with mass $1.4 M_\odot$, central density $\rho_{\max} = 1.0 \times 10^{15} \mathrm{gcm}^{-3}$ and average strength of the surface magnetic fields 10^{15} G, the strengths of the *poloidal* magnetic fields could be $10^{16} - 10^{17}$G. We also consider weak magnetized magnetars with average strength of the surface magnetic fields 10^{13} G (Rea et al. 2010). If we apply our equilibrium models, the strengths of the *poloidal* magnetic fields could be $10^{14} - 10^{15}$G. Since these strong *poloidal* magnetic fields located nearly along the magnetic axis in the central core region, the magnetic structures in the core region are highly anisotropic. If extremely strong magnetic *poloidal* fields are hidden within the core region, there could be magnetic fields with higher order multipole moments.

If the neutron star shape is deformed by a strong magnetic field and the magnetic axis is not aligned the rotational axis, gravitational waves will be emitted (Cutler 2002; Haskell et al. 2008; Mastrano et al. 2011). Gravitational wave emission tends to become stronger as the ellipticity of the meridional plane of the star becomes larger. For our models, decreasing m increases the value of $1 - q$ in the B_{sur} constant sequence (see the value of $1 - q$ in Table 2.1). Thus those models with highly localized magnetic field here may be efficient emitters of gravitational wave.

2.4.4 Some features of highly magnetized white dwarfs

It is widely believed that the effect of the stellar magnetic fields play a significant role in astrophysics. For example, isolated magnetized white dwarfs tend to have a higher mass than non-magnetic white dwarfs (Wickramasinghe & Ferrario 2000). According to observations, the surface magnetic field strength of white dwarfs varies from very little to 10^9 G (Wickramasinghe & Ferrario 2000). Therefore, there are some strongly magnetized white dwarfs whose surface magnetic field about 10^8-10^9G. For example, Jordan et al. (1998) estimated the field range 3.0×10^8-7.0×10^8 G in GD 299. EUVE J0317-855 is a massive high-field magnetic white dwarf with rapid rotation. Its magnetic field was calculated by an offset dipole model with 4.5×10^8G and period of 725 s. PG 1031+234 is a high-field magnetized white dwarf. Schmidt et al. (1986) and Latter et al. (1987) estimated its rotation period 3.4 h and its magnetic field as 5.0×10^8 - 1.0×10^9 G. The observed spectral variations cannot be fitted well by a simple dipole magnetic or offset dipole model, so they have proposed a two-component model composed of a nearly centered dipole and a strongly off-centered dipole. In other words, the magnetic field structures of several strongly magnetized white dwarfs could not be explained by applying simple dipole structures.

We have obtained strongly magnetized white dwarfs with higher order magnetic multipole moments in this chapter. If we apply our configurations with negative m, some strongly magnetized star such as PG 1031+234 may have strong interior magnetic fields. According to our numerical results, B_c could reach as high as 10^{12} G when $B_{sur} \sim 3.0 \times 10^9$ G for a highly localized ($m = -3.0$) and high mass ($\rho_c = 1.0 \times 10^9$, $M \sim 1.34 M_\odot$) model (see Fig. 2.7). Since the central magnetic field strength B_c depends on the equation of state as we have shown in Sec.3.6.2, it becomes higher as the central density increases. Thus high mass white dwarfs could have strong *poloidal* magnetic fields according to our models with negative m. As we have displayed in Sec. 2.3.1, $N = 1.5$ polytropes with negative values of m have rather large higher order magnetic multipole moments. The same is the case for magnetized white dwarf models, i.e. they have rather large higher order magnetic multipole moments. Therefore, the magnetic fields outside of such stars are far from simple dipole fields if the magnetized white dwarfs have highly localized strong *poloidal* magnetic fields deep inside the stars.

2.4.5 Comments on stability of magnetized barotropes

Once equilibrium configurations are obtained, it would be desirable to investigate their stability. However, a satisfactory formulation for the linear stability analysis for general magnetic configurations has not been fully developed, although there is a stability criterion only for purely *toroidal* magnetic configurations (Tayler 1973). For purely *poloidal* or mixed *poloidal-toroidal* magnetic configurations, magnetic configurations with rotation or other general situations, no authors have ever succeeded in obtaining a clear stability criterion (see e.g. Markey & Tayler 1973; Wright 1973; Markey & Tayler 1974; Tayler 1980; Bonanno & Urpin 2008). Therefore the stability of the configurations obtained in this chapter contain both *poloidal* and *toroidal*

magnetic fields has not been investigated.

By contrast, the stability of magnetized stars may be investigated through that time-dependent evolutionary computations of the magnetic configurations. Thanks to powerful computers, some authors have recently employed magnetohydrodynamical codes to follow the time evolutions of magnetized configurations and find out whether these configurations would settle down to certain 'stable equilibrium states'. Such investigations concerning the magnetic configurations have been carried out by Braithwaite and his coworkers as mentioned in Introduction (see e.g. Braithwaite & Spruit 2004; Braithwaite & Nordlund 2006; Braithwaite & Spruit 2006; Braithwaite 2006; Braithwaite 2007; Braithwaite 2009; Duez et al. 2010). According to their results, purely *toroidal* configurations and purely *poloidal* configurations are shown to be all unstable, as previously shown or expected (e.g. Tayler 1973; Markey & Tayler 1973; Flowers & Ruderman 1977. However, see Geppert & Rheinhardt 2006 for some results about stability). Concerning the mixed *poloidal-toroidal* magnetic configurations, recent numerical studies (Braithwaite 2009; Duez et al. 2010) have shown that they are stable as long as the following condition is satisfied:

$$\alpha \frac{\mathcal{M}}{|W|} \leq \frac{\mathcal{M}_p}{\mathcal{M}} \leq 0.8 \,, \tag{2.55}$$

where this α is a numerical factor of $10-10^3$ depending on the stellar structures. By performing 3D MHD simulations, it has been shown that non-axisymmetric perturbations to equilibrium stars grow when this condition is not satisfied. Stars with mixed magnetic fields whose dominant component is *poloidal* field seem to evolve toward non-axisymmetric configurations until the amplitude of the perturbations reach nonlinear regime and saturate. As can be seen from tables in this chapter, we have found no models that satisfy that criterion (Eq. 2.55) for our particular choice of functional forms presented above (see Sec.2.2.2), because the energy stored in the *toroidal* magnetic field is at most a few per cent for all of our models. In order to obtain configurations that satisfy the criterion, we need to choose different functional forms from those used in this chapter. We should be careful to apply the criterion, however, to general configurations of magnetic fields. The class of solutions with both *toroidal* and *poloidal* magnetic fields obtained here may be rather different from the ones studied by Braithwaite and his collaborators, even if they share the obvious characteristics of twisted-torus structures of magnetic fields. As is seen in completely different stability natures of seemingly similar configurations in Geppert & Rheinhardt (2006) and Braithwaite (2007), it is quite uncertain at this moment that failure to satisfy the criterion (Eq. 2.55) for our models here means unstable nature of them. It would be interesting to study the stability nature of our configurations thorough either linear perturbation analysis or direct MHD simulations.

2.4.6 Conclusions

In this chapter, we have presented an extended formulation for obtaining axisymmetric and stationary barotropic configurations with both the *poloidal* and *toroidal* magnetic fields. We

have shown the possibility that magnetized stars have strong *poloidal* magnetic fields inside the star. Our findings and conjectures can be summarized as follows.

1. By choosing the functional form for one of the arbitrary functions that appear in the basic formulation for the configurations under the assumptions mentioned before, we have obtained magnetized configurations in which extremely strong *poloidal* fields are confined within the central part of the near axis region. When we apply our models to magnetars, the interior magnetic strength would be 10^{17} G while the surface magnetic strength is 10^{14-15} G. On the other hand, if we apply our models to magnetized white dwarfs with mass $\sim 1.34 M_{\odot}$, the surface field strength would be 10^{9} G and B_c reaches 10^{12} G.

2. If stars have extremely strong *poloidal* magnetic fields deep inside, the contours of magnetic field strengths are not spherical but rather column-like shapes as shown in the figures.

3. If stars have extremely strong magnetic fields deep inside, contributions from higher order magnetic multipole moments to the outer fields around the stars cannot be neglected. This implies that if stars have highly localized and extremely strong magnetic fields deep inside, then observations of magnetic fields around the stars could not be explained by the simple dipole models that have been used in most situations.

What we wish, we readily believe, and what we ourselves think, we imagine others think also .
(Gaius Julius Caesar)

3

Oppositely flowing toroidal current: key to large toroidal fields

We have obtained magnetized equilibrium states with extremely strong poloidal magnetic fields fixing and changing the functional form in chapter 2. Although these solutions have very strong magnetic field deep inside the star, the magnetic field is highly localized near the center and the toroidal component of the magnetic field is much smaller than the poloidal component. Thereupon, we consider magnetized equilibrium states with large toroidal magnetic fields in this chapter.

3.1 Introduction

Analytic studies have shown that any configurations with either purely poloidal or purely toroidal magnetic fields are unstable (Tayler 1973; Markey & Tayler 1973). Stable magnetized stars should have both the poloidal and the toroidal magnetic fields. Moreover, the magnitudes of the toroidal fields must be comparable with those of the poloidal fields (Tayler 1980). This argument has been shown to be the case from the recent simulations. Braithwaite & Spruit (2004) have shown that an initial random magnetic field in stably stratified stellar layers relaxes on the stable twisted-torus magnetic field configuration after several Alfvén timescale. Similar twisted-torus magnetic field configurations have been also obtained in many previous works by numerically exact computations of the axisymmetric stationary states of magnetized stars (Tomimura & Eriguchi 2005; Yoshida & Eriguchi 2006; Lander & Jones 2009; Lander et al. 2012), structure separated Grad-Shafranov (GS) solving method (Ciolfi et al. 2009; Glampedakis et al. 2012) or zero-flux-boundary method (Prendergast 1956; Ioka & Sasaki

2004; Duez & Mathis 2010; Yoshida et al. 2012). The stabilities of these fields, however, have not been clarified yet because it is difficult to analyze their stability by linear stability analyses or other means based on the stationary configurations. On the other hand, Braithwaite (2009) and Duez et al. (2010) have shown that the stability criteria of the magnetized stars could be expressed as below:

$$\alpha \frac{\mathcal{M}}{|W|} < \frac{\mathcal{M}_p}{\mathcal{M}} \leq 0.8, \tag{3.1}$$

where $\mathcal{M}/|W|$ is the ratio of the magnetic energy to the gravitational energy. $\mathcal{M}_p/\mathcal{M}$ is the ratio of the poloidal magnetic energy to the total magnetic energy and α is a certain dimensionless factor of order 10 for main-sequence stars and of order 10^3 for neutron stars. The right hand side of this inequality means that the strong poloidal magnetic field configurations are unstable (we define that the poloidal fields are strong when $\mathcal{M}_p/\mathcal{M} > 0.8$ in this chapter).

On the other hand, the majority of investigations in which stationary states of the magnetized stars have been treated (e.g. Yoshida & Eriguchi 2006; Yoshida et al. 2006; Lander & Jones 2009; Ciolfi et al. 2009; Lander et al. 2012) and chapter 2 in this thesis failed to obtain configurations with strong toroidal magnetic fields. In these studies, stationary states of magnetized stars have been pursued either by numerically exact methods (e.g. Tomimura & Eriguchi 2005) or structure separated GS solving methods (e.g. Ciolfi et al. 2009). However, they have only found that it was very difficult to obtain stationary states of magnetized stars with very strong toroidal magnetic fields. In some of their solutions the toroidal magnetic fields have been almost as strong as the poloidal magnetic fields only in the particular local regions inside the stars, but the total energies of the toroidal magnetic fields as a whole are much smaller than those of the total poloidal magnetic fields. In other words, the ratios of $\mathcal{M}_p/\mathcal{M}$ in their solutions are much bigger than 0.8.

By contrast, some studies of magnetized stationary configurations by structure separated GS solving method (Glampedakis et al. 2012) by zero-flux-boundary method (Duez & Mathis 2010; Yoshida et al. 2012) have succeeded in obtaining the magnetized equilibria with strong toroidal magnetic fields by choosing very special boundary conditions for the poloidal magnetic fields. The boundary condition adopted by Tomimura & Eriguchi (2005) and Ciolfi et al. (2009) in which they failed to obtain configurations with strong toroidal magnetic fields is that the poloidal magnetic field lines should continue smoothly through the stellar surfaces into the vacuum region which is considered to be outside of the stars. On the other hand, the boundary condition employed by Glampedakis et al. (2012) is different. The poloidal magnetic field lines need not continue smoothly at the stellar surfaces, because in some of their models it has been allowed for the surface currents to exist. By specifying such a boundary condition, they have succeeded in finding that magnetized configurations whose total energies of the toroidal magnetic fields become much stronger as the surface currents are increased.

Duez & Mathis (2010) and Yoshida et al. (2012) also obtained the stationary configurations with strong toroidal magnetic fields, but the boundary condition which they adopted is of dif-

ferent kind from those mentioned above. Their assumptions are essentially the same as those in the previous works (Prendergast 1956; Woltjer 1959a,b, 1960; Ioka & Sasaki 2004). They imposed the boundary condition that the magnetic flux on the stellar surfaces should vanish, so all of poloidal field lines are closed and confined inside the stars and no poloidal magnetic fields penetrate to the vacuum region outside of stars. In their solutions, the region where the toroidal magnetic fields exist inside the star is much larger than that of any other models. However, they did not explain the reason why the magnetized stars can sustain such configurations with large toroidal magnetic energies under their special boundary condition.

In this chapter we will deal with magnetized configurations with large amount of the magnetic energies in the toroidal fields and present the reason why the magnetized stars can sustain strong toroidal magnetic fields within the stars. As will be shown, we have found that the total currents of the magnetized stars are important keys to understand this problem systematically and the values of the total currents seem to be deeply related to the boundary condition of the magnetic fields.

It should be noted that for the stationary configurations the magnetic fields are governed by the Grad-Shafranov equation which is of the elliptic type partial differential equation for the magnetic flux function. Therefore, the solutions of the GS equation are necessarily strongly depending on the boundary condition(s).

In this chapter, we use both the numerically exact non-force-free method (Tomimura & Eriguchi 2005) and the method in which boundary conditions are applied at finite locations from the stellar centre (e.g., Prendergast 1956; Ioka & Sasaki 2004; Duez & Mathis 2010). We will show configurations with negative surface currents or with the regions where the current become negative can sustain the strong toroidal magnetic fields inside the star. Here the term 'negative' means that the currents flow in the opposite direction to the flow direction of the bulk of the interior currents.

3.2 Formulation

Our formulation of the problem and the numerical methods are essentially the same as that of Tomimura & Eriguchi (2005) and chapter 2, i.e. the numerically exact method, and that of Duez & Mathis (2010), i.e. the zero-flux-boundary method.

3.2.1 Grad-Shafranov equation

We calculate self-gravitating, axisymmetric, stationary magnetized stars in order to obtain magnetized equilibria with strong toroidal fields in the Newtonian gravity. We assume that the system is in a stationary and axisymmetry state. For rotating stars, the rotational axis and the magnetic axis coincide and the rotation is assumed to be rigid. The star has no meridional flows. The conductivity of the stellar matter is infinite, i.e. the ideal MHD approximation is employed. There is no magnetosphere around the star. In other words, no electric current exists in the vacuum region. Therefore, the toroidal magnetic field is confined within the star and the

only poloidal component can penetrate the surface and extend to the outside of the star. We use the polytropic equation of state and fix $N = 1$ for simplicity when we compute stationary configurations by using the numerically exact method. This choice of N is the same as that adopted in the previous works (e.g. Lander & Jones 2009).

Using the flux function Ψ, we derive the Grad-Shafranov equation from Maxwell equations as follows:

$$\Delta^*\Psi \equiv \frac{\partial^2\Psi}{\partial r^2} + \frac{\sin\theta}{r^2}\frac{\partial}{\partial\theta}\left(\frac{1}{\sin\theta}\frac{\partial\Psi}{\partial\theta}\right) = -4\pi r\sin\theta\frac{j_\varphi}{c}, \tag{3.2}$$

and the form of Grad-Shafranov equation can be rewritten as (see chapter 2):

$$\Delta(A_\varphi\sin\varphi) = -\frac{4\pi}{c}j_\varphi\sin\varphi, \tag{3.3}$$

where, Δ denotes the ordinary Laplacian operator. We consider the homogeneous general solution of Eq. (3.3) in this chapter. By taking the boundary condition for the vector potential into account and using Green's function which satisfies the boundary condition, we derive the integral form of the GS equation as follows:

$$A_\varphi(\boldsymbol{r})\sin\varphi = \frac{1}{c}\int\frac{j_\varphi(\boldsymbol{r}')}{|\boldsymbol{r}-\boldsymbol{r}'|}\sin\varphi'\,d^3\boldsymbol{r}' + A_{\varphi,h}(r,\theta)\sin\varphi, \tag{3.4}$$

where $A_{\varphi,h}$ is a homogeneous general solution to Eq. (3.3) as follows:

$$A_{\varphi,h}(r,\theta) = \sum_{n=0}^{\infty}\left[a_n\frac{r_0^{n+2}}{r^{n+1}} + b_n\frac{r^n}{r_0^{n-1}}\right]P_n^1(\cos\theta). \tag{3.5}$$

Here, r_0 is a certain constant which is the stellar radius for spherical configurations, and a_n and b_n are constant coefficients which are obtained by applying the boundary condition. We will be able to obtain the stationary distributions of the magnetic vector potentials by solving this equation. Since these equations are of elliptic type partial differential equations whose source term is j_φ, the boundary conditions are very important and have significant influences on the global structures of the vector potentials or the magnetic flux functions. We will deal with this problem about the boundary condition in Sec. 3.3.

3.2.2 Toroidal magnetic fields

Once we have obtained the flux function by solving the GS equation, it is easy to calculate the poloidal magnetic fields directly. On the other hand, we can obtain the toroidal component of the magnetic field by using the conserved quantity along the flux function which can be expressed by an arbitrary function of Ψ. This arbitrary function appears because of the assumption of the axisymmetry. This function is called $\kappa(\Psi)$ in Tomimura & Eriguchi (2005) (chapter 2), F in Duez & Mathis (2010) and T in Glampedakis et al. (2012). The toroidal component

of the magnetic field is obtained from the following relation

$$B_\varphi = \frac{\kappa(\Psi)}{r\sin\theta}. \tag{3.6}$$

This arbitrary function also appears in the expression of the current density as follows:

$$\frac{\boldsymbol{j}}{c} = \frac{1}{4\pi}\frac{d\kappa(\Psi)}{d\Psi}\boldsymbol{B} + \rho r\sin\theta\mu(\Psi)\boldsymbol{e}_\varphi\ , \tag{3.7}$$

where, $\mu(\Psi)$ is another arbitrary function of Ψ. The arbitrary function $\mu(\Psi)$ is the same as G in Duez & Mathis (2010) and F in Glampedakis et al. (2012). Then, we express the φ component of the current density as below:

$$\frac{j_\varphi}{c} = \frac{1}{4\pi}\frac{d\kappa(\Psi)}{d\Psi}\frac{\kappa(\Psi)}{r\sin\theta} + \rho r\sin\theta\mu(\Psi)\ . \tag{3.8}$$

The first term of Eq. (3.8) is the force-free current density part and the second term is the non-force-free current part because of $\nabla\times\boldsymbol{B} = 4\pi\boldsymbol{j}/c$. If $\mu = 0$ in a certain region, the magnetic field there is force-free, because $\boldsymbol{j}\propto\alpha\boldsymbol{B}$ in that region. We will call the first term as the κ term, and the second term as the μ term of the current density in this chapter. In a naive treatment, it seems to be enough to make the contribution from the κ term larger in order to make the toroidal magnetic fields larger. However, it has been very difficult to make the influence from the κ term strong. The reason for that is as follows. The distribution of Ψ is obtained by solving the GS equation, but the source term of the GS equation contains the κ term which is an arbitrary function of Ψ and is confined to a restricted region in the interior of the star because we impose the magnetic flux function to be *smoothly* connected on the stellar surface. Therefore, if we change the functional form and values of parameters which appear in the functional form of κ as well as the the region where κ does not vanish, the distribution of the flux function also changes according to the changes of κ. We will discuss this difficulty in Sec. 3.4.2.

3.3 Surface currents

In this section, we deal with the relation between the surface current and the magnetic field, which is deeply influenced by the boundary conditions. The surface current can be defined either by the discontinuity of the derivative of the magnetic flux function, or by the homogeneous term in the integral representation for the vector potential. The both definitions for the surface current give exactly the same values as we will see later.

3.3.1 Relation between the surface current and the discontinuity of the magnetic field

At first, we will show a relation between the surface current and the discontinuity of the magnetic field as follows. If the Ampére's equation is applied to an area S bounded by a boundary

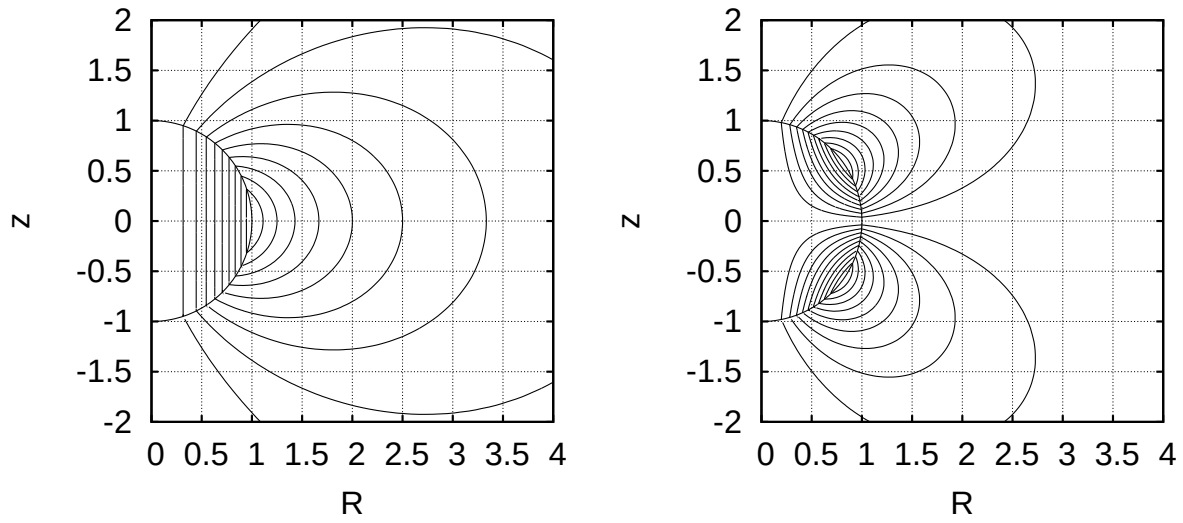

Figure 3.1: Poloidal magnetic field lines with a purely dipole (n=1) surface current (left) and a purely quadrupole $(n = 2)$ surface current (right).

∂S, we can write it by an integral form as follows:

$$\oint_{\partial S} \boldsymbol{B} \cdot d\boldsymbol{\ell} = \frac{4\pi}{c} \int_S \boldsymbol{j} \cdot d\boldsymbol{S}, \tag{3.9}$$

where $d\boldsymbol{\ell}$ and $d\boldsymbol{S}$ are a line element and a surface element, respectively. We apply this equation to an infinitely small area in the meridional plane of the star bounded by four lines as follows:

$$r = r_s(\theta_1) - \frac{\Delta r}{2}\,, \tag{3.10}$$

$$r = r_s(\theta_1) + \frac{\Delta r}{2}\,, \tag{3.11}$$

$$\theta = \theta_1\,, \tag{3.12}$$

$$\theta = \theta_1 + \Delta\theta\,, \tag{3.13}$$

where θ_1, Δr and $\Delta\theta$ are a constant, infinitesimal widths in the r-direction and in the θ-directions, respectively. For this infinitesimal area, we obtain

$$\begin{aligned} &\Big[B_r^{ex}(r_s,\theta) - B_r^{in}(r_s,\theta)\Big]\Delta r + \Big[B_\theta^{ex}(r_s,\theta) - B_\theta^{in}(r_s,\theta)\Big] r_s \Delta\theta \\ &= \frac{4\pi}{c} \int_{r_s-\Delta r/2}^{r_s+\Delta r/2} j_\varphi(r,\theta) r\, dr \Delta\theta, \end{aligned} \tag{3.14}$$

where B^{ex} and B^{in} are the exterior and interior values of the magnetic fields. Here, if the current density is a surface current on the stellar surface $(r = r_s(\theta))$ defined by $j_\varphi(r,\theta) = j_{sur}(\theta)\delta(r - r_s(\theta))$, we can integrate the equation as below

$$\int_{r_s-\Delta r/2}^{r_s+\Delta r/2} j_\varphi(r,\theta) r\, dr = \int_{r_s-\Delta r/2}^{r_s+\Delta r/2} j_{sur}(\theta)\delta(r - r_s) r\, dr = r_s j_{sur}(\theta). \tag{3.15}$$

Since the r dependence of the magnetic fields are continuous on the stellar surface ($r = r_s(\theta)$), we obtain a relation as follows:

$$B_\theta^{ex}(r_s,\theta) - B_\theta^{in}(r_s,\theta) = \frac{4\pi}{c} j_{sur}(\theta). \tag{3.16}$$

The surface current is expressed by the discontinuity of the θ-component of the magnetic field. For more general situations, we can obtain the following equation for the surface current using the parallel component $B_{||}$ to the stellar surface,

$$B_{||}^{ex}(r_s,\theta) - B_{||}^{in}(r_s,\theta) = \frac{4\pi}{c} j_{sur}(\theta). \tag{3.17}$$

If the surface current exits, the parallel component of the magnetic field must be discontinuous. We emphasize that the value of the discontinuity of the magnetic field between just inside and just outside of the stellar surface equals the surface current density.

Glampedakis et al. (2012) expressed the surface current density in a different way as follows. They defined the surface current by imposing the discontinuity of poloidal magnetic fields at the stellar surface (see Eq. 67 in Glampedakis et al. 2012). Their discontinuous boundary condition is just an *assumption* without a firm foundation as follows:

$$b_\theta^{in} = \xi b_\theta^{ex} \Leftrightarrow b_\theta^{ex} - b_\theta^{in} = (1-\xi) b_\theta^{ex} = j_{sur}. \tag{3.18}$$

Here b and ξ indicate the magnetic field and a discontinuity parameter, respectively, in their chapter. Since their model is a purely dipole configuration, the exterior solution of b_θ is $b_\theta^{ex}(x) = \frac{1}{2x} d\hat{\alpha}/dx \sin\theta$ (Eq. 61 in Glampedakis et al. 2012). Here α and x indicate the r-component of the flux function and the dimensionless radius normalized by the stellar radius. Then we can calculate the distribution of their surface current density as follows,

$$j_{sur} = \left[(1-\xi) \frac{1}{2x} \frac{d\alpha}{dx} \sin\theta \right]_{(x=1)} = -j_0 \sin\theta, \tag{3.19}$$

where

$$j_0 = \left[(\xi - 1) \frac{1}{2x} \frac{\partial \hat{\alpha}}{\partial x} \right]_{(x=1)}.$$

Since they calculated only models with $\xi > 1$ in their paper, the surface current density of their models flows in the opposite direction to the interior bulk toroidal current density inside the star. In other words their surface current is negatively flowing with respect to the bulk interior currents. According to Glampedakis et al. (2012), if the value for the discontinuity for the poloidal magnetic field is increased, the energy of the toroidal magnetic fields becomes larger (see Fig. 5 in Glampedakis et al. 2012). Therefore we conclude that the negative surface current sustain strong toroidal magnetic fields comparing with those in Tomimura & Eriguchi models without surface currents.

3.3.2 Surface currents in the integral representation

Using the integral representation for the vector potential, we can see the surface current from a different point of view. We assume that a magnetized star has no currents in the stellar interior except for the surface current. It implies that the source term for the GS equation consists only of the surface current. We can obtain the magnetic field by calculating Eq. (3.4),

$$A_\varphi \sin\varphi = \frac{1}{c}\int \frac{j_{sur}(r',\theta')}{|\boldsymbol{r}-\boldsymbol{r}'|}\sin\varphi'\, d^3\boldsymbol{r}'. \tag{3.20}$$

Since the surface current exists on the stellar surface $r = r_s$, we can describe the surface current density using the Dirac's delta function:

$$\frac{j_{sur}(r',\theta')}{c} = \delta(r'-r_s)j_{sur}(\theta')\ , \tag{3.21}$$

where $j_{sur}(\theta)$ is the surface current which flows along the surface. We can expand and integrate Eq. (3.20) using the Legendre functions and the axisymmetry of the system. We obtain the solutions for A_φ as follows:

$$A_\varphi(r,\theta) = \sum_{n=1}^{\infty}\frac{2\pi}{n(n+1)}P_n^1(\cos\theta)f_n(r,r_s)r_s^2\int_0^\pi \sin\theta' P_n^1(\cos\theta')j_{sur}(\theta')\,d\theta', \tag{3.22}$$

where f_n is a function defined by

$$f_n(r,r_s) = \begin{cases} r_s^n/r^{n+1}, & (r \geq r_s) \\ r^n/r_s^{n+1}. & (r \leq r_s) \end{cases}\ . \tag{3.23}$$

Now we calculate the vector potential and the magnetic field by giving a θ-distribution for the surface current density. We assume the θ-distribution of the surface current can be expressed by the expansion using Legendre functions,

$$j_{sur}(\theta) = \sum_{n=1}^{\infty}\frac{2n+1}{4\pi}\alpha_n P_n^1(\cos\theta), \tag{3.24}$$

where α_n's are dimensionless coefficients related to the nth associate Legendre function $P_n^1(\cos\theta)$. Then using the orthogonality among the Legendre functions,

$$\int_0^\pi \sin\theta' P_n^1(\cos\theta')P_n^1(\cos\theta')\,d\theta' = 2\frac{(n+1)n}{2n+1}, \tag{3.25}$$

we can obtain an analytically expressed solutions as follows:

$$A_\varphi(r,\theta) = \sum_{n=1}^{\infty}\alpha_n r_s^2 f_n(r,r_s)P_n^1(\cos\theta), \tag{3.26}$$

and

$$\Psi(r,\theta) = \sum_{n=1}^{\infty} \alpha_n r r_s^2 f_n(r, r_s) P_n^1(\cos\theta)\sin\theta. \tag{3.27}$$

If we set $\alpha_n = a_n + b_n$, the right hand side of Eq. (3.26) is exactly the same as homogeneous general solutions of Eq. (3.5). Therefore, adding the homogeneous term to the inhomogeneous solution of the GS equation corresponds exactly to adding the surface current at the boundary surface.

Fig. 3.1 shows the poloidal magnetic field lines for configurations with the purely dipole ($n = 1$) surface current (left panel) and with the purely quadrupole ($n = 2$) surface current (right panel). It should be noted that each model has no interior currents except for the surface currents as we have described in this section.

3.4 Numerically exact configurations for open magnetic fields with surface currents

We will show numerically exact structures of magnetized stars with open field lines and with/without surface currents in this section. At first, we will display configurations which have no surface currents. Although they are the same as those obtained in Yoshida & Eriguchi (2006) and Lander & Jones (2009), we will check these models from a different point of view, i.e. in the context of the influence of the surface currents. Next, magnetized stars which have surface currents will be treated and discussed.

3.4.1 Setting of the problem

As discussed before, we have solved the integral equation derived from the GS equation by considering the presence of the surface currents as follows:

$$A_\varphi(\boldsymbol{r})\sin\varphi = \frac{1}{c}\int \frac{j_\varphi(\boldsymbol{r}') + j_{sur}(\boldsymbol{r}')}{|\boldsymbol{r}-\boldsymbol{r}'|}\sin\varphi'\, d^3\boldsymbol{r}'\ , \tag{3.28}$$

where j_{sur} is the surface current density of the magnetized star. We choose the following two different distributions for the surface currents:

$$\frac{j_{sur}(r,\theta)}{c} = -j_0 \sin\theta\delta(r - r_s(\theta)),\ (\text{dipole distribution})\ , \tag{3.29}$$

and

$$\frac{j_{sur}(r,\theta)}{c} = -j_0 \sin\theta\cos\theta\delta(r - r_s(\theta)).\ (\text{quadrupole distribution}) \tag{3.30}$$

As for the arbitrary functions appearing in our formulation, we choose the following forms

in this chapter:

$$\mu(\Psi) = \mu_0 \,, \tag{3.31}$$

$$\int \mu(\Psi)\, d\Psi = \mu_0 \Psi \,, \tag{3.32}$$

$$\kappa(\Psi) = \begin{cases} 0, & \text{for } \Psi \leq \Psi_{V\max} \,, \\ \dfrac{\kappa_0}{k+1}(\Psi - \Psi_{V\max})^{k+1}, & \text{for } \Psi > \Psi_{V\max} \,, \end{cases} \tag{3.33}$$

and

$$\kappa'(\Psi) = \begin{cases} 0, & \text{for } \Psi \leq \Psi_{V\max} \,, \\ \kappa_0(\Psi - \Psi_{V\max})^{k}, & \text{for } \Psi > \Psi_{V\max} \,, \end{cases} \tag{3.34}$$

Here, μ_0, k and κ_0 are constant parameters and $\Psi_{V\max}$ means the maximum value of Ψ in the vacuum region. In this chapter, we fix $k = 0.1$. These functional forms and the value of k are the same as those chosen in other papers (Yoshida & Eriguchi 2006; Lander & Jones 2009) and chapter 2. In this section, we set the polytropic index $N = 1$ (e.g. Lander & Jones 2009), and $q = 0.9$ where q is the ratio of the polar radius to the equatorial radius defined by (see chapter 2)

$$q \equiv \frac{r_s(\theta = 0)}{r_s(\theta = \pi/2)}. \tag{3.35}$$

Concerning the angular velocity Ω, we choose values of $\hat{\Omega} = \text{constant} \equiv \hat{\Omega}_0 = 1.0\text{E-}2$ for rigidly rotating configurations and $\hat{\Omega}_0 = 0.0$ for non-rotating models. Here quantities with $\hat{}$ represent the corresponding ones transformed into dimensionless forms as shown in chapter 2.

Although the equations of state influence the strengths of the toroidal magnetic fields (see Kiuchi & Kotake 2008), we have treated only $N = 1$ polytropes because the main concern in this chapter is how the surface current density affects the distributions of the magnetic fields, in particular to the toroidal magnetic fields.

In order to examine the accuracies of solutions, we have used the virial relation as shown in chapter 2. As for mesh points, we use two computational regions because we need to integrate poloidal magnetic field energy even at a far distant place from the star. One is $\hat{r} = [0, 1]$, $\theta = [0, \pi]$, i.e. for the stellar interior region, and the other is $\hat{r} = [1, 100]$, $\theta = [0, \pi]$, i.e. for the vacuum region. We discretize the stellar interior region into mesh points with an equal interval $d\hat{r}$ and the vacuum region into mesh points with an equal interval $d\hat{s}$ where $\hat{s}$ is defined as below:

$$\hat{s} = \frac{\hat{r}}{1 + \hat{r}}. \tag{3.36}$$

The region of $\hat{r}[1, 100]$ corresponds to the region of $\hat{s}[1/2, 100/101]$. We use the same mesh number in these two regions. As for the θ-direction, we discretize it into mesh points with an

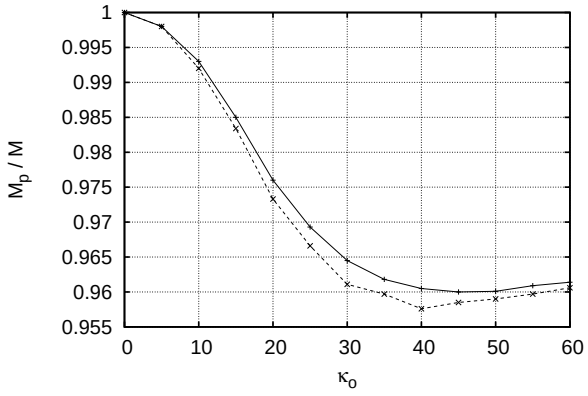

Figure 3.2: The ratio of the poloidal magnetic energy to the total magnetic energy against the parameter $\hat{\kappa}_0$. The solid line denotes a rigidly rotating sequence with $\hat{\Omega}_0 = 1.0$E-2.0 and the dashed line denotes a non-rotating sequence, i.e. a sequence with $\hat{\Omega}_0 = 0.0$. Minimum values seem to be attained at $\hat{\kappa}_0 \sim 40$ (for the non-rotating sequence) and $\hat{\kappa}_0 \sim 45$ (for the rigidly rotating sequence).

equal interval ($d\theta$). We compute some configurations and change the number of grid points. If we use mesh numbers, $N_r = 513$ and $N_\theta = 513$, the typical VC values are smaller than $1.0 \times 10^{-4} \sim 10^{-5}$. These values are small enough to be able to consider the systems are in equilibrium states (see also chapter 2; Hachisu 1986a). Thus we fixed the mesh numbers $N_r = 513$ and $N_\theta = 513$ during all calculations in this chapter to obtain accurate magnetized configurations.

3.4.2 Configurations without surface currents

Since the value of $\hat{\kappa}_0$ affects the local behavior of the toroidal magnetic field distributions, in particular on its maximum value (see Lander & Jones 2009), we have solved the magnetized configurations by changing the value of $\hat{\kappa}_0$ for two values of $\hat{\Omega}_0$.

Obtained results are plotted in Fig. 3.2 which shows the ratio of $\mathcal{M}_p/\mathcal{M}$ against $\hat{\kappa}_0$. As seen from this figure, there is a minimum value of the ratio. It implies that the toroidal magnetic field energy increases to its maximum value at $\hat{\kappa_0} \sim 40$ for non-rotating configurations and at $\hat{\kappa}_0 \sim 45$ for rigidly rotating models. Since the term related to the rotation does not appear in the current density formula (see Eq. 3.7), the rotation affects the toroidal magnetic field distributions only slightly. Therefore, we will display and discuss only configurations with rotation in the following part of this section.

In many investigations which have been done by applying numerically exact methods or by structure separated GS solving method zero-flux-boundary methods, almost similar results as ours shown in Fig. 3.2 have been obtained (see Table 2 in Lander & Jones 2009, Fig. 12 in Ciolfi et al. 2009, Fig. 4 in Glampedakis et al. 2012). Therefore, this behavior of the toroidal magnetic field against the value of $\hat{\kappa_0}$ is likely to be a general feature of stationary magnetized stars which have open magnetic fields.

In order to consider the reason of the presence of these minimum values, in Fig. 3.3 shown

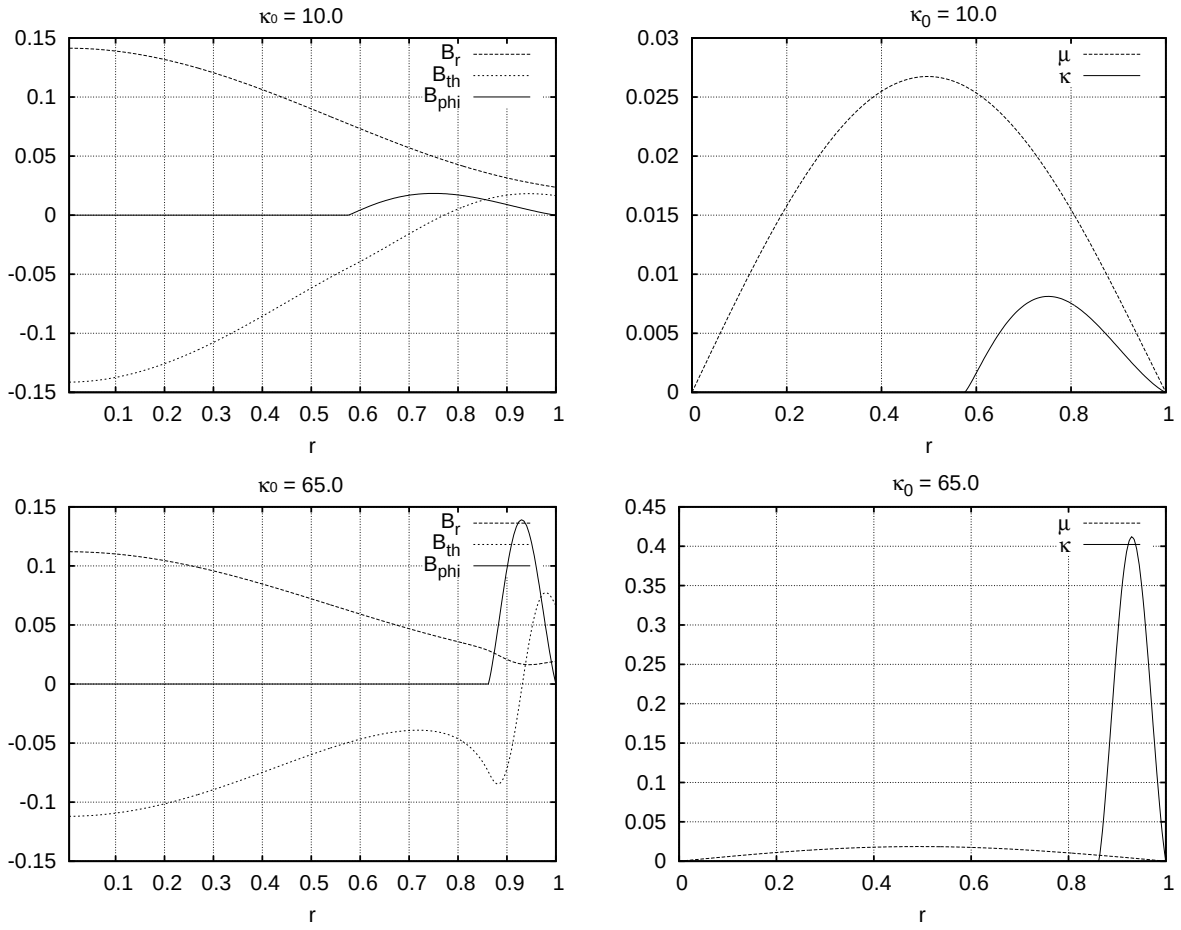

Figure 3.3: Left panels: Distributions of the components of the magnetic field $[\hat{B}_r(\theta = 0), \hat{B}_\theta(\theta = \pi/2), \hat{B}_\varphi(\theta = \pi/2)]$ are shown. Right panels : Distributions of the two source terms on the equator, which appear in the current density formula, are shown. Chosen values of $\hat{\kappa}$ are $\hat{\kappa}_0 = 10$ (top) and $\hat{\kappa}_0 = 65$ (bottom).

are the distributions of the magnetic field components (left panels) and those of the two components of the current density formula (right panels). Different curves in the left panels mean $\hat{B}_r(\theta = 0)$ (dotted line), $\hat{B}_\theta(\theta = \pi/2)$(dashed line) and $\hat{B}_\varphi(\theta = \pi/2)$(solid line) distributions for the region $\hat{r}[0, 1.0]$. In the right panels, the solid line denotes the force-free κ term and the dashed line denotes the non-force-free μ term in the current density formula.

As seen from these panels, by increasing the value of $\hat{\kappa}_0$, which corresponds to increasing the maximum strength of the toroidal magnetic field, from top panels to bottom panels, we can find that the width of the toroidal magnetic field region becomes narrower. The values of the toroidal magnetic field energy seem to depend on the distributions of the toroidal magnetic fields and of the current densities, in particular, on the maximum value and the width of the toroidal magnetic field distribution. Although the maximum value of the κ term of the current density increases with $\hat{\kappa}_0$, its width becomes narrower as $\hat{\kappa}_0$ is increasing. It implies that the slope of the distribution of the κ term becomes steeper for the large value of the current density. This tendency is also seen in the distribution of B_φ. By contrast with this, the distributions of the μ term are almost the same because we fix q and $\hat{\Omega}_0$ which are related to the characteristic nature of the non-force-free magnetic fields.

From Eq. (3.7) and our numerical results, we can find that in order to sustain strong toroidal magnetic fields (appearing in the right hand side of the equation), the strong toroidal current density (appearing in the left hand side of the equation) is required. It should be noted that the strength of the toroidal magnetic field seems to be related deeply to the strength of the total current density. This can be seen from the following argument. We introduce several definitions about integrated currents as follows:

$$\hat{J}^{(+)}_{tot} \equiv \int_{S_{mer}} \hat{j}^{(+)}_\varphi dS \ , \tag{3.37}$$

$$\hat{J}^{(-)}_{tot} \equiv \int_{S_{mer}} \hat{j}^{(-)}_\varphi dS \ , \tag{3.38}$$

$$\hat{J}^{\kappa}_{tot} \equiv \int_{S_{mer}} \hat{j}^{\kappa}_\varphi dS \ , \tag{3.39}$$

$$\hat{J}^{\mu}_{tot} \equiv \int_{S_{mer}} \hat{j}^{\mu}_\varphi dS \ , \tag{3.40}$$

$$\hat{J}_{sur} \equiv \int_{S_{mer}} \hat{j}_{sur} dS = -\hat{j}_0 \int_0^\pi r_s(\theta) \sin\theta d\theta \ , \tag{3.41}$$

$$\hat{J}_{tot} \equiv \hat{J}^{(-)}_{tot} + \hat{J}^{(+)}_{tot} + \hat{J}_{sur} = \hat{J}^{\kappa}_{tot} + \hat{J}^{\mu}_{tot} + \hat{J}_{sur} \ , \tag{3.42}$$

where S_{mer} denotes the meridional plane which is perpendicular to the φ-coordinate and dS is an area element in the meridional plane. Here, $\hat{j}^{(+)}_\varphi$, $\hat{j}^{(-)}_\varphi$, $\hat{j}^{\kappa}_\varphi$ and $\hat{J}^{\mu}_\varphi$ the φ-component of the positively flowing interior current density, the φ-component of the negatively flowing interior current density, the κ term of the current density and the μ term. Furthermore, $\hat{J}^{(+)}_{tot}$, $\hat{J}^{(-)}_{tot}$, $\hat{J}^{\kappa}_{tot}$, $\hat{J}^{\mu}_{tot}$, $\hat{J}_{sur}$ and $\hat{J}_{tot}$ are the total *positive* bulk interior current, the total *negative* bulk interior current, the total κ term bulk interior current, the total μ term bulk interior current, the total

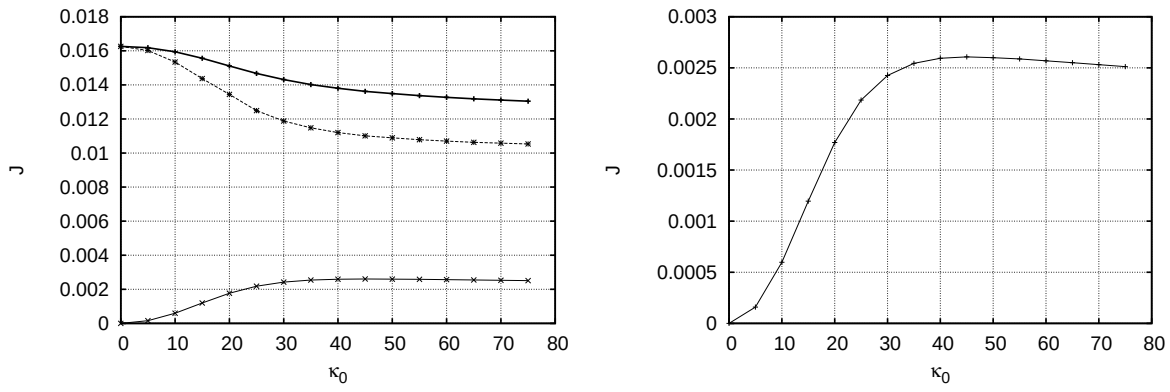

Figure 3.4: Left panels: The total current $\hat{J}_{tot}$ (thick solid line), the total μ term interior current $\hat{J}^{\mu}_{tot}$ (dashed line) and the total κ term interior current $\hat{J}^{\kappa}_{tot}$ (thin solid line) are plotted against $\hat{\kappa}_0$ for configurations without surface currents. Right panels: Only the $\hat{J}^{\kappa}_{tot}$ is plotted against $\hat{\kappa}_0$. The magnitude of the $\hat{J}^{\kappa}_{tot}$ has an upper bound near at $\hat{\kappa}_0 \sim 45$.

surface current and the total (bulk + surface) current in the meridional plane, respectively. As we shall see, these quantities will play key roles to understand the problem.

In Fig. 3.4, the total current, the total μ current and the total κ current of the star is plotted against $\hat{\kappa}_0$. We find from Fig. 3.4 that the total current does not increase as κ_0 increases and the total κ current increases to its maximum value near at $\hat{\kappa}_0 \sim 45$. We will denote the maximum value of the total current as $J^{(max)}_{tot}$ in this chapter. This $\hat{\kappa}_0$ value is the same as that for the minimum value of $\mathcal{M}_p/\mathcal{M}$. Therefore it is important to note that there is an upper bound of the total current for configurations if we consider a stationary sequence with different values of $\hat{\kappa}_0$.

This upper bound comes from our boundary condition for the current density. Since we have imposed that the outside of the star is vacuum, the current density needs to vanish in that vacuum region. As we have seen, the magnetized stars need large and strong toroidal currents in order to sustain strong toroidal magnetic fields. However, the boundary condition sets limit to the total current of the star as seen from Fig. 3.4. As a result, the region where the current density attains a rather large value becomes smaller and the slope of the distribution of the current density becomes steeper in order to sustain the stronger toroidal magnetic field in the narrower region.

Moreover, larger values of $\hat{\kappa}_0$ cause the maximum value of the magnetic flux function in the *vacuum* region larger, in general. As far as our boundary condition for the magnetic flux function to be smooth at the stellar surface is employed, the support of the κ function becomes smaller and smaller as the value of $\hat{\kappa}_0$ is increased. In other words, increasing the value of $\hat{\kappa}_0$ might, in ordinary situations, result in increasing the interior currents but at the same time decreasing the support region of the function κ because the maximum value of the magnetic flux function in the vacuum region also becomes larger as explained before.

This is the reason why in the present investigation as well as in other works thus far done nobody could obtain solutions which exceed this upper bound. To overcome this limitation

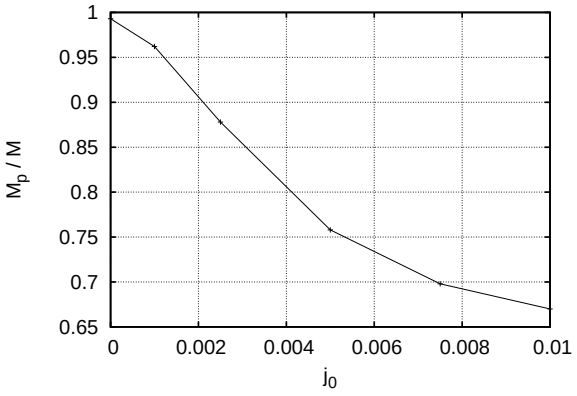

Figure 3.5: The ratio of the poloidal magnetic energy to the total magnetic energy of the models with surface current against the parameter $\hat{j}_0$.

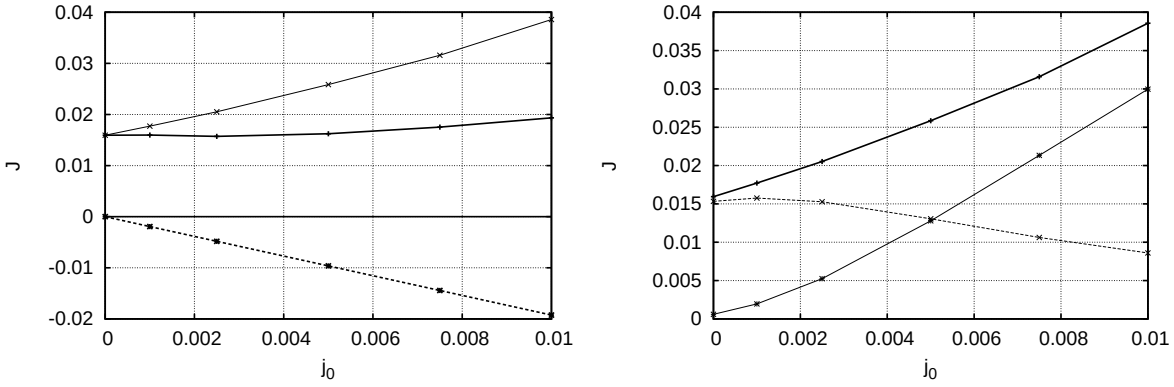

Figure 3.6: Left panel: $\hat{J}_{tot}$ (thick solid line), $\hat{J}^{(+)}_{tot}$ (thin solid line) and $\hat{J}_{sur}$ (thick dashed line) are plotted against $\hat{j}_0$. Right panel: $\hat{J}^{(+)}_{tot}$ (thick solid line), $\hat{J}^{\mu}_{tot}$ (thin dashed line) and $\hat{J}^{\kappa}_{tot}$ (thin solid line) are plotted against $\hat{j}_0$.

about the size of the confined region of the large toroidal magnetic field, the magnetized stars needs other kinds of distributions for the toroidal current densities.

From these consideration, we need to devise some means to fulfill the following seemingly contradicted requirements at the same time.

(1) φ-currents must be increased. In ordinary situations, this would results in reducing the support region of the function κ because of the increase of the maximum value of the magnetic flux function in the vacuum. (2) The support region for the function must be widened. In ordinary situations, the support region of the function κ is wider for the smaller values of κ_0.

These two seemingly contradictory requirements could be realized by introducing *negatively flowing* currents near/on the surface because the negatively flowing currents allow the positively flowing interior currents to become larger and at the same time negatively flowing currents near/on the surface could reduce the value of the magnetic flux function in the vacuum region and result in the smaller value for Ψ_{Vmax}.

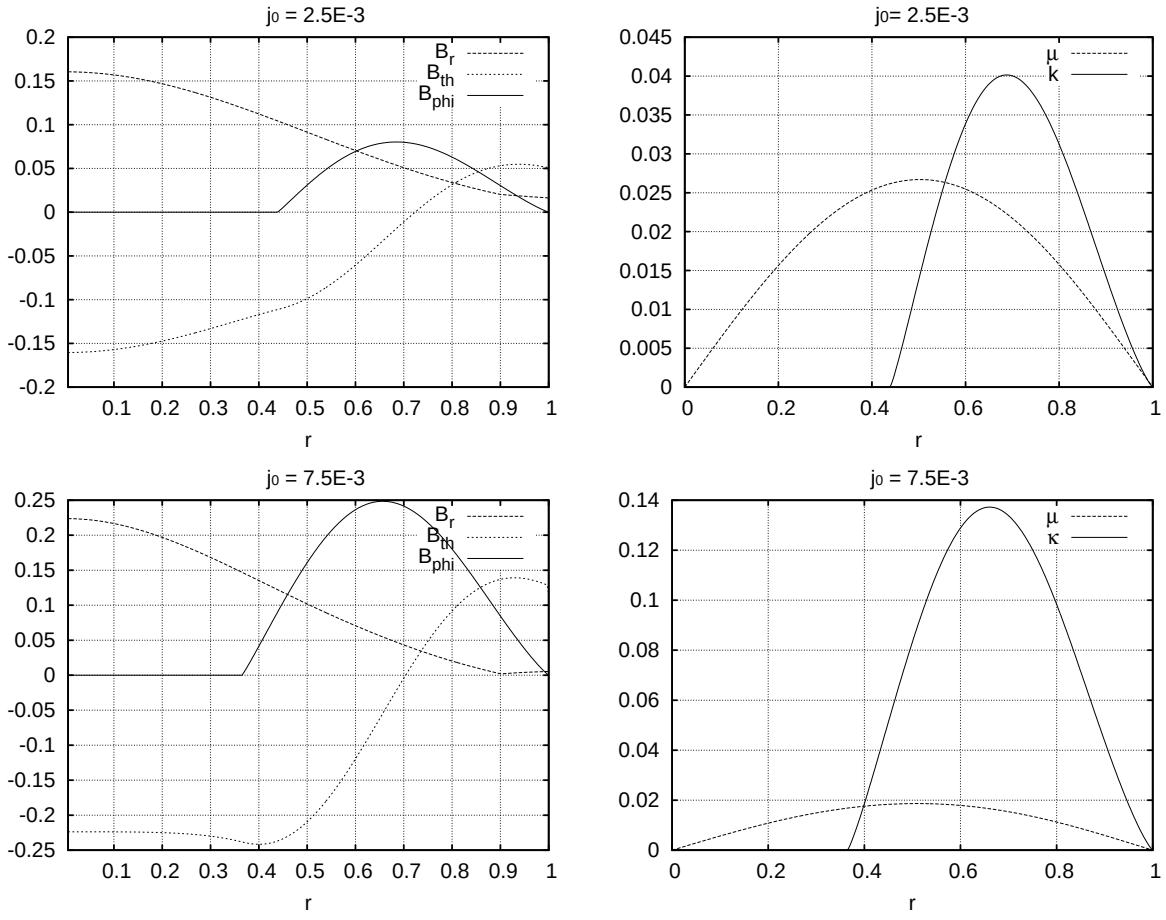

Figure 3.7: The same as Fig. 3.3 except for configurations with non vanishing surface currents, i.e. configurations with $\hat{j}_0 = 2.5 \times 10^{-3}$ (top) and $\hat{j}_0 = 7.5 \times 10^{-3}$ (bottom).

3.4.3 Configurations with surface currents – Dipole currents

As explained in the previous subsection, in order to exceed the upper bound of $\hat{J}_{tot}$ found in this chapter and to reduce the value of Ψ_{Vmax}, we will try to investigate the magnetized stars which contain oppositely flowing surface toroidal currents against the interior 'bulk' currents which are flowing in a certain direction. We will call such oppositely flowing currents as *negative* currents, hereafter. In short, we will assume that there could be toroidal surface currents which flow to the negative direction compared to the flow direction of the interior main currents which we will call the *interior bulk* currents. In fact the effects of the presence of the oppositely flowing surface currents are similar to those of the boundary conditions treated in section 5.2 of Glampedakis et al. (2012) as we have shown in Sec. 3.3.1. As we shall show, magnetized stars with negative surface currents will be able to sustain much stronger interior bulk currents and have much stronger toroidal magnetic fields because the oppositely flowing surface current cancels the effects of the interior toroidal currents to certain extent and results in configurations which have the following two special characteristics.

1. In such configurations, although the total currents $\hat{J}_{tot}$ are below the upper bound $\hat{J}_{tot}^{(max)}$ discussed before, much stronger positive interior bulk currents $\hat{J}_{tot}^{(+)}$ are allowed to exist.
2. At the same time, in such configurations, the absolute values of the magnetic flux function in the outer vacuum region can become smaller than those of configurations without negatively flowing surface currents. Thus the support region for the arbitrary function $\kappa(\Psi)$ can become wider than that for configurations without surface currents.

In this subsection, as an example, the dipole-like distribution for the surface current as Eq. (3.29) is employed. If the magnetized stars are purely spherical with no interior currents within the stars, dipole-like surface currents result in uniformly distributed interior magnetic fields and purely dipole exterior magnetic fields (see Fig. 3.1). Thus, if the surface current densities are much stronger than the interior current densities, the interior magnetic fields become almost uniform and there are no closed magnetic fields inside of the stars. The toroidal magnetic fields could not appear in such configurations.

We have calculated many stationary configurations with surface currents for several values of $\hat{\kappa}_0$. As a result, we found that a model with $\hat{\kappa}_0 = 10$ has the smallest value of $\mathcal{M}_p/\mathcal{M}$ in all our stationary solutions. Thus we will show only configurations with $\hat{\kappa}_0 = 10$ in this chapter, but it should be noted that all other models show almost the same tendency as that of configurations with $\hat{\kappa}_0 = 10$ which we will describe below. Fig. 3.5 shows the values of $\mathcal{M}_p/\mathcal{M}$ and Fig. 3.6 shows the values of $\hat{J}_{tot}$ (thick solid line), $\hat{J}_{tot}^{(+)}$ (thin solid line) and $\hat{J}_{sur}$ (thick dashed line) in the left panel and the value of $\hat{J}_{tot}^{(+)}$ (thick solid line), $\hat{J}_{tot}^{\mu}$ (thin dashed line) and $\hat{J}_{tot}^{\kappa}$ (thin solid line) in the right panel against the values of $\hat{j}_0$ for configurations with $\hat{\kappa}_0 = 10$. In these models, there is no negative current $\hat{j}_{\varphi}^{(-)}$ in the star. Therefore, $\hat{J}_{tot}^{(-)} = 0$ and $\hat{J}_{tot}^{(+)} = \hat{J}_{tot}^{\kappa} + \hat{J}_{tot}^{\mu}$ in these configurations. From this figures, we can see that if we increase the value of $\hat{j}_0$, the total bulk current of the magnetized star, $\hat{J}_{tot}^{(+)}$, becomes larger (Fig. 3.6) and the value of $\mathcal{M}_p/\mathcal{M}$ becomes smaller (Fig. 3.5). We can see from left panel of Fig. 3.6 that

the total current $\hat{J}_{tot}$ is almost the same as the upper bound of the total current $\hat{J}_{tot}^{(max)}$ defined before. However, the total positive current $\hat{J}_{tot}^{(+)}$ becomes much larger than this upper bound. Especially noted from the right panel in Fig. 3.6, the total κ current term becomes much larger and the total μ current term becomes slightly small. This can be considered as an evidence that the negative surface current cancels some contributions of the positively flowing interior toroidal current from the κ term current. It is remarkable that the value of $\mathcal{M}_p/\mathcal{M}$ attains about 0.7 when $\hat{j}_0 = 7.5 \times 10^{-3}$. It implies that the magnitude of the toroidal magnetic field energy is almost the same order as that of the poloidal magnetic energy for those models around $\hat{j}_0 = 7.5 \times 10^{-3}$. The ratio $\mathcal{M}_p/\mathcal{M} \sim 0.65$ seems to be the minimum value in the present parameter space because we could not succeed in obtaining numerical solutions when $\hat{j}_0 > 1.0 \times 10^{-2}$. Since the surface current with $\hat{j}_0 = 2.0 \times 10^{-2}$ should be considered tremendously strong, their fields would become nearly uniform in the interior and purely dipole in the outside of the star by the surface current as seen Fig. 3.1. Moreover, when there are no closed poloidal magnetic field lines inside the stars, the magnetized stars cannot have toroidal magnetic fields because the poloidal magnetic fields are originated from the closed current densities which are assumed to be parallel to the closed poloidal magnetic fields as seen from the current density formula.

Fig. 3.7 shows the components of the magnetic fields (left) and the non-force-free and the force-free term in the current density formula (right) are plotted against $\hat{r}$. We choose $\hat{j}_0 = 2.5 \times 10^{-3}$ (top panels) and $\hat{j}_0 = 7.5 \times 10^{-3}$ (bottom panels). From these panels, we can see both the width and the strength of the κ term are increasing as $\hat{j}_0$, but that the strength of the μ term does not change so much. This result means that the oppositely flowing surface current affects only the force-free term in the current density formula significantly. As discussed before, since the μ term is non-force-free and affected mainly from the global structures of the stars, i.e. by the value of the axis ratio q. The distributions of μ term in the current density formula would not show large change. We have computed these configurations by fixing the values of q and $\hat{\Omega}_0$ and the total magnetic strengths of the stars are nearly the same for the different configurations. Therefore, the distributions of the μ terms are nearly the same for different values of $\hat{j}_0$.

It is needless to say that in order to increase the total current keeping the μ term nearly the same, the κ term must become larger and stronger as we see in these panels and Fig. 3.6. Since the stronger and steeper distributions of the κ term result in the stronger toroidal magnetic fields, the presence of the oppositely flowing surface current should be required for the larger and stronger toroidal magnetic fields. In other words, the oppositely flowing surface current density can sustain the strong toroidal magnetic fields. The maximum value of the toroidal magnetic field and the size of the region where the most of the toroidal magnetic field exists can be increased by adding and increasing the surface current densities.

In Fig. 3.8 the distributions of the magnetic flux functions on the equator ($\theta = \pi/2$) for two configurations, one without surface current (left panel) and the other with surface current (right panel), are displayed. As seen from left panel, the value of the magnetic flux function at the equatorial surface for the configuration without surface current becomes bigger as the $\hat{\kappa}_0$

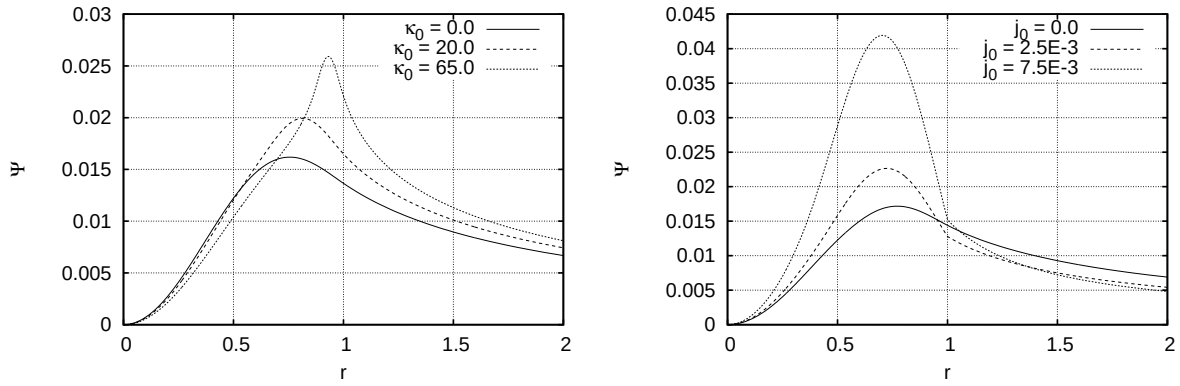

Figure 3.8: The distributions of magnetic flux function on the equator ($\theta = \pi/2$). Left panel: These lines denote $\hat{\kappa}$ = 0.0 (solid line), $\hat{\kappa}_0$ = 20.0 (dashed line) and $\hat{\kappa}_0 = 65.0$ (dotted line) model without surface current respectively. Right panel: These lines denote $\hat{j}_0 = 0.0$ (solid line), $\hat{j}_0 = 2.5 \times 10^{-3}$ (dashed line) and $\hat{j}_0 = 7.5 \times 10^{-3}$ (dotted line) model with surface current respectively.

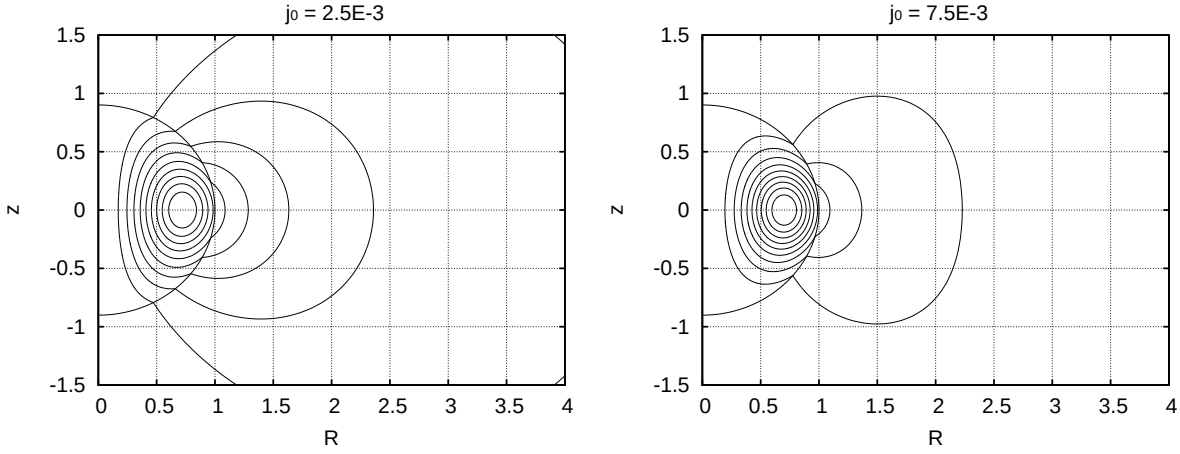

Figure 3.9: Distributions of the poloidal magnetic fields. Parallel components of the poloidal magnetic fields along the surfaces are discontinuous on the stellar surfaces. The values of $\mathcal{M}_p/\mathcal{M} \sim 0.8785$ (left) and ~ 0.6979 (right).

increases, because the maximum value of the flux function becomes bigger. On the other hand, the value of the magnetic flux at the equatorial plane with surface current (right panel) does not change very much even if the values of $\Psi_{\max}$ increase. Therefore, the negative surface current make the flux function at the equatorial surface smaller than that for the configuration without surface current. This reduction of the value of the magnetic flux function in the vacuum region can allow the wider support region to exist.

As for the geometry of magnetic fields, the surface currents bend the poloidal magnetic fields on the stellar surface as we have described in Sec. 3.3.1. Fig. 3.9 shows that the poloidal magnetic field lines bend due to the presence of the surface currents for configurations with $\hat{j}_0 = 2.5 \times 10^{-3}$ (left) and $\hat{j}_0 = 7.5 \times 10^{-3}$ (right).

Thus far, nobody has obtained configurations with the surface currents in previous works (e.g. see Fig. 2 in chapter 2). On the other hand, configurations shown in Fig. 3.9 have discontinuities on their surfaces. The directions of the discontinuities depend on the directions of the surface currents. In the northern hemisphere, the outward poloidal field lines are bended

to the left side by the oppositely flowing surface currents. On the other hand, if we add the surface currents whose flowing direction is the same as that of the interior bulk current, they are bended to the right side and the toroidal magnetic fields become weak because the surface currents flowing to the same direction as the interior bulk currents work so as to reduce the strengths of the interior bulk currents. The discontinuities of the magnetic fields in our models are the same as those of Glampedakis et al. (2012) (see Fig. 5 in their paper carefully). In fact, what they did in their paper, i.e. by imposing structures in which the magnetic fields on the stellar surfaces have some amount of discontinuities are effectively the same as adding the oppositely flowing surface currents to the magnetized stars.

3.4.4 Configurations with surface currents – Quadrupole currents

We consider configurations with other surface current distributions. We add the surface currents expressed by Eq. (3.30), which results in the quadrupole distribution of the poloidal magnetic fields. However, the toroidal magnetic field for this surface current cannot become large enough. As the strength of the surface current is increased, we get configurations with no toroidal magnetic fields whose poloidal magnetic fields are not closed inside of the stars (see the right panel in Fig. 3.1). The toroidal component of the magnetic field vanishes in such a configuration.

In order to sustain strong toroidal magnetic fields, we need strong toroidal currents in the stellar interior as discussed for the dipole-like distributions of the surface currents. However, as seen from the results for the quadrupole-like surface currents, surface currents contain both the negative component and the positive component in the surface currents. Moreover, the strengths of those oppositely flowing currents are the same. Therefore, the total surface current due to the purely quadrupole surface current of the purely spherical star vanishes as

$$\int_{S_{\rm mer}} \hat{j}_{sur} dS = -\int_0^{\pi} r_s j_0 \sin\theta\cos\theta d\theta = 0. \tag{3.43}$$

Consequently, this kind of surface current cannot counteract or cancel the effect of the interior bulk current density. It implies that we need 2^{ℓ}-th poles with $\ell =$ odd numbers of the magnetic moments (dipole, octopole etc.) or locally strong surface currents which are not anti-symmetric about the equatorial plane in order to sustain the strong toroidal fields.

3.5 Reasons for appearance of strong toroidal magnetic fields

In the previous section we have discussed that the presence of negative (oppositely flowing) surface currents in addition to positive interior bulk currents could allow more interior currents to exist within the stars. In particular, large interior toroidal currents could be realized by introducing negatively flowing surface currents in addition to positively flowing interior currents. Consequently, such negatively flowing toroidal currents lead to larger positively flowing total currents, $\hat{J}^{(+)}_{tot}$, within the stars, although the total currents, $\hat{J}_{tot}$, have their upper bound as ex-

plained before. Thus it is these larger positively flowing interior currents, $\hat{J}_{tot}^{(+)}$, that cause the toroidal magnetic fields stronger.

Among stationary magnetized stars thus far obtained in many papers, some authors have found configurations with large toroidal magnetic fields by treating the problem differently (see Ioka & Sasaki 2004, Duez & Mathis 2010 and Yoshida et al. 2012). However, no authors have explained reasons why there can appear such magnetic fields with large values of the toroidal magnetic field energies.

3.5.1 Zero-flux-boundary approach: $N = 0$ magnetized spherical configurations

In this subsection, we will reconsider simple configurations with large toroidal magnetic fields from our standpoint of taking the negatively flowing currents into account. In order to clarify the reasons for existence of large toroidal magnetic fields, it would be helpful to employ as simple configurations as possible.

As for the mechanical structures of the magnetized stars we consider $N = 0$ polytropes, i.e, incompressible fluids. Although the magnetic fields might become very strong, the shapes of the stellar configurations are assumed to be spheres. It is possible to consider that strongly magnetized stars have spherical surfaces by confining all the magnetic fields within the surfaces. This situation could be realized by treating the closed magnetic fields not only for the toroidal fields but also for the poloidal fields. Under these assumptions, the formulations used by several authors (Chandrasekhar & Prendergast 1956; Prendergast 1956; Duez & Mathis 2010; Glampedakis et al. 2012; Yoshida et al. 2012) can be applied. Since our purpose of this part of the paper is not to obtain 'new' stationary configurations but to understand the *reasons* for appearance of large toroidal magnetic fields, we will follow mostly the zero-flux-boundary scheme of Prendergast (1956) (see also Duez & Mathis 2010), but we take account of the presence of negatively flowing surface currents as well as negatively flowing interior currents in addition to positively flowing interior currents.

As for the arbitrary functions, we choose the functional form of κ as follows:

$$\kappa(\Psi) \equiv \kappa_0 \Psi, \tag{3.44}$$

and consequently

$$\frac{d\kappa(\Psi)}{d\Psi} \equiv \kappa_0. \tag{3.45}$$

This choice for $\kappa(\Psi)$ as well as the form for $\mu(\Psi) = \mu_0(\text{constant})$ have been commonly used in almost all zero-flux-boundary approaches which have treated configurations with closed dipole magnetic fields (see Prendergast 1956, Ioka & Sasaki 2004, Duez & Mathis 2010 and Yoshida et al. 2012). From Eq. (3.7), the form of the current density becomes as below:

$$\frac{j_\varphi}{c} = \frac{\kappa_0^2}{4\pi r \sin\theta} \Psi + \rho r \sin\theta \mu_0. \tag{3.46}$$

Since the GS equation is an elliptic type partial differential equation of the second order, we need to impose boundary conditions to obtain solutions consistently. We should note that, in all zero-flux-boundary approaches thus far carried out, the constant κ_0 plays a role as an eigenvalue of the problem because boundary conditions have been imposed at finite places in the space in most investigations. One example of the boundary conditions might be as follows:

$$\Psi|_{r=0} = 0\ , (\text{at the centre}), \tag{3.47}$$

$$\Psi\big|_{r=r_s^{(s)}} = 0\ , (\text{on the stellar surface})\ , \tag{3.48}$$

where $r_s^{(s)}$ is the radius of the spherical incompressible magnetized stars treated in this section. It should be noted that solutions with $d\Psi/dr\big|_{r=r_s^{(s)}} = 0$ in our models, which can be found only after we have obtained stationary configurations and checked values of the derivative $d\Psi/dr\big|_{r=r_s^{(s)}}$ for all the models, are essentially the same as those of Duez & Mathis (2010). It should be stressed once again that solutions which satisfy the condition $d\Psi/dr\big|_{r=r_s^{(s)}} = 0$ would not always be found. It would be fortunate if one could find such solutions not by imposing that condition as one of boundary conditions but by just calculating solutions with the boundary conditions (3.47) and (3.48).

3.5.2 Magnetic flux functions for spherical incompressible fluids with magnetic fields confined within the stellar surfaces

In this section, we continue to follow mostly the formulation of Prendergast (1956) (see also Duez & Mathis 2010), in which the surface currents were not taken into account explicitly, but in this chapter we include the surface currents explicitly by modifying their formulation.

They treated incompressible fluid stars, i.e. $N = 0$ polytropes by specifying arbitrary functions as we have already explained before. Although incompressible stars seem far from realistic situations, from the standpoint of considering oppositely flowing currents including surface currents stressed in this chapter, it is very useful to be able to get such solutions and discuss the role of the oppositely flowing currents analytically. Nevertheless, in this chapter, we will also compute $N = 1$ polytropes and discuss the effect of the equation of state. We see details of solutions in chapter 4.

For the functional forms we have chosen, the Grad-Shafranov equation, Eq. (3.2), can be written as below:

$$\Delta^*\Psi + \kappa_0^2\Psi = -4\pi\mu_0\bar{\rho}r^2\sin^2\theta \equiv S(r,\theta). \tag{3.49}$$

where $\bar{\rho}$ is the averaged value of the density. It should be noted that this is a linear equation for the magnetic flux function Ψ. When ρ is constant throughout the stellar interior, we can integrate this GS equation easily by expressing the solution in the integral form by using Green's function and spherical Bessel functions and Gegenbauer polynomials as follows:

$$\Psi(r,\theta) = \Psi_s + \Psi_h, \tag{3.50}$$

$$
\begin{aligned}
\Psi_s &\equiv \sum_{\ell=0} \Psi_\ell \\
&= -4\pi\mu_0 \sum_{\ell=0} \kappa_{0,\ell} \left[\frac{2\ell+3}{2(\ell+1)(\ell+2)}\right] \sin^2\theta C_\ell^{3/2}(\cos\theta) \\
&\left\{ \frac{r}{r_s^{(s)}} J_{\ell+1}\left(\kappa_{0,\ell}\frac{r}{r_s^{(s)}}\right) \int_r^{r_s^{(s)}} r' Y_{\ell+1}\left(\kappa_{0,\ell}\frac{r'}{r_s^{(s)}}\right) \bar{\rho}\, dr' \right. \\
&\left. + \frac{r}{r_s^{(s)}} Y_{\ell+1}\left(\kappa_{0,\ell}\frac{r}{r_s^{(s)}}\right) \int_0^{r} r' J_{\ell+1}\left(\kappa_{0,\ell}\frac{r'}{r_s^{(s)}}\right) \bar{\rho}\, dr' \right\} \\
&\times \int_{-1}^{1} S(r', \cos\theta') C_\ell^{3/2}(\cos\theta') d\cos\theta',
\end{aligned}
\tag{3.51}
$$

$$
\Psi_h = \sum_{\ell=0} \left[K_{1,\ell}\kappa_{0,\ell}\frac{r}{r_s^{(s)}} J_{\ell+1}\left(\kappa_{0,\ell}\frac{r}{r_s^{(s)}}\right) + K_{2,\ell}\kappa_{0,\ell}\frac{r}{r_s^{(s)}} Y_{\ell+1}\left(\kappa_{0,\ell}\frac{r}{r_s'^{(s)}}\right) \right] \sin^2\theta C_\ell^{3/2}(\cos\theta). \tag{3.52}
$$

Here Ψ_s and Ψ_h denote the inhomogeneous solution and the homogeneous solution to the GS equation, respectively and J_ℓ's and Y_ℓ's are the spherical Bessel functions of the first kind and the second kind, respectively and $C_\ell^{3/2}$'s are the Gegenbauer polynomials. Ψ_ℓ, $\kappa_{0,\ell}$ and $K_{1,\ell}$, $K_{2,\ell}$ denote the ℓ-th expansion terms of the magnetic flux function, the eigenvalues corresponding to κ for the ℓ-th component equations appearing in the expansion of the magnetic flux function as above, and coefficients of homogeneous solutions, respectively. It should be noted that, here in this chapter, we consider only the dipole term ($\ell = 0$) which can be considered as the simplest configuration for the spherical incompressible magnetized fluid star. Moreover it is important to note that even such simple configurations contain the essential natures of the configurations we are seeking to understand.

As we have described before, we impose boundary conditions for Ψ. One condition is $\Psi = 0$ at the centre of the star. This condition can be fulfilled simply in our situation here by setting $K_2^0 = 0$, because the spherical Bessel function of the second kind $Y_{\ell=0}$ does not vanish at the centre ($r = 0$) for the homogeneous solutions. As a result, we obtain the general expression of the solution as follows:

$$
\begin{aligned}
\Psi =& K_1\kappa_0 \frac{r}{r_s^{(s)}} J_1\left(\kappa_0\frac{r}{r_s^{(s)}}\right) \sin^2\theta \\
&- 4\pi\mu_0\kappa_0 \sin^2\theta \left\{ \frac{r}{r_s^{(s)}} J_1\left(\kappa_0\frac{r}{r_s^{(s)}}\right) \int_r^{r_s^{(s)}} Y_1\left(\kappa_0\frac{r'}{r_s^{(s)}}\right) \bar{\rho} r'^3\, dr' \right. \\
&\left. + \frac{r}{r_s^{(s)}} Y_1\left(\kappa_0\frac{r}{r_s^{(s)}}\right) \int_0^{r} J_1\left(\kappa_0\frac{r'}{r_s^{(s)}}\right) \bar{\rho} r'^3\, dr' \right\}.
\end{aligned}
\tag{3.53}
$$

Explicit forms of J_1, Y_1 and $C_0^{3/2}$ are as below:

$$J_1(\lambda) = \frac{1}{\lambda^2}(\sin\lambda - \lambda\cos\lambda), \tag{3.54}$$

$$Y_1(\lambda) = -\frac{1}{\lambda^2}(\cos\lambda + \lambda\sin\lambda), \tag{3.55}$$

$$C_0^{3/2}(\cos\theta) = 1. \tag{3.56}$$

We denote κ_0^0 as κ_0 and K_1^0 as K_1 for simplicity in the following part of this chapter.

Next, we impose the other boundary condition $\Psi = 0$ at the stellar surface. This condition is written as follows

$$K_1 J_1(\kappa_0) = 4\pi\mu_0 Y_1(\kappa_0) \int_0^{r_s^{(s)}} J_1\left(\kappa_0 \frac{r'}{r_s^{(s)}}\right) \bar{\rho} r'^3 \, dr'. \tag{3.57}$$

From this equation we can obtain a relation between κ_0 and K_1 of our problem at hand. Thus just by giving either κ_0 or K_1, one *complete* solution in our problem can be obtained. This is a nice feature of the simplest configurations, i.e. the $N = 0$ polytropic configurations only with the $\ell = 0$ component for the confined poloidal closed magnetic fields.

Finally, we will derive the surface current for our problem. The homogeneous term of this solution is related to the surface current as we have calculated in Sec. 3.3.2. Thus the surface current is expressed as

$$\frac{j_{sur}(\theta)}{c} = \frac{1}{4\pi}(B_\theta^{ex} - B_\theta^{in}) = \frac{1}{4\pi r\sin\theta}\frac{\partial\Psi(r,\theta)}{\partial r}\bigg|_{r=r_s^{(s)}}. \tag{3.58}$$

Since the solution for the magnetic flux function behaves as $\sin^2\theta$, the following quantity becomes a constant and so we will write its constant value as j_0:

$$\frac{1}{4\pi r\sin^2\theta}\frac{\partial\Psi(r,\theta)}{\partial r}\bigg|_{r=r_s^{(s)}} \equiv j_0. \tag{3.59}$$

Thus the distribution of the surface current can be written as below:

$$\frac{j_{sur}}{c} = j_0\sin\theta. \tag{3.60}$$

Explicit forms of K_1 and j_0 are

$$K_1 \;= 4\pi\mu_0\bar{\rho}\frac{r_s^{(s)2}}{\kappa_0^4}\left(\frac{-\cos\kappa_0 - \kappa_0\sin\kappa_0}{\sin\kappa_0 - \kappa_0\cos\kappa_0}\right)\left((3-\kappa_0^2)\sin(\kappa_0) - 3\kappa_0\cos\kappa_0\right), \tag{3.61}$$

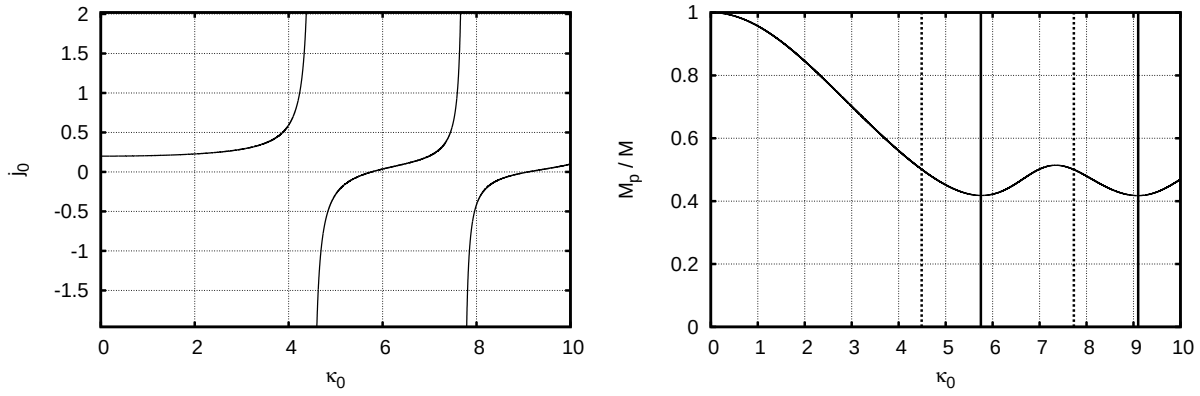

Figure 3.10: Left: Plotted is j_0 against κ_0 for configurations with the parameter satisfying $r_s^{(s)2}\mu_0\bar{\rho} = -1$. We can see that there are *two solutions without surface currents* at $\kappa_0 \sim 5.76$ and at $\kappa_0 \sim 9.10$ and that there exist two singularities at $\kappa_0 \sim 4.49$ and at $\kappa_0 \sim 7.73$ within the range $0. \leq \kappa_0 \leq 10.$. Right: The energy ratio $\mathcal{M}_p/\mathcal{M}$ is plotted against κ_0. The solid lines and dotted lines denote the values of κ_0 for the solutions without surface currents and the singularities, respectively. The toroidal magnetic field vanishes at $\kappa_0 = 0$.

and

$$
\begin{aligned}
j_0 \equiv & \frac{1}{4\pi r \sin^2\theta}\frac{\partial\Psi(r,\theta)}{\partial r}\bigg|_{r=r_s^{(s)}} \\
= & \frac{1}{4\pi r_s^{(s)}}\left[\frac{K_1}{\kappa_0}\Big\{(\kappa_0^2-1)\sin\kappa_0+\kappa_0\cos\kappa_0\Big\}\right. \\
& +\frac{4\pi\mu_0\bar{\rho}r_s^{(s)2}}{\kappa_0^5}\Big\{(2\kappa_0^3-3\kappa_0)\sin^2\kappa_0+(-2\kappa_0^4+8\kappa_0^2-3)\cos\kappa_0\sin\kappa_0\Big\} \\
& \left.+\frac{4\pi\mu_0\bar{\rho}r_s^{(s)2}}{\kappa_0^3}\Big\{-\kappa_0\sin^2\kappa_0+(\kappa_0^2-1)\cos\kappa_0\sin\kappa_0+\kappa_0\cos^2\kappa_0\Big\}\right].
\end{aligned}
\tag{3.62}
$$

Therefore, if the star has negative surface currents, values of the magnetic flux functions in the large part of the stellar interiors are positive because of $\partial\Psi/\partial r < 0$ on the stellar surfaces.

As explained before, we can calculate one eigenfunction just by choosing one value of κ_0. By changing the value of κ_0 and calculating the corresponding solution for Ψ, we have a series of solutions which are shown in Fig. 3.10 and Fig. 3.11. Fig. 3.12 displays the various total currents J_{tot}.

Fig. 3.10 shows how j_0 behaves for different value of κ_0 (left) and how $\mathcal{M}_p/\mathcal{M}$ behaves against the value of κ_0 (right). We set the parameters satisfying the relation $r_s^{(s)2}\hat{\mu}_0\bar{\rho} = -1$. As seen from these panels, the function $j_0(\kappa_0)$ has two special solutions which contain no surface currents at $\kappa_0 \sim 5.76$, and at $\kappa_0 \sim 9.10$. Furthermore, there appear two singularities along this curve at $\kappa_0 \sim 4.49$, and at $\kappa_0 \sim 7.73$. The sign of the magnetic flux function changes at the singularities. The value of $\mathcal{M}_p/\mathcal{M}$ decreases as the value of κ_0 increases until it reaches the first solution without a surface current at $\kappa_0 \sim 5.76$ and the value of the $\mathcal{M}_p/\mathcal{M}$ reaches its minimum of $\mathcal{M}_p/\mathcal{M} = 0.417$. Hereafter we will call the eigenvalue κ_0 of the first solution without a surface current as κ_m^1 and the eigenvalue κ_0 of the second solution without a surface

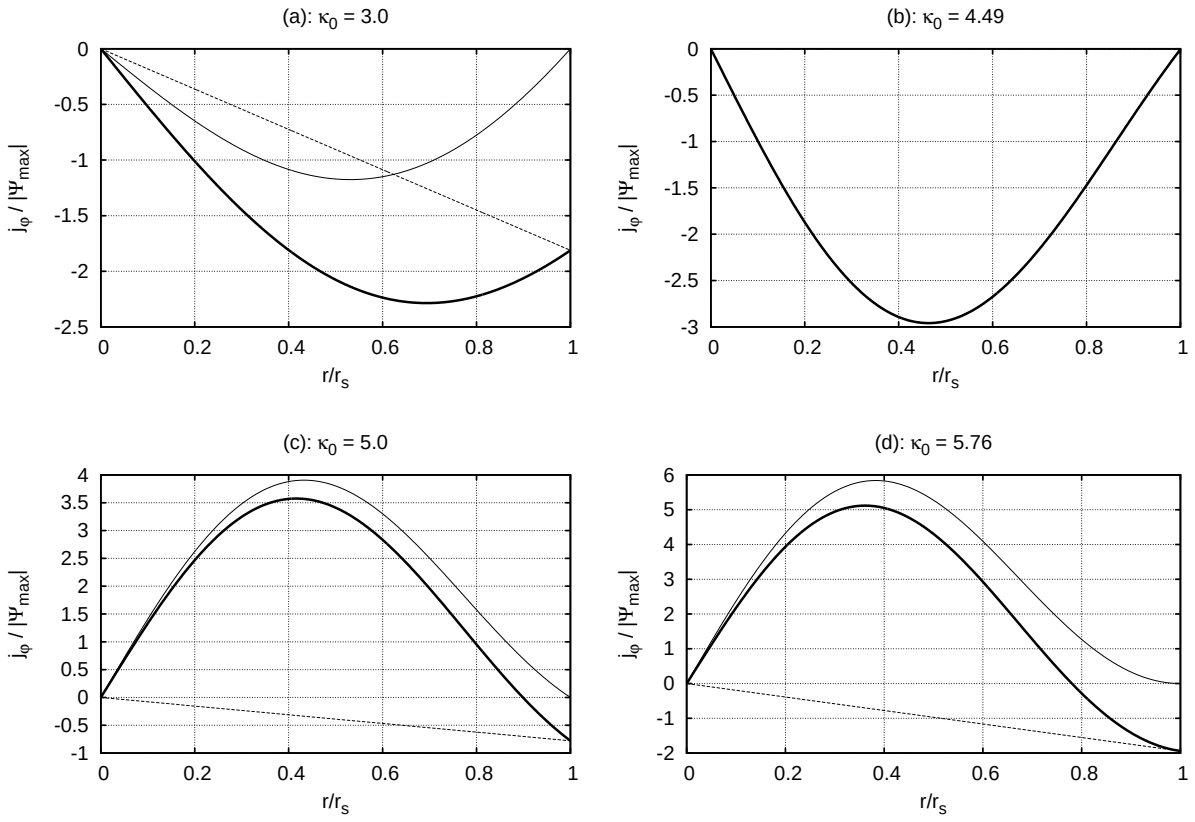

Figure 3.11: The distributions of j_φ/c normalized by the maximum strength of $|\Psi_{\max}|$, i.e. the absolute value of the maximum of the flux function, along the normalized radius on the equatorial plane. Each line denotes the value of j_φ (thick solid line), the component of j_φ due to the κ term (thin solid line) and the component of j_φ due to the μ term (thin dotted line). Type (a): In the range of $0 < \kappa_0 < \kappa_s^1$ the φ component of the current is negative in the whole star and the contributions to the current from the κ term and the μ term are also negative. $\mathcal{M}_p$ / $\mathcal{M}$ = 0.701 model. Type (b): In the range of $\kappa_0 \sim \kappa_s^1$, the contribution to the φ component of the current due to the μ term is nearly zero because of the large contribution from the κ term. $\mathcal{M}_p$ / $\mathcal{M}$ = 0.501 model. Type (c): In the range of $\kappa_s^1 < \kappa_0 < \kappa_m^1$, the φ component of the current is positive in most of the stellar interior. The contribution to the current due to the κ term is positive. whereas the contribution to the current due to the μ term is negative. $\mathcal{M}_p$ / $\mathcal{M}$ = 0.452 model. Type (d): At $\kappa_0 = \kappa_m^1$, the surface current vanishes because j_0 becomes zero, It is remarkable that not only the component of the current due to the κ term but also its derivative with respect to the position become 0 at the stellar surface. It corresponds to the null surface current. $\mathcal{M}_p$ / $\mathcal{M}$ = 0.417 model.

current as κ_m^2. We also denote values of κ_0 at the first and the second singular points along this curve as κ_s^1 and κ_s^2, respectively.

We will discuss the behaviors of Ψ and j_0 only around κ_m^1 in this chapter. However we see almost the similar behaviors for $\kappa_0 \sim \kappa_m^2$, which one can find in several papers (Ioka & Sasaki 2004; Duez & Mathis 2010; Yoshida et al. 2012).

We can classify the eigen solutions into four types according to the behaviors of the current densities as follows: Type (a) – solutions with $0 < \kappa_0 < \kappa_s^1$, Type (b) – solutions with $\kappa_0 \sim \kappa_s^1$, Type (c) – solutions with $\kappa_s^1 < \kappa_0 < \kappa_m^1$, and Type (d) – solution at $\kappa = \kappa_m^1$. As we can see in Fig. 3.10, concerning the ratio $\mathcal{M}_p/\mathcal{M}$, the following relations hold:

$$\frac{\mathcal{M}_p}{\mathcal{M}}\ (\text{Type a}) > \frac{\mathcal{M}_p}{\mathcal{M}}\ (\text{Type b}) \frac{\mathcal{M}_p}{\mathcal{M}}\ (\text{Type c}) > \frac{\mathcal{M}_p}{\mathcal{M}}\ (\text{Type d}). \tag{3.63}$$

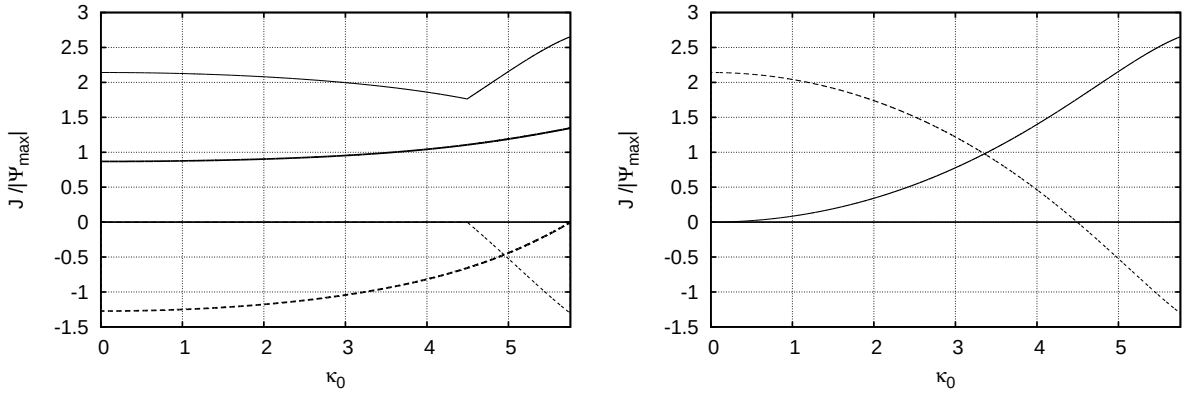

Figure 3.12: The total currents normalized $|\Psi_{\max}|$ are plotted against κ_0. We make J_{tot} positive in this figure. The left panel: Each line denotes J_{tot} (thick solid line), J_{sur} (thick dashed line), $J_{tot}^{(+)}$ (thin solid line) and $J_{tot}^{(-)}$ (thin dashed line) respectively. The right panel: Each line denotes J_{tot}^{κ} (solid line) and J_{tot}^{μ} (dashed line).

In Fig. 3.11, the distributions of j_φ normalized by the maximum value of the flux function $|\Psi_{max}|$ along the normalized radius on the equatorial plane are displayed. In this figure the interior toroidal current j_φ, the component of j_φ due to the κ term and the component of j_φ due to the μ term are displayed. The values of (κ_0, $\mathcal{M}_p/\mathcal{M}$) in the panels are (a) (3.0, 0.701), (b) (~ 4.49, 0.501), (c) (5.0, 0,452), and (d) (5.76, 0.417). In Fig. 3.12, we make that the sign of J_{tot} is always positive. In other words, we multiply $J_{tot}/|J_{tot}|$ in order to plot the distributions of J_{tot}. In the left panel of Fig. 3.12, each line denotes J_{tot} (thick solid line), $J_{tot}^{(+)}$ (thin solid line), J_{sur} (thick dashed line) and $J_{tot}^{(-)}$ (thin dashed line). In the right one, we decompose the $J_{tot}^{(+)}$ into the total κ current and the total μ current. The solid line show the J_{tot}^{κ} and the dashed line show the J_{tot}^{μ} respectively.

It is remarkable that these models have strong toroidal magnetic fields contrary to configurations whose magnetic fields without surface currents extend to the infinity, i.e. open fields, and cannot become large. From the panels in Fig. 3.11, the configurations of Types (a) and (b) have the positive surface current in the φ direction which is opposite to the interior negative current density in the φ direction, while the configurations of Type (c) have the negative φ-surface current while the interior φ-currents are positive in almost all of the interior region. The model of Type (d) has no surface current. However, the φ component of the interior currents are negative in the finite surface region while the φ component of the interior currents in the most inner region is positive. Therefore, in the range of $0 < \kappa_0 < \kappa_s^1$, $J_{tot}^{(+)} = J_{tot}^{\mu} + J_{tot}^{\kappa}$ and in the range of $\kappa_s^1 < \kappa_0 \leq \kappa_m^1$, $J_{tot}^{(+)} = J_{tot}^{\kappa}$ and $J_{tot}^{(-)} = J_{tot}^{\mu}$ respectively.

The signs of the κ term, the μ term and j_φ of the solutions of Type (a) are all negative within the whole region as seen from Fig. 3.11, while the surface current is positive because $j_0 > 0$. Therefore, the strong toroidal magnetic fields of the solutions of Type (a) are sustained by the oppositely flowing surface current as has been explained for the reasons why the numerically exact open field configurations with surface currents can have large toroidal magnetic fields in the previous section. For Type (a) solutions, the toroidal magnetic field energy increases monotonously as the magnitude of the surface current becomes larger.

The solutions of Type (b) show the extreme features corresponding to the singularity. Since the strength of the surface current becomes infinite, the κ term becomes larger and the contribution from the μ term becomes nearly zero compared with that of the κ term. Thus the non-force-free μ term contributes essentially nothing to the φ component of the current density and so those solutions of Type (b) can be considered to be almost the same as those force-free configurations obtained by Broderick & Narayan (2008).

As seen from these panels, the signs of the μ term and the κ term are different from each other for configurations of Types (c) and (d). In fact, the sign of the surface current changes from negative values to positive values between solutions of Type (a) and those of Type (c). As a result, the interior currents can become negative near the stellar surface region. Since the surface currents are negative in this parameter range, the toroidal magnetic fields can be sustained by both the negative surface currents and the negative interior currents near the stellar surface region (see Fig. 3.12). The toroidal magnetic field energies become larger in this parameter range than those in the parameter range where only oppositely flowing surface currents such as solutions of Types (a) and (b) are allowed. Moreover, the toroidal magnetic field energy reaches its maximum value for the model (d) which has no surface current. These phenomena imply that the effects of the surface currents are not so large compared with those due to the interior currents near the surface region which flow oppositely to the interior currents further inside.

The model (d) has only the interior negative current region without surface currents in addition to the interior positive currents in the inner part of the star. The effect of the interior negative current is larger than that of configurations of Type (c) (see Fig. 3.12). The solutions obtained by Ioka & Sasaki (2004) and Yoshida et al. (2012) can be considered to belong to the same type as the model (d) except for the compressible densities.

As seen from the left panel of Fig. 3.12, the total current J_{tot} becomes only slightly larger as κ_0 increases. On the other hand, $J_{tot}^{(+)}$ increases rapidly beyond the $\kappa_0 = \kappa_s^1$ where $J_{tot}^{(-)}$ starts decreasing. This means that the negative current region can cancel much larger interior bulk positive current than the negative surface current. Therefore, as we can see in Fig. 3.12, the total κ current becomes larger and the total μ current decreases rapidly as κ_0 increases beyond the $\kappa_0 = \kappa_s^1$. Since the ratio of $\mathcal{M}_p/\mathcal{M}$ reaches the minimum value for the model (d), this kind of configuration without surface currents but with the negative interior current region has the strongest toroidal magnetic field energy among all the configurations as far as the functional forms for κ and μ are the same as those chosen in this chapter.

We have also calculated $N = 1$ closed field configurations (see also chapter 4). We have used the shooting method to obtain the eigen solutions for the boundary value problems (see Ioka & Sasaki 2004). Obtained solutions of $N = 1$ polytropes have the same tendencies as those for the $N = 0$ solutions. The ratio $\mathcal{M}_p/\mathcal{M}$ reaches its minimum value 0.349 at $\kappa_m^1 = 7.42$. The toroidal magnetic field energy is slightly larger than that of the corresponding $N = 0$ configuration.

3.6 Discussion

3.6.1 Open field configurations vs closed field configurations

As we have calculated and seen in this chapter, the negative (oppositely flowing) surface currents and/or the negative (oppositely flowing) interior currents seem to generate strong toroidal magnetic fields within the stars. We have obtained the configuration having the minimum value of $\mathcal{M}_p/\mathcal{M} \sim 0.697$ when $\hat{j}_0 = 7.5 \times 10^{-3}$ for the solutions of open fields by taking the surface currents into account. On the other hand, the ratio $\mathcal{M}_p/\mathcal{M}$ reaches 0.349 when all the magnetic field lines are closed and confined inside the stellar surface for $N = 1$ polytropes. This value is much smaller than that for open field configurations with surface currents. The functional forms for the arbitrary functions and the boundary conditions of these two models, i.e. the closed field solution and the open field solution, are different from each other (see Eq. 3.33 and Eq. 3.46), but both configurations contain the interior region where the interior currents are negative (oppositely flowing) and there appear very strong toroidal magnetic fields.

From the right panels in Fig. 3.7, the signs of the μ term and the κ term are positive for our open field models with negative surface currents. In other words, the models do not contain the negative current regions. The open field models which we have obtained correspond to models of the Type (a) for the closed field configurations. Therefore, the stars could have stronger toroidal magnetic field energy if they can contain the negative interior current regions near the stellar surfaces. However, we could not find the functional form of κ for which the negative interior current region appears as the model of Type (d) in this chapter. In any case, the toroidal magnetic field energies of closed field models are larger than those of the corresponding open field models with negative surface currents. It should be noted that the model of Type (d) sustains the largest toroidal magnetic field energy among all of our solutions obtained in this chapter. We can conclude that the magnetized equilibria with strong toroidal magnetic field energies would be the closed field configurations.

3.6.2 Effects of compressibility to toroidal magnetic fields

We have employed polytropes with $N = 1$ and $N = 0$ in this chapter. Since we are mainly interested in the effects of surface currents, we adopt polytropes as equations of state, although polytropes are too simple equations of state. The different equations of state result in different density distributions as well as different magnetic field structures, because the current density formula contains the density depending term (Eq. 3.7). As we have described in Sec. 3.5.2, configurations for polytropes with $N = 1$ can sustain slightly larger toroidal magnetic fields than those with $N = 0$, i.e. the minimum value of $\mathcal{M}_p/\mathcal{M}$ is 0.417 for the $N = 0$ polytropes and the minimum value of $\mathcal{M}_p/\mathcal{M}$ is 0.349 for $N = 1$ polytropes as far as the other parameters are the same. Therefore, the configurations with softer equations of state can sustain stronger toroidal magnetic fields for polytropes.

How about for more realistic equations of state discussed by other authors ? Kiuchi & Ko-

take (2008) calculated twisted-torus magnetized equilibrium states using some realistic equations of state at zero temperature. Their method is the same as our method. Fig. 4 - Fig. 7 in their paper show the density contours and the magnetic field contours for different equations of state. The structures of the poloidal magnetic field lines and the regions of the toroidal magnetic fields within the stellar surfaces are different among the different equations of state. For example, among models of the Shen's equation of state (EOS), the position where the toroidal magnetic field attains its maximum strength is located near the stellar surface and the width of the region where the toroidal magnetic fields appear is relatively small, but for models with the FPS's EOS, the position of the maximum toroidal magnetic field is shifted to the inner part of the star and the size of the toroidal magnetic field region is much bigger than that for the Shen's EOS. Although they did not calculated the toroidal magnetic field energies and the ratio $\mathcal{M}_p/\mathcal{M}$, they showed the ratio of the local strength of the toroidal magnetic field to the poloidal magnetic field (h in Table 4). The value of h for FPS's EOS is about as twice as that for Shen's EOS. Therefore, although the influence of the equation of state might become more important if we would consider structures of neutron stars, it would not change the basic properties discussed in this chapter dramatically, although the values and/or the regions for the toroidal magnetic fields would surely be somewhat different from those obtained in this chapter.

3.6.3 Stability of configurations with oppositely flowing φ-currents within and/or on the stellar surfaces

It is very interesting and important to analyze stability of our models for open magnetic fields with surface currents. Since some of our solutions satisfy the Braithwaite's stability criteria, Eq. (3.1), our models could be stable. Although it is very difficult to tell the stability for a certain model exactly, we will be able to check the stability by several non-exact ways and get rough idea about the stability of the configuration.

First of all, we consider the stabilities of the magnetized stars with pure surface currents and with no interior currents (see the left panel in Fig. 3.1). The stability of the magnetized stars with surface currents in the surface region of an infinitely thin width could be considered to be essentially the same as that of configurations with pure surface currents. If the magnetized stars possess only the surface currents which generate the pure dipole magnetic fields outside the stars, their interior magnetic fields are uniform along the z axis (see the left panel of Fig. 3.1). The magnetic fields of this kind of configuration are unstable and decay within a few Alfvén time, because there is no toroidal magnetic fields (Markey & Tayler 1973). As Flowers & Ruderman (1977) also explained the instability of this kind of configuration and Braithwaite & Spruit (2006) carried out non-linear evolution of the instability by numerical simulations and showed unstable growth of the initial stationary states as explained above. Therefore, the fields of the magnetized stars with pure surface currents can be considered to be unstable.

By contrast, as for the configurations with surface currents, which might lay in, for example, the crusts of the neutron stars, the magnetic fields could become stable. In such configurations, we can assume that the widths of surface current layers are not infinitely thin any more and

the finite Lorentz force acts on the surface currents. Flowers & Ruderman (1977) considered configurations with surface current layers as well as with uniform magnetic fields and dipole magnetic fields inside and outside of the stellar surface, respectively, and found that those configurations with current layers might be stable. In realistic situations as neutron stars, when the solid crusts of neutron stars form after their proto-neutron phase, the crusts could sustain the Lorenz force to themselves and they could prevent growth of the instability of magnetic fields. For such situations, the magnetic fields can survive in much longer time than the Alfvén timescale.

Concerning direct computations of the evolutions starting from the perturbed initial stationary states, Braithwaite & Spruit (2006) carried out numerical evolutions of the twisted-torus interior magnetic fields with solid crusts. They included surface current layers with finite widths as their boundary condition for the magnetar's crust and used one of their quasi-stationary twisted configurations which they had obtained after long time simulations as initial values. Their numerical model is similar to our solution with surface currents. The magnetic fields of such stars do not decay within the Alfvén time scale in their simulations as far as the crusts can sustain the Lorentz force. Therefore, our twisted-torus models with surface currents would be also stable configurations.

Evolutions and stabilities of configurations for closed magnetic fields were argued by Duez et al. (2010). They performed numerical simulations using Duez & Mathis (2010) solutions as their initial states. They concluded that models with closed fields both with poloidal and toroidal magnetic fields do not show any sign of becoming unstable within their simulation time if the initial model satisfy the stability criteria in Eq. (3.1). Therefore, the closed magnetic field models which are obtained in this chapter would be stable configurations.

3.6.4 Application to magnetars

It is important to find out natural mechanisms to generate surface currents and/or their origins if we apply our models with surface currents to real bodies such as magnetized neutron stars, especially to magnetars. Magnetars are young neutron stars with very strong magnetic fields. The magnetars are considered as source objects of special high energetic phenomena such as the anomalous X-rays emission and the soft gamma-ray emission. Thus those pulsars are called the anomalous X-ray pulsars (AXPs) and the soft gamma-ray repeaters (SGRs), In particular, their high X-ray luminosities and giant flares have been considered to be deeply related to the strong magnetic fields of the stars (Thompson & Duncan 1995, 2001). The magnetic fields are nearly dipole poloidal fields globally, but there would be higher order (such as quadrupole and octopole) poloidal magnetic fields near the surface or toroidal fields winded up by rapid differential rotation during the proto-neutron star stages (Duncan & Thompson 1992) inside the star. Before we apply our models with surface currents to the magnetars with strong toroidal magnetic fields, we need to clarify or at least have some ideas about origins or formation mechanisms for the oppositely flowing surface currents or the discontinuity of the magnetic fields on the stellar surfaces. Then, what is the origin of the negative surface currents or the

negative current region? There might be two possibilities to explain it. One is related to the crusts of neutron stars and the other is related to the magnetospheres around neutron stars.

Since the physics of the crusts of the neutron stars is too complicated and difficult to deal with, we only assume that the crusts consist of highly conductive solid matter. If the crusts are highly conductive, the electric currents can exist within the crust regions. Then, the crusts can make parallel components of magnetic fields discontinuous near the stellar surfaces by the toroidal currents inside the crusts. The magnetic fields are frozen to the matter and fixed to the crusts because of their high conductivity. On the other hand, the interior matter of the magnetars is not solid. Thus the matter inside of the crusts can move differently from the crusts and the discontinuities of the magnetic fields would be born between the crusts and the interior regions. The interior fields begin to spread toward the stellar surfaces by the some kind of magnetic diffusion (Braithwaite & Spruit 2006) the discontinuities would be enlarged by the magnetic pressure. As we have seen before, Braithwaite & Spruit (2006) simulated this kind of configuration and found the growing of the Lorentz stress in the crusts. From the direction of the discontinuity, we expect that the stress is tensile one globally. If the crusts are cracked by the stress, it would result in flares of SGRs. Following this scenario, our models with strong toroidal fields as well as surface currents are considered as stationary states of the crusts with strong Lorentz forces before occurrence of giant flares. If a part of the crusts is cracking, the magnetic energy and the helicity are injected from the stars and would produce magnetized flows (Takahashi et al. 2009, 2011; Matsumoto et al. 2011). These kinds of magnetized outbursts would be giant flares of SGRs. We will consider this process by using our models with surface currents in the following.

At first, the surface currents in the crusts can sustain the strong toroidal fields by bending the poloidal magnetic fields as shown by the model with $\hat{j}_0 = 7.5 \times 10^{-3}$ in the right panel of Fig. 3.9. When the Lorentz force exceeds a certain critical value, a part of the crust begins to crack. We can consider this phenomena as decreasing the strength of the surface current, because a part of the conductive matter is disturbed by the cracking. We assume that a certain cracking reduces the value of $\hat{j}_0$ from 7.5×10^{-3} to 2.5×10^{-3} as an extreme example. The surface current with $\hat{j}_0 = 2.5 \times 10^{-3}$ cannot sustain the toroidal magnetic fields any more which the surface current with $\hat{j}_0 = 7.5 \times 10^{-3}$ has sustained. The toroidal magnetic energy and/or the magnetic helicity would be transferred out into the outside of the star in order to relax to the stationary state with $\hat{j}_0 = 2.5 \times 10^{-3}$ (transition from the right panel to the left panel in Fig. 3.9). Through this cracking, the dimensionless toroidal magnetic field energy $\hat{\mathcal{M}}_t$ changes from 2.49×10^{-2} to 9.92×10^{-3} according to our calculations. Therefore, about 60 % of the toroidal magnetic field energy would be released during the cracking. Although this is an extreme example, it is natural that the injection of the magnetic helicity and the release of the toroidal field come from the transition of the magnetized equilibria by the phenomena such as cracks of the crusts which reduce the surface current strength.

Another possibility is the effect due to the magnetosphere which excites oppositely flowing current densities near the stellar surfaces. Colaiuda et al. (2008) discussed the importance

of the magnetosphere as the boundary conditions for both the poloidal and toroidal magnetic fields on the stellar surfaces. Our present models and many configurations in other previous works assume that the outside of the star is vacuum where the current density and the toroidal magnetic fields do not exist. However, the presence of the magnetosphere changes the boundary condition for the magnetic field. This change of the boundary condition would significantly influence on the magnetic field configurations as we have seen.

As for rotation powered pulsars, there have been many investigations about their magnetospheric phenomena such as pulsar winds (see e.g. Goldreich & Julian 1969). Their rapid rotations produce enormously large electrical forces and the surface charged layers could not stay in their stationary states. Charged particles run away from the stellar surfaces and form the pulsar magnetospheres (see, for the recent particle pulsar wind simulations, Wada & Shibata 2007, 2011). This charged particles would produce the strong currents outside the star and the twisted magnetosphere would form.

The rotational speeds and the strengths of the magnetic fields of the magnetars are different from those of pulsars, but there would be some kinds of magnetospheres around the magnetars. The recent X-ray spectral observations show the presence of a magnetosphere for the magnetar (Rea et al. 2009). Very recently, Viganò et al. (2011) computed numerically a force-free twisted magnetar magnetosphere. They treated the stationary state of the magnetized star as an inner boundary condition for the magnetosphere. We can see the various magnetospheric structures by applying different inner boundary conditions in their paper. If the magnetosphere forms the oppositely flowing toroidal currents near the stellar surface, the magnetized star can sustain the strong toroidal magnetic field energy inside the star. However, the details of the calculation are beyond the scope of the present study.

3.7 Summary and Conclusion

In this chapter we have dealt with the effects of surface currents upon the interior toroidal magnetic fields. We have shown that the oppositely flowing surface currents can sustain the strong toroidal magnetic field energy inside the star both for the open and closed field configurations.

In the open field models, we have found that there is an upper bound of the total current of the star for a fixed set of parameter values. Increasing the maximum strength of the toroidal magnetic field decreases the region of the toroidal magnetic field due to this upper bound. Therefore this upper bound limits the ratio of the poloidal magnetic field energy to the total magnetic field energy. To exceed this upper bound, magnetized star needs the oppositely flowing surface currents to the interior toroidal currents. The interior current can overcome the upper bound and the ratio $\mathcal{M}_p/\mathcal{M}$ decreases significantly, because the surface current counteracts the interior toroidal current.

In the closed field models, we have found that a model with an oppositely flowing current region but with no surface current can sustain the strongest toroidal magnetic field among all of our magnetized stationary states. The negative surface currents can sustain the strong toroidal

magnetic fields in the models with closed magnetic fields. However, the strengths of the toroidal magnetic fields for models with negative surface currents cannot exceed a critical value even if the strength of the surface current becomes infinity. In order to overcome the critical value, the negative current region is required. Increasing the size of the negative interior current region decreases the negative surface current. As a result, the toroidal magnetic fields become the strongest when not only the negative interior current region becomes the largest but also the surface current disappears.

It should be also noted that, although we have not imposed a condition $d\Psi/dr|_{r=r_s^{(s)}} = 0$, the obtained two eigenfunctions without surface currents fulfill this condition and, moreover, that the values of $\mathcal{M}_p/\mathcal{M}$ are very small. This implies that by computing a series of eigen states with surface currents as well as with oppositely flowing interior currents we could have easily reached an eigen state whose eigen function behaves very *smoothly* for which the role of the toroidal magnetic fields becomes very important. Furthermore, it is remarkable that these solutions obtained by considering *in the wider functional space* without no restrictions about the slopes of the functions correspond to those solutions obtained by other authors (Duez & Mathis 2010).

We have applied the models of open magnetic fields with surface currents to explain the strong hidden toroidal magnetic fields inside the magnetars. We have considered two possibilities as the origin of their surface currents. One possibility is related to the crusts of the magnetars. Since the crusts are made of the solid matter, it could make the magnetic fields discontinuous at the crusts and the surface currents would appear due to these discontinuities. The magnetized stars can sustain the strong toroidal magnetic field energy by bending the poloidal magnetic fields within the crust zones.

The other possibility for the excitement of oppositely flowing currents inside and/or on the stellar surface might be related to magnetospheres which produce the oppositely flowing toroidal currents near and/or on the stellar surface. This kind of magnetosphere would also sustain the strong toroidal magnetic field energy inside the star. These models might be the key to reveal the mechanism of the giant flares of the magnetars.

Experience is the teacher of all things.
(Gaius Julius Caesar)

4

A sufficient condition for strong toroidal magnetic field

We have found that the oppositely flowing toroidal current densities cancel out the force-free toroidal current (κ current) and sustain the large toroidal magnetic fields in chapter 3. However, the physical meaning of such oppositely flowing toroidal current density is unclear. We consider and discuss the physical meaning of the oppositely flowing toroidal current density in this chapter.

4.1 Introduction

Anomalous X-ray Pulsars (AXP's) and Soft-Gamma-ray-Repeaters (SGR's) are considered as special classes of neutron stars, i.e. magnetars (Thompson & Duncan 1995). According to observations of rotational periods and their time derivatives, magnitudes of global dipole magnetic fields of magnetars reach about 10^{14-15}G. Recently, however, SGR's with weak dipole magnetic fields have been found (Rea et al. 2010, 2012). Their observational characteristics are very similar to those of ordinary SGR's but their global dipole magnetic fields are much weaker than those of ordinary magnetars. It might be explained by a possibility that such SGR's with small magnetic fields hide large toroidal magnetic fields under their surfaces and drive their activities by their internal toroidal magnetic energy (Rea et al. 2010). Recent X-ray observation of magnetar 4U 0142+61 also implies the presence of large toroidal magnetic fields (Makishima et al. 2014). By considering possible growth of magnetic fields of magnetars during proto-magnetar phases, strong differential rotation within proto-magnetars would amplify their toroidal magnetic fields (Duncan & Thompson 1992; Spruit 2009). Therefore, it would

be natural that some magnetars sustain large toroidal magnetic fields inside.

The large toroidal fields are required from the stability analyses of magnetic fields. Stability analyses have shown that stars with purely poloidal fields or purely toroidal fields are unstable (Markey & Tayler 1973; Tayler 1973). Stable magnetized stars should have both poloidal and toroidal magnetic fields. Moreover, the toroidal magnetic field strengths of the stable magnetized stars have been considered to be comparable with those of poloidal components (Tayler 1980). However, we have not yet known the exact stability condition and stable magnetic field configurations, because it is too difficult to carry out stability analyses of stars with both poloidal and toroidal magnetic fields.

Nevertheless, stabilities of magnetic fields have been studied by performing dynamical simulations. Braithwaite & Spruit (2004) showed that twisted-torus magnetic field structures are stable magnetic field configurations on dynamical timescale. Stabilities of purely toroidal magnetic field configurations or purely poloidal magnetic field configurations have been studied in the Newtonian framework (Braithwaite 2006, 2007) and in the full general relativistic framework (Kiuchi et al. 2011; Lasky et al. 2011; Ciolfi et al. 2011; Ciolfi & Rezzolla 2012). Braithwaite (2009) and Duez et al. (2010) have found a stability criterion of the twisted-torus magnetic fields. It could be expressed as

$$\alpha \frac{\mathcal{M}}{|W|} < \frac{\mathcal{M}_p}{\mathcal{M}} \leq 0.8, \tag{4.1}$$

where $\mathcal{M}/|W|$ is the ratio of the total magnetic energy to the gravitational energy. $\mathcal{M}_p/\mathcal{M}$ is the ratio of the poloidal magnetic field energy to the total magnetic field energy. α is a certain dimensionless factor of order of 10 for main-sequence stars and of order 10^3 for neutron stars. The ratio of $\mathcal{M}/|W|$ is a small value ($\sim 10^{-5}$) even for magnetars. Therefore, the criterion becomes

$$0.2 \leq \frac{\mathcal{M}_t}{\mathcal{M}} \lesssim 0.99, \tag{4.2}$$

where $\mathcal{M}_t$ is the toroidal magnetic field energy. Therefore, stellar magnetic fields are stable even for toroidal magnetic field dominated configurations. Therefore, it is very natural that the stable stationary magnetized stars have large toroidal magnetic fields.

Until recently, however, almost all numerically obtained equilibrium configurations for stationary and axisymmetric stars have only small fractions of toroidal magnetic fields, typically $\mathcal{M}_t/\mathcal{M} \sim 0.01$, even for twisted-torus magnetic field configurations in the Newtonian gravity (Tomimura & Eriguchi 2005; Yoshida & Eriguchi 2006; Yoshida et al. 2006; Lander & Jones 2009; Lander et al. 2012; Lander 2013, 2014) and in general relativistic perturbative solutions (Ciolfi et al. 2009; Ciolfi et al. 2010). They do not satisfy the stability criterion mentioned above.

On the other hand, there appeared several works which have successfully obtained the stationary states with strong toroidal magnetic fields by applying special boundary conditions. Glampedakis et al. (2012) obtained strong toroidal magnetic field models imposing surface

currents on the stellar surface as their boundary condition. Duez & Mathis (2010) imposed the boundary condition that the magnetic flux on the stellar surface should vanish. Since the magnetic fluxes of their models are zero on the stellar surfaces, all the magnetic field lines are confined within the stellar surfaces. They obtained configurations with strong toroidal magnetic fields which are essentially the same as those of classical works by Prendergast (1956) and Woltjer (1959a,b, 1960) and recent general relativistic works by Ioka & Sasaki (2004) and Yoshida et al. (2012).

We have found and shown that the strong toroidal magnetic fields within the stars require the oppositely (positively and negatively) flowing toroidal currents or oppositely flowing toroidal surface currents in chapter 3. Such oppositely flowing currents can sustain large toroidal magnetic fields in magnetized stars. It is also very recent that Ciolfi & Rezzolla (2013) have obtained stationary states of twisted-torus magnetic field structures with very strong toroidal magnetic fields using a special choice for the toroidal current. Their toroidal currents contain oppositely flowing current components and result in the large toroidal magnetic fields, although their paper does not explain the physical meanings for appearances of such oppositely, i.e. positively and negatively, flowing toroidal currents.

In this chapter, we consider and analyze configurations with oppositely flowing toroidal currents. In order to show the physical meaning of the oppositely flowing toroidal currents clearly, simplified analytical models are solved and we give a sufficient condition for presence of large toroidal magnetic fields within stars.

4.2 Spherical models with weak magnetic fields

4.2.1 Green's function approach

We follow the formulation and method in chapter 3. Therefore, the stationary condition for the configurations can be expressed as:

$$\int \frac{dp}{\rho} = -\phi_g + \int \mu(\Psi)\, d\Psi + C, \tag{4.3}$$

In order to obtain analytical solutions, we choose the functional forms as follow

$$\mu(\Psi) = \mu_0, \tag{4.4}$$

$$\kappa(\Psi) = \kappa_0 \Psi, \tag{4.5}$$

where μ_0 and κ_0 are constants. If we impose the boundary condition $\Psi = 0$ at the centre of the star, Ψ is described as follow (see chapter 3):

$$\begin{aligned}\frac{\Psi}{\sin^2\theta} &= K\kappa_0 r J_1(\kappa_0 r) \\ &- 4\pi\mu_0\kappa_0\left\{ rJ_1(\kappa_0 r)\int_r^{r_s} Y_1(\kappa_0 r')\,\rho(r')r'^3\,dr' + rY_1(\kappa_0 r)\int_0^r J_1(\kappa_0 r')\,\rho(r')r'^3\,dr' \right\},\end{aligned} \tag{4.6}$$

where we set the stellar radius $r_s = 1$ in this chapter. J_1 and Y_1 are the spherical Bessel functions of the first kind and the second kind, respectively and K is a coefficient which is determined by a boundary condition of Ψ at the surface. According to the θ-dependency of the inhomogeneous term, we search for solutions of the following form:

$$a(r)\sin^2\theta \equiv \Psi(r,\theta). \tag{4.7}$$

Therefore we obtain the solution for $a(r)$ by imposing the boundary condition at the surface and integrating Eq. (4.6).

In this chapter, we treat spherical polytropes with the polytropic indices $N = 0$ and $N = 1$. As for the configurations of the magnetic fields, we choose two types: (1) closed field models (e.g. Duez & Mathis 2010) and (2) open field models (e.g. Broderick & Narayan 2008). For closed field models, since all magnetic field lines are closed and confined within the star, the magnetic flux must vanish at the stellar surface as follows:

$$a(r_s) = 0. \tag{4.8}$$

For open field models, since the poloidal magnetic field lines must continue smoothly through the stellar surfaces into the outside. the boundary condition can be expressed as:

$$a(r_s) = -\left.\frac{da(r)}{dr}\right|_{r=r_s}. \tag{4.9}$$

The density profiles are

$$\rho(r) = \rho_c, \tag{4.10}$$

for $N = 0$ polytrope and

$$\rho(r) = \rho_c\frac{\sin(\pi r)}{\pi r}. \tag{4.11}$$

for $N = 1$ polytrope and ρ_c is the central density.

We calculate four analytical solutions according to these conditions. We can obtain four different analytical solutions according to four different situations. We name them as $a_{0C}(r)$ ($N = 0$ with closed fields), $a_{0O}(r)$ ($N = 0$ with open fields), $a_{1C}(r)$ ($N = 1$ with closed fields) and $a_{1O}(r)$ ($N = 1$ with open fields).

Since the poloidal magnetic field lines are continuous smoothly at the surfaces for open field models, their external solutions $a^{ex}(r)$ must be expressed as:

$$a^{ex}(r) = \frac{a(r_s)}{r} \, . \tag{4.12}$$

It should be noted that the toroidal magnetic fields for open field models and the poloidal magnetic fields for closed field models are discontinuous at the surfaces except for solutions with special values of κ_0, i.e. eigen solutions with corresponding eigen values (Broderick & Narayan 2008; Duez & Mathis 2010; chapter 3). Therefore, these non-eigen configurations have toroidal and poloidal surface currents. Such surface currents make the Lorentz stress on the stellar surface (Broderick & Narayan 2008).

The toroidal surface current density can be expressed as follows:

$$\begin{aligned} \frac{j_{\varphi,sur}(\theta)}{c} &= \frac{1}{4\pi}(B_\theta^{ex} - B_\theta^{in})\bigg|_{r=r_s} \\ &= \frac{1}{4\pi r_s \sin\theta}\left(\frac{\partial \Psi^{ex}}{\partial r} - \frac{\partial \Psi^{in}}{\partial r}\right)\bigg|_{r=r_s} \\ &= \frac{\sin\theta}{4\pi r_s}\left(\frac{da^{ex}}{dr} - \frac{da^{in}}{dr}\right)\bigg|_{r=r_s} \\ &= j_0 \sin\theta, \end{aligned} \tag{4.13}$$

where superscript ^{in} denotes an internal solution and j_0 is a coefficient of the surface current density.

4.2.2 Analytic Solutions

Four different inner solutions $(0 \leq r \leq 1)$ can be obtained according to four different situations as follows:

$$a_{0C}(r) = 4\pi\mu_0\rho_c \left[\frac{\sin(\kappa_0 r) - \kappa_0 r\cos(\kappa_0 r)}{r\kappa_0^2(\sin\kappa_0 - \kappa_0\cos\kappa_0)} - \frac{r^2}{\kappa_0^2}\right], \tag{4.14}$$

$$a_{0O}(r) = 4\pi\mu_0\rho_c \left[\frac{3\{\sin(\kappa_0 r) - \kappa_0 r\cos(\kappa_0 r)\}}{r\kappa_0^4\sin\kappa_0} - \frac{r^2}{\kappa_0^2}\right], \tag{4.15}$$

$$\begin{aligned} a_{1C}(r) =& \frac{\mu_0\rho_c}{r(\kappa_0^2 - \pi^2)^2}\Bigg[\frac{8\pi\{\sin(\kappa_0 r) - \kappa_0 r\cos(\kappa_0 r)\}}{\sin\kappa_0 - \kappa_0\cos\kappa_0} \\ &- \left\{\left(4\kappa_0^2 - 4\pi^2\right)r^2 + 8\right\}\sin(\pi r) + 8\pi r\cos(\pi r)\Bigg], \end{aligned} \tag{4.16}$$

$$a_{1O}(r) = \frac{\mu_0 \rho_c}{r(\kappa_0^2 - \pi^2)^2} \left[\frac{(4\pi^3 - 4\pi\kappa_0^2)\{\sin(\kappa_0 r) - \kappa_0 r \cos(\kappa_0 r)\}}{\kappa_0^2 \sin\kappa_0} \right. \\ \left. - \left\{(4\kappa_0^2 - 4\pi^2)r^2 + 8\right\} \sin(\pi r) + 8\pi r \cos(\pi r) \right] . \tag{4.17}$$

The open field models (a_{0O} and a_{1O}) continue to the external solutions ($r \geq 1$) expressed by Eq.(4.12). Here it would be helpful to explain several different kinds of characteristic solutions.

First, for $a_{1C}(r)$ solutions there appears a singular solution at $\kappa_0 = \pi$ (Haskell et al. 2008), while the solution a_{0C} is not singular at $\kappa_0 = \pi$ (see chapter 3).

Second, although most solutions are accompanied by surface currents, some special solutions have no surface currents. We call such solutions without surface currents as eigen solutions and the values of κ_0 as eigen values.

Third, there are solutions whose magnetic flux functions become higher-order ones (see figures in Broderick & Narayan 2008; Duez & Mathis 2010). Those solutions appear when the value of κ_0 exceeds the first eigen value of κ_0 for each situation.

Fourth, special solutions with different polytropic indices come to coincide with each other. In other words, those solutions do not depend on the matter distributions. As seen from the expression for the current density, the contribution from the μ current term needs to disappear. It implies that those solutions are determined only by the κ current. Since the κ currents do not contribute to the Lorentz force, these solutions can be called as the force-free solutions. The force-free solution is expressed by the following form:

$$a_{ff}(r) = \frac{K}{\kappa_0 r} \left\{\sin(\kappa_0 r) - \kappa_0 r \cos(\kappa_0 r)\right\} . \tag{4.18}$$

In Fig. 4.1, the ratio of the toroidal magnetic field energy $\mathcal{M}_t$ to the total magnetic field energy $\mathcal{M} = \mathcal{M}_p + \mathcal{M}_t$ of each model is plotted for different situations. The solution becomes force-free at the point denoted by the vertical solid lines (Broderick & Narayan 2008; chapter 3). The dashed vertical lines denote the critical values of κ_0 for appearance of higher-order solutions (see figures in Ioka & Sasaki 2004; Broderick & Narayan 2008; Duez & Mathis 2010; Yoshida et al. 2012). Hereafter, we focus on solutions with κ_0 less than the lowest eigenvalue. However, our analyses and results could be general and would be valid even when the configurations are higher-order.

As seen from Fig. 4.1, $N = 0$ solutions and $N = 1$ solutions cross at $k_0 \sim 4.49$ and 7.73 for closed field models and $k_0 \sim 3.14$ and 6.28 for open field models. The solutions at these points are force-free solutions as mentioned before.

We denote the value of κ_0 in the n-th force-free solutions as κ_{FOn} for open field models and κ_{FCn} for closed field models. The values are $\kappa_{FO1} \sim 4.49$, $\kappa_{FO2} \sim 7.73$ and $\kappa_{FC1} = \pi$, $\kappa_{FC2} = 2\pi$. These values are consistent with the result obtained by Broderick & Narayan (2008). As seen from Fig. 4.1, the energy ratio is $\mathcal{M}_t/\mathcal{M} \sim 0.5$ when the solutions are the first force-free configurations.

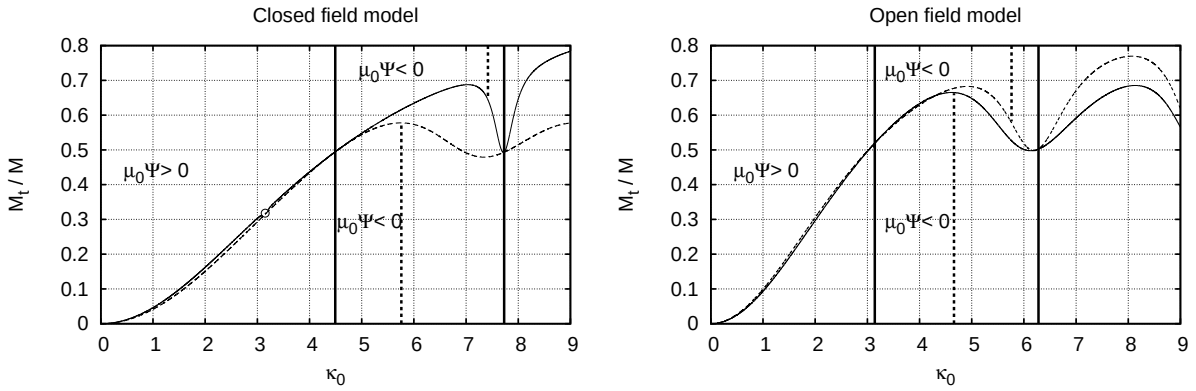

Figure 4.1: Energy ratio $\mathcal{M}_t/\mathcal{M}$ is plotted against the value of κ_0. Closed (left panel) and open (right panel) field solutions are shown. The solid and dashed curves denote $N = 1$ and $N = 0$ solutions, respectively. The vertical solid lines mean force-free solutions: Closed force-free solutions appear at $\kappa_0 \sim 4.49$ and $\kappa_0 \sim 7.73$ and open force-free solutions at $\kappa_0 = \pi$ and $\kappa_0 = 2\pi$. The toroidal current densities are composed of two oppositely flowing components beyond the vertical dashed lines: $\kappa_0 \sim 5.76$ for the a_{0c} solution (dashed curve in left panel), $\kappa_0 \sim 7.42$ for the a_{1c} solution (solid curve in left panel), $\kappa_0 \sim 5.76$ for the a_{0o} solution (dashed curve in right panel) and $\kappa_0 \sim 4.66$ for the a_{1o} (solid curve in right panel). The open circle in the left panel denotes the singular solution for $a_{1C}(r)$.

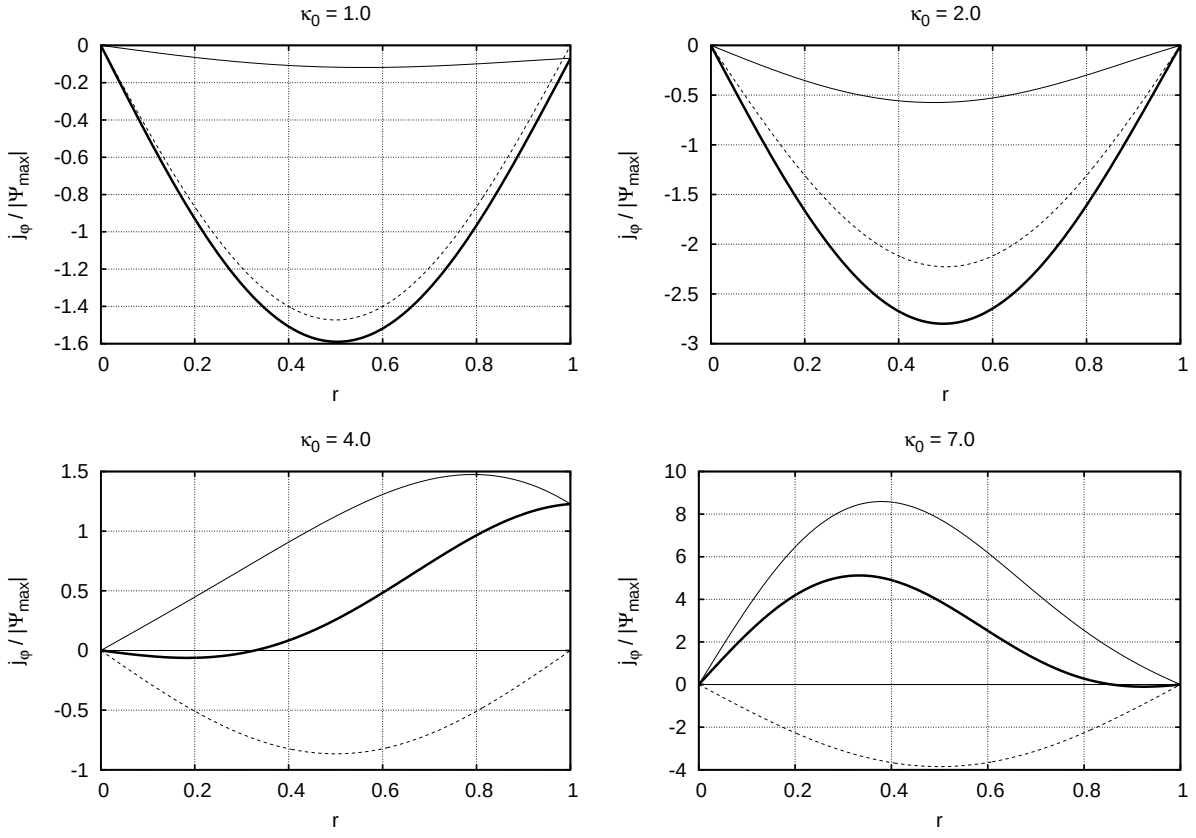

Figure 4.2: Distributions of the toroidal current density normalized by the maximum strength of $|\Psi_{\max}|$ are shown along the equatorial plane. Curves with different types denote the behaviors of the total toroidal current density, j_φ/c, (thick solid line), the toroidal κ_0 current density (thin solid line) and the toroidal μ_0 current density (thin dotted line). We set $\mu_0 = -1$ in order to plot these distributions. Left panels show the profiles of solution a_{1O} with $\kappa_0 = 1.0$ and 4.0 and right panels show those of solution a_{1C} with $\kappa_0 = 2.0$ and 7.0.

In Fig. 4.2, distributions of the normalized j_φ/c (thick solid line), the κ current (thin solid line) and the μ current term (dashed line) along the equatorial plane are shown for solutions of a_{1O} (with $\kappa_0 = 1.0, 4.0$) and a_{1C} (with $\kappa_0 = 2.0, 7.0$). We have fixed $\mu_0 = -1$ following the chapter 3 in order to plot these curves.

The energy ratios are $\mathcal{M}_t/\mathcal{M} \sim 0.09$ for the open field model with $\kappa_0 = 1.0$, $\mathcal{M}_t/\mathcal{M} \sim 0.63$ for the open field model with $\kappa_0 = 4.0$, $\mathcal{M}_t/\mathcal{M} \sim 0.16$ for the closed field model with $\kappa_0 = 2.0$, and $\mathcal{M}_t/\mathcal{M} \sim 0.68$ for closed field model with $\kappa_0 = 7.0$. Therefore, the solutions with $\kappa_0 = 1.0$ and $\kappa_0 = 2.0$ are poloidal magnetic field dominated configurations, while solutions with $\kappa_0 = 4.0$ and $\kappa_0 = 7.0$ are toroidal magnetic field dominated configurations. The configuration changes from poloidal magnetic field dominated to toroidal magnetic field dominated models occur at the first force-free solutions (Fig. 4.1).

As seen from this figure (Fig. 4.2), directions (signs) of the μ current, i.e. non force-free current, and the κ current, i.e. force-free current, are the same for poloidal magnetic field dominated solutions ($\kappa_0 = 1.0$ and $\kappa_0 = 2.0$). By contrast, for toroidal magnetic field dominated solutions ($\kappa_0 = 4.0$ and $\kappa_0 = 7.0$), the μ current flows oppositely to the κ current (chapter 3). Moreover, most of the j_φ/c (thick solid line) for solutions with $\kappa_0 = 4.0$ and $\kappa_0 = 7.0$ flows oppositely against the corresponding μ current. Since the sign of the total toroidal current determines the sign of the magnetic flux function, this implies that the sign of $\mu_0\Psi$ changes from $\mu_0\Psi > 0$ to $\mu_0\Psi < 0$ at the force-free solutions. The toroidal magnetic fields are dominant for $\mu_0\Psi < 0$ models, while the poloidal magnetic fields are dominant for $\mu_0\Psi > 0$ models (see Fig. 4.1). The oppositely flowing non-force free current ($\mu_0\Psi < 0$) is required for large toroidal magnetic fields.

On the other hand, the surface toroidal currents in the closed field models are always oppositely flowing to the total toroidal currents because of the zero-flux boundary condition Eq. (4.8) and the form of the surface current Eq. (4.13).

4.2.3 Deep relation between the oppositely flowing toroidal current and the poloidal deformations of stars

The toroidal magnetic fields tend to deform stellar shapes prolate, while the poloidal magnetic fields tend to deform them oblate (Haskell et al. 2008). The oppositely flowing toroidal current seems to relate to the stellar deformations as well as to the presence of large toroidal magnetic fields, because the relation can be studied by investigating the Lorentz forces which are produced by the interactions of the currents and the magnetic fields.

In our analytic models, the Lorentz force $\boldsymbol{L}$ is expressed using the arbitrary function $\mu(\Psi)$ as

$$\begin{aligned}\boldsymbol{L} &= \left(\frac{\boldsymbol{j}}{c} \times \boldsymbol{B}\right) = \rho\nabla \int \mu(\Psi)\, d\Psi = \rho\mu(\Psi)\nabla\Psi \\ &= \rho\mu_0 \frac{da}{dr} \sin^2\theta \boldsymbol{e}_r + 2\rho\mu_0 \frac{a}{r} \sin\theta\cos\theta \boldsymbol{e}_\theta.\end{aligned} \tag{4.19}$$

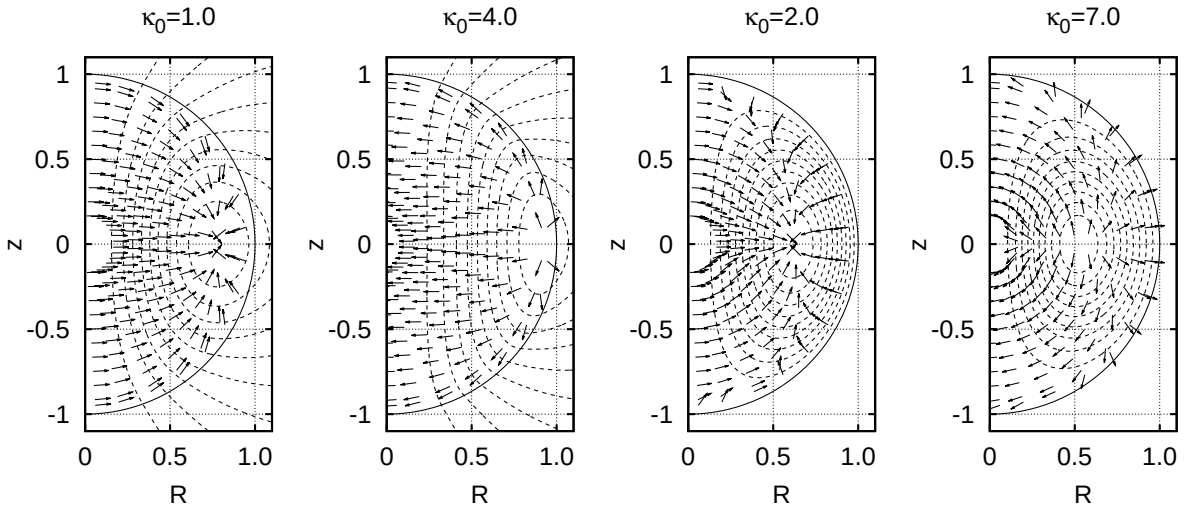

Figure 4.3: Poloidal magnetic field structures (dashed curves) and Lorentz force vector fields (arrows) for the open field models ($\kappa_0 = 1.0$, $\kappa_0 = 4.0$) and the closed field models ($\kappa_0 = 2.0$ and $\kappa_0 = 7.0$) are displayed.Vectors only show their directions but are not scaled to their absolute values.

In Fig. 4.3, the contours of Ψ (dashed curves) and the directions of Lorentz force vectors (arrows) are displayed. It should be noted that directions of the Lorentz forces are totally opposite between models with smaller values of κ_0 and those with larger values of κ_0. In other words, force-free solutions divide two different types of the Lorentz force vectors.

Following Haskell et al. (2008), we consider the stellar quadrupole deformations of $N = 1$ polytropic stars. We assume that the influence of the magnetic fields to the stellar structures are small and that their effects can be treated perturbatively. Due to the effects of the magnetic fields, a certain physical quantity $X(r, \theta)$ is assumed to be expressed as

$$X(r, \theta) = X(r) + \sum_{n=0}^{\infty} \delta X^{(n)}(r) P_n(\cos\theta), \tag{4.20}$$

where $\delta X^{(n)}$ denotes a small change of order $O(B^2)$ of the quantity X due to the Lorentz force. The angular dependencies are treated by the Legendre polynomial expansions and the coefficient of each Legendre polynomial is expressed as $\delta X^{(n)}(r)$. This expansion is also applied to the Lorentz force as follows:

$$\boldsymbol{L}(r, \theta) = \sum_{n=0}^{\infty} \boldsymbol{L}^{(n)}(r) P_n(\cos\theta). \tag{4.21}$$

From the perturbed equilibrium condition equations, the following relations can be derived:

$$\frac{d\delta p^{(n)}}{dr} + \rho \frac{d\delta\phi_g^{(n)}}{dr} + \delta\rho^{(n)} \frac{d\phi_g}{dr} = L_r^{(n)}, \tag{4.22}$$

$$\delta p^{(n)} + \rho\delta\phi_g^{(n)} = r L_\theta^{(n)} \ . \tag{4.23}$$

Since we are interested in the quadruple deformation, we consider only $n = 2$ components of Lorentz force as follows:

$$\begin{aligned} L_r^{(2)} &= -\frac{2\rho\mu_0}{3}\frac{da(r)}{dr} \\ L_\theta^{(2)} &= -\frac{2\rho\mu_0}{3}\frac{a(r)}{r} \\ L^{(2)} &\equiv L_r^{(2)} - \frac{d(rL_\theta^{(2)})}{dr} \\ &= -\frac{2\rho\mu_0}{3}\frac{da(r)}{dr} + \frac{2\mu_0}{3}\frac{d(a(r)\rho(r))}{dr} \\ &= \frac{2\mu_0}{3}\frac{d\rho}{dr}a(r). \end{aligned} \tag{4.24}$$

The change of the stellar surface to the order of the quadrupole term can be expressed as

$$r_d(\theta) = r_s\{1 + \varepsilon P_2(\cos\theta)\} = r_s\left\{1 + \frac{\varepsilon}{2}(3\cos^2\theta - 1)\right\}, \tag{4.25}$$

where $r_d(\theta)$ denotes the deformed surface radius and ε is a small quantity which represents the fraction of the stellar surface along the pole. Following this expression, the stellar shape is prolate for $\varepsilon > 0$ and oblate for $\varepsilon < 0$.

Deformation of $N \neq 0$ polytrope

Using these equations, the quadrupole change of the density is described by:

$$\delta\rho^{(2)} = \left(\frac{d\rho}{dr}\delta\phi_g^{(2)} + L^{(2)}\right)\left(\frac{d\phi_g}{dr}\right)^{-1}. \tag{4.26}$$

Since the surface of the deformed star is defined by a set of points where the pressure vanishes, i.e.

$$p(r_d(\theta)) = \delta p(r_s) + \varepsilon r_s P_2(\cos\theta)\frac{dp}{dr}\Big|_{r=r_s} = 0\,. \tag{4.27}$$

we can derive

$$r_s\varepsilon\frac{d\rho_0}{dr}\Big|_{r=r_s} + \delta\rho^{(2)}\Big|_{r=r_s} = 0\,, \tag{4.28}$$

for polytropes with $N \neq 0$. For $N = 0$ polytrope, this equation is reduced to trivial relation $0 = 0$ and so we will treat $N = 0$ polytrope differently as will be shown in the next section. Therefore, the quadrupole surface deformation ε for $N \neq 0$ is obtained by

$$\varepsilon = -\left(\frac{d\rho}{dr}\right)^{-1}\frac{\delta\rho^{(2)}}{r_s}\Big|_{r=r_s}. \tag{4.29}$$

It is clearly seen that, since $\frac{d\rho}{dr} < 0$ at the surface, the stellar deformation is prolate for $\delta\rho^{(2)} > 0$

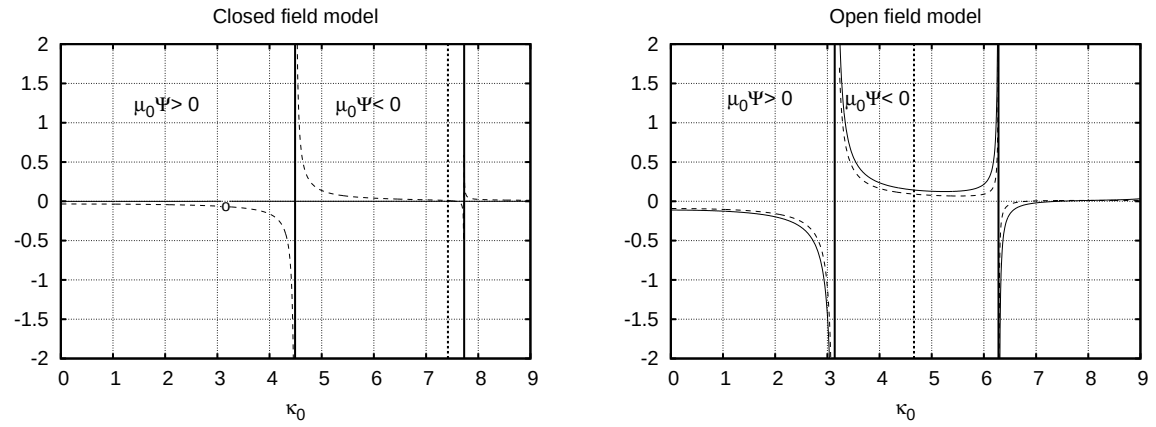

Figure 4.4: The values of $-2\mu_0 a(x=\pi)/3$ (thin solid line) and $-\delta\phi_g^{(2)}(x=\pi)$ (thin dashed line) in closed field model (left panel) and open field model (right panel) are plotted. The thick vertical lines denotes force-free limit. The toroidal current densities consist of oppositely flowing flows beyond the dashed thick vertical lines. We set $\mu_0 = -1$ and $\rho_c = 1$ in order to plot these graphs.

and oblate for $\delta\rho^{(2)} < 0$. In our situation, the explicit form of $\delta\rho^{(2)}$ can be expressed as

$$\delta\rho^{(2)} = \frac{d\rho}{dr}\left(\frac{2\mu_0}{3}a(r_s) + \delta\phi_g^{(2)}(r_s)\right)\left(\frac{d\phi_g}{dr}\right)^{-1}\Big|_{r=r_s}, \tag{4.30}$$

and ε for $N \neq 0$ polytropes becomes as

$$\begin{aligned}\varepsilon &= -\left(\frac{2\mu_0}{3}a(r_s) + \delta\phi_g^{(2)}(r)\right)\left(\frac{d\phi_g^{(2)}}{dr}\right)^{-1}\Big|_{r=r_s} \\ &= \rho\left(\frac{dp}{dr}\right)^{-1}\left(\frac{2\mu_0}{3}a(r_s) + \delta\phi_g^{(2)}(r)\right)\Big|_{r=r_s}.\end{aligned} \tag{4.31}$$

As shown in App. A.2.1 the gravitational change for $N = 1$ polytrope can be obtained as

$$\delta\phi_g^{(2)}(x) = \frac{F^{(p)}(x)}{x^3} - \frac{1}{\pi^2}\frac{dF^{(p)}(\pi)}{dx}\Big|_{x=\pi} j_2(x)\,. \tag{4.32}$$

Thus for $x = \pi$, i.e. on the surface,

$$\delta\phi_g^{(2)}(\pi) = \frac{F^{(p)}(\pi)}{\pi^3} - \frac{3}{\pi^4}\frac{dF^{(p)}}{dx}\Big|_{x=\pi}, \tag{4.33}$$

where $j_2(\pi) = 3/\pi^2$ is used. Here the function $F^{(p)}(x)$ is defined in App. A.2.1.

Since the expression for the function $F^{(p)}$ is so complicated, it is not clearly seen the sign of the quantity $(\delta\phi_g^{(2)}(r_s) + 2\mu_0 a(r_s)/3)$ which determines the sign of the quantity ε. In Fig. 4.4 we show the behaviors of $-\delta\phi_g^{(2)}(r_s)$ and $-2\mu_0 a(r_s)/3$ against the value of κ_0. As seen from this figure, the shape change from the effect due to the gravitational change is the same as that from the Lorentz term. Thus the sign of the quantity ε is essentially determined by the sign of

the Lorentz term, i.e., the sign of the quantity $\mu_0 a(r_s)$. Since $\rho(r)(dp/dr)^{-1} < 0$, the stellar shape is oblate for $\mu_0\Psi(r_s,\theta) > 0$ and prolate for $\mu_0\Psi(r_s,\theta) < 0$ as far as the global poloidal magnetic field is dipole.

On the other hand, as we have seen in Figs. 4.1 and 4.2, the poloidal magnetic field energy is dominant for $\mu_0\Psi < 0$ and toroidal magnetic field energy is dominant for $\mu_0\Psi > 0$. Therefore, what we have shown thus far is summarized as follows. The presence of the large toroidal magnetic field inside the star corresponds to the two conditions; (1) the presence of the oppositely flowing non force-free toroidal current density whose contribution to the term $\int \mu(\Psi)d\Psi$ in the stationary condition needs to be negative and (2) the oppositely flowing non force-free current makes the stellar shape prolate.

Deformation for $N = 0$ polytrope

For $N = 0$ polytrope, the gravitational change and the shape change are written as follows as shown in App. A.2.2:

$$\delta\phi_g^{(2)} = -\frac{4}{5}\pi G\rho_0\varepsilon r^2 \,, \tag{4.34}$$

and

$$\varepsilon = \left\{-\frac{4}{3}\pi G\rho_0 r_s^2 - \left(-\frac{4}{5}\pi G\rho_0 r_s^2\right)\right\}^{-1}\frac{2\mu_0}{3}a(r_s) = -\frac{5\mu_0}{4\pi G\rho_0}a(r_s). \tag{4.35}$$

Here we use the stationary condition

$$\delta p^{(2)} + \rho_0\delta\phi_g^{(2)} = rL_\theta^{(2)} \,, \tag{4.36}$$

and the surface condition Eq. (4.27).

Thus the sign of the quantity ε is exactly determined by the sign of the Lorentz term, i.e., the sign of the quantity $\mu_0 a(r_s)$. The stellar shape is oblate for $\mu_0\Psi(r_s,\theta) > 0$ and prolate for $\mu_0\Psi(r_s,\theta) < 0$ as far as the global poloidal magnetic field is dipole.

Sufficient condition for appearance of toroidal magnetic field dominated configurations

Consequently, we can conclude that a sufficient condition for appearance of toroidal magnetic field dominated configurations is that the arbitrary function $\mu(\Psi)$ satisfies the following condition:

$$\int \mu(\Psi)d\Psi\Big|_{r=r_s} < 0 \,, \tag{4.37}$$

when the functional forms are Eqs. (4.4) and (4.5). Although, exactly speaking, these analyses and conditions are valid within the present parameter settings, our results would be useful for more general situations. This might be naively seen from the contribution of the term $\int \mu d\Psi$ in the stationary condition equation Eq. (4.3). If this term is negative, it implies that the action

of the Lorentz term is opposite to that of the centrifugal force which is expressed by the term $\int \Omega(R)^2 R dR$ and is always positive. Thus the density distribution could be 'anti-oblate', i.e. prolate (see also chapter 7).

Although the sufficient condition presented in this chapter might not be always correct, we could obtain the large toroidal magnetic fields by employing this criterion for more complicated calculations.

4.3 Discussion and Conclusion

4.3.1 Oppositely flowing toroidal surface current density and Lorentz pressure

As we have shown in chapter 3, the oppositely flowing (negative) toroidal surface current density can sustain the strong toroidal magnetic fields, because the negative surface current cancels out the κ current and can have the relative large κ current within the star. Although such configurations cannot have toroidal component magnetic field dominated structure ($\mathcal{M}_t > \mathcal{M}_p$), they have relatively large toroidal magnetic field energy within the star. The typical value of the energy ratio is $\mathcal{M}_t/\mathcal{M} \sim 0.2 - 0.3$ (chapter 3) for twisted-torus (open) fields configurations with the negative surface current. We consider the physical meaning f the negative surface current following the discussion in Sec. 4.2.3. If we consider the dipole negative surface toroidal current, such surface current under the dipole magnetic fields exerts the θ-component of Lorentz pressure (Braithwaite & Spruit 2006) as

$$S_\theta \sim \frac{j_s}{c} B_r \sim -j_0 P_2(\cos\theta), \tag{4.38}$$

where j_0 is a coefficient of surface current. Therefore the θ-component of the quadrupole ($n = 2$) stress ($S_\theta^{(2)}$) by the negative surface current is

$$S_\theta^{(2)} \sim -j_0. \tag{4.39}$$

Since the toroidal surface current is negative ($j_0 < 0$), the sign of $S_\theta^{(2)}$ is positive. The Lorentz stress by the negative surface current is directed to the poles. Such stress makes the stellar shape prolate. Therefore, the physical meaning of the negative surface current density is the Lorentz pressure which tends to make the stellar shape prolate in the same way as the oppositely flowing μ term does.

4.3.2 Twisted-torus configuration with large toroidal magnetic field

Almost all previously carried out investigations for magnetized equilibrium states having twisted-torus magnetic fields had failed to obtain toroidal magnetic field dominated ($\mathcal{M}_t > \mathcal{M}_p$) models. We have found that most models of their works do not satisfy the condition of Eq. (4.37) and the magnetized stellar shapes are oblate due to the μ current term. The κ term in those

works has been chosen as follows:

$$\kappa(\Psi) = \kappa_0(\Psi - \Psi_{\rm max})^{k_1+1}\Theta(\Psi - \Psi_{\rm max}), \tag{4.40}$$

where, k_1 is a constant and Θ is the Heaviside step function and $\Psi_{\rm max}$ is the maximum value of Ψ on the last closed field line within the star. This functional form was used by Tomimura & Eriguchi (2005) for the first time and results in the twisted-torus configurations. The same choice for the κ has been employed by many authors (e.g. Yoshida & Eriguchi 2006; Yoshida et al. 2006; Kiuchi & Kotake 2008; Lander & Jones 2009; Ciolfi et al. 2009; Ciolfi et al. 2011 ;Glampedakis et al. 2012; Lander et al. 2012; Lander 2013, 2014; chapters 2 & 3). While the functional form $\mu(\Psi) = \mu_0$ (constant) has been used in many investigations, we have used a different functional form in chapter 2 as

$$\mu(\Psi) = \mu_0(\Psi + \epsilon)^m, \tag{4.41}$$

where m and ϵ are positive constants. They have obtained highly localized poloidal magnetic field configurations using this type of functional from. However, their works did not satisfy the condition of Eq. (4.37) and did not obtain models with large toroidal magnetic fields.

Very recently, Ciolfi & Rezzolla (2013) have succeeded in obtaining magnetized equilibrium states with twisted-torus magnetic fields whose toroidal fields are large. Their functional form of κ is

$$\kappa(\Psi) = \kappa_0\Psi(|\Psi/\Psi_{\rm max}| - 1)\Theta(|\Psi/\Psi_{\rm max}| - 1). \tag{4.42}$$

On the other hand, the functional form of μ is

$$\mu(\Psi) = c_0\left[(1 - |\Psi/\Psi_{\rm max}|)^2\,\Theta(1 - |\Psi/\Psi_{\rm max}|) - \bar{k}\right] + X_0\kappa(\Psi)\frac{d\kappa(\Psi)}{d\Psi}, \tag{4.43}$$

where c_0, $\bar{k}(> 0)$ and X_0 are constants. The toroidal magnetic field is confined within the last closed field line in these functional forms. Outside the toroidal magnetic field region, the function κ vanishes and μ becomes

$$\mu(\Psi) = c_0\left[(1 - |\Psi/\Psi_{\rm max}|)^2 - \bar{k}\right]. \tag{4.44}$$

Since the first term and the second term are positive and negative, respectively, this function with larger $\bar{k}$ tends to satisfy the condition of Eq. (4.37). As they noted, larger values of $\bar{k}$ result in larger energy ratios $\mathcal{M}_t/\mathcal{M}$. As the value of k increases, the energy ratio $\mathcal{M}_t/\mathcal{M}$ increases and the stellar shape becomes more prolate in general (see Tab. 1 in Ciolfi & Rezzolla 2013). However, they assumed that the magnetic field configuration is purely dipole but their functional forms and toroidal current density distribution are far from dipole one (see bottom panels of Fig. 2 in Ciolfi & Rezzolla 2013). We need to calculate magnetic field configurations with higher order components for large toroidal models in the future.

4.3.3 Concluding remarks

We have obtained four analytic solutions with both open and closed magnetic fields for spherical polytropes with weak magnetic fields.

Using the obtained solutions we have discussed the condition for which the toroidal magnetic field dominated configurations appear. The toroidal magnetic field become strong if there appear oppositely flowing toroidal current components. Such oppositely current density makes the stellar shape prolate. This situation can be related to the condition for the non force-free toroidal current contribution, i.e. $\int \mu(\Psi) d\Psi$, in the stationary state condition Eq. (4.3). The sufficient condition (Eq. 4.37) for appearance of large toroidal magnetic fields in the stationary axisymmetric magnetized stars found in this chapter means that it acts as decreasing the density mainly in the equatorial direction, i.e. making the stellar shape prolate.

Gallia est omnis divisa in partes tres.
All Gaul is divided into three parts.
(Caesar, The Gallic War)

5

Magnetic fields of magnetar throughout its interior and exterior

We have found that the large toroidal magnetic fields result in and result from the oppositely flowing non force-free toroidal current density and the direction of Lorentz force which tends to stellar shape prolate in chapter 4. In this chapter, we consider the magnetic field configurations of magnetar throughout its interior and exterior - core, crust and magnetosphere. The deformation of the crust relates to the core toroidal magnetic fields. On the other hand, the change of the stress on the crust has influence on the magnetic field structures in the magnetosphere.

5.1 Introduction

Neutron stars have the strong magnetic fields among the stars in the universe. Especially, Anomalous X-ray Pulsars (AXPs) and Soft Gamma-ray Repeaters (SGRs) are considered as special classes of magnetized neutron star, magnetar. Magnetars have very strong dipole magnetic fields whose typical strength reaches about 10^{15} G at their surfaces. They show the stationary intense emissions and dynamical flares releasing magnetic energy (Thompson & Duncan 1995). Such magnetic activities are also considered as heating source of them (Pons et al. 2007). The magnetic field configurations are important for these astrophysical events, because the magnetic energy decaying depends on their structure deeply. Especially for flares, both exterior and interior magnetic fields structures are considered to be essential by many studies (e.g. Thompson & Duncan 2001; Thompson et al. 2002; Beloborodov & Thompson 2007; Masada et al. 2010). Recently, numerical simulations of crustal Hall magnetohydrodynamics (MHD) secular evolutions (Perna & Pons 2011) and strongly twisted force-free magnetospheric dy-

namical evolutions (Parfrey et al. 2013) have been performed in order to understand the flares. However, since the magnetic field structures of both core-crust (interior) and magnetosphere (exterior) should be coupled, we need to consider them at the same time. As a first step, we have calculated equilibrium magnetic field structure of both internal and external simultaneously and systematically in this chapter.

The Hall drift within the crust is considered as a key for the magnetar internal magnetic field structures. The Hall drift itself does not dissipate the magnetic fields, but it makes higher order components of magnetic field during the Hall cascade process. Such higher order components magnetic field promotes the Ohmic dissipation more efficiently (Jones 1988; Goldreich & Reisenegger 1992; Naito & Kojima 1994; Urpin & Shalybkov 1995; Shalybkov & Urpin 1997; Geppert & Rheinhardt 2002; Rheinhardt & Geppert 2002; Rheinhardt et al. 2004; Hollerbach & Rüdiger 2002; Hollerbach & Rüdiger 2004; Cumming et al. 2004; Reisenegger et al. 2007; Pons & Geppert 2007). The timescale of the Hall drift is determined by the strength of the magnetic fields within the crust. The Hall drift is characterized by magnetic Reynolds number $\mathcal{R}_m$ (Pons & Geppert 2007) as,

$$\mathcal{R}_m \equiv \frac{t_{Ohm}}{t_{Hall}} = \frac{\sigma B}{ecn_e} \sim 10^3 \left(\frac{B}{10^{15}\mathrm{G}}\right)\left(\frac{\sigma}{10^{25}\mathrm{s}^{-1}}\right), \tag{5.1}$$

where t_{Ohm} and t_{Hall} are Hall drift and Ohmic dissipation timescale respectively. σ, c, n_e and e are electrical conductivity of the crust, the speed of light, the electron number density and a charge of an electron. This value would reach 1000 locally within the magnetar crust, because the crustal magnetic fields of magnetar are sufficient large ($\geq 10^{15}$G). The Hall drift would become very effective in the magnetar crust and its timescale is faster than or comparable to the lifetime of magnetars. Recently, Hall MHD numerical simulations have been performed (Kojima & Kisaka 2012; Viganò & Pons 2012; Viganò et al. 2012; Viganò et al. 2013; Gourgouliatos & Cumming 2014) and these works have succeeded in examining the Hall drift during the secular timescale magnetic field evolution.

As recent works showed, the toroidal magnetic fields decrease rapidly during the Hall drift timescale because the toroidal fields are changed into the higher order poloidal components by the Hall cascade and the Ohmic dissipation is promoted by the higher order components (Kojima & Kisaka 2012; Viganò et al. 2013; Gourgouliatos & Cumming 2014). The Hall cascade becomes very effective when the initial toroidal magnetic field energy is much larger than poloidal magnetic field energy. The toroidal magnetic field energy ratio and its evolution are very important to consider the Hall drift and the magnetar secular evolution during its lifetime. Therefore, we should include the Hall drift in order to consider the internal magnetic field configurations in equilibrium. One approach is the Hall equilibrium study.

Gourgouliatos et al. (2013) have calculated Hall equilibrium states with both poloidal and toroidal magnetic fields solving Grad-Shafranov equation. As Gourgouliatos et al. (2013) have pointed out, the Hall equilibrium state is very similar to MHD equilibrium state which have been studied for sixty years since Chandrasekhar and his colleagues pioneering works (Chan-

drasekhar & Fermi 1953; Ferraro 1954; Chandrasekhar 1956b; Chandrasekhar & Prendergast 1956; Prendergast 1956; Woltjer 1959a; Woltjer 1959b; Wentzel 1961; Ostriker & Hartwick 1968; Miketinac 1973; Miketinac 1975; Bocquet et al. 1995; Konno et al. 1999; Ioka & Sasaki 2004; Kiuchi & Yoshida 2008; Haskell et al. 2008; Lander & Jones 2009; Ciolfi et al. 2009; Ciolfi et al. 2010; Duez & Mathis 2010; Ciolfi & Rezzolla 2013). Both analytical and theoretical methods for magnetized stellar equilibrium states have been developed and investigated by these works. Recently, some works have considered more realistic and complex physical conditions in neutron star and magnetar interiors. Yoshida et al. (2012) have considered stratification by chemical potentials in the neutron star interior and obtained stably stratified magnetized stars in general relativistic equilibrium. Lander et al. (2012) and Glampedakis et al. (2012) have calculated magnetized neutron star equilibria with stratification and type II superconductivity in Newtonian framework. Lander (2013) and Lander (2014) have solved the superconducting flux tube tension and obtained magnetic field configurations of neutron star with superconducting core and normal MHD crust self-consistently, but these studies have not calculated a magnetosphere around the star. Very recently, Glampedakis et al. (2014) have studied MHD magnetized star in equilibrium with force-free magnetosphere self-consistently. However, previous Hall equilibrium studies (Cumming et al. 2004; Glampedakis et al. 2014) have considered crustal magnetic fields only. They have not taken account of the influence of the core magnetic fields and magnetosphere on the crustal fields. On the other hand, Glampedakis et al. (2014) have not distinguished between its core and crust. Therefore, nobody have obtained magnetized equilibrium state throughout core-crust-magnetosphere which would be essential for magnetar understanding.

In this chapter, we have extended the recent Hall equilibrium study (Gourgouliatos et al. 2013) and magnetized star with magnetosphere study (Glampedakis et al. 2014) in order to take one more step towards magnetic field structures of magnetars. We have succeeded in obtaining the magnetic field structures across core, crust and magnetosphere simultaneously and systematically for the first time. We consider a magnetar with strong magnetic field whose magnitude exceeds $\sim 10^{15}$ G at the surface in this chapter. Since the Hall drift would be very effective within the crust of such magnetar (see Eq. 5.1), we assume that the crustal magnetic fields structure in Hall equilibrium. As for core magnetic fields, we assume that they are in MHD equilibrium for simplicity. As we have described, the formulation of Hall equilibrium state is very similar to MHD equilibrium state (Gourgouliatos et al. 2013), but their physical meaning is different from each other. The MHD equilibrium state depends on the mass density profiles, because it describes the matter force balance. On the other hand, the Hall equilibrium state in the crust is determined by electron density distribution within the crust only and neglects the force balance of the crust. Therefore, the crust in this chapter is elastic and stressed by Lorentz force of the crustal magnetic fields. We have considered magnetosphere as a twisted force-free one. As simple examples of the twisted magnetosphere, we have calculated the equatorial shearing and ring models (Parfrey et al. 2013). Since we are interested in the magnetosphere near the star, we have neglected the rotation of the magnetosphere (Glampedakis et al. 2014).

In summary, we have calculated MHD equilibrium core, Hall equilibrium crust and twisted force-free magnetosphere in this chapter.

We have obtained both analytical and numerical solutions using Green function relaxation method with arbitrary current sheets on boundaries developed in chapter 3. Since we are able to include the boundary conditions easily using the Green function, we have calculated many equilibrium states under various boundary conditions.

5.2 Formulation and models

5.2.1 Basic equations and integral form

We consider the MHD equilibrium core, the Hall equilibrium crust and twisted force-free magnetosphere simultaneously in this chapter. The ranges of each region are core $(0 \leq r \leq r_{in})$, crust $(r_{in} \leq r \leq r_s)$ and magnetosphere $(r \geq r_s)$ respectively. r_{in} and r_s denote a core-crust boundary radius and the stellar radius. The crust exists between r_{in} and r_s region in our models.

We assume the system is stationary and axisymmetry. In order to obtain the magnetized equilibria, we also need to solve the elliptic type equation as follow:

$$\Delta^* \Psi = -4\pi r \sin\theta \frac{j_\varphi}{c}. \tag{5.2}$$

The right hand side of this equation contains the toroidal current density as a source term. The toroidal current density is derived from the matter equation in each region.

The Hall equilibrium state within the crust is described by the Hall equilibrium equation (Gourgouliatos et al. 2013). The Hall evolution of the magnetic field is governed by the induction equation as,

$$\frac{\partial}{\partial t}\boldsymbol{B} = -c\nabla \times \boldsymbol{E}. \tag{5.3}$$

The electric field in the crust is expressed as (Goldreich & Reisenegger 1992),

$$\boldsymbol{E} = \frac{\boldsymbol{j}}{\sigma} + \frac{1}{en_e c}\Big(\boldsymbol{B} \times \boldsymbol{j}\Big) + \nabla\eta, \tag{5.4}$$

where $\nabla\eta$ denotes the gradient of the total chemical potential term in the crust. Therefore, the Hall MHD evolutionary equation is expressed by

$$\frac{\partial}{\partial t}\boldsymbol{B} = -\nabla \times \left(\frac{c^2}{4\pi\sigma}\nabla \times \boldsymbol{B}\right) + \nabla \times \Big[\frac{c}{4\pi e n_e}\boldsymbol{B} \times (\nabla \times \boldsymbol{B})\Big]. \tag{5.5}$$

The first term is the Ohmic diffusion and the second one is the Hall drift. If the Hall drift is much faster then the Ohmic diffusion and the magnetic field reaches nearly stationary, the left hand side and the firs term of the equation vanish. The evolutionary equation becomes the Hall

equilibrium condition as follow:

$$\nabla \times \left[\frac{c}{4\pi e n_e} \boldsymbol{B} \times (\nabla \times \boldsymbol{B}) \right] = 0. \tag{5.6}$$

Since c and e are physical constants, the equation implies the presence of a scalar function S as

$$\nabla S = \frac{1}{n_e} \left(\boldsymbol{B} \times \frac{\boldsymbol{j}}{c} \right). \tag{5.7}$$

From the axisymmetry condition results in

$$\frac{1}{n_e} \left(\boldsymbol{B} \times \frac{\boldsymbol{j}}{c} \right)_{\varphi} = 0. \tag{5.8}$$

These conditions are as same form as the stationary conditions in barotropic axisymmetric MHD except for n_e. The physical dimensions of these equations are different, but the physical meaning of them is almost same. The Hall drift term comes from the Lorentz force to the electron and these conditions mean the force balance condition in the axisymmetric system. Therefore, we obtain following condition from toroidal component in Eq. (5.8)

$$\nabla \Psi \times \nabla \kappa = 0 \Leftrightarrow \kappa \equiv \kappa(\Psi). \tag{5.9}$$

From meridional component in Eq. (5.7), the functional form of toroidal current density is obtained as:

$$4\pi \frac{j_\varphi}{c} = \frac{\kappa(\Psi)\kappa'(\Psi)}{r \sin\theta} + 4\pi n_e r \sin\theta S(\Psi), \tag{5.10}$$

As Gourgouliatos et al. (2013) pointed out, the toroidal current density in the Hall equilibrium system is similar to that of barotropic MHD equilibrium system. As we have seen, the toroidal current density is described as

$$4\pi \frac{j_\varphi}{c} = \frac{\kappa(\Psi)\kappa'(\Psi)}{r \sin\theta} + 4\pi \rho r \sin\theta \mu(\Psi), \tag{5.11}$$

The core toroidal current density is expressed by this equation.

The twisted magnetosphere without rotation satisfies the force-free condition as

$$\frac{\boldsymbol{j}}{c} \times \boldsymbol{B} = 0. \tag{5.12}$$

Using this condition, we derive the functional form of toroidal current density as

$$4\pi \frac{j_\varphi}{c} = \frac{\kappa(\Psi)\kappa'(\Psi)}{r \sin\theta}. \tag{5.13}$$

The magnetospheric toroidal current density is described by arbitrary function $\kappa(\Psi)$ only.

We calculate magnetized equilibrium states using these functional forms of j_φ throughout the star. In order to include the boundary conditions easily, we calculate the integrated form of

Eq. (5.2) using Green function,

$$\frac{\Psi(\boldsymbol{r})}{r\sin\theta}\sin\varphi = \frac{1}{c}\int_V \frac{j_\varphi(\boldsymbol{r'})}{|\boldsymbol{r}-\boldsymbol{r'}|}\sin\varphi' dV' + h.ts, \tag{5.14}$$

where $h.ts$ denotes a homogeneous term of Laplacian as below:

$$h.ts = \sum_{n=1}^{\infty}\Big(a_n r^n P_n^1(\cos\theta) + b_n r^{-n-1}P_n^1(\cos\theta)\Big)\sin\varphi. \tag{5.15}$$

Where $P_n^1(\cos\theta)$ is associated Legendre functions. The coefficients a_n and b_n are determined by the boundary conditions of Ψ. These homogeneous terms come from current sheets on the boundaries (see chapter 3).

The physical dimension of $\mu(\Psi)$ is different from $S(\Psi)$, because the dimensions of ρ and n_e differ (Gourgouliatos et al. 2013). Therefore, we consider that S and μ can take different values along one poloidal magnetic field line (Ψ =constant line). In other word, the functional forms of S and μ are different from each other in each region. On the other hand, the physical dimension of $\kappa(\Psi)$ in each region is same, because this conserved quantity is obtained from the axisymmetry condition only. We treat that the κ is the conserved quantity throughout stellar interior and exterior in this chapter.

5.2.2 Models of internal magnetic fields

We have made four internal magnetic field models according to the core-crust toroidal current density and boundary conditions. We must fix the functional forms of $\kappa(\Psi)$, $\mu(\Psi)$ and $S(\Psi)$ and the current sheet on the core-crust boundary in order to achieve these models. The magnetic field configuration of each model is displayed in Fig. 5.1. We describe each model:

1. Model I is a purely crustal open magnetic fields in Hall equilibrium. Both poloidal and toroidal magnetic fields satisfy the Hall equilibrium state. This model is equivalent to configurations in Gourgouliatos et al. (2013). This model requires the opposite current sheet on the core-crust boundary to prevent the poloidal magnetic fields entering the core (see App. A.3). The inner boundary conditions in this case are $\Psi = 0$ and $\kappa = 0$ on the core-crust boundary.

2. Model II is a purely *crustal current* model. The poloidal magnetic fields can penetrate the core region, but the toroidal magnetic field is confined within the crust region in this model. The current density exists within the crust only. This model does not have the opposite current sheet on the core-crust boundary. Therefore the core magnetic field is the inner vacuum solution of the crustal current. The inner boundary condition in this model is $\Psi \neq 0$ and $\kappa = 0$ on the core-crust boundary.

3. Model III is a core-crust current model. Both poloidal and toroidal magnetic fields can exist in the core and crust region. In other word, both poloidal and toroidal current density

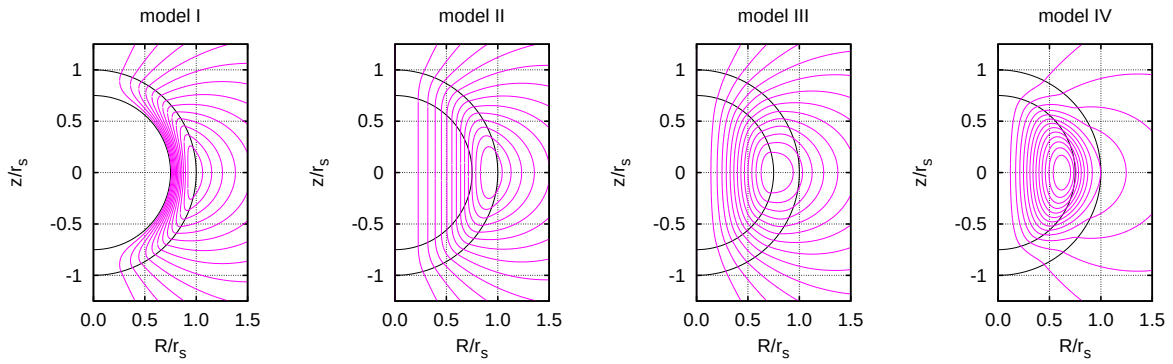

Figure 5.1: The contours of the Ψ of each analytical model (see App. A.3). The inner curve is core-crust boundary and the outer curve is the stellar surface. Model I: This model has purely crustal open magnetic fields. There is the negative current sheet on the core crust boundary in order to exclude the core magnetic fields. Model II: This model has purely crustal toroidal current. The core magnetic fields are an inner vacuum solution of the crustal toroidal current. Model III: This model has both crustal and core toroidal current. The core magnetic field configuration is different from Model II. Model IV: This model has oppositely flowing toroidal current density. The core magnetic fields are stronger than crustal magnetic fields.

can exist in the core and crust region. The toroidal current density in the core flows same direction to the crust current in this model. The inner boundary condition in this model is $\Psi \neq 0$ and $\kappa \neq 0$ on the core-crust boundary.

4. Model IV is a core-crust current model and the toroidal current density in the core flows opposite direction to the crustal current in this model. The core magnetic fields energy in this model is much larger than the crustal magnetic fields energy, because such oppositely flowing toroidal current density makes the core magnetic fields energy much larger (chapter 3). The inner boundary condition in this model is $\Psi \neq 0$ and $\kappa \neq 0$ on the core-crust boundary.

We have calculated analytical solutions of these models without toroidal magnetic fields (see App. A.3). Model III and IV can have arbitrary current sheets on the core-crust boundaries. Such current sheet means the arbitrary magnetic pressure on the bottom of the crust (Braithwaite & Spruit 2006). We treat only dipole current sheet in these models but we can calculate the arbitrary higher order current sheet (see details of the current sheet in chapter 3). We have calculated solutions III and IV with and without current sheets in order to examine the influence of the current sheet. Therefore, we have calculated a total of 6 type of solutions for internal magnetic field in Sec. 5.3.1.

We must fix the functional forms in order to achieve the core and magnetosphere conditions we have described in actual numerical calculations. There are two arbitrary functions in both Hall equilibrium (S, κ) and MHD equilibrium (μ, κ) regions. We choose ones of the simplest form as S (Gourgouliatos et al. 2013) and μ as

$$S(\Psi) = S_0, \tag{5.16}$$

$$\mu(\Psi) = \mu_0. \tag{5.17}$$

We can compute using more complex functional forms (see chapters 2 and 6 and Ciolfi & Rezzolla 2013), but we are interested in magnetic field configurations throughout the star and the influence of the boundary conditions in this chapter. As a first step, we use these forms simples functional form in order to examine them easily and clearly. Especially noted, S_0 and μ_0 must satisfy the conditions of $S_0\mu_0 > 0$ (model III) and $S_0\mu_0 < 0$ (model IV).

We need to choose the functional form of κ satisfying the boundary condition on the stellar surface and the core-crust surface. If we assume that the magnetosphere is not twisted ($B_\varphi = 0$, outside the star), the toroidal current density must vanish outside the star. We need to choose the functional form such as following one (Tomimura & Eriguchi 2005)

$$\kappa(\Psi) = \begin{cases} \kappa_0(\Psi - \Psi_{ex,\max})^{k+1} & (\Psi > \Psi_{ex,\max}) \\ 0 & (\Psi \leq \Psi_{ex,\max}) \end{cases}, \tag{5.18}$$

where, $\Psi_{ex,\max}$ is the maximum value of Ψ in the stellar exterior. We fix the parameter $k = 0.1$ in all of our numerical computations. This choice of the parameter is exactly same by Yoshida & Eriguchi (2006) (also Yoshida et al. 2006; Lander & Jones 2009; Ciolfi et al. 2009). As many previous works obtained and we have obtained in previous chapters, the choice of $k = 0.1$ results in the local strong internal toroidal magnetic fields.

The functional form of Eq. (5.18) is available in the model I, III and IV. When we calculate the model II, we change $\Psi_{ex,\max}$ into the maximum value of $\Psi_{ex,\max}$ and $\Psi_{c,\max}$, where $\Psi_{c,\max}$ is the maximum value of Ψ in the core. If we choose this kind of functional form, the current density vanishes outside the star and there are no toroidal magnetic fields. This functional form always satisfies the boundary condition $\kappa = 0$ at the stellar surface.

5.2.3 Models of twisted magnetosphere

We have calculated two types of twisted force-free magnetosphere, which are equatorial shearing model and ring model (see Parfrey et al. 2013). In order to obtain these models, we have chosen the functional forms below:

$$\kappa(\Psi) = \begin{cases} \kappa_0(\Psi - \Psi_{t,\max})^{k+1} & (\Psi > \Psi_{t,\max}) \\ 0 & (\Psi \leq \Psi_{t,\max}) \end{cases}, \tag{5.19}$$

for equatorial shearing models and

$$\kappa(\Psi) = \begin{cases} \kappa_0(\Psi - \Psi_{ex,\max})^{k+1} & (\Psi > \Psi_{t,\max}) \\ 0 & (\epsilon\Psi_{ex,\max} \leq \Psi \leq \Psi_{ex,\max}) \\ \kappa_1\{(\epsilon\Psi_{ex,\max} - \Psi)(\Psi - \Psi_{t,\max})\}^{k_2} & (\Psi_{t,\max} \leq \Psi \leq \epsilon\Psi_{ex,\max}) \\ 0 & (\Psi < \Psi_{t,\max}) \end{cases}, \tag{5.20}$$

for ring shearing model. Here, κ_1, ϵ and k_2 are parameters. $\Psi_{t,\max}$ denotes the maximum value of Ψ outside the twisted magnetosphere. We define the value of the maximum radius of the twisted field as r_M. The twisted field in magnetosphere is not allowed to exist beyond the r_M. The region of the twisted field in magnetosphere limited by the largest closed magnetic field line inside the radius r_M by this functional form. When the twisted field in magnetosphere is the ring model, the twisted field can exist within the limited region between the field lines $\Psi = \Psi_{t,\max}$ and $\Psi = \epsilon\Psi_{ex,\max}$ (see Eq. 5.20). The value of ϵ must take $0 < \epsilon < 1$ and this parameter determines the width of the twisted field. From the same reason why we select $k = 0.1$ in Eqs. (5.18) and (5.19), we fix $k_2 = 1.0$ and $\epsilon = 0.5$ in the ring model. We have also examined $k_2 > 1.0$ models, but we have not obtained as strong toroidal magnetic fields solutions as $k_2 = 1.0$. As a result, we have found that $k_2 = 1$ results in the local strong twisted magnetic fields within the ring regions.

5.2.4 Numerical Setting

We assume that the background star is spherical $N = 1$ polytrope, because the stellar deformation by the magnetic fields (Lorentz force) is very small even when the magnetic fields strength exceed 10^{15} G (see e.g. Haskell et al. 2008; Ciolfi & Rezzolla 2013). Therefore, the density profile is depend on r component only as follow:

$$\rho(r) = \frac{\sin(\pi r/r_s)}{\pi r/r_s}. \tag{5.21}$$

We set the number density profile is a parabolic type (Gourgouliatos et al. 2013) as

$$n_e(r) = (r_s^2 - r^2). \tag{5.22}$$

We also calculated magnetic field configurations with realistic equation of state (see App. B.4). We set the stellar radius at $r_s = 1$ and the core-crust boundary at $r_{in} = 0.75$ following Kojima & Kisaka (2012). The crust width of our model is thicker than that of typical value, but we have adopted the thicker crust in order to compute easily. Some of our numerical solutions have a current sheet on the core-crust boundary. We can calculate contributions from arbitrary current sheets (chapter 3), but we have calculated solutions with dipole current sheet only.

In order to evaluate the energy ratio, we calculate the poloidal magnetic energy $\mathcal{M}_p$ and the toroidal magnetic energy $\mathcal{M}_t$. We define the total magnetic energy as $\mathcal{M} = \mathcal{M}_p + \mathcal{M}_t$. We also calculate the core magnetic energy ($\mathcal{M}co$), the crust magnetic energy ($\mathcal{M}cr$) and the stellar magnetic energy ($\mathcal{M}st = \mathcal{M}co + \mathcal{M}cr$). Our numerical region is $[0, 1]$ (stellar region) and $[1, 2]$ (non-twisted magnetosphere models), $[1, 32]$ (twisted magnetosphere models) and $\theta = [0, \pi]$. We use the sufficient number of mesh in this chapter (see the numerical check in App. B.3). In actual numerical calculations which are tabulated and displayed in this chapter, we use $N_\theta = 1025$ ($\theta = [0 : \pi]$), $N_{r1} = 513$, $N_{r2} = 513$ ($r = [1 : 2]$ no magnetosphere models) $N_{r2} = 1025$, ($r = [1 : 32]$ magnetosphere models) in order to obtain more accuracy numerical

	κ_0	S_0	μ_0	model	$\mathcal{M}cr_t/\mathcal{M}cr$	$\mathcal{M}co_t/\mathcal{M}co$	$\mathcal{M}cr/\mathcal{M}$	$\mathcal{M}co/\mathcal{M}$	
(a)	150	1.0	0.0	I	5.77E-3	0.0	0.89	0.00	
(b)	50	1.0	0.0	II	8.23E-2	0.0	0.34	0.44	
(c)	25	1.0	1.0	III	1.54E-1	0.0	0.28	0.55	$j_s = 1.0$E0
(d)	20	1.0	5.0	III	1.78E-1	3.52E-5	0.24	0.62	
(e)	8	-1.0	1.0	IV	1.36E-1	2.29E-1	0.14	0.84	
(f)	8	-1.0	1.0	IV	1.41E-1	3.27E-1	0.07	0.92	$j_s = -5.0$E-1

Table 5.1: Parameters and numerical solutions of models with core magnetic fields. j_s denotes the strength of the current sheet on the core-crust boundary.

results. As for the Legendre polynomial, we sum of $P_n^1(\cos\theta)$ to $n_{\max} = 21$ in all numerical calculations in chapter 5.

5.3 Results

5.3.1 Core-crust solutions with non-twisted magnetosphere

First, we show the solutions with non-twisted magnetosphere ($B_\varphi = 0$, outside the star). Since the toroidal magnetic field energy ratio (within the crust, $\mathcal{M}cr_t/\mathcal{M}cr$) relates to the Hall drift activity within the crust (Kojima & Kisaka 2012; Viganò et al. 2013; Gourgouliatos & Cumming 2014), it is very interesting value to characterize the magnetized equilibrium states. We have computed many equilibrium states changing the value of κ_0 for 6 type of solutions as we have mentioned in Sec. 5.2.2. Each model displayed here has as strong toroidal magnetic field energy ratio ($\mathcal{M}cr_t/\mathcal{M}cr$) as possible within present functional forms. We label the obtained 6 solutions as following (a) - (f): solution (a) model I type, solution (b) model II type, solution (c) model III type with positive current sheet, solution (d) model III type, solution (e) model IV type, solution (f) model IV type with negative current sheet. The numerical solutions are tabulated in Table 5.1. The configurations of the poloidal magnetic fields and the toroidal magnetic fields are displayed in Fig. 5.2. The magnitude of the toroidal magnetic fields in Fig. 5.2 is normalized by that of the magnetic dipole component of each solution at the stellar north pole. As seen from Table 5.1, the core magnetic field energy ratio ($\mathcal{M}co/\mathcal{M}$) increases from the solution (a) to the solution (f) in order in Table 5.1. The value reaches $\mathcal{M}co/\mathcal{M} \sim 0.92$ in solution (f), while $\mathcal{M}co/\mathcal{M} \sim 0.44$ in solution (b). Since solutions (c) and (d) have current sheets on the core-crust boundary, the poloidal magnetic field lines are bent at this boundary. The direction of the bending depends on the sign of the current sheet.

First of all, the toroidal magnetic field energy ratios within the crust ($\mathcal{M}cr_t/\mathcal{M}cr$) of all models are smaller than 0.5. Therefore, the magnetic energies are dominated by poloidal one in all solutions, but the energy ratio changes according to the models. The size of the toroidal magnetic field region becomes larger as the core magnetic field ratio ($\mathcal{M}cr/\mathcal{M}$) increases (Fig. 5.2). Clearly, the core magnetic fields have influence on the Hall equilibrium states within the crust.

As seen from Table 5.1 and Fig. 5.2, the toroidal magnetic field region of solution (a) is very small and the energy ratio is also very small ($\mathcal{M}cr_t/\mathcal{M}cr \sim 10^{-2}$). This result is

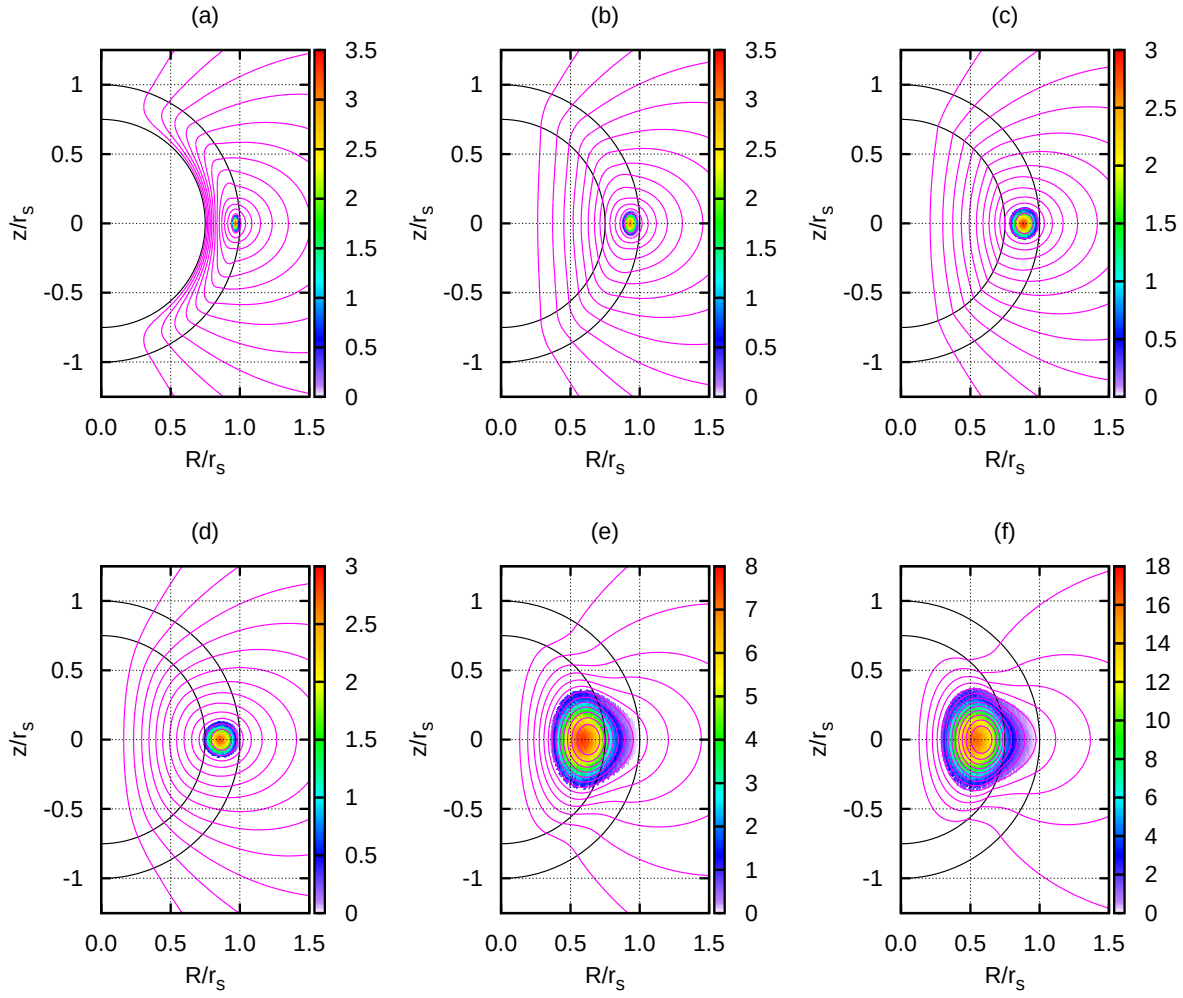

Figure 5.2: The contours of Ψ in each model (solid line). The inner curve and the outer curve denote the core-crust boundary and the stellar surface respectively. The colour maps denote the the magnitude of the toroidal magnetic field B_φ normalized by that of strength of the dipole component of the poloidal magnetic field at the north pole.

almost consistent with computations by Gourgouliatos et al. (2013) (see Fig. 9 in the paper). On the other hand, the energy ratio $\mathcal{M}cr_t/\mathcal{M}cr$ of solution (b) is slightly larger than that of solution (a). The toroidal magnetic field region also becomes slightly larger. Since the poloidal magnetic field lines penetrate into the core region in this model, the $\Psi \geq \Psi_{\rm max}$ region within the crust becomes large (compare the analytical profiles of model I with model II in Fig. A.1). As seen from Table 5.1, the core and the crustal magnetic energies of solution (b) are nearly equal ($\mathcal{M}cr \sim \mathcal{M}co$). Therefore, solution (b) has the crustal magnetic field comparable to the core magnetic field.

Solutions (c) and (d) are model III type solutions. They have core toroidal current density. Solution (c) has the positive current sheet on the core-crust boundary. The positive current sheet makes the core magnetic field energy slightly small (see Table 5.1). The core magnetic field energy ratios ($\mathcal{M}cr/\mathcal{M}$) of solutions (c) and (d) are larger than that of solution (b). The energy ratios ($\mathcal{M}cr_t/\mathcal{M}cr$) of solutions (c) and (d) reach about 0.15-0.17 and are much larger those that of solutions (a) and (b). On the other hand, the core toroidal magnetic fields are almost zero in solutions (c) and (d). As seen from solutions (c) and (d) in Fig. 5.2, almost all of the toroidal magnetic fields exist in the crusts. These numerical results show that the core magnetic field structures are important in order to consider the toroidal magnetic field energy in Hall equilibrium within the crust.

Solutions (e) and (f) are model IV type solutions. They have the opposite toroidal currents because the value of $\mu_0 S_0$ is always negative. As seen form Table 5.1, such oppositely flowing crustal toroidal current makes the core magnetic field energy ratio $(\mathcal{M}cr/\mathcal{M})$ large. These tendencies are consistent with the arguments in chapter 3. The ratio $\mathcal{M}cr/\mathcal{M}$ reaches about 0.8-0.9. These values are the strongest among our solutions. These solutions also sustain the large toroidal magnetic field energy in both core and crust region. The core toroidal magnetic field energy ratios are $\mathcal{M}co_t/\mathcal{M}co \sim 0.2 - 0.3$. The size of the toroidal magnetic field region is much larger than those of any other solutions. The boundary conditions of κ at the core-crust boundary are $\kappa \neq 0$ and the values of κ continue smoothly at the boundary. These numerical results means that the $\kappa \neq 0$ boundary conditions on the core-crust boundary broaden the size of the toroidal magnetic field regions within the crust of the Hall equilibrium.

The solutions (c) and (f) have the positive and negative current sheets respectively. The physical meaning and origin of the current sheet are unclear and difficult to understand in terms of micro physics (Lander 2013, 2014), but we can regard the current sheet under the magnetic fields as magnetic stress on the bottom of the crust (Braithwaite & Spruit 2006). The sign of the current sheet means the direction of the stress in the case. The positive and negative current sheets denote the magnetic stresses in the direction of the equator and polars respectively. As seen from Table 5.1, the positive current sheet decreases the core magnetic fields energy ratio $\mathcal{M}cr/\mathcal{M}$ (see solutions c and d), while the negative current sheet increases the ratio (see solutions e and f). Moreover, solution (c) has smaller value of $\mathcal{M}cr_t/\mathcal{M}$ than solution (d). Solution (f) also has larger values of $\mathcal{M}cr_t/\mathcal{M}$ and $\mathcal{M}cr_t/\mathcal{M}$ than solution (e). Especially noted, the maximum magnitude of the core toroidal magnetic fields in solution (f)

	r_M/r_s	κ_0	S_0	μ_0	model	$\mathcal{M}cr_t/\mathcal{M}cr$	$\mathcal{M}cr_t/\mathcal{M}cr$	$\mathcal{M}cr/\mathcal{M}$	$\mathcal{M}cr/\mathcal{M}$	$\mathcal{M}st/\mathcal{M}$	r_X/r_s
(m-a)	8.0	0.1	1.0	0.0	I	2.21E-4	0.0	0.90	0.0	0.90	-
(m-b)	8.0	1.0	1.0	0.0	I	1.58E-2	0.0	0.88	0.0	0.88	-
(m-c)	8.0	1.4	1.0	0.0	I	1.63E-2	0.0	0.87	0.0	0.87	3.34
(m-d)	8.0	0.1	1.0	1.0	III	8.34E-4	3.08E-4	0.16	0.68	0.84	-
(m-e)	8.0	1.0	1.0	1.0	III	4.11E-2	7.29E-2	0.16	0.64	0.80	-
(m-f)	8.0	1.2	1.0	1.0	III	3.92E-2	1.02E-2	0.16	0.63	0.79	3.20
(m-g)	8.0	0.1	-1.0	5.0	IV	6.13E-4	4.19E-4	0.12	0.83	0.95	-
(m-h)	8.0	0.5	-1.0	5.0	IV	1.40E-2	9.33E-3	0.12	0.82	0.94	-
(m-i)	8.0	1.1	-1.0	5.0	IV	3.35E-2	2.28E-2	0.11	0.80	0.91	3.40

Table 5.2: Parameters and solutions with equatorial shearing models. Model I magnetic solutions (m-a, m-b, m-c), model III magnetic solutions (m-d, m-e, m-f) and model IV magnetic solutions (m-g, m-h, m-i) are tabulated.

reaches about 18 times as large as the its dipole magnetic component at the north pole. This means that the current sheet (magnetic stress) at the bottom of the crust can sustain the strong core toroidal magnetic fields (see also 3.6.4 in chapter 3). These results show that the core-crust stress affect both crustal and core toroidal magnetic fields strength.

As we have seen, the magnitude of the toroidal magnetic field energy ratio within the crust is significantly affected by the boundary conditions and the core magnetic field configurations. This means that the Hall MHD evolution is also dependent on the core magnetic field condition strongly as recent numerical simulation by Viganò et al. (2013). We discuss the boundary condition influence on the Hall MHD evolution in Sec. 5.4.1.

5.3.2 Solutions with equatorial shearing model

We have calculated solutions with equatorial shearing using functional form $\kappa(\Psi)$ in Eq. (5.19). At first, we have obtained nine solutions changing the value of κ_0 and using three types of internal magnetic field models (I, III, IV). In increasing order of the value of κ_0, they are solutions (m-a), (m-b), (m-c) (with model I internal field), solutions (m-d), (m-e), (m-f) (with model III internal field) and solutions (m-g), (m-h), (m-i) (with model IV internal field). The numerical results are tabulated in Table 5.2 and displayed in Fig. 5.3. Three contours of Ψ (m-d, m-e and m-f) are displayed in Fig. 5.3. We also display the profiles Ψ normalized by its surface values on the equatorial plane in Fig. 5.3. The equatorial shearing becomes strong as the value of κ_0 increases, because the value of κ_0 represents the twisted strength (toroidal component) of the magnetic fields.

As seen from Fig. 5.3, the exterior poloidal magnetic field configuration changes as the shearing (the value of κ_0) increases. The poloidal magnetic field lines near the equatorial plane are stretched outward by equatorial shearing current (compare m-d with m-e in Fig. 5.3). Since the energy ratio $\mathcal{M}st/\mathcal{M}$ decreases as the value of κ_0 increases from Table 5.2, the magnetic field energy increases in the stellar exterior. We have found an interesting magnetic field structure near $r/r_s \sim 3.2$ in the left bottom panel in Fig. 5.3 (solution m-f). As seen from the bottom right panel in Fig. 5.3, solutions (m-d) and (m-e) decreases monotonically outside the star ($r \geq r_s$), but solution (m-f) has the local minimum value near $r/r_s \sim 3.2$ where r derivative of Ψ becomes 0. Since the sign of r derivative of Ψ represents the direction of B_θ,

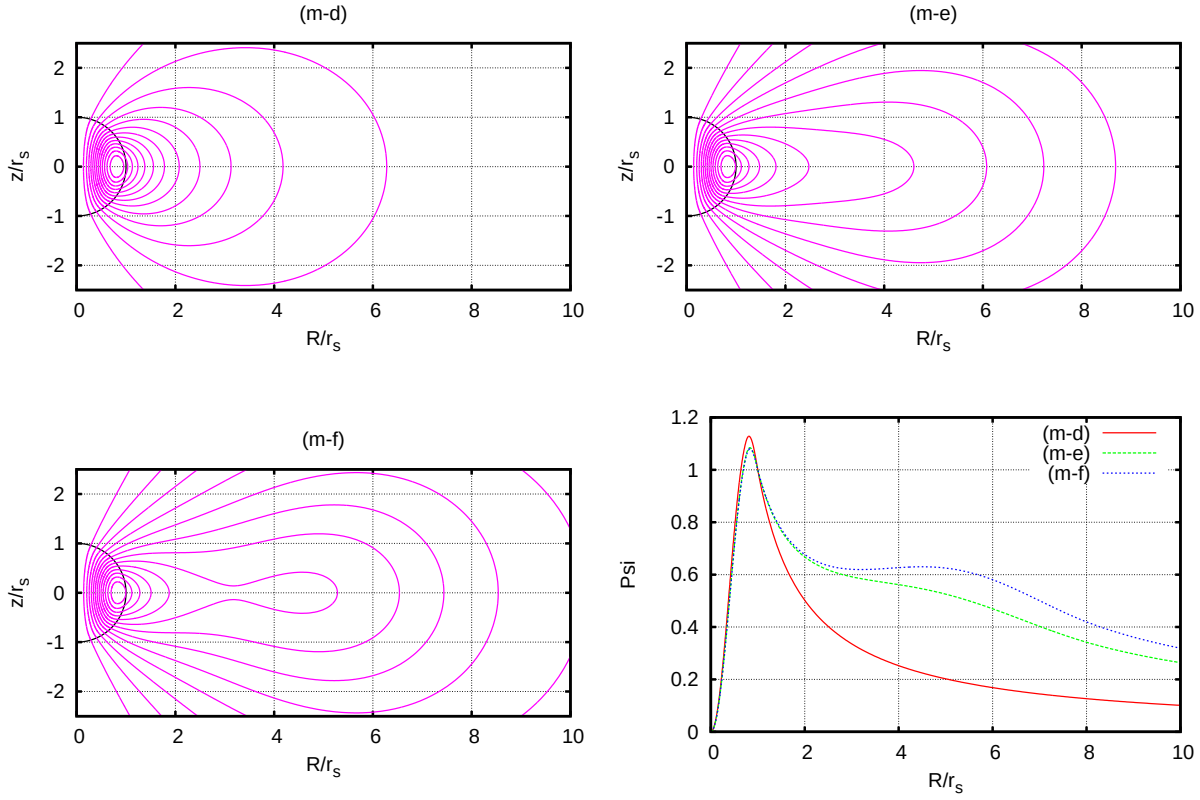

Figure 5.3: Top panels and bottom left panel: The contour of Ψ of solutions (m-d), (m-e) and (m-f). The inner curve denotes the stellar surface. As the value of κ_0 increases, the X-point geometry appears near $r/r_s \sim 3.2$. Bottom right panel: The profiles of Ψ on the equatorial plane normalized by each surface value. Each line denotes (m-d) (solid line), (m-e) (dashed line) and (m-f) (dotted line). The outside of the star ($r/r_s \geq 1$), (m-d) and (m-e) decreases monotonically, but (m-f) has the local minimum value at r/r_s because of X-point geometry.

	r_M/r_s	κ_0	S_0	μ_0	model	$\mathcal{M}cr_t/\mathcal{M}cr$	$\mathcal{M}cr_t/\mathcal{M}cr$	$\mathcal{M}cr/\mathcal{M}$	$\mathcal{M}cr/\mathcal{M}$	$\mathcal{M}st/\mathcal{M}$	r_X/r_s
(s-a)	8.0	1.0	-1.0	5.0	IV	5.45E-2	2.15E-2	0.11	0.80	0.91	-
(s-b)	8.0	1.0	-1.0	5.0	IV	6.00E-2	1.88E-2	0.15	0.73	0.88	-
(s-c)	8.0	1.0	-1.0	5.0	IV	6.46E-2	1.54E-2	0.17	0.68	0.85	3.34
(s-d)	8.0	1.0	-1.0	5.0	IV	6.70E-2	1.37E-2	0.18	0.66	0.84	3.17
(e-a)	4.0	3	1.0	0.0	I	2.84E-3	0.0	0.84	0.0	0.84	1.53
(e-b)	8.0	1.45	1.0	0.0	I	3.91E-3	0.0	0.87	0.0	0.87	3.17
(e-c)	15.0	0.8	1.0	0.0	I	2.63E-3	0.0	0.89	0.0	0.89	6.10

Table 5.3: Parameters and solutions with equatorial models. The solutions with current sheet (s-a, s-b, s-c, s-d) and without current sheet changing the value of r_M (e-a, e-b, e-c) are tabulated. The magnitude of the current sheet is j_s =0.0E0 (s-a), $j_s = 1.0$E0 (s-b), $j_s = 3.0$E0 (s-c) and $j_s = 5.0$E0 (s-d).

the direction of the poloidal magnetic fields reverses at the point. Therefore, poloidal magnetic field lines cross and an X-point geometry forms at the point. We define r_X as the distance to the point. We have also found the X-point geometries in solutions (m-c) and (m-i), but we have not obtained them when the parameter $k > 0.1$ in Eq. (5.19). This X-point geometry of the poloidal magnetic field have not seen in the previous equilibrium studies (Glampedakis et al. 2014; Viganò et al. 2011) and the equilibrium models by numerical simulation study (Parfrey et al. 2013). The X-point geometry would be unstable because it would cause the magnetic reconnection as Parfrey et al. (2013) have calculated. Our numerical result shows that the X-point geometry appears as the strength of the equatorial shearing (magnetospheric toroidal current density) exceed a certain value.

Next, we have calculated the structures with X-point in the magnetosphere when a solution has current sheet on the core-crust boundary. This X-point geometry is formed by the strong magnetospheric twisted field (magnetospheric toroidal current density) comparing to the stellar magnetic fields (stellar toroidal current density) (see the values of $\mathcal{M}st/\mathcal{M}$ in Table 5.2). Therefore, the stronger magnetospheric twisted field (Fig. 5.3) or weaker stellar magnetic fields are required to form the X-point geometry in the magnetosphere. In order to weaken the stellar magnetic fields by the current sheet on the core-crust boundary, we have studied the influence of the current sheet and obtained four solutions. They are solutions (s-a), (s-b), (s-c) and (s-d) (with model IV core magnetic fields). We have calculated them using same parameter sets except the strength of the current sheet on the core-crust boundary. We add the positive current sheet to change the stellar toroidal current density. The numerical results are tabulated in the upper column of Table 5.3 and displayed in Fig. 5.4. Fig. 5.4 shows the Ψ profiles on the equatorial surface normalized by each surface value.

As seen from the Table 5.3, the presence of the current sheet decreases the stellar magnetic field energy ratio (see $\mathcal{M}st/\mathcal{M}$). Fig. 5.4 shows that the maximum values of Ψ in the stellar interior ($0 \leq r/r_s \leq 1$) also become small by the current sheet. In the exterior of the star ($r/r_s \geq 1$), the profiles of solutions (s-a) and (s-b) shows the monotonic decrease of Ψ, but the profile of solution (s-d) has the local maximum value near $r/r_s \sim 3.17$ where the r derivative of the Ψ becomes 0. Therefore, the stellar toroidal current density is decreased by the presence of the positive current sheet on the core-crust boundary. As a result, the X-point geometry is formed within the twisted region in the solutions (s-c) and (s-d) (see the bottom left panel in

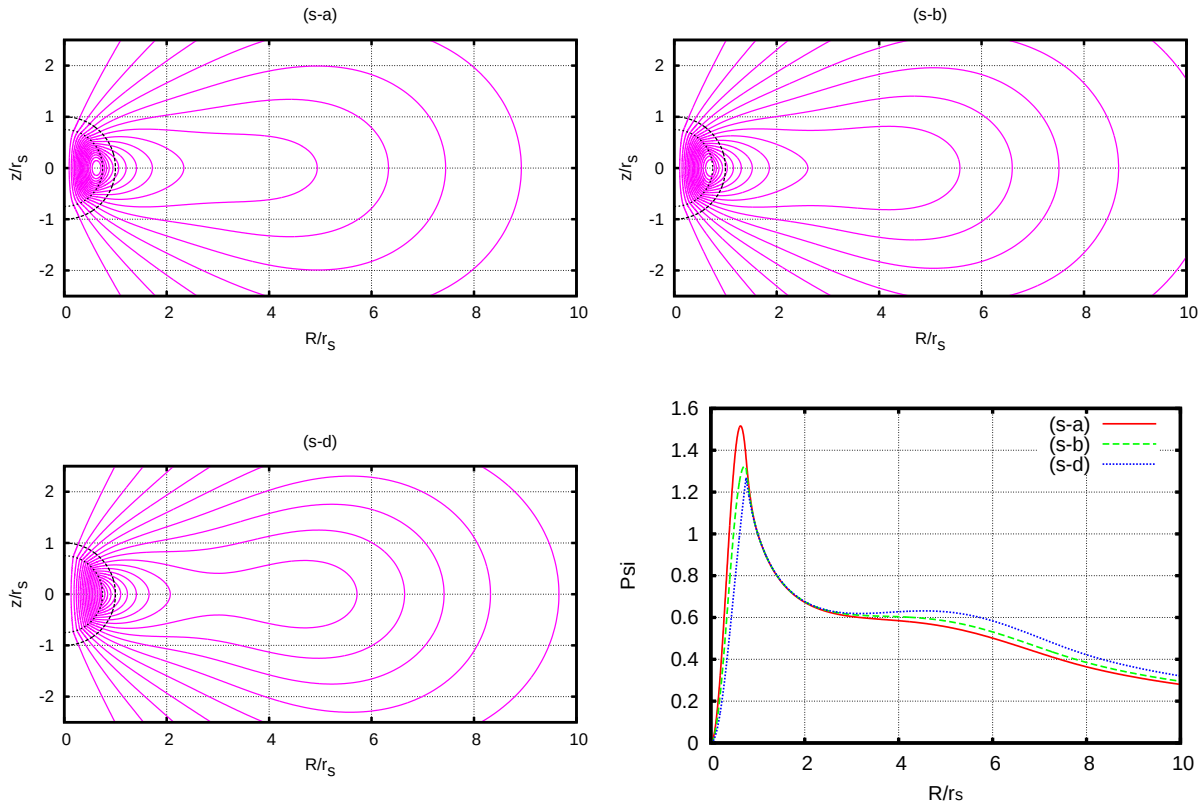

Figure 5.4: Top panels and bottom left: The contour of Ψ of the equatorial models with current sheet (solutions s-a and s-d). (s-a) do not have the X-point geometry while (s-d) has X geometry point at $r/r_s \sim 3.17$. Bottom right panel: The profiles of Ψ on the equatorial plane normalized by each surface value. Each line denotes (s-a) (solid line), (s-b) (dashed line) and (s-d) (dotted line). The outside of the star ($r/r_s \geq 1$), (s-a) and (s-b) decrease monotonically, but (s-d) has the local maximum value at $r/r_s \sim 3.17$.

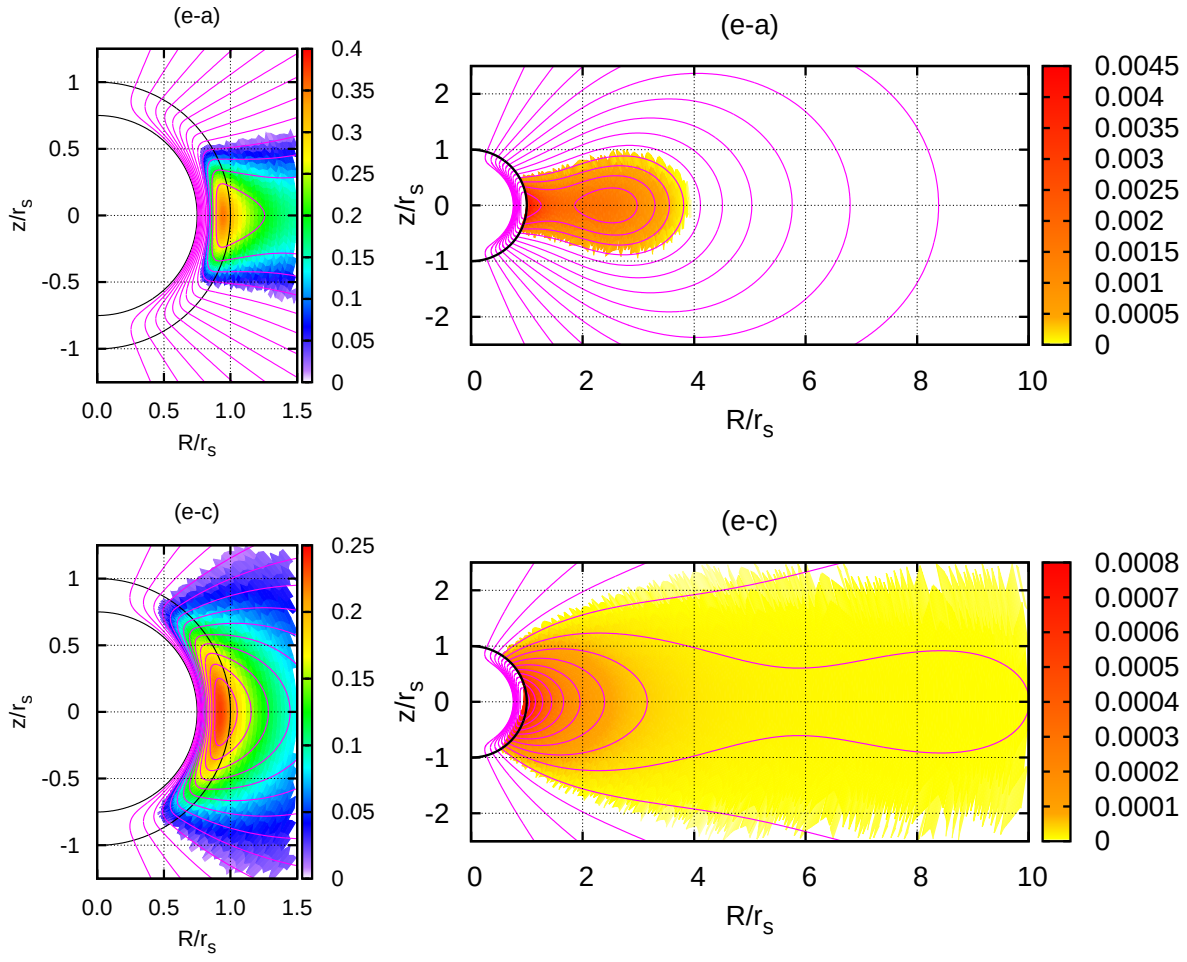

Figure 5.5: Left panels :The counter of Ψ (solid line) and the distribution of B_φ (color map) normalized by the magnetic dipole component strength at the north pole. Right panels: The counter of Ψ (solid line) and the distributions of j_φ/c (color map) of the equatorial models. The toroidal magnetic field region within the crust becomes large as the size of the magnetosphere increases. Right panels :The contour of Ψ (solid line) and the distribution of j_φ/c (color map). Both (e-a) and (e-c) have X-points geometry field near $r/r_s \sim 1.53$ (e-a), $r/r_s \sim 6.10$ (e-c).

	r_M/r_s	κ_0	κ_1	ϵ	S_0	μ_0	$\mathcal{M}cr._t/\mathcal{M}cr$	$\mathcal{M}cr._t/\mathcal{M}cr.$	$\mathcal{M}cr/\mathcal{M}$	$\mathcal{M}cr/\mathcal{M}$	$\mathcal{M}st/\mathcal{M}$	r_X/r_s
(r-a)	0.0	5.0	0.0	0.0	-1.0	5.0	4.38E-2	4.81E-2	0.12	0.81	0.93	-
(r-b)	4.0	5.0	24.0	0.5	-1.0	5.0	4.40E-2	4.79E-2	0.12	0.81	0.93	-
(r-c)	8.0	5.0	8.0	0.5	-1.0	5.0	4.37E-2	4.77E-2	0.12	0.81	0.93	-
(r-d)	15.0	5.0	4.0	0.5	-1.0	5.0	4.37E-2	4.79E-2	0.12	0.81	0.93	-
(r-e)	30.0	5.0	2.2	0.5	-1.0	5.0	4.37E-2	4.80E-2	0.12	0.81	0.93	12.6

Table 5.4: Parameters and solutions with type IV core magnetic field and ring sharing (r-a, r-b, r-c, r-d, r-e).

Fig. 5.4). These numerical results imply that the core-crust boundary condition can change the magnetospheric configurations and make the X-point geometry within the twisted region. We have discussions of X-point geometry in Sec. 5.4.2.

Finally, we see the interior magnetic field configurations changing the value of r_M. We have calculated three solutions (e-a) ($r_M = 4.0$), (e-b) ($r_M = 8.0$) and (e-c) ($r_M = 15.0$) with model I internal magnetic fields. The numerical solutions are tabulated lower column in Table 5.3 and displayed in Fig. 5.5. The right panels in Fig. 5.5 shows the Ψ contours (poloidal magnetic field) and B_φ colour map normalized surface dipole magnetic field strength. The left panel in Fig. 5.5 shows the exterior poloidal magnetic field configurations and magnetospheric toroidal current density (colour maps). As seen from the right panels in Fig. 5.5, the size of the toroidal magnetic field region within the crust becomes much larger than those without magnetosphere (compare with Fig. 5.2). As the size of the twisted field becomes larger (from e-a to e-c in order), the size of the toroidal magnetic field region within the crust becomes also larger dramatically. As seen from the Table 5.3, however, the internal toroidal magnetic fields energy ratio $\mathcal{M}cr_t/\mathcal{M}cr$ does not change very much even if the star has large twisted magnetosphere in (e-c). Since the boundary condition of κ is $\kappa \neq 0$ in the region ($\Psi > \Psi_{t,\max}$), the nonzero boundary condition of κ broadens the size of the toroidal magnetic fields region within crust significantly.

All these solutions have X-point geometries. The energy ration $\mathcal{M}st/\mathcal{M}$ increases from 0.84 (e-a) to 0.89 (e-c) as the size of the twisted field becomes large, in other words, the magnetospheric magnetic energy decreases. This result implies that the we need stronger magnetospheric toroidal current (twist) to make X-point geometry near the stellar surface (e-a) than those of (e-b) and (e-c). We see this tendency in following subsection.

5.3.3 Solutions with ring shearing model

Finally, we have calculated magnetized equilibrium states of model IV internal magnetic fields with ring shearing (Parfrey et al. 2013). The numerical results are tabulated in Table 5.4 and shown in Fig. 5.6. The twisted region is limited between the field lines $\Psi = \Psi_{t,\max}$ and $\Psi = \epsilon\Psi_{ex,\max}$ (see Eq. 5.20). The magnetospheric toroidal current density of ring model has both positive and negative values (see bottom panels in Fig. 5.6) in the magnetosphere. This distribution is similar to the solutions by Parfrey et al. (2013) (see the figure 4 in the paper).

The energy ratio $\mathcal{M}cr_t/\mathcal{M}cr$ of solutions (r-b, r-c, r-d, r-e) do not change well comparing to the vacuum solution (r-a) (see Table 5.4). As we have seen the bottom panels in Fig. 5.6, the

effective total amount of the magnetospheric toroidal current density (the value of $\int_V \frac{j_\varphi}{|\boldsymbol{r}-\boldsymbol{r}'|}dV$ within the ring magnetosphere) is much smaller than that of the equatorial model, because the magnetospheric toroidal current is limited within the narrow regions and takes both positive and negative values. The ring magnetospheric current density does not have influence on the internal magnetic field configurations very well.

The solutions (r-b, r-c, r-d) do not have X-point geometries, because the magnetospheric toroidal current density within the ring shearing model is much smaller than that of equatorial shearing model. In order to form the X-point geometry, we need larger size of twisted region in magnetosphere because the weak magnetospheric toroidal current cannot make it near the surface as we have seen previous subsection. The X-point geometry appears only when the size of the ring twist is sufficient large such as solution (r-e) ($r_M/r_s = 30$). These numerical result show that the X-point geometry in the ring shearing model cannot appear near the stellar surface such as the equatorial shearing models. The X-point geometry in the ring shearing model tends to appear the outer region of the equatorial shearing X-point geometry. The minimum value of r_X/r_s in the ring shearing model is much larger than equatorial shearing model in these calculations. This result means that the minimum value of r_X/r_s changes according to the shearing model and the size of the twisted field in the magnetosphere.

5.4 Discussion and concluding remarks

5.4.1 The influence on the Hall MHD evolution

The boundary conditions of the crust play very important roles for the Hall MHD secular evolutions. Very recently, Viganò et al. (2013) performed Hall MHD simulations under three types of core magnetic fields models (see Fig. 2 in Viganò et al. 2013). They showed that the evolutionary path is affected by the core magnetic field. We discuss the influence of the core magnetic fields on the crustal magnetic fields in Hall equilibrium using our equilibrium solutions.

We have calculated six solutions and found the Hall equilibrium states within crust are affected by boundary conditions significantly. As we have seen in Sec. 5.3.1, the core magnetic field configurations would change the crustal toroidal magnetic fields strength in Hall equilibrium. The strong core magnetic fields would make the magnitude of the crustal toroidal magnetic field strong (solutions c, d, e, f) in Hall equilibrium. On the other hand, the core toroidal magnetic fields and the twisted magnetosphere around the star broaden the crustal toroidal magnetic field regions in Hall equilibrium. These influences of the boundary conditions affect the Hall cascade during the secular magnetic field evolution.

As we have described in Sec. 5.1, the initial strong toroidal magnetic fields strengthen the Hall drift activity (Kojima & Kisaka 2012; Gourgouliatos & Cumming 2014). If the crustal magnetic fields are large ($\geq 10^{15}$G) enough to drive the Hall cascade very effectively, the timescale of the Hall drift is much faster than Ohmic timescale (see Eq. 5.1). In the case, the Hall drift would stop when the initial toroidal magnetic fields have been changed into poloidal

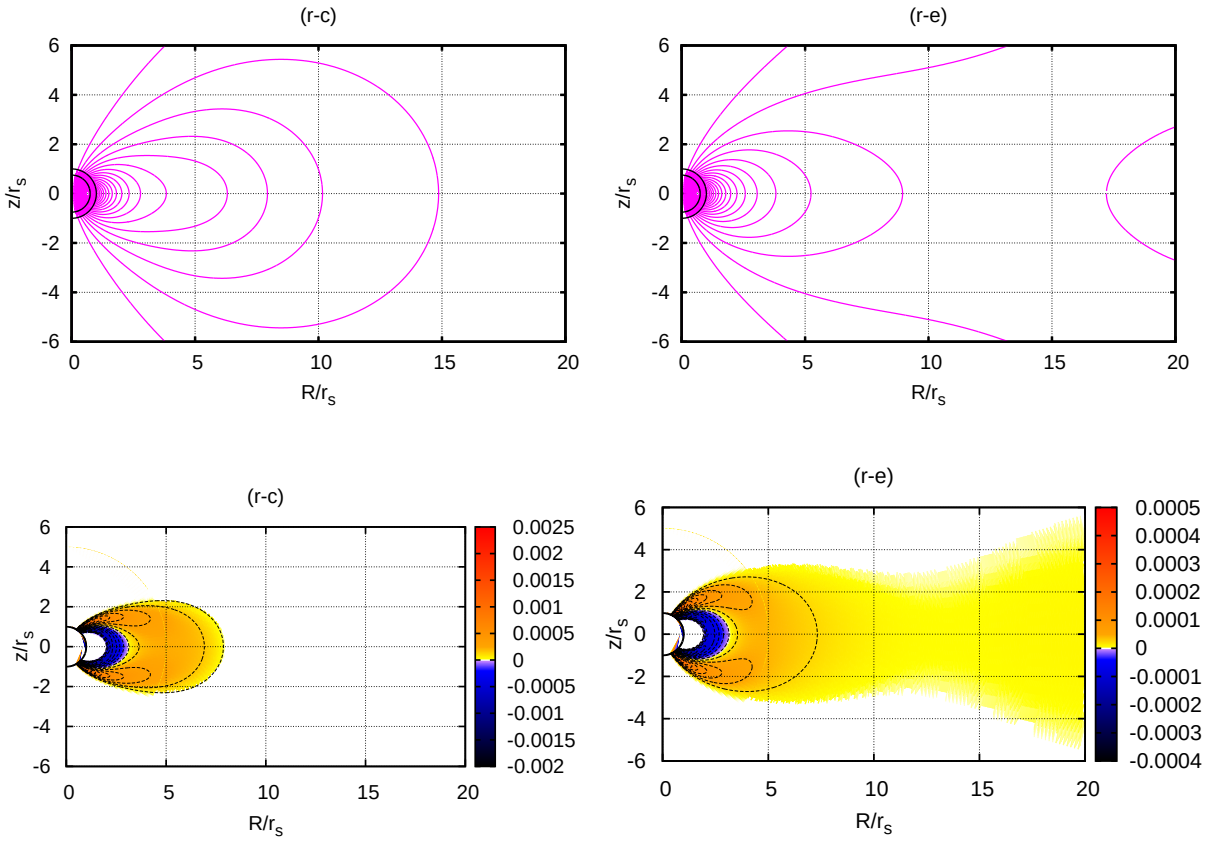

Figure 5.6: Top panels :The counter of Ψ. The X-point geometry appears near $r/r_s \sim 12.6$ in the (r-e) solution (right panel). Bottom panels : The color maps and the contours of j_φ/c in the magnetosphere. The inner circles in all panels are the stellar surfaces. The ring magnetosphere have both positive and negative magnetospheric toroidal current density regions.

component by the Hall cascade and have reached Hall equilibrium configurations. Therefore the energy ratio $\mathcal{M}cr_t/\mathcal{M}cr$ of the Hall equilibria would represents the efficiency of the Hall cascade, if the magnetar has strong initial toroidal component magnetic fields at the beginning of the Hall MHD secular evolution.

The initial magnetic field configurations in the magnetar interior are sill unclear, but they would have strong toroidal magnetic fields by the rapid differential rotation (Duncan & Thompson 1992; Spruit 2009). The magnetar would become stable MHD equilibrium state during the proto-magnetar because the Alfvén timescale ($= \sqrt{4\pi\rho}r_s/B \sim 0.1$s for typical magnetar with magnetic fields of order of $B = 10^{15}$G) is much faster than the dynamical and crust forming timescale. The MHD equilibria with strong toroidal magnetic fields would be stable because it satisfies Braithwaite's stability criterion (Braithwaite 2009; Duez et al. 2010):

$$a\frac{\mathcal{M}}{|W|} < \frac{\mathcal{M}_p}{\mathcal{M}} \leq 0.8,$$

Thus, the left-hand side of this inequality could be less than about 10^{-2}. Therefore, this criterion means the configurations with the twisted torus magnetic fields are stable even if the toroidal magnetic fields are much stronger than the poloidal magnetic fields. As a result, it is natural that the magnetar has strong initial toroidal magnetic fields in their interiors.

Here we assume that the magnetar has very large strong initial toroidal magnetic fields and the toroidal magnetic fields are changed into the poloidal components by the Hall cascade until the system reaches the Hall equilibrium state. This situation is different from initial models in Viganò et al. (2013) except for A14T, because they do not have initial toroidal magnetic fields. If the value of $\mathcal{M}cr_t/\mathcal{M}cr$ in Hall equilibrium is very small ($\sim 0.1\%$), the Hall drift would be effective because the almost of all initial toroidal magnetic components are changed into the poloidal magnetic components by the Hall drift. On the other hand, if the value of $\mathcal{M}cr_t/\mathcal{M}cr$ in Hall equilibrium is not small ($\sim 10\%$), the Hall drift would not be less effective. Therefore, we can evaluate the efficiency of the Hall drift using the toroidal magnetic field energy ratio of each solutions.

The Hall drift of the model I such as the solution (a) would be very active because the almost of all toroidal magnetic field component would be changed into the poloidal magnetic fields component. This is consistent with the calculations by Kojima & Kisaka (2012) (see the left panel of Fig. 5 in Kojima & Kisaka 2012). By contrast this, the values of energy ratio $\mathcal{M}cr_t/\mathcal{M}cr$ of (c) and (d) are much larger than that of (a). These numerical results mean that the Hall cascade in these configurations would be more passive than the configuration such as solution (a). Therefore, the presence of the core magnetic fields could tend to weaken the Hall drift within the crust region.

The crustal magnetic field in Hall equilibrium with magnetosphere also have very large size of the toroidal magnetic field region. Since the size of the toroidal magnetic field region of the equatorial twisted model is much larger than that of non-twisted model, the Hall cascade with magnetosphere would decrease. We see same tendency in 2.1.2 of Pons & Geppert (2007).

They calculated force-free boundary models and argued that the Hall drift within the crust is reduced by magnetosphere.

5.4.2 Magnetic X-point geometry and flare

We have calculated core-crust magnetic field configurations with twisted force-free magnetosphere. We have found the interesting poloidal magnetic field configurations in the magnetosphere. When the magnetospheric toroidal current density is sufficient large, the magnetic X-point geometry is formed in the equatorial plane of the magnetosphere. This X-point geometry constitute anti-parallel poloidal magnetic fields around the point. These anti-parallel magnetic fields would cause the magnetic reconnection and result in the giant-flare of the magnetar (Masada et al. 2010; Parfrey et al. 2013). The distance of the X-point geometry changes according to the shearing models. The equatorial sharing model can make the X-point geometry near the stellar surface and a minimum value of r_X/r_s is ~ 1.53 in solution (e-a) (Table 5.1). By contrast this, the ring model cannot make the X-point geometry near the stellar surface and a minimum value of r_X/r_s is ~ 12.6 in solution (r-e) (Table 5.3). The location of the magnetic reconnection in the magnetosphere would depend on the magnetospheric models deeply.

Next, we consider the physical process for the X-point geometry. We have obtained the X-point geometry by changing three parameters. The X-point geometry appears by (1) increasing the value of toroidal magnetic fields (κ_0) (solutions m-c, m-f and m-i), (2) increasing the magnitude of the current sheet (j_s) on core-crust boundary (solutions s-c and s-d) and (3) increasing the size of twisted magnetosphere (r_M) (the size of the surface toroidal magnetic field) (solution r-e).

Condition (1) is satisfied such as the case that the magnetospheric toroidal current is accumulated by the fixed stellar current (Parfrey et al. 2013). The value of κ_0 increases as the energy of the toroidal magnetic field in the magnetosphere increases in the case. Condition (2) is satisfied such as the case that the internal magnetic field configurations and elastic force balance in the crust are changed by the dynamical events such as glitch or elastic crust cracking. Since the core-crust boundary condition would be changed by these events, the value of j_0 varies in the case as we have changed the current sheet on the boundary. Condition (3) is satisfied such as the case that the toroidal magnetic fields emerge out of the crust. The size of the surface toroidal magnetic fields (twisted magnetosphere) is enlarged as we have changed the value of r_M. The largely crust cracking would result in the toroidal magnetic fields emerging. Such cracking release stress on the crust and decrease the negative current sheet on the core-crust boundary. The internal magnetic field configurations would change from a configuration such as solution (f) to solution (e) during this process. Since the energy ratio $\mathcal{M}cr_t/\mathcal{M}cr$ decreases from solution (f) to (e), the core toroidal magnetic field would be ejected from the star (Thompson & Duncan 2001). Probably, such toroidal magnetic energy injection would make the giant magnetic loops (Gourgouliatos & Lynden-Bell 2008; Takahashi et al. 2009, 2011; Matsumoto et al. 2011). These dynamical events in the stellar interior and the changes of the toroidal magnetic field on the surface would result in the reconnection within the magnetosphere and giant

flare. Our numerical result would be a key to the physical mechanisms of magnetar giant flare.

5.4.3 Concluding remarks

We have calculated magnetized equilibrium states throughout MHD equilibrium core, Hall equilibrium crust and twisted force-free magnetosphere with both poloidal and toroidal magnetic fields using Green function method under the various boundary conditions simultaneously and systematically. We have found that the magnetic field configuration in each region is affected each other deeply.

We have found that the Hall equilibrium states are affected by both inner (core) and outer (twisted-magnetosphere) boundary conditions significantly. The strong core toroidal magnetic fields models as solutions (e) and (f) broaden the size of the crustal toroidal magnetic fields region. The twisted force-free magnetosphere around the star also widens the size of the crustal toroidal magnetic field region. We would evaluate the efficiency of the Hall cascade from the toroidal magnetic field energy ratio $\mathcal{M}cr_t/\mathcal{M}cr$ in Hall equilibrium. The presence of the strong core magnetic fields would weaken the efficiency of the Hall cascade, because they have not small crustal toroidal magnetic field energy when the magnetic fields reach in Hall equilibrium. Since the twisted magnetosphere also widen the size of the crustal toroidal magnetic field region, it also weakens the Hall cascade within the crust.

The magnetosphere around the star forms the magnetic X-point geometry when the magnetospheric toroidal current density is sufficient large or the stellar total current is sufficient small. The magnetic X-point geometry can be made by the stellar interior physical event between core and crust such as glitch or magnetic fields changing. The X-point geometry causes the magnetic reconnection which would be an origin of the giant flare of magnetar. The location of the X-point geometry depends on the shearing model. The equatorial shearing can make the X-point geometry near the stellar surface ($r_X/r_s \sim 1.53$), but the ring sharing cannot make the X-point geometry near the surface. The X-point geometry in the ring model appears at the distant region near $r_X/r_s \sim 12.6$. These numerical results show that both Hall MHD secular evolution and magnetospheric dynamical evolution would be affected by magnetic field configurations of another regions and the core-crust boundary conditions. We need to consider core, crustal and magnetospheric magnetic field configurations simultaneously in order to investigate the magnetar physics.

Sed fortuna, quae plurimum potest cum in reliquis rebus tum praecipue in bello, parvis momentis magnas rerum commutationes efficit; ut tum accidit.
Fortune, which has a great deal of power in other matters but especially in war, can bring about great changes in a situation through very slight forces.
(Gaius Julius Caesar, The Civil War)

6

Counter effects of meridional flows and magnetic fields

Meridional flows inside the stellar object are also interesting physical mechanism for equilibrium states. We extend the formulation without meridional flows in the previous chapters and present the most general formulation for the stationary and axisymmetric barotropic systems. The meridional flows have the influence on the stellar structures.

6.1 Introductory analysis and motivation

6.1.1 Theoretical treatment of stationary states of axisymmetric magnetized self-gravitating barotropes under the ideal MHD approximation

In this chapter, we give new expressions for the current density and the vorticity vector inside the stationary and axisymmetric magnetized self-gravitating barotropes with internal gaseous motions under the ideal magnetohydrodynamics (MHD) approximation. Although stationary states of the magnetized self-gravitating barotropes without internal flows have been investigated in many classical papers (e.g., Chandrasekhar & Fermi 1953; Lüst & Schlüter 1954; Ferraro 1954; Gjellestad 1954; Roberts 1955; Chandrasekhar 1956a; Chandrasekhar 1956c; Chandrasekhar & Prendergast 1956; Prendergast 1956; Sykes 1957; Woltjer 1959a; Woltjer 1959b; Woltjer 1960; Ostriker & Hartwick 1968) and in recent papers (e.g., Tomimura & Eriguchi 2005; Yoshida & Eriguchi 2006; Yoshida et al. 2006; Otani et al. 2009), the effects of the internal flows on structures of magnetized self-gravitating barotropes have barely studied so far.

Dynamic equilibrium equations for *stationary states of magnetized self-gravitating bodies with internal flows* are given by

$$\frac{1}{\rho}\nabla p = -\nabla\phi_g - \nabla\phi_c - \frac{1}{2}\nabla|\boldsymbol{v}|^2 + \boldsymbol{v}\times\boldsymbol{\omega} + \frac{1}{c\rho}\boldsymbol{j}\times\boldsymbol{B}\,, \tag{6.1}$$

where $\boldsymbol{\omega}$ is the vorticity. In this chapter, the gravitational potential of external objects is assumed to be given by

$$\phi_c = -\frac{GM_c}{r}\,, \tag{6.2}$$

where M_c, G, and r denote the mass of the central external object, the gravitational constant, and the distance from the central object, respectively. Using the expressions for the current density and the vorticity vector inside the stationary, axisymmetric and infinitely conducting barotropes we may simplify the forth term in the right-hand side of Eq. (6.1) as

$$\boldsymbol{v}\times\boldsymbol{\omega} = \begin{cases} \Omega(\Psi)\nabla(Rv_\varphi) + \dfrac{1}{4\pi c\rho}\dfrac{dQ(\Psi)}{d\Psi}\boldsymbol{B}\times\boldsymbol{\omega}\,, & (\text{for } \boldsymbol{B}\neq 0, \boldsymbol{v}_p\neq 0) \\ \nu(Q)\nabla Q\,, & (\text{for } \boldsymbol{B}=0, \boldsymbol{v}_p\neq 0) \\ \frac{1}{2}\nabla(R^2\Omega^2(R)) + R\Omega^2(R)\boldsymbol{e}_R\,, & (\text{for } \boldsymbol{B}=0, \boldsymbol{v}_p=0) \end{cases} \tag{6.3}$$

where Q is the stream functions, Ω and ν are arbitrary functions of the given argument, and R and $\boldsymbol{e}_R$ are the radial coordinate and base vector for the cylindrical coordinate with respect to the symmetry axis, respectively. Here, $\boldsymbol{v}_p$ and v_φ stand for the poloidal velocity and the toroidal velocity, given by

$$\boldsymbol{v}_p \equiv \frac{1}{4\pi\rho}\nabla Q\times\nabla\varphi\,, \tag{6.4}$$

$$v_\varphi = R\Omega + \frac{1}{4\pi c\rho}\frac{dQ(\Psi)}{d\Psi}B_\varphi\,, \tag{6.5}$$

with φ and B_φ being the azimuthal angle and the toroidal magnetic field, respectively. The stream function Q is a function of the flux function Ψ if and only if $\boldsymbol{B}\neq 0$ and $\boldsymbol{v}_p\neq 0$. Thus, equi-stream function surfaces are similar to equi-magnetic flux function surfaces if $\boldsymbol{B}\neq 0$ and $\boldsymbol{v}_p\neq 0$. Similarly, the Lorentz force term appearing in the fifth term in the right-hand side of Eq. (6.1) may be rewritten as

$$\frac{1}{c\rho}\boldsymbol{j}\times\boldsymbol{B} = \begin{cases} \nabla(\Omega(\Psi))Rv_\varphi + \mu(\Psi)\nabla\Psi + \dfrac{1}{4\pi c\rho}\dfrac{dQ(\Psi)}{d\Psi}\boldsymbol{\omega}\times\boldsymbol{B}\,, & (\text{for } \boldsymbol{B}\neq 0) \\ 0\,, & (\text{for } \boldsymbol{B}=0) \end{cases} \tag{6.6}$$

where $\mu(\Psi)$ is an arbitrary function. From Eqs. (6.1)–(6.6), we obtain Bernoulli's equations

for the present situation:

$$\int \frac{dp}{\rho} = \begin{cases} -\phi_g + \dfrac{GM_c}{r} - \dfrac{1}{2}(|\boldsymbol{v}_p|^2 + v_\varphi^2) + Rv_\varphi\Omega(\Psi) + \displaystyle\int^{\Psi} \mu(\Psi)d\Psi + C\,, \\ \quad (\text{for } \boldsymbol{B} \neq 0) \\ -\phi_g + \dfrac{GM_c}{r} - \dfrac{1}{2}(|\boldsymbol{v}_p|^2 + v_\varphi^2) + \displaystyle\int^{Q} \nu(Q)dQ + C\,, \\ \quad (\text{for } \boldsymbol{B} = 0, \boldsymbol{v}_p \neq 0) \\ -\phi_g + \dfrac{GM_c}{r} + \displaystyle\int^{R} R\Omega^2 dR + C\,, \\ \quad (\text{for } \boldsymbol{B} = 0, \boldsymbol{v}_p = 0) \end{cases} \tag{6.7}$$

where C is an integration constant. It should be emphasized that these three expressions cannot be united to a single expression as can be understood from Eqs. (6.3) and (6.6), but the formulations of ($\boldsymbol{B} \neq 0$) and ($\boldsymbol{B} = 0, \boldsymbol{v}_p \neq 0$) can be treated systematically using the master potential by Gourgoulhon et al. (2011). Note that in this study, we do not consider the case of $\boldsymbol{B}_p = 0$ and $B_\varphi \neq 0$, for which Bernoulli's equations differ from Eq. (6.7).

By comparing Bernoulli's equation for the case of $\boldsymbol{B} = 0$ and $\boldsymbol{v}_p = 0$ with that for the case of $\boldsymbol{B} = 0$ and $\boldsymbol{v}_p \neq 0$, we may expect that *the presence of the meridional flows* tends to decrease the volume occupied by the fluid. This is because the kinetic energy of the meridional flow contributes to the fluicd as *positive ram pressures* (dynamic pressure), which result in reducing the fluid pressure and consequently decreasing the density of stationary fluid objects. In contrast to the effect of the meridional flow, for magnetized equilibrium configurations with $\boldsymbol{v}_p = 0$ whose magnetic fields are generated by positive toroidal currents, the poloidal magnetic field is apt to expand the fluid region to the direction perpendicular to the symmetry axis like the centrifugal force (see, e.g. classical papers Ferraro 1954; Gjellestad 1954; Roberts 1955; and recent papers Tomimura & Eriguchi 2005; Yoshida & Eriguchi 2006; Yoshida et al. 2006). Therefore, simultaneous presence of the meridional flows and the poloidal magnetic fields could result in almost no changes in the matter distributions. So far, such effects have not been investigated because stationary states of axisymmetric magnetized barotropes with meridional flows have not been obtained. Thus it is one of the purposes in this study to show the above statements could be proved to hold in some numerical examples.

6.1.2 Toroids: Best astrophysical systems in which both meridional flows and magnetic fields would work simultaneously but differently

In order to show clearly the oppositely working effects of the above mentioned two quantities, meridional flows and poloidal magnetic fields, we will show numerical results of stationary configurations of axisymmetric magnetized self-gravitating *toroidal* barotropes with meridional flows which locate around central point masses in the framework of Newtonian gravity under the ideal MHD approximation. For toroidal configurations, matter distribution changes in wider space would be expected compared to size changes of spheroidal objects because toroids

could change their shapes to *two* opposite directions, i.e. to the outside direction and to the inside direction of the toroids. Thus we will solve stationary states of axisymmetric magnetized barotropic *toroids* with meridional flows under the ideal MHD approximation and clarify the oppositely working effects explicitly in this study.

Concerning self-gravitating toroidal configurations or disks, we need to take recent results of fully general relativistic (GR) numerical simulations into account. These simulations show that a few-solar-mass black hole and a highly dense toroid whose maximum density can reach 10^{10} - $10^{11}\mathrm{g/cm}^3$ around the black hole could be formed after merging of binary neutron stars (Shibata & Uryū 2000; Shibata et al. 2003; Shibata et al. 2005; Kiuchi et al. 2009; Hotokezaka et al. 2011), after merging of a neutron star and a black hole in binary systems (Shibata & Uryū 2006;Shibata & Uryu 2007; Shibata & Taniguchi 2008; Kyutoku et al. 2010; Kyutoku et al. 2011) or after collapsing of a supermassive rotating star (Shibata 2000; Shibata & Shapiro 2002; Shibata 2003; Sekiguchi & Shibata 2004; Sekiguchi & Shibata 2007; Sekiguchi & Shibata 2011). Therefore, dense toroids and central compact objects could be formed after collapsing or merging of compact objects. Similar kinds of systems with *magnetic fields* have also been investigated by several groups (e.g. Narayan et al. 2001; Shibata & Sekiguchi 2005; Duez et al. 2006; Shibata et al. 2007). Although, in order to understand the origin and dynamical formation processes of these systems, we must take into account many realistic physics and compute stationary configurations with magnetic fields in GR, nobody has yet succeeded in solving stationary states both with poloidal and toroidal magnetic fields *in GR at present*. Therefore, we explore such stationary states of axisymmetric magnetized barotropic systems in the framework of Newtonian gravity. Although there were many papers to obtain magnetized stationary states of disks/toroids only with poloidal magnetic fields (e.g. Bisnovatyi-Kogan & Blinnikov 1972; Bisnovatyi-Kogan & Seidov 1985; Baureis et al. 1989; Li & Shu 1996) and disks/toroids only with toroidal magnetic fields inside the disks/toroids (e.g. Okada et al. 1989; Banerjee et al. 1995; Ghanbari & Abbassi 2004), no solutions both with poloidal and toroidal components of magnetic fields have been obtained yet. This is because it has been difficult to solve the Grad-Shafranov equation as well as the equations of motion consistently by some means. Concerning this type of systems, the most general formulation was derived by Lovelace et al. (1986) systematically. However, Lovelace et al. (1986) computed solutions only with poloidal magnetic fields for non-self-gravitating disks.

Recently, Otani et al. (2009) have obtained magnetized self-gravitating equilibrium states both with poloidal and toroidal magnetic fields self-consistently in the framework of Newtonian gravity. Their method is based on Tomimura & Eriguchi (2005). In this study we have extended the method employed in Otani et al. (2009) to the most general configurations for the stationary states of axisymmetric magnetized barotropic toroids with meridional flows under the ideal MHD approximation and obtained sequences of stationary states. Comparing these results with those of non-magnetized toroids without meridional flows (e.g. Ostriker 1964; Wong 1974), with those of magnetized toroids without meridional flows (e.g. Otani et al. 2009) or with those of non-magnetized toroids with meridional flows (e.g. Eriguchi et al. 1986), we will be able

to clearly see the effect of the presence of both physical quantities, i.e. meridional flows and magnetic fields as explained in the previous subsection.

6.2 Brief description of the problem

In this study, as mentioned, we investigate *stationary configurations of axisymmetric magnetized polytropic toroids with internal fluid motions*. We consider *inviscid and infinitely conductive toroids with equatorial symmetry* located around *central point masses* in the framework of *Newtonian gravity*. Since a similar problem, but without meridional flows, was already treated by Otani et al. (2009) and our strategy is basically the same as theirs, we briefly summarize the basic equations, boundary conditions, and solving scheme. We use similar scheme in chapter 6.

Pressure balance equations for stationary states are respectively given by

$$\frac{1}{\rho}\nabla p = -\nabla\phi_g + \nabla\left(\frac{GM_c}{r}\right) - \frac{1}{2}\nabla|\boldsymbol{v}^2| + \boldsymbol{v}\times\boldsymbol{\omega} + \frac{1}{\rho}\left(\frac{\boldsymbol{j}}{c}\times\boldsymbol{B}\right). \tag{6.8}$$

In order to obtain the magnetized configurations, we also solve the equation as

$$\Delta^*\Psi = -4\pi R\frac{j_\varphi}{c}. \tag{6.9}$$

This equation is equivalent to the so called Grad-Shafranov equation for this problem, but we treat the right-hand side of Eq. (6.9) as the source term of the differential operator in the left-hand side of Eq. (6.9) even though j_φ includes the term proportional to the left-hand side of Eq. (6.9) if $\boldsymbol{v}_p \neq 0$. Explicit expression for j_φ is given as

$$\frac{\boldsymbol{j}}{c} = \left[\kappa'(\Psi) + Rv_\varphi Q''(\Psi)\right]\frac{\boldsymbol{B}}{4\pi} + Q'(\Psi)\frac{\boldsymbol{\omega}}{4\pi} + \rho R\left[\mu(\Psi) + Rv_\varphi\Omega'(\Psi)\right]\boldsymbol{e}_\varphi\,. \tag{6.10}$$

As we have calculated in previous chapters in this thesis, we use Green function in order to solve the equation and include the boundary condition as infinite.

In general, the toroid cannot approach indefinitely to the central object because gravitational effects of the central object can unboundedly increase as the distance from the central object to the toroid decreases and any forces counteracting the gravity cannot stanch the matter flow shedding from the inner edge of the toroid if their distance is shorter than some critical value. In the present numerical scheme to obtain magnetized toroids, the distance from the central object to the inner edge of the toroid (or the width of the toroid) is characterized by a dimensionless parameter q, defined by

$$q \equiv \frac{R_{\rm inner}}{R_{\rm outer}}, \tag{6.11}$$

where $R_{\rm inner}$ and $R_{\rm outer}$ are the shortest and the longest distances from the symmetry axis to the toroid, respectively. In terms of q, this disappearance property of the equilibrium states

describes as the existence of q_c such that there is no stationary solution of the toroid for $q < q_c$. Note that the value of q_c depends on what parameters characterizing equilibrium sequences keep constant when the value of q changes. Following Otani et al. (2009), we call equilibrium solutions characterized by $q = q_c$ the critical configuration or the critical state. The distance from the symmetry axis to the inner edge of the toroid for the critical configuration is named the *critical distance*. In this study, we focus only on the critical configurations.

Otani et al. (2009) investigated the critical configuration for the magnetized toroids without meridional flows and found the following properties. (i) The critical configuration features cusp-like structures at the inner edge of the toroids. (ii) The critical configuration rotates very slowly. This implies that the critical toroids are mainly sustained by the balance among the magnetic forces, the gravity of the central objects and the pressure gradients. (iii) The critical distances are almost independent of the mass ratio of the toroids to the central objects. (iv) The critical distances are much larger than $6GM_c/c^2$, the radius of the innermost stable circular orbit for the Schwarzschild black hole with the gravitational mass M_c. This means that making use of Newtonian gravity is reasonable to investigate structures of the toroids considered in Otani et al. (2009).

6.3 Numerical results

Following Otani et al. (2009), we consider two polytropic indices $N = 1.5$ and $N = 3$ only in the present study. As for the arbitrary functions, which need to be specified to obtain particular solutions, we employ the same functional forms as those used in Yoshida et al. (2006) and Otani et al. (2009) except for the toroidal current function μ. For the toroidal current function μ, we choose the same functional form as that used in chapter 2 in order for the inner edge of the toroid to have stronger magnetic fields. As for the stream function Q', which does not appear in Otani et al. (2009), a similar functional form to that of the poloidal current function κ is employed. The functional forms are as follow:

$$\kappa(\Psi) = \begin{cases} 0\,, & \text{for} \quad \Psi \leq \Psi_{\max}\,, \\ \dfrac{\kappa_0}{k+1}(\Psi - \Psi_{\max})^{k+1}\,, & \text{for} \quad \Psi \geq \Psi_{\max}\,, \end{cases} \tag{6.12}$$

$$Q'(\Psi) = \begin{cases} 0\,, & \text{for} \quad \Psi \leq \epsilon_Q \Psi_{\max}\,, \\ \dfrac{Q_0}{k+1}(\Psi - \epsilon_Q\Psi_{\max})^{k+1}\,, & \text{for} \quad \Psi \geq \epsilon_Q \Psi_{\max}\,, \end{cases} \tag{6.13}$$

$$\Omega(\Psi) = \Omega_0(\Psi^2 + d^2)^{\alpha}\,, \tag{6.14}$$

$$\mu(\Psi) = \mu_0(\Psi + \epsilon)^m\,, \tag{6.15}$$

where, κ_0, k, Q_0, ϵ_Q, Ω_0, d, μ_0, ϵ, α, and m are constant parameters. This choice of κ is the same as that employed in Tomimura & Eriguchi (2005), Yoshida & Eriguchi (2006), Yoshida

et al. (2006), and Otani et al. (2009). We introduce the parameter ϵ_Q in Eq. (6.13) and set $\epsilon_Q = 1.1$ in order to restrict the region where meridional flows exist well inside the surface of the toroid. Choosing these functional forms, we can avoid singular behavior of the solutions which could appear on the surface of the toroid.

As mentioned before, recent numerical simulations performed with numerical relativity show that geometrically thick toroids rotating around black holes form after mergers of neutron star binaries, mergers of black hole-neutron star binaries, or collapses of supermassive rotating stars (e.g. Sekiguchi & Shibata 2007; Sekiguchi & Shibata 2011). Typical values of physical quantities of such black hole-toroid systems are given by $M_t = 1.0 \times 10^{-1} M_\odot$, $M_c = 5.0 M_\odot$ ($M_t/M_c = 2.0 \times 10^{-2}$), and $\rho_{\rm max} = 1.0 \times 10^{11} {\rm g/cm^3}$, where M_t and $\rho_{\rm max}$ are the mass and the maximum density of the toroid, respectively. Since these black hole-toroid systems are of large significance in high energy astrophysics, we focus on the models characterized by the mass ratio $M_t/M_c = 2.0 \times 10^{-2}$ and use these values of the mass of the central object and the maximum density of the toroid to estimate values of other physical quantities with physical dimension, e.g. $|\boldsymbol{B}|$ and R_{inner}.

To check numerical accuracies of the stationary configurations obtained in this study, we estimate values of a virial relation, which vanishes for exact stationary solutions:

$$\mathrm{VC} = \left| \frac{2T + W + 3\Pi + \mathcal{M}}{W} \right| . \tag{6.16}$$

In the present study, we choose the grid number as $N_r = 513$ and $N_\theta = 513$ because this grid number is sufficiently large to obtain numerical solutions with acceptable accuracy. Since we assume that the gravitational potential of the central object has a singularity at $\hat{r} = 0$, we consider the region defined by $\hat{r} \in [1.0 \times 10^{-2}, 4.0]$ and $\theta \in [0, \pi/2]$ as our computational space. In order to resolve structures of the toroid properly, we use non-uniformly distributed grid points used in chapter 2.

6.3.1 Widening of the widths of toroids: Effect of the localized poloidal magnetic fields

The counter effects of the meridional flows against the magnetic forces on structures of magnetized toroids would be clearly seen for toroids with rather widened shapes due to poloidal magnetic fields. Thus, in this subsection, we will try to compute magnetized toroids with highly localized poloidal magnetic fields because such equilibrium configurations could be toroids with a rather small value of q, i.e. the width of toroids on the equatorial plane being rather wide (see e.g. chapter 2).

To investigate effects of the localized poloidal magnetic fields on the toroid structures, no fluid flow inside the toroid is considered here.

Thus, values of the parameters $\hat{Q}_0$, $\hat{\Omega}_0^2$, α, and d are taken to be $\hat{Q}_0 = 0$, $\hat{\Omega}_0^2 = 0$, $\alpha = 0$, and $d = 0$ Here, physical quantities with $(\hat{\ })$ are dimensionless quantities defined in App. B.1. As for $\hat{\kappa}_0$, following Otani et al. (2009), we take $\hat{\kappa}_0 = 4.5$. Since there are no rotation and no meridional flows, the toroids are in stationary states by the balance among the gravitational

m	q_c	$\hat{\mu}_0$	r_e(cm)	$\lvert\hat{W}\rvert$	$\mathcal{M}/\lvert W\rvert$	$U/\lvert W\rvert$	VC
				$N = 1.5$			
0.5	0.680	6.960E+00	2.984E+07	2.573E-02	6.509E-01	1.164E-01	2.763E-05
0.3	0.650	4.700E+00	2.791E+07	3.893E-02	6.421E-01	1.193E-01	2.713E-05
0.0	0.598	2.984E+00	2.518E+07	7.401E-02	6.272E-01	1.243E-01	2.610E-05
-0.1	0.578	2.661E+00	2.432E+07	9.226E-02	6.218E-01	1.261E-01	2.575E-05
-0.3	0.533	2.238E+00	2.264E+07	1.449E-01	6.100E-01	1.300E-01	2.525E-05
-0.5	0.481	2.033E+00	2.105E+07	2.312E-01	5.966E-01	1.345E-01	2.444E-05
-0.7	0.419	1.996E+00	1.954E+07	3.754E-01	5.812E-01	1.396E-01	2.381E-05
-0.9	0.344	2.117E+00	1.812E+07	6.201E-01	5.631E-01	1.456E-01	2.329E-05
-1.1	0.252	2.408E+00	1.683E+07	1.036E+00	5.415E-01	1.528E-01	2.274E-05
-1.4	0.067	2.956E+00	1.564E+07	1.923E+00	5.111E-01	1.630E-01	2.471E-05
				$N = 3$			
0.5	0.720	1.159E+01	4.653E+07	1.747E-03	6.910E-01	1.030E-01	6.433E-05
0.3	0.687	6.031E+00	4.243E+07	3.080E-03	6.807E-01	1.065E-01	6.073E-05
0.0	0.628	2.742E+00	3.656E+07	7.732E-03	6.639E-01	1.121E-01	5.472E-05
-0.1	0.605	2.227E+00	3.473E+07	1.064E-02	6.578E-01	1.141E-01	5.279E-05
-0.3	0.554	1.600E+00	3.129E+07	2.044E-02	6.446E-01	1.185E-01	4.880E-05
-0.5	0.495	1.289E+00	2.814E+07	3.993E-02	6.297E-01	1.234E-01	4.470E-05
-0.7	0.425	1.164E+00	2.529E+07	7.927E-02	6.127E-01	1.291E-01	4.064E-05
-0.9	0.342	1.173E+00	2.274E+07	1.593E-01	5.926E-01	1.358E-01	3.644E-05
-1.1	0.242	1.298E+00	2.057E+07	3.195E-01	5.678E-01	1.441E-01	3.224E-05
-1.4	0.057	1.467E+00	1.901E+07	6.864E-01	5.261E-01	1.580E-01	2.944E-05

Table 6.1: Physical quantities for the critical configurations with $\hat{Q}_0 = 0.0$ (no meridional flow), $\hat{\Omega}_0 = 0.0$ (no rotation) and $\hat{\kappa}_0 = 4.5$.

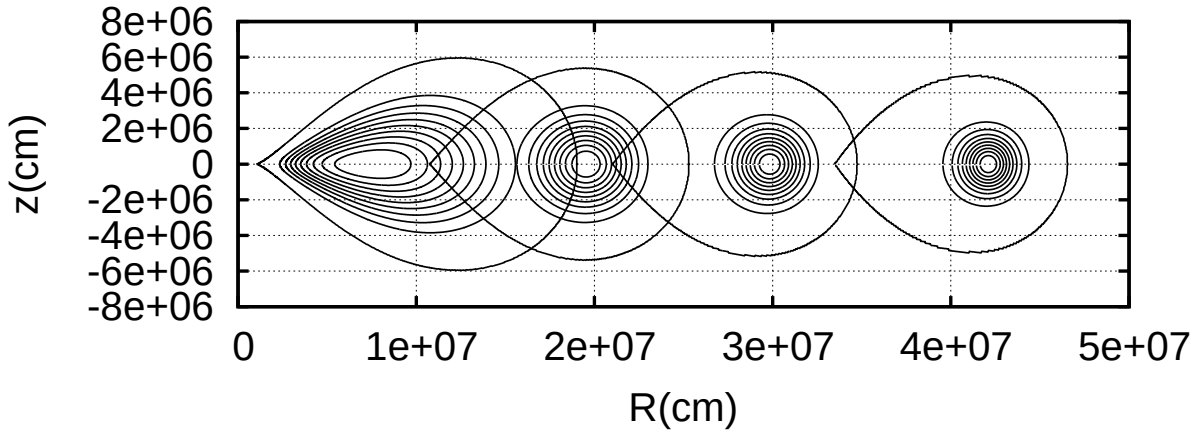

Figure 6.1: The density contours on the meridional cross section for four critical configurations with different values of m. From left to right, the density contours correspond to the toroids with $m = -1.4$, $m = -0.7$, $m = -0.1$, and $m = 0.5$, respectively. Values of the other parameters are $N = 3$, $\hat{Q}_0 = 0$, $\hat{\Omega}_0 = 0$, and $\hat{\kappa}_0 = 4.5$. The tear-shaped closure curves with a cusp-like structure indicate the surfaces of the toroids. The density difference between two adjacent contours is one-tenth of the maximum density. It is observed that the width of the toroid on the equator becomes wider as values of m decrease.

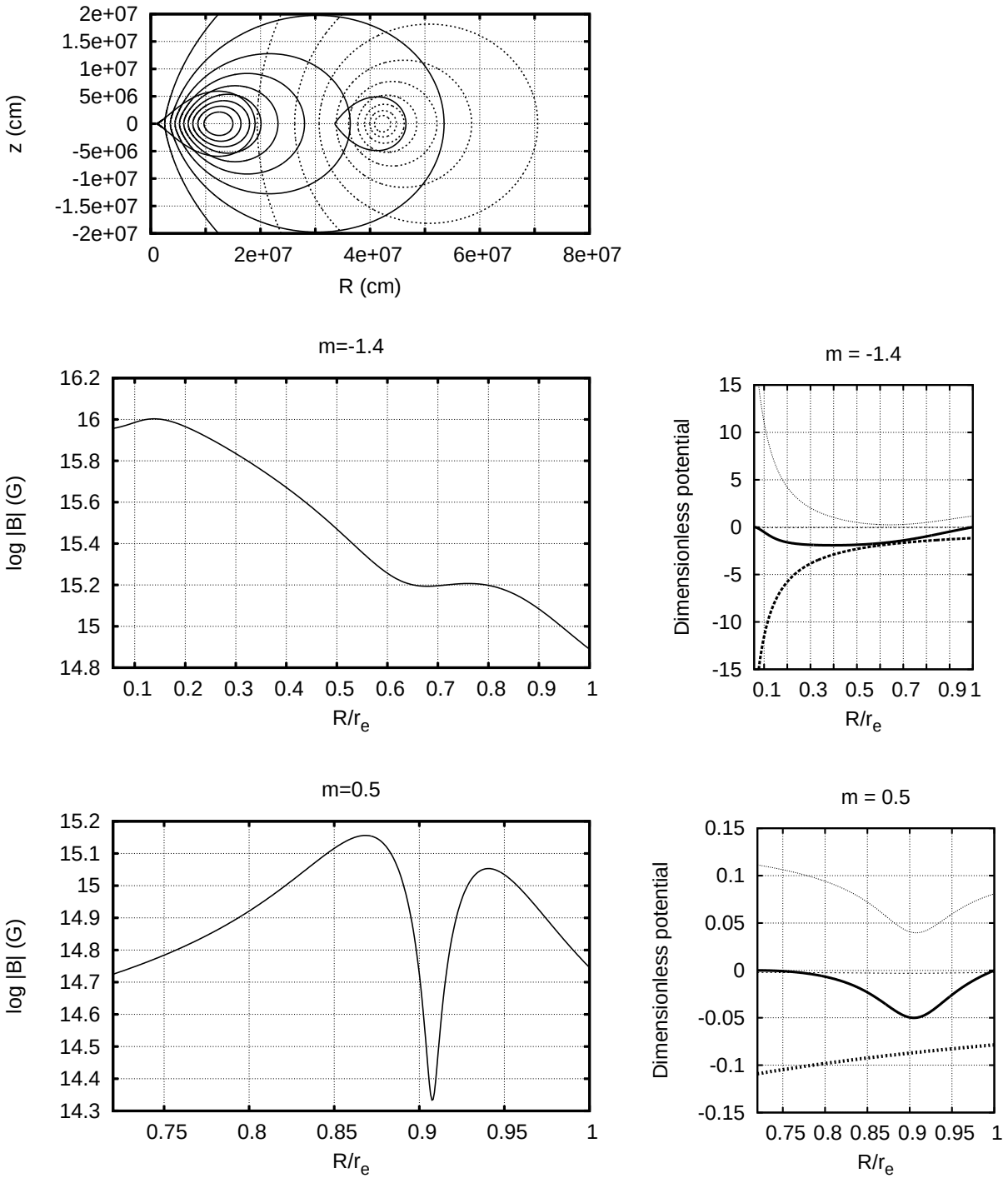

Figure 6.2: Top panel: The poloidal magnetic fields on the meridional plane for the $N = 3$ toroids with $m = -1.4$ (solid curves) and $m = 0.5$ (dashed curves). Values of the other model parameters are the same as those of the models given in Fig. 6.1. The tear-shaped closure curves with a cusp-like structure indicate the surfaces of the toroids. Middle left and bottom left panels: $\log_{10} |\boldsymbol{B}|$ on the equator for two critical configurations with $m = -1.4$ (middle) and $m = 0.5$ (bottom), given as functions of R/r_e. The horizontal axises range from $R_{inner}/r_e(= q_c)$ to $R_{outer}/r_e(= 1)$. Middle right and bottom right panels: $-\hat{M}_c/4\pi\hat{r}$ (thick dashed curve), $\hat{\phi}_g$ (thin dashed curve), $-\int \hat{\mu}(\hat{\Psi})\, d\hat{\hat{\Psi}} - \hat{C}$ (dotted curve), and sum of these three potentials (solid curve) on the equator for the critical configurations with $m = -1.4$ (middle) and $m = 0.5$ (bottom), given as functions of R/r_e. The horizontal axises range from $R_{inner}/r_e(= q_c)$ to $R_{outer}/r_e(= 1)$.

force of the central object, the Lorentz force and the gas pressure gradient. If there could be very strong poloidal magnetic fields near the central objects, stronger gravitational forces of the central objects could be balanced by the *strong* magnetic forces near the central objects. For such situations the toroids could be elongated toward the central objects and have wider widths.

We have showed that the poloidal magnetic field distributions substantially depend on the parameter m in the arbitrary function $\mu(\Psi)$ for magnetized stars in chapter 2. In particular, we have found that negative values of m result in concentration of the poloidal magnetic fields near the symmetry axis of magnetized stars. Thus, it is expected that we may obtain toroids in which poloidal magnetic fields are concentrated near the inner edge of the toroids by choosing an appropriate value of m.

We show our numerical results for critical configurations of $N = 1.5$ and $N = 3$ polytropic sequences in Table 6.1 and density contours on the meridional cross section of $N = 3$ polytropes with $m = -1.4$, $m = -0.7$, $m = -0.1$ and $m = 0.5$ in Fig. 6.1. As seen from these table and figure, the critical distance decreases as the value of m decreases. The density distribution of the $m = -1.4$ toroid is stretched toward the central object because of the strong gravity of the central object. In addition to this, the cusp-like shape at the inner edge of the toroids becomes 'sharper' as the value of m becomes smaller. We find the same tendency for the $N = 1.5$ polytropes.

The top panel of Fig. 6.2 shows the structures of the magnetic fields on the meridional plane for the $N = 3$ critical configurations with $m = -1.4$ (solid curves) and $m = 0.5$ (dashed curves). In this figure, the surfaces of the toroids are indicated by the tear-shaped closure curves. The structures of the magnetic fields for the model with $m = -1.4$ are remarkably different from those for the model with $m = 0.5$. The shapes of the contours of the magnetic flux function for the toroid with $m = 0.5$ look nearly circle, but those for the toroid with $m = -1.4$ deform oblately. Moreover, the magnetic field lines are more densely distributed near the inner edge region of the toroid for the toroid with $m = -1.4$ compared to those for the toroid with $m = 0.5$. In other words, the magnetic fields are highly localized toward the central object for the toroid with $m = -1.4$ compared to those of the toroid with $m = 0.5$.

The panels in the middle left and the bottom left of Fig. 6.2 show distributions of $\log_{10}|\boldsymbol{B}|$ on the equatorial plane, and the panels in the middle right and the bottom right of Fig. 6.2 show values of each term in the right-hand side of the first line of Eq. (6.7) on the equatorial plane. Note that the horizontal axises of these figures range from $R_{inner}/r_e(= q_c)$ to $R_{outer}/r_e(= 1)$. As seen from the middle left and the bottom left panels of Fig. 6.2, the distributions of the magnetic fields are significantly different for the two equilibrium configurations. The ring of maximum magnetic field strength locates near the inner edge of the toroid for the model with $m = -1.4$, while it locates near the central region of the meridional cross section of the toroid for the model with $m = 0.5$. The toroids with $m = -1.4$ can sustain highly localized and strong magnetic fields in the nearer region from the central object compared to the toroids with $m = 0.5$ and can extend themselves toward the central object although the gravitational force of the central object is much stronger there. This implies that the toroids with $m = -1.4$ can

produce strong magnetic force near their inner edge, which is balanced against the gravitational force of the central compact object as shown later.

In the middle right and the bottom right panels of Fig. 6.2, the gravitational potential of the central object, $-\hat{M}_c/4\pi\hat{r}$ (thick dashed curve), the gravitational potential of the toroids, $\hat{\phi}_g$ (thin dashed curve), the magnetic potential (chapter 2), $-\int \hat{\mu}\, d\hat{\Psi} - \hat{C}$ (dotted curve) and the sum of all the potentials (thick solid curve) are shown as functions of R/r_e. From these figures, it is clearly seen that the magnetic force is the primary agent supporting the toroid against the gravitational force of the central object. The gradient of the gravitational potential of the central object for the toroid with $m = -1.4$ is steeper than that for the toroid with $m = 0.5$ because the $m = -1.4$ toroid is located closer to the central object than the $m = 0.5$ toroid. The magnetic potentials behave very differently for these two equilibrium configurations with different values of m. For the $m = 0.5$ toroid, the magnetic potential curve has a substantial local minimum at $R/r_e \sim 0.9$. For the $m = -1.4$ toroid, however, the magnetic potential curve is shallower and extends within a broader region and its slope is steepest near the inner edge of the toroid. As a result, the strong magnetic fields can exist near the inner edge region of the toroid and their magnetic force supports the toroid against the gravitational force of the central compact object. In this way, the $m = -1.4$ toroid can be in a stationary state even if the gravitational potential becomes much steeper as approaching to the central object.

6.3.2 Effects of the meridional flows on the magnetized configurations

Basic features of magnetized configurations with meridional flows

Concerning the parameters which appear in the arbitrary functions, to examine effects of the meridional flow on toroid structures, the following values are chosen in this subsection: $\hat{\kappa}_0 = 0.5$, $\alpha = -0.5$, $d = 0.1$, $m = 0$ and $\hat{\Omega}_0^2 = 1.0 \times 10^{-5}$. Note that smaller values of $\hat{\kappa}_0$ result in more rapid meridional flows and that this small value of $\hat{\Omega}_0$ gives equilibrium configurations with almost no rotation. Parameters for the rotation law are the same as those in Yoshida et al. (2006).

The left panel of Fig. 6.3 shows contours of the flux function Ψ on the meridional plane for the critical configuration of an $N = 1.5$ polytrope with meridional flows. Direction of the fluid velocity on the meridional cross section in the critical configuration is shown in the right panel of Fig. 6.3. Here, the lengths of the vectors are not proportional to the absolute values of the fluid velocities. Note that the region where the meridional flows are present is only a part of the meridional cross section of the toroid because a particular functional form for $\hat{Q}'(\Psi)$ is used to avoid singular behaviors of the meridional flow near the toroid surface (see Eq. 6.13). The bottom panel of Fig. 6.3 displays the velocity distributions normalized by the local Kepler velocity, on the equatorial plane. The solid and dashed curves denote the absolute value of the meridional velocity and the rotational velocity, respectively. As seen from this panel, the rotational velocity is sub-Keplarian, because our rotational parameter $\hat{\Omega}_0$ is assumed to be small in this chapter. On the other hand, the meridional velocity is slightly faster than the rotational

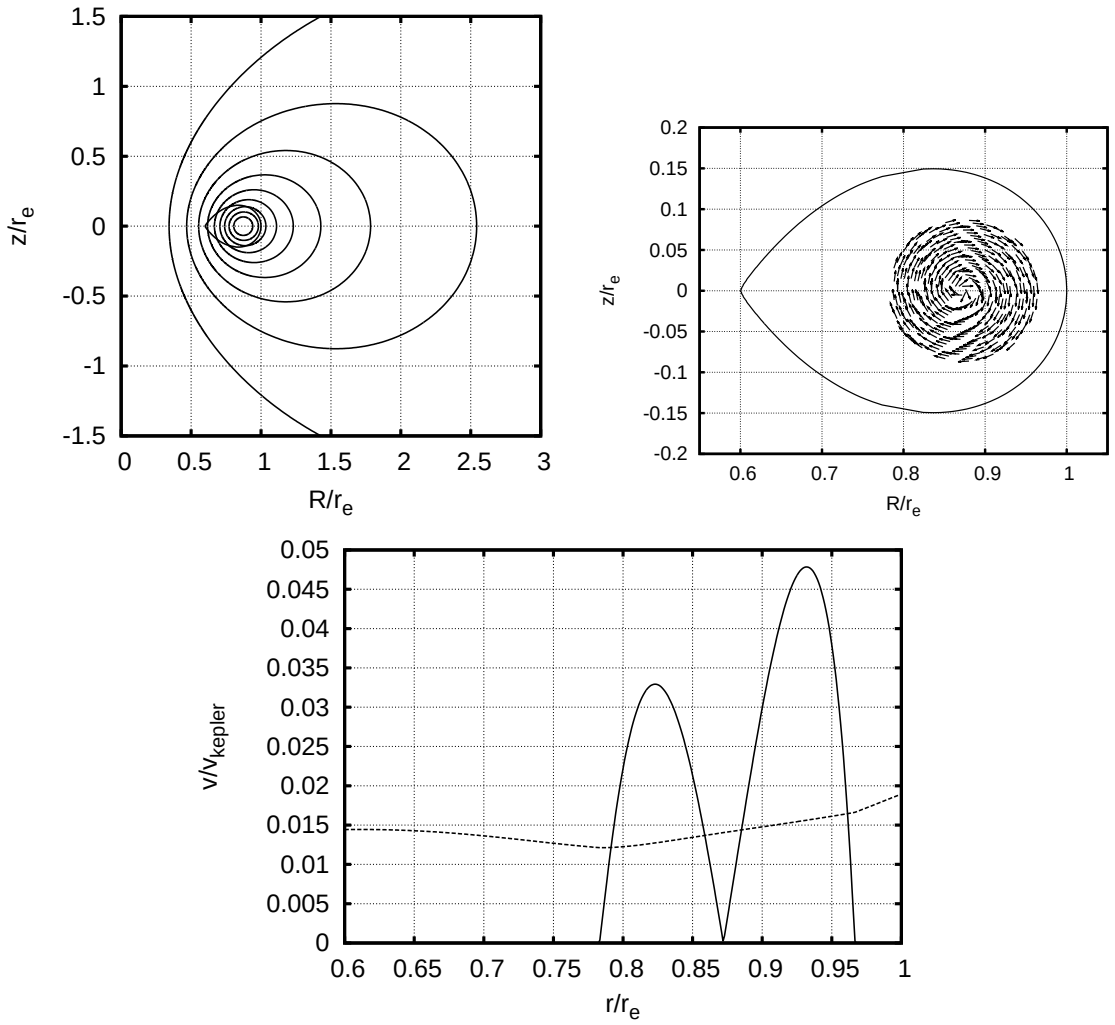

Figure 6.3: The poloidal magnetic fields (left), the meridional flow pattern (right) on the meridional plane for the toroid with $N = 1.5$, $\hat{Q}_0 = 20$, $\hat{\Omega}_0 = 1.0 \times 10^{-5}$, $m = 0$, $q = 0.6$, and $\hat{\kappa}_0 = 0.5$. The tear-shaped closure curves with a cusp-like structure indicate the surfaces of the toroids. Length of vectors given in the right panel is not proportional to the speed of the meridional flows and does not have any physical meaning. The bottom panel shows the distribution of the absolute value of the meridional velocity (solid line) and the rotational velocity (dashed line) normalized by the local Kepler velocity on the equatorial plane.

$\hat{Q}_0$	q_c	$\hat{\mu}_0$	r_e(cm)	$\mathcal{M}/\|W\|$	$\Pi/\|W\|$	$T/\|W\|$	$T_p/\|W\|$	VC
				$N = 1.5$				
0	0.597	3.047E+00	2.500E7	6.213E-01	1.262E-01	8.322E-05	0.000E+00	2.656E-05
20	0.600	3.020E+00	2.514E7	6.226E-01	1.255E-01	4.138E-04	3.185E-04	3.032E-05
40	0.605	2.942E+00	2.555E7	6.268E-01	1.235E-01	1.431E-03	1.314E-03	4.271E-05
60	0.615	2.817E+00	2.627E7	6.338E-01	1.199E-01	3.217E-03	3.063E-03	6.505E-05
80	0.629	2.653E+00	2.759E7	6.437E-01	1.148E-01	6.101E-03	5.875E-03	1.595E-04
				$N = 3$				
0	0.625	2.810E+00	3.551E7	6.583E-01	1.133E-01	9.202E-04	0.000E+00	5.497E-05
20	0.628	2.784E+00	3.570E7	6.598E-01	1.125E-01	1.464E-03	4.866E-04	3.642E-05
40	0.632	2.711E+00	3.622E7	6.639E-01	1.101E-01	2.935E-03	1.842E-03	3.115E-05

Table 6.2: Physical quantities for the critical configurations with meridional flows. Model parameters are $\hat{\kappa}_0 = 0.5$, $\hat{\Omega}_0^2 = 1.0 \times 10^{-5}$, and $m = 0$.

velocity in this parameter region ($\hat{Q}_0$ = 20).

As shown in Figs. 6.2 and 6.3 (see, also, Table 6.2 given later), general structures of the toroids and their magnetic fields do not change significantly even when the fluid flows exist on the meridional plane. As argued later, however, the presence of the meridional flows changes the density distributions of the toroids slightly and increases the critical distance a little bit.

Critical distances for magnetized toroids with meridional flows

In order to study the influence of the meridional flows on the critical distances, we calculate two polytropic sequences ($N = 1.5$, $N = 3$) by changing the value of $\hat{Q}_0$ for the $m = 0$ toroidal current function. We fix the other parameters as $\hat{\kappa}_0 = 0.5$, $\alpha = -0.5$, $d = 0.1$, and $\hat{\Omega}_0^2 = 1.0 \times 10^{-5}$ in this subsection. Physical quantities for several models belonging to the two polytropic sequences are tabulated in Table 6.2. Here, T_p denotes the kinetic energy of the meridional flow.

As seen from this table, the energy ratio $T_p/|W|$ is much smaller than that of $\mathcal{M}/|W|$, thus, the kinetic energy of the meridional flow is much smaller than the magnetic energy for the models obtained in the present study. This means that the magnetic forces mainly support the toroids against the gravitational forces of the central objects even when the meridional flow becomes stronger in the present parameter space. The meridional flow cannot change global structures of the toroids and their magnetic fields significantly. However, the energy ratio $T_p/|W|$ reaches $\sim 1.0 \times 10^{-3}$ when $\hat{Q}_0 > 40$ ($N = 1.5$) and $\hat{Q}_0 = 40$ ($N = 3$). In fact, the critical distance q_c increases as $\hat{Q}_0$ increases as shown in Table 6.2. This implies that the toroids tend to shed their mass when the meridional flow becomes stronger. In some sense, therefore, the influence of the meridional flow on the density distribution of the toroids should not be considered to be small. The rotational velocities of these models are also sub-Keplarian. The typical value is about 2 % of the Kepler velocity which is similar to that given in Fig. 6.3. On the other hand, the meridional flow velocity is about several times as large as the rotational velocity. The maximum velocity of the meridional flow for the $\hat{Q}_0 = 80$ model reaches about 10 times as large as that of the rotational velocity.

In order to clarify the effects of the meridional flows, let us investigate the density distributions of toroids and the profiles of potential terms on the equatorial planes for the $N = 1.5$

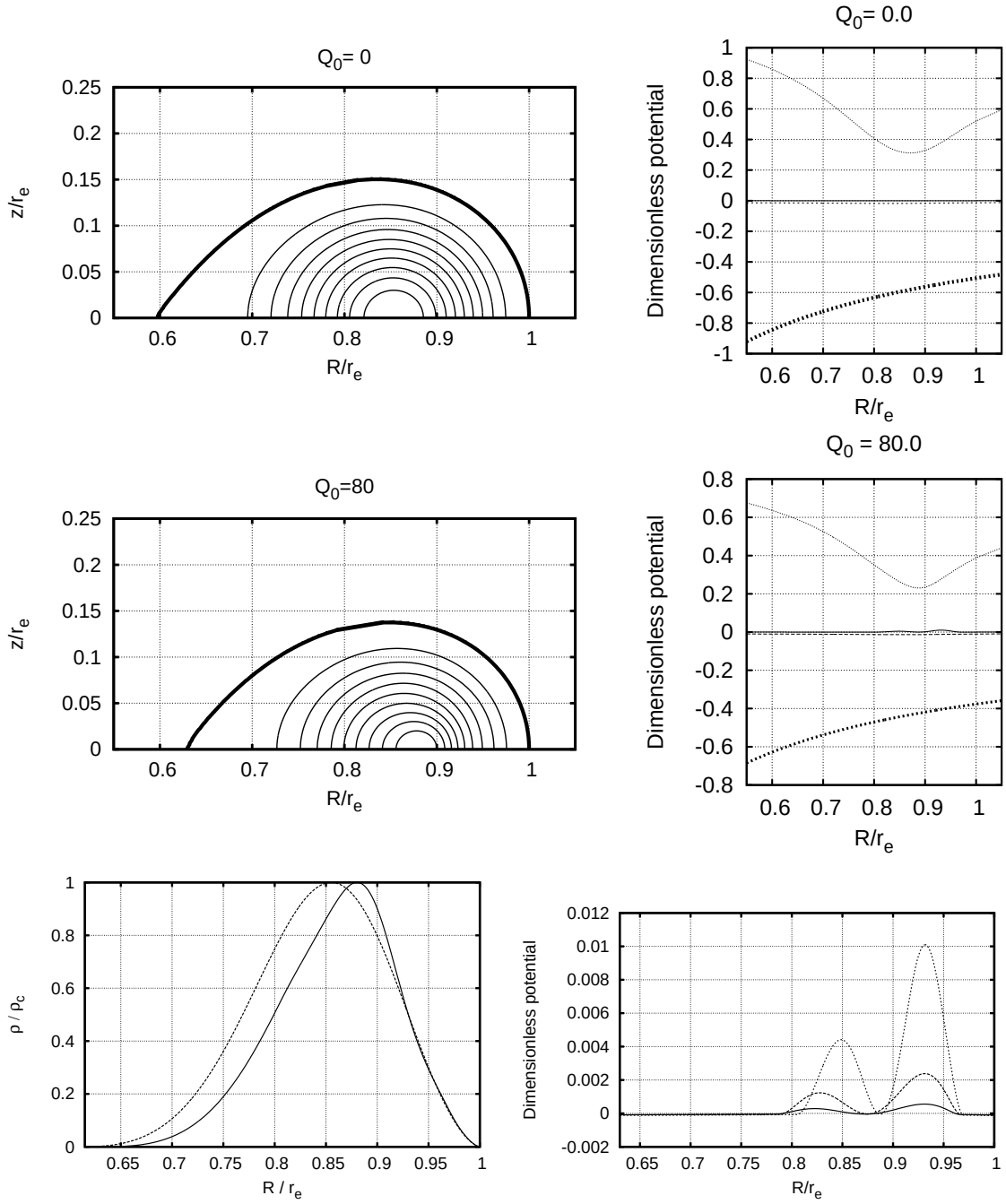

Figure 6.4: Top left and middle left panels: Density contours on the meridional cross section for the critical configurations with $\hat{Q}_0 = 0$ (top left) and $\hat{Q}_0 = 80$ (middle left). The heavy curves indicate the surfaces of the toroids. The density difference between two adjacent contours is one-tenth of the maximum density. Top right and middle right panels: $\frac{1}{2}|\hat{\boldsymbol{v}}^2| - \hat{R}\hat{v}_\varphi\hat{\Omega}$ (solid curve), $-\hat{M}_c/4\pi\hat{r}$ (thick dashed curve), $-\int \hat{\mu}\, d\hat{\Psi} - \hat{C}$ (dotted curve) for the critical configurations with $\hat{Q}_0 = 0$ (top right) and $\hat{Q}_0 = 80$ (middle right), given as functions of R/r_e. The horizontal axis ranges from $R_{inner}/r_e(= q_c)$ to $R_{outer}/r_e(= 1)$. Bottom left panel: Densities normalized by $\rho_{\max}$ on the equatorial plane for the critical configurations with $\hat{Q}_0 = 0$ (dashed curve) and $\hat{Q}_0 = 80$ (solid curve), given as functions of R/r_e. The horizontal axises range from $R_{inner}/r_e(= q_c)$ to $R_{outer}/r_e(= 1)$. Bottom right panel: The dimensionless velocity potential term, $\frac{1}{2}|\hat{\boldsymbol{v}}^2| - \hat{R}\boldsymbol{v}_\varphi\hat{\Omega}$, on the equatorial plane for the the critical configurations with $\hat{Q}_0 = 20$ (solid curve), $\hat{Q}_0 = 40$ (dashed curve) and $\hat{Q}_0 = 80$ (dotted curve), given as functions of R/r_e. The horizontal axis ranges from $R_{inner}/r_e(= q_c)$ to $R_{outer}/r_e(= 1)$. The model parameters are $m = 0$, $N = 1.5$, $\hat{\kappa}_0 = 0.5$, and $\hat{\Omega}_0^2 = 1.0 \times 10^{-5}$.

toroids with and without meridional flows. Fig. 6.4 shows the density contours on the meridional plane (top left and middle left) and the profiles of the potentials on the equator (top right and middle right). Bottom panels of Fig. 6.4 show the profiles of the density on the equator (left) and the velocity potential term, $\frac{1}{2}|\hat{\boldsymbol{v}}^2| - \hat{R}\hat{v}_\varphi\hat{\Omega}$, on the equator (right) as functions of R/r_e. In the top right panel of Fig. 6.4, each curve denotes $\frac{1}{2}|\hat{\boldsymbol{v}}^2| - \hat{R}\hat{v}_\varphi\hat{\Omega}$ (solid curve), $-\hat{M}_c/4\pi\hat{r}$ (thick dashed curve), $\hat{\phi}_g$ (thin dashed curve) and $-\int \hat{\mu}d\hat{\Psi} - \hat{C}$ (doted curve). As seen from these profiles, in both the models, the gravitational potentials of the toroid make a tiny contribution to the equilibrium solutions and the balance between the term $-\int \hat{\mu}d\hat{\Psi} - C$ and the gravitational potential of the central object mainly determines the stationary states of the toroid. Taking a detailed look at the middle right panel of Fig. 6.4, we observe that the potential terms due to the meridional flow and rotation (solid curve) show their maximum value near the radius of $R/r_e = 0.95$ for the $N = 1.5$ models with $\hat{Q}_0 = 80.0$. This very tiny protuberance is considered to appear due to the presence of the meridional flows because as shown in Table 6.2, the kinetic energy due to rotation is negligibly small. More detailed structures of the velocity potential terms can be seen by enlarging these tiny protuberances. The bottom right panel of Fig. 6.4 shows the profiles of $\frac{1}{2}|\hat{\boldsymbol{v}}^2| - \hat{R}\hat{v}_\varphi\hat{\Omega}$ on the equator for $N = 1.5$ polytopes with $\hat{Q}_0 = 20$ (solid curve), $\hat{Q}_0 = 40$ (dashed curve) and $\hat{Q}_0 = 80$ (dotted curve). These profiles have double peaks which locate at $\hat{R} \sim 0.85$ and $\hat{R} \sim 0.92$. These double peaks appear from the balance of the density distributions of the toroids and the meridional flows. As we have described in Sec. 6.1, the presence of the poloidal velocity fields results in reducing the density of toroids (see Eq. 6.7). For our numerical examples, the presence of the poloidal velocity fields decreases the density on the equatorial plane around radii of $\hat{R} \sim 0.85$ and $\hat{R} \sim 0.92$, which can be observed in the bottom two panels of Fig. 6.4 (more detailed considerations are given below).

The top left and middle left panels of Fig. 6.4 show the density distributions of $N = 1.5$ toroids with $\hat{Q}_0 = 0.0$ and $\hat{Q}_0 = 80$, respectively. Comparing the top left panel with the middle left panel, we see that the matter distribution of the toroid with $\hat{Q}_0 = 80$ is shifted outward slightly. The bottom left panel of Fig. 6.4 displays the density profiles on the equator for each toroid. The dotted and solid curves denote the density profiles for the models with $\hat{Q}_0 = 0.0$ and $\hat{Q}_0 = 80$, respectively. As seen form this panel, the meridional flows shift the place where the density takes its maximum value outward and make the density gradient around $\hat{R} \sim 0.92$ steeper. This is due to the double peak structure of the velocity potential profiles. The inner peak of this potential affects to decrease the density around $\hat{R} \sim 0.85$ where the density takes the maximum value if there is no meridional flow. On the other hand, the outer peak of this potential also leads to decrease in the density around $\hat{R} \sim 0.92$. Since the density decreases around $\hat{R} \sim 0.85$ and $\hat{R} \sim 0.92$ by the presence of the meridional flows, the place where the density becomes maximum moves outward and the density gradient becomes steeper if the toroids have rapid meridional flows ($\hat{Q}_0 = 80$ model). These effects result in decreasing the critical distances.

Next, we deal with the influence of the equation of state on the critical distance. As we have seen in Table 6.2, the critical distances of the $N = 3$ toroids are larger than those of the

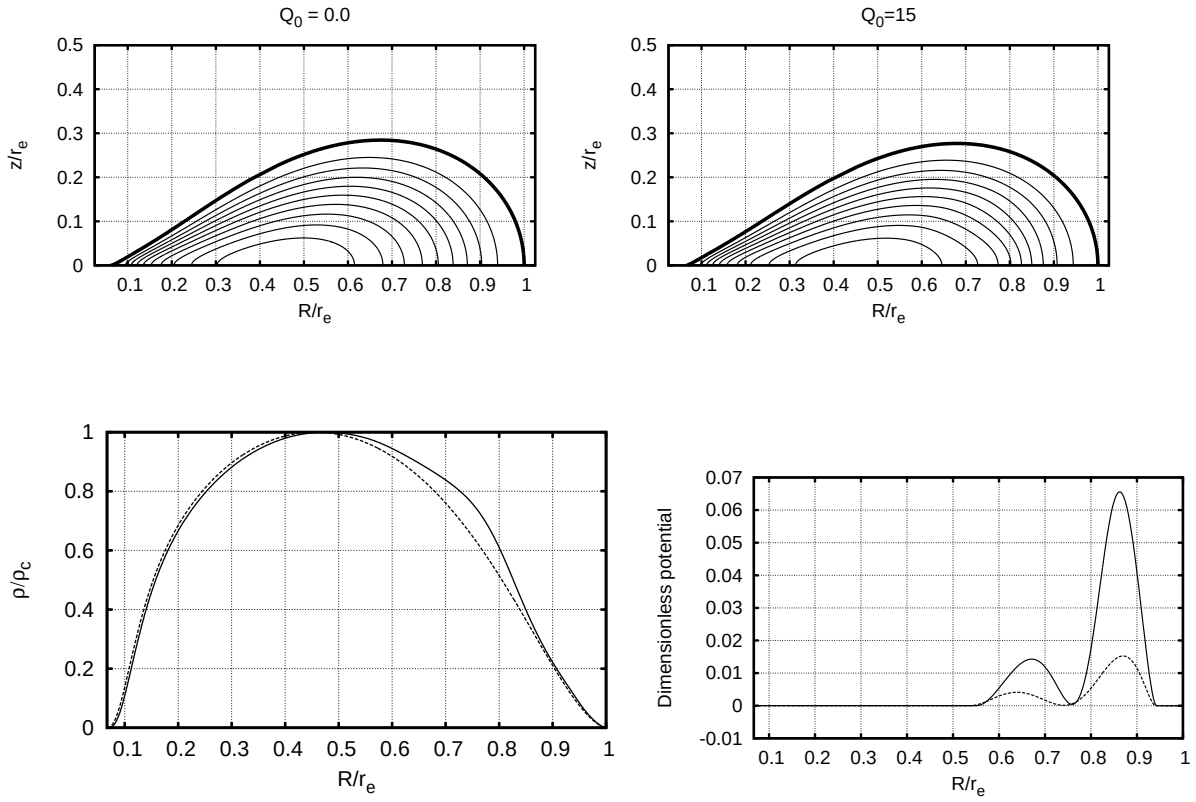

Figure 6.5: Top panels: The density contours on the meridional cross section for the critical configurations with $\hat{Q}_0 = 0.0$ (left panel) and $\hat{Q}_0 = 15$ (right panel). The heavy curves denote the surfaces of the toroids. The density difference between two adjacent contours is one-tenth of the maximum density. Bottom left panel: Densities normalized by $\rho_{\max}$ on the equatorial plane for critical configurations with $\hat{Q}_0 = 0$ (dashed curve) and $\hat{Q}_0 = 15$ (solid curve), given as functions of R/r_e. The horizontal axis ranges from $R_{inner}/r_e(= q_c)$ to $R_{outer}/r_e(= 1)$. Bottom right panel : The dimensionless velocity potential term, $\frac{1}{2}|\hat{\boldsymbol{v}}^2| - \hat{R}\hat{\boldsymbol{v}}_\varphi\hat{\Omega}$, on the equatorial plane for critical configurations with $\hat{Q}_0 = 10$ (dashed curve), $\hat{Q}_0 = 15$ (solid curve), given as functions of R/r_e. The horizontal axis ranges from $R_{inner}/r_e(= q_c)$ to $R_{outer}/r_e(= 1)$. The model parameters are $m = -1.4$, $N = 1.5$, $\hat{\kappa}_0 = 0.5$, and $\hat{\Omega}_0^2 = 1.0 \times 10^{-5}$.

$N = 1.5$ toroids. The same tendency in the equilibrium configurations without meridional flows found in Otani et al. (2009). This is because that the mass shedding from the inner edge of the toroids is more likely to occur for softer equations of state.

Effects of meridional flows on equilibrium configurations with highly localized poloidal magnetic fields

Finally, we unveil the effects of the meridional flows on structures of the toroid having highly localized poloidal magnetic fields. We consider the $N = 1.5$ toroid models only in this subsection because basic properties are independent of the equation of state. Fig. 6.5 displays typical models characterized by highly localized magnetic fields with and without strong meridional flows. Here, we take $m = -1.4$, with which highly localized poloidal magnetic fields are obtained inside the toroid as argued in Sec. 6.3. Other parameters are $\hat{\kappa}_0 = 0.5$, $\alpha = -0.5$, $d = 0.1$, and $\hat{\Omega}_0^2 = 1.0 \times 10^{-5}$, which are the same as those used in Sec. 6.3.2. The top two panels of Fig. 6.5 show the density distributions on the meridional cross section for the toroids

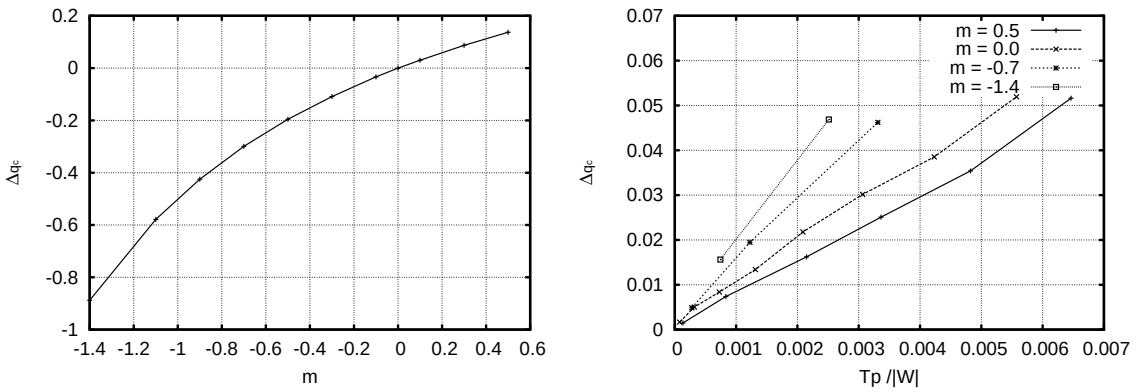

Figure 6.6: $\Delta_{q_c}(0, m, ; 0, 0)$ vs. m (left panel) and $\Delta_{q_c}(\hat{Q}_0, m, ; 0, m)$ vs. $T_p/|W|$ for the critical configurations with $m = 0.5,\ 0,\ -0.7,\ -1.4$ (right panel). Here, $\Delta_{q_c}(Q_1, m_1; Q_2, m_2) \equiv q_c(Q_1, m_1)/q_c(Q_2, m_2) - 1$ and $T_p/|W|$ is given as a function of $\hat{Q}_0$ for the sequence of the critical configurations.

with no meridional flow (left) and with strong meridional flows (right). The bottom two panels of Fig. 6.5 display the densities (left) and the velocity potential terms (right) on the equatorial plane as functions of R/r_e. In the bottom left (right) panel, the solid and dashed curves are correspond to the models with $\hat{Q}_0 = 15$ ($\hat{Q}_0 = 15$) and $\hat{Q}_0 = 0$ ($\hat{Q}_0 = 10$), respectively. Comparing the bottom two panels of Fig. 6.5 to those of Fig. 6.4, we observe that the density profiles of the $m = -1.4$ models are substantially different from those of the $m = 0$ models though behaviors of their velocity potential terms are similar in the sense that they show similar double peaks. The toroids with highly localized magnetic fields (the $m = -1.4$ models) are extended inward due to the strong gravity of the central object in comparison with the $m = 0$ models (Compare the bottom left panels of Figs. 6.4 and 6.5). As shown in the bottom left panel of Fig. 6.5, the positions of the maximum density rings for the $m = -1.4$ models are nearly independent of values of $\hat{Q}_0$, but the density gradient of the $\hat{Q}_0 = 15$ model is steeper than that of the $\hat{Q}_0 = 0$ model around $\hat{R} \sim 0.85$ because of the presence of the meridional flows. As a result, the matter distribution around $\hat{R} \sim 0.7$ is stretched outward. The presence of the meridional flows also decreases the critical distance slightly as shown in the bottom left panel of Fig. 6.5, which can be seen more clearly for the $m = 0$ models (see the bottom left panel of Fig. 6.4).

As we have exhibited in numerical examples so far, values of q_c decrease as values of m decrease, while they increase as values of $\hat{Q}_0 (> 0)$ increase. In other words, the poloidal magnetic fields generated by positive toroidal currents are apt to expand the toroids to the directions normal to the equi-flux function surfaces in particular when the magnetic fields are highly localized around the inner edge of the toroids and the meridional flows act as an agent for shrinking the region where the fluid matter occupies. In order to quantify the influence of the highly localized magnetic fields and the meridional flows on the critical distance, we introduce a quantity $\Delta_{q_c}(Q_1, m_1; Q_2, m_2)$, defined by

$$\Delta_{q_c}(Q_1, m_1; Q_2, m_2) \equiv \frac{q_c(Q_1, m_1)}{q_c(Q_2, m_2)} - 1\,, \tag{6.17}$$

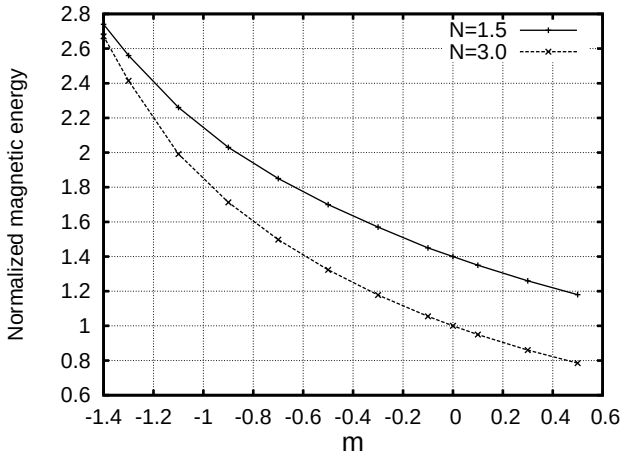

Figure 6.7: The magnetic energy normalized by the value of the equilibrium configuration with $m = 0.0$ and $N = 3$, given as functions of m. The solid and dashed curves correspond to the $N = 1.5$ and $N = 3$ polytropes, respectively.

where $q_c(Q_0, m_0)$ is the critical distance of the equilibrium sequence of the toroid characterized by $N = 1.5$, $M_t/M_c = 2.0 \times 10^{-2}$, $\hat{Q} = Q_0$, and $m = m_0$. Positive (Negative) values of Δ_{q_c} mean that the critical distance for the sequence with (Q_1, m_1) increases (decreases) or its width of the toroid decreases (increases) compared to that with (Q_2, m_2). In the left and right panels of the Fig. 6.6, $\Delta_{q_c}(0, m; 0, 0)$ is given as a function of m and $\Delta_{q_c}(\hat{Q}_0, m; 0., m)$'s are given as functions of $T_p/|W|$ for several fixed values of m, respectively. The left panel shows that the values of Δ_{q_c} range from about -0.9 to 0.2. Highly localized magnetic fields (for models with negative values of m) show the significant influence on the critical distances. On the other hand, the right panel shows that Δ_{q_c} can reach about 0.05 due to the effects of the meridional flows. Regardless of the sign of m, the values of $T_p/|W|$ range up to ~ 0.006 and the maximum value of Δ_{q_c} can reach 0.05 as the values of $\hat{Q}_0$ are changed. Thus, the maximum value of Δ_{q_c} would be 0.05 when the meridional flows exist. This means that the influence of the meridional flows on the critical distances is much smaller than that of the highly localized magnetic fields, but it is certainly true that the meridional flows work as an increasing factor for the critical distances. We also find that the effects of the poloidal magnetic fields and the meridional flows may nearly cancel out for the toroids characterized by $T_p/|W| \sim 0.005$ and $m = -0.2$. For this model, the critical distance or the width of the toroids is similar to that of the model with $T_p/|W| = 0$ and $m = 0$. As expected in Sec. 6.1.1, thus, we confirm that the oppositely working effects of the highly localized magnetic fields and the meridional flows result in nearly no change in the critical distance for some particular toroid model.

6.4 Discussion and concluding remarks

6.4.1 Strength of the magnetic fields inside the toroids

As shown in the middle left and bottom left panels of Fig. 6.2, for some particular set of the parameters, the toroids in the critical states have very strong magnetic fields and their strength are about 10^{15} G if we take $M_c = 5.0M_\odot$ and $\rho_{\rm max} = 1.0 \times 10^{11}{\rm g/cm^3}$. Fig. 6.7 shows the magnetic energy of the toroids as functions of m. Here, the magnetic energy is normalized by that of the $m = 0.0$ and $N = 3$ model. From this figure, it is found that the magnetic energy becomes larger as the value of m decreases. The magnetic energies of the $m = -1.4$ models are nearly three times larger than that of the $m = 0.0$ and $N = 3$ model. Therefore, we conclude that larger magnetic energy can be sustained in the toroids whose magnetic fields are highly localized around the inner edge of the toroids and which locate closer to the central compact object.

6.4.2 Critical distances for magnetized toroids with meridional flows and highly localized magnetic fields

Assuming the toroidal current function μ to be constant ($m = 0$), Otani et al. (2009) showed that there appears a critical distance in the self-gravitating toroids with the magnetic fields and that the critical distances are much larger than the radii of the inner-most stable circular orbit (ISCO) of the Schwarzschild black hole with the mass $M = M_c$. In this study, we show that their conclusions hold true when the meridional flows are taken into account and the functional form of μ is generalized to the cases of $m \geq 0$. For the cases of $m < 0$, however, we find that the critical distance can be much shorter than that of the $m = 0$ case. The radius of ISCO of the Schwarzschild black hole with the mass $M = M_c$, $r_{\rm ISCO}$, is given by

$$r_{\rm ISCO} = \frac{6GM_c}{c^2}\,. \tag{6.18}$$

If $M_c = 5.0M_\odot$, which is the fiducial value in this study, $r_{\rm ISCO} \sim 4.43 \times 10^6$cm. For the $N = 3$ models with $m = 0.0$ and $m = -1.4$, using results given in Table 6.1, we respectively obtain

$$r_{\rm in} = q \times r_e \sim 2.30 \times 10^7{\rm cm} > r_{\rm ISCO}\,, \tag{6.19}$$

and

$$r_{\rm in} = q \times r_e \sim 1.08 \times 10^6{\rm cm} \lessapprox r_{\rm ISCO}\,. \tag{6.20}$$

Therefore, the critical distance can be the same order or even smaller than the radius of the ISCO in this parameter space. Since this study is done within the framework of Newtonian gravity, the quantitative evaluation is not correct if $r_{\rm in} = O(r_{\rm ISCO})$, while the results given in the present study are reasonable as long as $r_{\rm in} \gg r_{\rm ISCO}$. We need to use general relativity for the toroids with $r_{\rm in} = O(r_{\rm ISCO})$. However, this is beyond the scope of the present study as

mentioned before.

6.4.3 Concluding remarks

In this chapter, we have investigated and calculated the stationary states of magnetized self-gravitating toroids with meridional flows and various kinds of the magnetic fields around central compact objects. As a result, we have obtained the toroids with strong meridional flows and with strong poloidal magnetic fields. Our findings and conjectures are summarized as follows.

1. Choosing the functional forms of arbitrary functions, we can change the strengths of the meridional flows. The critical distances for stationary toroids with meridional flows become larger than those for stationary toroids without meridional flows. In addition to this, the distances increase as the strengths of meridional flows becomes larger. This is what we have discussed in Sec. 6.1, i.e. the effects of the meridional flows and the magnetic fields are oppositely working.

2. Changing the value of the parameter m in the certain choice of the arbitrary function μ, we can change the distributions of the poloidal magnetic fields inside the toroids. In particular, the critical distances could be smaller as the value of m is decreased. If we adopt $M_c = 5.0 M_\odot$ and the maximum density of the toroid to be $\rho_{\rm max} = 1.0 \times 10^{11} {\rm g/cm}^3$, the critical distance for the $m = -1.4$ toroids becomes the same order as that of the ISCO of the Schwarzschild black hole with mass M_c. For such toroids, a general relativistic treatment is necessary for their correct description.

3. The magnetic energy for the critical configuration could increase as the value of m is decreased. The magnetic energy for the critical configuration with $m = -1.4$ is about three times larger than that for the $m = 0.5$ critical configuration.

4. By obtaining stationary configurations of axisymmetric magnetized self-gravitating polytropic toroid with meridional flows under the ideal MHD approximation, we have shown that the effects of the meridional flows would work oppositely to those of the poloidal magnetic fields. In other words, the oppositely working effects can be easily understood if we consider that the dense magnetic field lines expand the gaseous configurations due to the repulsive nature of the magnetic field lines and that the presence of the meridional flows works as lowering the gas pressure due to the appearance of the ram pressure as seen from the stationary condition equation.

Fere libenter homines id quod volunt credunt.
Men generally believe what they want to.
(Gaius Julius Caesar, The Gallic War)

7

Prolate stars due to meridional flows

Meridional flow changes the stellar shape as we have calculated in chapter 6. Following the magnetized equilibrium studies as we have seen in this thesis, we consider the meridional flow as poloidal velocity inside the star and evaluate the deformation by the meridional flow quantitatively.

7.1 Introduction

Stellar shapes have long been considered to be oblate (including a spherical shape) due to the effects of centrifugal and/or magnetic forces. However, recently Kuhn et al. (2012) have revealed that the shape of our Sun is 'perfectly round' against the common expectation of an oblate shape due to its rotation. At present, no clues have been proposed to solve this 'strange' problem (see e.g. Gough 2012).

Concerning stellar deformation, the effect of magnetic fields has been widely investigated (see e.g. Chandrasekhar & Fermi 1953; Ferraro 1954; Tomimura & Eriguchi 2005; Yoshida & Eriguchi 2006; Haskell et al. 2008; Yoshida et al. 2006; Lander & Jones 2009; and chapter 2).

The results found thus far are that purely poloidal magnetic fields make stars oblate, while purely toroidal magnetic fields lead stars to become prolate. Very recently, Ciolfi & Rezzolla (2013) succeeded in obtaining equilibrium states of magnetized stars with mixed poloidal-toroidal magnetic fields, even for configurations with very large toroidal magnetic fields. They showed that configurations with *strong toroidal* magnetic fields could be prolate. Thus, poloidal and toroidal magnetic fields act as increasing and decreasing mechanisms for the stellar oblateness, respectively.

However, we should point out that flows within stars might work as one deforming mechanism of stellar configurations as we have seen in chapter 6. In particular, the effect of meridional flows might make stellar shapes prolate, as shown in Eriguchi et al. (1986) and Birkl et al. (2011), although they did not describe their results quantitatively from the point of deformation due to meridional flows.

In this chapter, we deal analytically with meridional circulations of incompressible stars with *slow flow velocities* in order to show the deformation due to meridional flows quantitatively and clearly.

7.2 Problem and Solution

7.2.1 Stationary states of axisymmetric barotropic stars

Axisymmetric barotropic stars in *stationary states* need to satisfy the following condition:

$$\int \frac{dp}{\rho} = -\phi_g - \frac{1}{2}(v_r^2 + v_\theta^2) - \int \frac{\omega_\varphi}{\rho r \sin\theta} d\psi + \int R\Omega^2 dR + C \ . \tag{7.1}$$

Here ω_φ and ψ are φ-component of vorticity and the stream function defined in this chapter. We assume the density is a constant in order to find analytical solutions, i.e

$$\rho(r,\theta) = \rho_0(\text{constant}) \ . \tag{7.2}$$

We also assume the star has no wind external to itself, i.e

$$\rho(r,\theta) = 0(\text{outside}) \ . \tag{7.3}$$

The stream function in this chapter is defined by

$$v_r \equiv \frac{1}{r^2 \sin\theta \rho_0} \frac{\partial \psi}{\partial \theta} \ , \tag{7.4}$$

$$v_\theta \equiv -\frac{1}{r \sin\theta \rho_0} \frac{\partial \psi}{\partial r} \ , \tag{7.5}$$

and $\psi = 4\pi Q$, where Q is a stream function defined in chapter 6. It should be noted that in this expression the following situations must be taken into account in order to satisfy the integrability condition of the equations of motion:

$$\frac{\omega_\varphi}{\rho_0 R} = -\nu(\psi) \ , \tag{7.6}$$

$$\Omega = \Omega(R) \ , \tag{7.7}$$

where $\nu(\psi)$ is an arbitrary function of the stream function and the angular velocity Ω is an arbitrary function of R.

We need to note that our calculations should be used either for purely rotating stars or for stars with purely circulating flows within meridional planes. The reason for this is that we have not taken into account the φ-component of the equation of motion, i.e.

$$\boldsymbol{v} \cdot \nabla(R\Omega) = 0 \ . \tag{7.8}$$

As is explained in Eriguchi et al. (1986), for non-singular angular velocity distributions, this condition results in two situations: (i) purely rotating stars, i.e. $v_r = 0$ and $v_\theta = 0$, or (ii) configurations with constant angular momentum throughout the whole star, i.e. Ω needs to vanish to avoid singular behavior of the angular velocity on the rotation axis. Thus our solutions in this chapter need to be used for either rotating stars without meridional flows or for non-rotating stars with meridional flows.

The stream function must satisfy the following equation:

$$\frac{\partial^2 \psi}{\partial r^2} + \frac{\sin\theta}{r^2}\frac{\partial}{\partial \theta}\left(\frac{1}{\sin\theta}\frac{\partial \psi}{\partial \theta}\right) = -r\sin\theta\rho_0\omega_\varphi \ , \tag{7.9}$$

This equation is similar to Eq. (2.23) in chapter 2, Eq. (3.2) in chapter 3, Eq. (5.2) and Eq. (6.9) in chapter 6, but we solve this equation for stream function ψ in this chapter.

The distributions of the density, pressure and stream function can be obtained from the above stationary condition and the equation for the stream function, once the forms of arbitrary functions $\nu(\psi)$ and $\Omega(R)$ and the barotropic relation between the density and the pressure are specified.

The boundary conditions for the gravitational potential and the stream function are as follows: (i) the gravitational potential behaves as $1/r$ at infinity and the steam function is constant along the (unknown) stellar surface. Considering these boundary conditions, the gravitational potential and the stream function can be expressed by the integral forms as

$$\phi_g(r,\theta) = -4\pi G \sum_{n=0}^{\infty} P_{2n}(\cos\theta) \int_0^{\pi/2} d\theta' \sin\theta P_{2n}(\cos\theta') \int_0^{r_s(\theta')} dr' r'^2 f_{2n}(r,r')\rho_0 \ , \tag{7.10}$$

$$\begin{aligned} \psi(r,\theta) &= r\sin\theta \sum_{n=1}^{\infty} \frac{P^1_{2n-1}(\cos\theta)}{2n(2n-1)} \int_0^{\pi/2} d\theta' \sin\theta' P^1_{2n-1}(\cos\theta') \int_0^{r_s(\theta')} dr' r'^2 f_{2n-1}(r,r') \\ &\times \rho_0\omega_\varphi(r',\theta') + r\sin\theta \sum_{n=1}^{\infty} \alpha_{2n-1} P^1_{2n-1}(\cos\theta) r^{2n-1} \ , \end{aligned} \tag{7.11}$$

where P_n is the Legendre function and $r_s(\theta)$ expresses the shape of the deformed surface of the star,

$$f_n(r,r') = \begin{cases} r'^n/r^{n+1}, & (r \geq r'), \\ r^n/r'^{n+1}, & (r \leq r'). \end{cases} \tag{7.12}$$

and α_n are coefficients. Since we have assumed that there is no external wind, the r component

of the velocity (v_r) must vanish at the surface. Therefore, the boundary condition for the stream function on the surface is as follows:

$$\psi(r_s, \theta) = 0. \tag{7.13}$$

We fix the coefficients to fulfill this boundary condition (Eriguchi et al. 1986; chapter 3).

7.2.2 Stationary configurations of incompressible fluids with very slow flow velocities

In order to find analytical solutions to the basic equations described above, we further assume the following situation. (i) The form of the arbitrary function $\nu(\psi)$ is specified as follows:

$$\nu(\psi) = \varepsilon\nu_0(\text{constant}) \ . \tag{7.14}$$

(ii) The rotational velocity is a constant, i.e.,

$$\Omega = \varepsilon\Omega_0(\text{constant}) \ , \tag{7.15}$$

where ε is a small constant that expresses the slow fluid velocities in both the meridional plane and the φ-direction.

For an incompressible body, we need only to solve for the surface shape by setting $p = 0$ on the surface, instead of solving for the density distribution. Thus, the solutions for our problem can be studied by expanding the quantities with respect to the small quantity ε, as

$$r_s(\theta) = \sum_{n=0}^{\infty} \varepsilon^{2n} r_s^{(2n)}(\theta) \ , \tag{7.16}$$

$$\psi(r, \theta) = \sum_{n=0}^{\infty} \varepsilon^{n} \psi^{(n)}(r, \theta) \ , \tag{7.17}$$

where $r_s^{(2n)}$ and $\psi^{(n)}$ are corresponding quantities of the surface shape and the stream function, respectively. Other physical quantities are also expanded, as

$$F(r, \theta) = \sum_{n=0}^{\infty} \varepsilon^{n} F^{(n)}(r, \theta) \ , \tag{7.18}$$

where $F(r, \theta)$ expresses a certain physical quantity.

For simplicity, we choose the spherical configurations without flows as the $n = 0$ terms, i.e.

$$r_s^{(0)}(\theta) = r_0(\text{constant}) \ , \tag{7.19}$$

$$\psi^{(0)}(r, \theta) = 0 \ , \tag{7.20}$$

$$\frac{dp^{(0)}(r,\theta)}{dr} = -\rho_0 \frac{d\phi_g^{(0)}}{dr} \ . \tag{7.21}$$

The stationary equations are written to the second lowest order with respect to the small quantity ε as follows:

$$\begin{aligned} \frac{p^{(0)}}{\rho_0} + \frac{\varepsilon^2 p^{(2)}}{\rho_0} =& -\phi_g^{(0)}(r) + C^{(0)} \\ & +\varepsilon^2 \left[-\phi_g^{(2)}(r,\theta) - \frac{1}{2}(v_r^{(1)2}(r,\theta) + v_\theta^{(1)2}(r,\theta)) \right. \\ & \left. + \nu_0 \psi^{(1)}(r,\theta) + \frac{1}{2} r^2 \sin^2\theta \Omega_0^2 + C^{(2)} \right] \ , \end{aligned} \tag{7.22}$$

where

$$\varepsilon\psi^{(1)}(r,\theta) = -\frac{1}{30}\varepsilon\rho_0^2\nu_0 r^2(5r_0^2 - 3r^2)\sin^2\theta + r_0 \sin\theta \varepsilon \sum_{n=1}^{\infty} \alpha_{2n-1}^{(1)} P_{2n-1}^1(\cos\theta) r^{2n-1} \ . \tag{7.23}$$

When we apply the boundary condition to the above stationary equation on a *deformed surface*, i.e.

$$p^{(0)}(r_0) + \varepsilon^2 \frac{dp^{(0)}(r)}{dr}|_{r=r_0} r_s^{(2)}(\theta) + \varepsilon^2 p^{(2)}(r_0,\theta) = 0 \ , \tag{7.24}$$

we obtain

$$\begin{aligned} 0 &= -\phi_g^{(0)}(r_0) - \varepsilon^2 \frac{d\phi_g^{(0)}(r)}{dr}|_{r=r_0} r_s^{(2)}(\theta) + C^{(0)} \\ &+ \varepsilon^2 \left[-\phi_g^{(2)}(r_0,\theta) - \frac{1}{2}(v_r^{(1)2}(r_0,\theta) + v_\theta^{(1)2}(r_0,\theta)) \right. \\ &+ \left. \nu_0 \psi^{(1)}(r_0,\theta) + \frac{1}{2} r_0^2 \sin^2\theta \Omega_0^2 + C^{(2)} \right] \ . \end{aligned} \tag{7.25}$$

Here

$$\phi_g^{(0)}(r) = \frac{2\pi G}{3}\rho_0 r^2 - 2\pi G \rho_0 r_0^2 \ , \tag{7.26}$$

$$\psi^{(0)}(r,\theta) = r\sin\theta \sum_{n=1}^{\infty} \alpha_{2n-1}^{(0)} P_{2n-1}^1(\cos\theta) r^{2n-1} = 0 \ , \tag{7.27}$$

$$\psi^{(1)}(r,\theta) = -\frac{1}{30}\rho_0^2\nu_0 r^2(-3r^2 + 5r_0^2)\sin^2\theta + r\sin\theta \sum_{n=1}^{\infty} \alpha_{2n-1}^{(1)} P_{2n-1}^1(\cos\theta) r^{2n-1} \ . \tag{7.28}$$

Since this quantity $\psi^{(1)}$ is the first order term with respect to ε, we only need to consider the

boundary condition for the stream function on the *undeformed surface*. Thus,

$$\psi^{(1)}(r,\theta) = \frac{1}{10}\rho_0^2\nu_0 \sin^2\theta r^2(r^2 - r_0^2) \,, \tag{7.29}$$

$$v_r(r,\theta) = \frac{1}{5}\rho_0\nu_0(r^2 - r_0^2)\cos\theta \,, \tag{7.30}$$

$$v_\theta(r,\theta) = -\frac{1}{5}\rho_0\nu_0(2r^2 - r_0^2)\sin\theta \,. \tag{7.31}$$

can be obtained. These can be expressed by using $\alpha_{2n-1}^{(k)}$ as follows:

$$\begin{aligned} \alpha_{2n-1}^{(0)} &= 0 \,, \\ \alpha_1^{(1)} &= \frac{1}{15}\rho_0^2\nu_0 r_0^2 \,, \\ \alpha_{2n+1}^{(1)} &= 0 \,, \end{aligned} \tag{7.32}$$

where $n = 1, 2, \ldots$.

From the second order terms with respect to ε, the following condition can be derived:

$$\begin{aligned} 0 = -\frac{4\pi G}{3}\rho_0 r_0 r_s^{(2)}(\theta) \; &+ 4\pi G\rho_0 r_0 \sum_{n=0}^{\infty} P_{2n}(\cos\theta) \int_0^{\pi/2} d\theta' \sin\theta' P_{2n}(\cos\theta') r_s^{(2)}(\theta') \\ &- \frac{1}{2}v_\theta^{(1)2}(r_0,\theta) + \frac{1}{2}r_0^2\sin^2\theta\Omega_0^2 + C^{(2)} \,. \end{aligned} \tag{7.33}$$

By expanding the quantity $r_s^{(2)}(\theta)$ as follows:

$$r_s^{(2)}(\theta) = \sum_{n=0}^{\infty} \beta_{2n}^{(2)} P_{2n}(\cos\theta) \,, \tag{7.34}$$

where $\beta_{2n}^{(2)}$ are certain constants, we obtain the following results for unknown quantities:

$$C^{(0)} = -\frac{4\pi G\rho_0}{3}r_0^2 \,, \tag{7.35}$$

$$C^{(2)} = -\frac{8\pi G\rho_0}{3}r_0\beta_0^{(2)} + \frac{1}{75}\rho_0^2\nu_0^2 r_0^4 - \frac{1}{3}r_0^2\Omega_0^2 \,, \tag{7.36}$$

$$\beta_2^{(2)} = \frac{1}{8\pi G}\left[\frac{1}{5}\rho_0\nu_0^2 r_0^3 - \frac{5}{\rho_0}r_0\Omega_0^2\right] \,, \tag{7.37}$$

$$\beta_{2n}^{(2)} = 0 \; (n = 2, 3, \ldots) \,. \tag{7.38}$$

Here if we require some condition for the scale of the star, we can calculate the value of $\beta_0^{(2)}$

and complete solutions for our problem to the second order in ε can be obtained.

7.2.3 Rotation vs circulation

From the analysis in the previous subsection, the change of the surface due to circulation and/or the rotation can be expressed to second order of a certain small quantity ε as follows:

$$r_s(\theta) = r_0 + \varepsilon^2 \left[\beta_0 + \frac{1}{8\pi G} \left(\frac{1}{5}\rho_0 \nu_0^2 r_0^3 - \frac{5}{\rho_0} r_0 \Omega_0^2 \right) P_2(\cos\theta) \right] . \tag{7.39}$$

From this equation

$$\frac{r_{\rm equator} - r_{\rm pole}}{r_0} = -\frac{3}{16\pi G} \left(\frac{1}{5}\rho_0 \nu_0^2 r_0^2 - \frac{5}{\rho_0}\Omega_0^2 \right) , \tag{7.40}$$

where $r_{\rm pole}$ and $r_{\rm equator}$ are the polar and equatorial radii, respectively. As is easily seen, uniformly *rotating* configurations without circulation ($\Omega_0 \neq 0, \nu_0 = 0$) become *oblate*, while non-rotating configurations with *circulation* ($\Omega_0 = 0, \nu_0 \neq 0$) are *prolate*. In other words, the presence of meridional flows acts as an *effective force* perpendicular to the equatorial plane.

This can be clearly seen by defining the effective force due to meridional flows with $\Omega_0 = 0$ as

$$\boldsymbol{F} \equiv -\frac{\rho_0}{2}\nabla|v_r^2 + v_\theta^2| + \rho_0(\boldsymbol{v} \times \boldsymbol{\omega}) , \tag{7.41}$$

The r and θ components of this force for our incompressible configurations with $\Omega_0 = 0$ are

$$F_r = \frac{\nu_0^2 \rho_0^3}{50} \left\{ (-4r^3 + 4r_0^2 r) + (8r^3 - 6r_0^2 r)\sin^2\theta \right\} , \tag{7.42}$$

$$F_\theta = \frac{\nu_0 \rho_0^3}{50} \left\{ (4r^3 - 6r_0^2 r)\sin\theta\cos\theta \right\} . \tag{7.43}$$

They are shown in the central panel of Fig. 7.1. In this figure, the centrifugal force due to uniformly rotating configurations, i.e. $R\Omega_0^2$, is also shown in the right panel.

In order to estimate deformation by meridional flows quantitatively, we define the deformation ratio Λ as

$$\Lambda \equiv \left| \frac{r_{\rm c.equator} - r_{\rm c.pole}}{r_{\rm r.equator} - r_{\rm r.pole}} \right| , \tag{7.44}$$

where subscripts 'c' and 'r' denote configurations with meridional circulation and with rotation, respectively. For incompressible fluids with *very slow flow velocities*,

$$\begin{aligned} \Lambda &= \frac{1}{25}\frac{r_s^2 \nu_0^2 \rho_0^2}{\Omega_0^2} \\ &= \frac{v_p^2(r_s\pi/2)}{r_s^2\Omega_0^2} , \end{aligned} \tag{7.45}$$

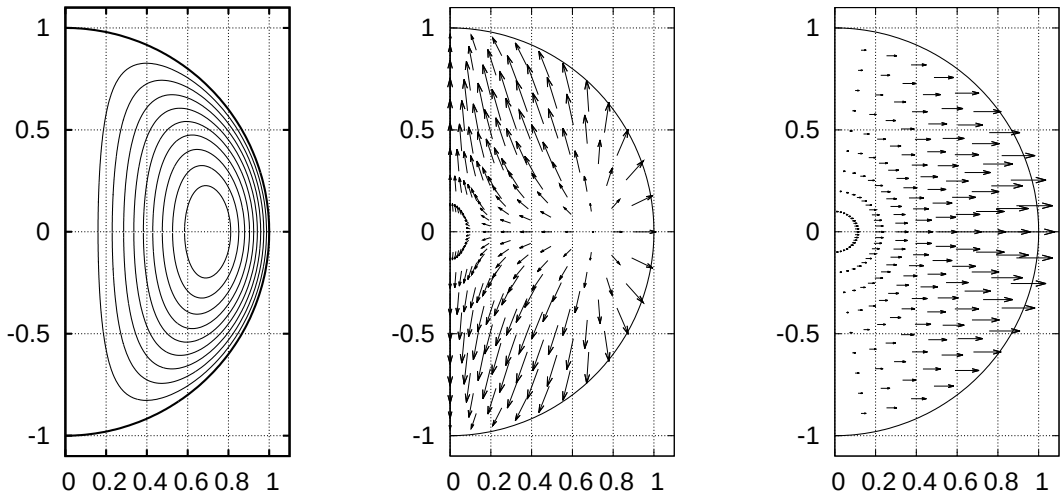

Figure 7.1: Left: contours of $\psi^{(1)}(r.\theta)$ in Eq. (7.29). The difference between two adjacent contours with lines is 1/10 of the maximum value of $\psi^{(1)}(r,\theta)$. The outermost curve denotes the stellar surface. Centre: the force due to the meridional flows (Eq. 7.42 and Eq. 7.43). Right: the centrifugal force of uniform rotation.

where v_p is the poloidal velocity, defined as $v_p^2 = v_r^2 + v_\theta^2$. Therefore, the stellar deformation depends on the ratio of the meridional velocity to the rotational velocity at the equatorial surface. When we use the solar radius and rotational velocity, for example,

$$\Lambda \sim 1.0 \left(\frac{v_p}{1.81 \times 10^5 \mathrm{cm/s}} \right)^2 \left(\frac{r_0}{6.96 \times 10^{10} \mathrm{cm}} \right)^{-2} \left(\frac{\Omega_0}{2\pi/28.0 \mathrm{day}} \right)^{-2} . \tag{7.46}$$

The *commonly believed* solar convective flow or meridional flow velocities (e.g. Miesch 2005; Nordlund et al. 2009) are a few tens or a hundred times smaller than the meridional flow velocity chosen here, but those values are not too small to be neglected. Thus, this simple model shows that the meridional flows have small but non-zero influence on stellar deformation comparing with stellar rotation, which is considered as the most powerful deformation mechanism within stars.

7.3 Discussion and conclusion

In this chapter, we have obtained the expression for stellar deformation due to meridional flows analytically. In order to treat the problem analytically, we have assumed stationary incompressible stars and imposed a $\psi = 0$ boundary condition on stellar surfaces.

We have shown that meridional flows make stars prolate under the conditions of our model. This might imply that meridional flows within stars work to decrease the oblateness of rotating stars. Although we have assumed incompressible fluids, the role of meridional flows would not disappear for compressible stars. As explained in the Introduction, according to the recent very accurate observation by Kuhn et al. (2012), the solar oblateness is unexpectedly smaller than the theoretical value, which is derived by considering only rotation (Armstrong & Kuhn 1999). Gough (2012) argued that magnetic fields and/or stresses due to turbulence could be possible

mechanisms causing the small oblateness. However, they did not consider the influence of meridional flows, which could be one of the possible mechanisms, as we have shown in this chapter.

One might argue that the velocities of solar meridional flows are believed to be much smaller than the values required to reduce the rotational effect, as seen from Eq. (7.46). This belief has been based on theoretical analysis of many observational data on *surface* phenomena (Zhao et al. 2012). On the other hand, we can rely on the theories that are used to 'estimate' physical quantities within the solar interior. One approach for us is to take even the 'curious' observational data seriously and to consider possible mechanisms thoroughly, even though those mechanism might seem to be far from the *widely believed* theories and/or values. The 'perfectly round' Sun might be offering us an important hint about its interior.

In the end, it is impossible not to become what others believe you are.
(Gaius Julius Caesar)

8

Conclusions and Remarks

Throughout this work, we have considered and calculated a number of different aspects of equilibrium states with magnetic fields and meridional flows in many astrophysical objects, neutron star, white dwarf, magnater, magnetosphere around the magnetar, compact toroid, and the Sun. Although these studies seem to belong to different category each other, these phenomena are very closely linked in many respects.

We have obtained magnetized equilibrium states with extremely strong but highly localized poloidal magnetic fields in chapter 2. We have changed the functional from of the arbitrary function μ which represents the non force-free current density in order to obtain such a configuration. When we apply these models to magnetars, the interior poloidal magnetic field strength near the central region would be 10^{17}G while the surface magnetic field strength is 10^{14-15}G. If we apply these models to magnetized white dwarfs with mass $\sim 1.34M_{\odot}$, the strength of the surface field would be 10^{9} G and the magnetic fields near the central region would reach 10^{12}G. If the star has such extreme strong but localized poloidal magnetic field deep inside, the contributions from higher order magnetic multipole moments to the outer fields around the star cannot be neglected. The toroidal magnetic field energy in these solutions, however, is much weaker than poloidal magnetic field energy.

We have investigated the boundary value problems for the axisymmetric stationary magnetic fields using the integral form of solution and homogeneous terms in 3. These homogeneous terms come from the surface current (current sheets) for the magnetic fields or the surface vorticity (vorticity sheets) for yjr meridional flows at the boundaries. The homogeneous terms appear as integral forms of general boundary conditions as we have seen in chapter 3. We can impose the arbitrary boundary conditions of stationary magnetic fields and meridional flows using the homogeneous terms. We have found the importance of the coexistence of the oppo-

site flowing toroidal current density to the larger toroidal magnetic fields with surface current adding the homogeneous terms in chapter 3. The oppositely flowing toroidal current density cancel out the force-free toroidal current density which is related to toroidal magnetic fields. As a result, the oppositely flowing toroidal current density can sustain the large toroidal magnetic fields.

The physical meaning of the oppositely flowing toroidal current density has been discussed in chapter 4. Using simple analytical solutions, we have found the large toroidal magnetic field is deeply re;ated to the prolate stellar deformation by the oppositely flowing non force-free toroidal current densities. We have found a sufficient condition expressed by the combination of the arbitrary function μ and the flux function. The condition is required for large toroidal magnetic field models and prolate stellar shape. This is the physical meaning of the oppositely flowing toroidal current density.

We have investigated magnetic fields configurations of magnetar throughout its interior and exterior - core, crust and magnetosphere in chapter 5. We have calculated many crustal magnetic field configurations in Hall equilibrium under various boundary conditions. These numerical results imply that the Hall drift of the secular Hall MHD evolution would be affected by both inner and outer boundary conditions. On the other hand, the magnetosphere around the star forms the magnetic X-point geometry when the magnetospheric toroidal current density is sufficiently large or the stellar total current is sufficiently small. The magnetic X-point geometry can be produced by the stellar interior physical event between core and crust such as glitch or magnetic fields changing. The X-point geometry causes the magnetic reconnection which would be an origin of the giant flare of magnetar.

We have investigated the most general formulation of magnetized equilibrium states in stationary and axisymetric barotropes. We have calculated magnetized toroid with meridional flow and found the meridional flow changes the equilibrium structures effectively in chapter 6. We have shown that the effects of the meridional flows would work oppositely to those of the poloidal magnetic fields. In other words, the oppositely working effects can be easily understood if we consider that the dense magnetic field lines expand the gaseous configurations due to the repulsive nature of the magnetic field lines and that the presence of the meridional flows works as lowering the gas pressure due to the appearance of the ram pressure as seen from the stationary condition equation. This idea is very important for the stellar deformation with circulation.

We have considered the stellar deformation by meridional flows in chapter 7. We have evaluated the deformation by meridional flows analytically using similar methods we have used in chapters 3 and 4. Our results have showed that the circulations inside the Sun would have influence on the deformation comparing to the rotation quantitatively. This means that the 'perfectly round' Sun might be offering us an important hint about its interior.

This thesis shows that these astrophysical phenomena are very closely linked. We can solve one problem easily using a method which has been investigated for another problem. We understand these problems deeply using the simple models and formulations carefully. As we

have seen in this thesis, the object orientated approach is not sufficient for different problems in astrophysics, because we generally believe what we want to. We should employ many different points of views and see problems from new directions different from prebious works in order to understand them deeply and essentially and get new and wide insights about the problems.

Veni, vidi,vici.
I came, I saw, I conquered.
(Gaius Julius Caesar, oral declaration)

Acknowledgements

I would like to thank everyone who helped to get me here!

Above all, I would like to thank my supervisor, Yoshiharu Eriguchi for warm and kind encouragement.

I would like to thank Keisuke Taniguchi, Shin'ichirou Yoshida, Rohta Takahashi, Shijun Yoshida, Shota Kisaka and Koji Uryu for their discussions and useful comments.

I would like to thank the members of the Plasma physics seminar at NAOJ for their very interesting discussion on Friday evening. I would like to thank Yukio Isozaki and Keiko Hisaga for very interesting ordinary conversation. I give a special thanks to my colleagues in 823 and 824.

Finally, I would like to express my gratitude to my family for their support and warm encouragements.

The greatest enemy will hide in the last place you would ever look.
(Gaius Julius Caesar)

A

Details of formulations and equations

A.1 Derivations of equations

A.1.1 Flux function based formulation: Current density formula

Here, we derive the first integral of equations of motions. The basic equations are as follows: The continuity equation of a fluid:

$$\nabla \cdot (\rho \boldsymbol{v}) = 0. \tag{A.1}$$

The equations of motions:

$$\frac{1}{\rho}\nabla p = -\nabla \phi_g - \frac{1}{2}\nabla |\boldsymbol{v}|^2 + \boldsymbol{v} \times \boldsymbol{\omega} + \frac{1}{\rho}\left(\frac{\boldsymbol{j}}{c} \times \boldsymbol{B}\right). \tag{A.2}$$

The Poisson equation for the gravitational potential:

$$\Delta \phi_g = 4\pi G \rho. \tag{A.3}$$

Gauss's law for magnetic field:

$$\nabla \cdot \boldsymbol{B} = 0. \tag{A.4}$$

Maxwell-Faraday equation:

$$\nabla \times \boldsymbol{E} = 0. \tag{A.5}$$

Ampére's law:

$$\nabla \times \boldsymbol{B} = 4\pi \frac{\boldsymbol{j}}{c}, \tag{A.6}$$

Ideal MHD condition:

$$\boldsymbol{E} + \frac{\boldsymbol{v}}{c} \times \boldsymbol{B} = 0. \tag{A.7}$$

At first, we define the stream function Q and the flux function Ψ using the continuity equation(A.1) and Gauss's law, Eq. (A.4) as below:

$$v_R \equiv -\frac{1}{4\pi\rho R}\frac{\partial Q}{\partial z}, v_z \equiv \frac{1}{4\pi\rho R}\frac{\partial Q}{\partial R} \tag{A.8}$$

$$B_R \equiv -\frac{1}{R}\frac{\partial \Psi}{\partial z}, \quad B_z \equiv \frac{1}{R}\frac{\partial \Psi}{\partial R}. \tag{A.9}$$

Using the ideal MHD condition, Eq. (A.7), and the Maxwell-Fraraday equation, Eq. (A.5), and Gauss's law, Eq. (A.4), we obtain

$$\begin{aligned} &\nabla \times \boldsymbol{E} = -\nabla \times \left(\frac{\boldsymbol{v}}{c} \times \boldsymbol{B}\right) = 0 \\ \Rightarrow \quad &\frac{\partial}{\partial z} E_\varphi \boldsymbol{e}_R - \left(\frac{\partial E_R}{\partial z} - \frac{\partial E_z}{\partial R}\right)\boldsymbol{e}_\varphi - \frac{1}{R}(RE_\varphi)\boldsymbol{e}_z = 0. \end{aligned} \tag{A.10}$$

Using $E_\varphi = 0$ and the ideal MHD condition, we have a relation as

$$-E_\varphi = \left\{\frac{\boldsymbol{v}}{c} \times \boldsymbol{B}\right\}_\varphi = \frac{v_z}{c}B_R - \frac{v_R}{c}B_z = 0. \tag{A.11}$$

Substituting this equation into Eq. (A.8), we obtain

$$\begin{aligned} \frac{1}{\rho R}\frac{\partial Q}{\partial R}\frac{1}{R}\frac{\partial \Psi}{\partial z} - \frac{1}{\rho R}\frac{\partial Q}{\partial z}\frac{1}{R}\frac{\partial \Psi}{\partial R} &= 0 \\ \Rightarrow \frac{\partial Q}{\partial z}\frac{\partial \Psi}{\partial R} - \frac{\partial \Psi}{\partial z}\frac{\partial Q}{\partial R} &= 0. \end{aligned} \tag{A.12}$$

Then, the stream function Q is a function of Ψ only

$$Q = Q(\Psi). \tag{A.13}$$

This relation means that the directions of magnetic field and velocity are the same. In other words, the magnetic field is froze in the fluid. From Ampére's law (A.6), we express the electric current density by the magnetic field,

$$\frac{\boldsymbol{j}}{c} = \frac{1}{4\pi}\nabla \times \boldsymbol{B} = -\frac{1}{4\pi}\frac{\partial B_\varphi}{\partial z}\boldsymbol{e}_R + \frac{1}{4\pi}\left(\frac{\partial B_R}{\partial z} - \frac{\partial B_z}{\partial R}\right)\boldsymbol{e}_\varphi + \frac{1}{4\pi}\frac{1}{R}\frac{\partial}{\partial R}(RB_\varphi)\boldsymbol{e}_z, \tag{A.14}$$

For vorticity $\boldsymbol{\omega}$ we have

$$\boldsymbol{\omega} = \nabla \times \boldsymbol{v} = -\frac{\partial v_\varphi}{\partial z}\boldsymbol{e}_R + \left(\frac{\partial v_R}{\partial z} - \frac{\partial v_z}{\partial R}\right) + \frac{1}{R}\frac{\partial}{\partial R}(Rv_\varphi)\boldsymbol{e}_z. \tag{A.15}$$

Since we have assumed axisymmetry, the φ component of Eq. (A.2) is

$$(v_z\omega_R - v_R\omega_z) + \frac{1}{\rho}(j_z B_R - j_R B_z) = 0. \tag{A.16}$$

Substituting Eqs. (A.14) and (A.15) into this equation, we have

$$-v_z\frac{\partial v_\varphi}{\partial z} - v_R\frac{1}{R}\frac{\partial}{\partial R}(Rv_\varphi) + \frac{1}{\rho}B_R\frac{1}{4\pi}\frac{1}{R}\frac{\partial}{\partial R}(RB_\varphi) - \frac{1}{\rho}B_z\left(-\frac{1}{4\pi}\frac{\partial B_\varphi}{\partial z}\right) = 0. \tag{A.17}$$

Using Eqs. (A.1.1) and (A.13), this equation is written as,

$$\frac{\partial\Psi}{\partial R}\frac{\partial}{\partial z}(RB_\varphi - Q'Rv_\varphi) - \frac{\partial\Psi}{\partial z}\frac{\partial}{\partial R}(RB_\varphi - Q'Rv_\varphi) = 0, \tag{A.18}$$

where we multiply ρR^2 to Eq. (A.17). Defining

$$\kappa \equiv RB_\varphi - Q'Rv_\varphi, \tag{A.19}$$

we obtain

$$\kappa = \kappa(\Psi), \tag{A.20}$$

from Eq. (A.18). The function κ is an arbitrary function of Ψ and means the conservation of the angular momentum along the Ψ.

From Eqs. (A.5) and (A.7), we have

$$(\nabla \times \boldsymbol{E})_\varphi = 0 \Rightarrow \frac{\partial E_R}{\partial z} - \frac{\partial E_z}{\partial R} = 0.$$

$$\Rightarrow \frac{\partial}{\partial z}\left(-\frac{1}{R}\frac{\partial\Psi}{\partial R}v_\varphi + \frac{Q'}{4\pi\rho R}\frac{\partial\Psi}{\partial R}B_\varphi\right) - \frac{\partial}{\partial R}\left(-\frac{1}{R}\frac{\partial\Psi}{\partial z}v_\varphi + \frac{Q'}{4\pi\rho R}\frac{\partial\Psi}{\partial z}B_\varphi\right) = 0. \tag{A.21}$$

Then, we obtain a relation,

$$\frac{\partial\Psi}{\partial R}\frac{\partial}{\partial z}\left(-\frac{1}{R}v_\varphi + \frac{Q'}{4\pi\rho R}B_\varphi\right) - \frac{\partial\Psi}{\partial z}\frac{\partial}{\partial R}\left(-\frac{1}{R}v_\varphi + \frac{Q'}{4\pi\rho R}B_\varphi\right) = 0. \tag{A.22}$$

Defining Ω

$$\Omega \equiv \frac{v_\varphi}{R} - \frac{Q'B_\varphi}{4\pi\rho R}, \tag{A.23}$$

we obtain

$$\Omega = \Omega(\Psi), \tag{A.24}$$

from Eq. (A.22). Where, Ω means the rotational law. The function Ω is an arbitrary function of Ψ and means the rotational law.

Considering the poloidal components of the equations of motion, we operate the cross product of $\nabla\times$,

$$\nabla \times \left[\boldsymbol{v} \times \boldsymbol{\omega} + \frac{1}{\rho} \left(\frac{j_\varphi}{c} \times \boldsymbol{B} \right) \right] = 0.$$

Using Eqs. (A.14) and (A.15), we rewrite this equation as

$$\begin{aligned} &\frac{\partial}{\partial z} \left\{ \left[\frac{v_\varphi}{R} \frac{\partial}{\partial R}(Rv_\varphi) - \frac{\omega_\varphi}{4\pi\rho R} \frac{\partial Q}{\partial R} \right] + \left[\frac{j_\varphi/c}{\rho R} \frac{\partial \Psi}{\partial z} - \frac{B_\varphi}{4\pi\rho R} \frac{\partial B_\varphi}{\partial z} \right] \right\} \\ -&\frac{\partial}{\partial R} \left\{ \left[\frac{v_\varphi}{R} \frac{\partial}{\partial z}(Rv_\varphi) - \frac{\omega_\varphi}{4\pi\rho R} \frac{\partial Q}{\partial z} \right] + \left[\frac{j_\varphi/c}{\rho R} \frac{\partial \Psi}{\partial z} - \frac{B_\varphi}{4\pi\rho R} \frac{\partial B_\varphi}{\partial z} \right] \right\} = 0. \end{aligned} \tag{A.25}$$

Using κ, Ω and Q, we obtain

$$\begin{aligned} &\frac{\partial \Psi}{\partial R} \frac{\partial}{\partial z} \left(\frac{j_\varphi}{c} + \frac{-\kappa' B_\varphi - RQ'' v_\varphi - \omega_\varphi Q'}{4\pi\rho R} - \Omega' R v_\varphi \right) \\ -&\frac{\partial \Psi}{\partial z} \frac{\partial}{\partial R} \left(\frac{j_\varphi}{c} + \frac{-\kappa' B_\varphi - RQ'' v_\varphi - \omega_\varphi Q'}{4\pi\rho R} - \Omega' R v_\varphi \right) = 0. \end{aligned} \tag{A.26}$$

We define

$$-\frac{B_\varphi \kappa'(\Psi)}{4\pi\rho R} - R v_\varphi \Omega'(\Psi) - \frac{v_\varphi Q''(\Psi) B_\varphi}{4\pi\rho} + \frac{j_\varphi/c}{\rho R} - \frac{\omega_\varphi Q'(\Psi)}{4\pi\rho R} \equiv \mu(\Psi)\ , \tag{A.27}$$

and obtain

$$\mu \equiv \mu(\Psi), \tag{A.28}$$

from Eq. (A.26). Now, we have four arbitrary functions and obtain the functional form of the current density as follows:

$$\frac{\boldsymbol{j}}{c} = \left[\kappa'(\Psi) + Q''(\Psi) R v_\varphi \right] \frac{\boldsymbol{B}}{4\pi} + Q'(\Psi) \frac{\boldsymbol{\omega}}{4\pi} + \rho R \left[\mu(\Psi) + \Omega' R v_\varphi \right] \boldsymbol{e}_\varphi. \tag{A.29}$$

Using these functionals, we integrate the equations of motion and obtain the first integral. Rewriting the third term and forth term of the right hand side of the equations of motion, Eq. (A.2), we have

$$\begin{aligned} \boldsymbol{v} \times \boldsymbol{\omega} + \frac{1}{\rho} \left(\frac{\boldsymbol{j}}{c} \times \boldsymbol{B} \right) &= \left\{ \mu \frac{\partial \Psi}{\partial R} + \frac{\partial}{\partial R}(\Omega R v_\varphi) \right\} \boldsymbol{e}_R + \left\{ \mu \frac{\partial \Psi}{\partial z} + \frac{\partial}{\partial z}(\Omega R v_\varphi) \right\} \boldsymbol{e}_z \\ &= \nabla \int \mu \, d\Psi + \nabla(\Omega R v_\varphi), \end{aligned}$$

Then, we obtain the first integral as,

$$\int \frac{dp}{\rho} = -\phi_g - \frac{1}{2}|\boldsymbol{v}^2| + \int_\Psi \mu(\Psi)\, d\Psi + Rv_\varphi \Omega(\Psi) + C, \tag{A.30}$$

where, the term of $\int \mu(\Psi)\, d\Psi + C$ means the conservation of the energy flow along the Ψ Lovelace et al. (1986).

It should be noted that in this current density formula, the four arbitrary functions appear and that each function is related to different physical quantities corresponding to each term in the right-hand side of Eq. (A.29). Lovelace et al. (1986) obtained the current density including another arbitrary function which is related to the entropy. This arbitrary function, related to the entropy, does not appear in our problem because uniform entropy distributions is implicitly assumed.

A.1.2 Stream function based formulation: Vorticity formula

So far, we consider the situations in which the poloidal magnetic fields exist everywhere except in vacuum region. For such situations, as already shown, the flux function Ψ can be a principal variable by which all the magnetohydrodynamical quantities are determined. If we assume that the poloidal velocity fields exist everywhere inside the fluid region, the same problem as that treated in this study may be formulated by considering the stream function Q as a principal variable, which is named "the stream function based formulation". For this formulation, the magnetic flux function is given by a function of the stream function,

$$\Psi = \Psi(Q)\ . \tag{A.31}$$

The other arbitrary functions of the magnetic flux function defined in Appendix A.1.1 are regarded as functions of Q. Then, the vorticity vector may be written as:

$$\boldsymbol{\omega} = 4\pi\rho \left\{ \frac{d\ell(Q)}{dQ} + R\frac{d^2\Psi(Q)}{dQ^2} B_\varphi \right\} \boldsymbol{v} + 4\pi \frac{d\Psi(Q)}{dQ} \frac{\boldsymbol{j}}{c} + \rho R \left\{ -\nu(Q) + R\frac{d\sigma(Q)}{dQ} B_\varphi \right\} \boldsymbol{e}_\varphi \ , \tag{A.32}$$

where $\ell(Q)$, $\nu(Q)$ and $\sigma(Q)$ are another set of arbitrary functions of Q for the stream function based formulation. The arbitrary functions $\ell(Q)$ and $\sigma(Q)$ are related to the physical quantities v_φ and B_φ through

$$\ell(Q) = Rv_\varphi - R\frac{d\Psi(Q)}{dQ} B_\varphi\ , \tag{A.33}$$

$$\sigma(Q) = \frac{B_\varphi}{\rho R} - \frac{4\pi}{R} v_\varphi \frac{d\Psi(Q)}{dQ}\ . \tag{A.34}$$

A.2 Change of the gravitational potential

A.2.1 $N = 1$ polytrope

We show the details of the change of the gravitational potential in chapter 4. The gravitational potential perturbation for $N = 1$ polytrope is governed by the quadrupole component of Poisson's equation under two boundary conditions ($\delta\phi_g^{(2)}$ is regular at $r = 0$ and continues the external solution smoothly at $r = r_s$):

$$\frac{d^2\delta\phi_g^{(2)}}{dr^2} + \frac{2}{r}\frac{d\delta\phi_g^{(2)}}{dr} - \frac{6}{r^2}\delta\phi_g^{(2)} = 4\pi G\delta\rho^{(2)} \ . \tag{A.35}$$

Considering the density perturbation expressed by Eq. (4.26) in chapter 4, this equation can be rewritten as

$$\frac{d^2\delta\phi_g^{(2)}}{dr^2} + \frac{2}{r}\frac{d\delta\phi_g^{(2)}}{dr} + \left(\pi^2 - \frac{6}{r^2}\right)\delta\phi_g^{(2)} = 4\pi G\left(\frac{d\phi_g}{dr}\right)^{-1} L^{(2)}(r). \tag{A.36}$$

By introducing the new variable $x = \pi r$, the left-hand side of the equation is reduced to

$$\frac{d^2\delta\phi_g^{(2)}}{dx^2} + \frac{2}{x}\frac{d\delta\phi_g^{(2)}}{dx} + \left(1 - \frac{6}{x^2}\right)\delta\phi_g^{(2)} = \frac{4\pi G}{\pi^2}\left(\frac{d\phi_g}{dr}\right)^{-1} L^{(2)}(r). \tag{A.37}$$

The solution to this equation can be obtained by taking the boundary conditions into account as follows:

$$\delta\phi_g^{(2)}(x) = \frac{F^{(p)}(x)}{x^3} - \frac{1}{\pi^2}\frac{dF^{(p)}(\pi)}{dx}\Big|_{x=\pi} j_2(x), \tag{A.38}$$

where

$$\begin{aligned} F^{(p)}(x) = \ & - \frac{2}{3}\mu_0 A_1 \frac{\pi^2}{\kappa_0^2(\pi^2-\kappa_0^2)^2}\left[\left\{6\pi^2\kappa_0^2 + \left(\pi^2 - 3\kappa_0^2\right)\kappa_0^2 x^2\right\}\sin\left(\frac{\kappa_0}{\pi}x\right)\right. \\ & - \left.\frac{\kappa_0}{\pi}x\left\{6\pi^2\kappa_0^2 + \left(\pi^2-\kappa_0^2\right)\kappa_0^2 x^2\right\}\cos\left(\frac{\kappa_0}{\pi}x\right)\right] \\ & - \frac{2}{3}\mu_0 A_2\left[\frac{1}{2}x^4\sin x + \frac{1}{6}\left(\frac{\kappa_0^2}{\pi^2} - 1\right)x^5\cos x\right] \ . \end{aligned} \tag{A.39}$$

Here the coefficients A_1 and A_2 are defined as

$$A_1 = \frac{8\pi^2\mu_0\rho_c}{(\kappa_0^2-\pi^2)^2}\frac{1}{(\sin\kappa_0 - \kappa_0\cos\kappa_0)}, \tag{A.40}$$

$$A_2 = \frac{4\pi\mu_0\rho_c}{(\kappa_0^2-\pi^2)^2}, \tag{A.41}$$

for $N = 1$ closed configurations and

$$A_1 = -\frac{4\pi^2\mu_0\rho_c}{\kappa_0^2(\kappa_0^2-\pi^2)}\frac{1}{\sin\kappa_0}, \tag{A.42}$$

$$A_2 = \frac{4\pi\mu_0\rho_c}{(\kappa_0^2-\pi^2)^2}, \tag{A.43}$$

for $N = 1$ open configurations.

A.2.2 Surface change for $N = 0$ polytrope

The change of the gravitational potential due to the change of the surface, i.e. $\varepsilon r_s P_2(\cos\theta)$, can be obtained by

$$\begin{aligned}\delta\phi_g^{(2)}(r) &= -4\pi G\rho_0\int_0^\pi d\theta' P_2(\cos\theta')\int_{r_s}^{r_s(1+\varepsilon)P_2(\cos\theta')} dr' r'^2\frac{r^2}{r'^3}\\ &= -\frac{4\pi G\rho_0}{5}r^2\varepsilon\ .\end{aligned}$$

A.3 Analytical solutions for Hall equilibrium states

We show the analytical solution of each model in chapter 5. When the magnetic field is purely poloidal ($\kappa = 0$) and the functional forms are $S = S_0$ and $\mu = \mu_0$, we can calculate analytical solutions easily. We obtain the exact solutions integrating j_φ and throughout the whole region. We set $\rho = \rho_0$ and $n_e = n_0$, but we can also obtain the solutions with arbitrary ρ and n_e distributions. The functional form of toroidal current density becomes

$$\frac{j_\varphi}{c} = \begin{cases}\rho_0\mu_0 r\sin\theta & (0 \le r < r_{in})\\ n_0 S_0 r\sin\theta & (r_{in} \le r \le r_s)\\ 0 & (r_s < r)\end{cases}\ . \tag{A.44}$$

Now, we obtain the analytical solutions.

A.3.1 Model I

The magnetic field within the core ($0 \le r < r_{in}$) is excluded by the Meissner effect in this model. The current density also does not exist in the core. Therefore, we fix $\mu_0 = 0$. Then the integration of the Green function is expressed by

$$\begin{aligned}\Psi(r,\theta) &= 2\pi r\sin\theta S_0\sum_{n=1}^\infty\frac{P_n^1(\cos\theta)}{n(n+1)}\int_0^\infty f_n(r,r')r'^2dr'\int_0^\pi P_n^1(\cos\theta')\sin\theta' d\theta'\,(n_0 r'\sin\theta')\\ &+ \sum_{n=1}^\infty\Big(a_n r^{n+1}P_n^1(\cos\theta) + b_n r^{-n}P_n^1(\cos\theta)\Big)\sin\theta.\end{aligned} \tag{A.45}$$

Since the number density profile is independent of θ, we can integrate θ component. From the orthogonality of the associate Legendre function,

$$\int_0^\pi \sin\theta' P_n^1(\cos\theta') P_n^1(\cos\theta') d\theta' = 2\frac{n(n+1)}{2n+1}, \tag{A.46}$$

higher terms ($n \geq 2$) must vanish. Then the equation becomes

$$\Psi(r,\theta) = \frac{4\pi}{3} r \sin^2\theta S_0 n_0 \int_0^\infty f_1(r,r') r'^3 dr' + \left(a_1 r^2 + b_1 r^{-1}\right)\sin^2\theta. \tag{A.47}$$

The electrons exit within finite region ($r_{in} \leq r \leq r_s$) of the star. Then, the r integral classified into three types, the inner vacuum solution, the interior solution and the outer vacuum solution as below:

$$\int_0^\infty f_1(r,r') r'^2 dr' = \begin{cases} r\left(\int_{r_{in}}^{r_s} r r'\, dr'\right) = \frac{1}{2} r_s^2 r^2 - \frac{1}{2} r_{in}^2 r^2 & (0 \leq r \leq r_{in}) \\ r\left(\int_{r_{in}}^{r} \frac{r'^4}{r^2}\, dr' + \int_r^\infty r r'\, dr'\right) = \left(\frac{1}{5} r^4 - \frac{1}{5}\frac{r_{in}^5}{r}\right) + \left(\frac{1}{2} r_s^2 r^2 - \frac{1}{2} r^4\right) & (r_{in} \leq r \leq r_s) \\ r\left(\int_{r_{in}}^{r_s} \frac{r'^4}{r^2}\, dr'\right) = \left(\frac{1}{5}\frac{r_s^5}{r} - \frac{1}{5}\frac{r_{in}^5}{r}\right) & (r_s \leq r) \end{cases} . \tag{A.48}$$

If we neglect the homogeneous terms, there is not any current sheet in the system and the crustal magnetic fields penetrate core. Since the magnetic field cannot penetrate within $r \leq r_{in}$ region by the Meissner effect in this model, we must impose the boundary condition $\Psi(r_{in},\theta) = 0$. We need to choose the coefficients of the homogeneous terms in the case. The terms represent the contribution from toroidal current sheet on $r = r_{in}$ (Fujisawa & Eriguchi 2013). Therefore, we add the toroidal current sheet on $r = r_{in}$ in order to satisfy the boundary condition $\Psi(r_{in},\theta) = 0$ as follow:

$$\Psi(r,\theta) = \begin{cases} \frac{4\pi S_0 n_0}{3}\sin^2\theta\left[\frac{1}{2} r_s^2 r^2 - \frac{1}{2} r_{in}^2 r^2\right] + j_s r^2 \sin^2\theta = 0 & (0 \leq r \leq r_{in}) \\ \frac{4\pi S_0 n_0}{3}\sin^2\theta\left[\left(\frac{1}{5} r^4 - \frac{1}{5}\frac{r_{in}^5}{r}\right) + \left(\frac{1}{2} r_s^2 r^2 - \frac{1}{2} r^4\right)\right] + j_s r_{in}^3 r^{-1}\sin^2\theta & (r_{in} \leq r \leq r_s) \\ \frac{4\pi S_0 n_0}{3}\sin^2\theta\left[\left(\frac{1}{5}\frac{r_s^5}{r} - \frac{1}{5}\frac{r_{in}^5}{r}\right)\right] + j_s r_{in}^3 r^{-1}\sin^2\theta & (r_s \leq r) \end{cases} , \tag{A.49}$$

where j_s is a strength of the toroidal current sheet ($j_s = a_1 = r_{in}^3 b_1$). Since the a_1 term is the inner solution and the b_1 term is the outer solution, a_1 is determined by the boundary condition $\Psi(r_{in},\theta) = 0$ and the explicit form of j_s is

$$j_s = \frac{2\pi S_0 n_0}{3}(r_{in}^2 - r_s^2) \quad (0 < r_{in}) \tag{A.50}$$

and the sign of j_s is negative. This means that the Meissner effect equals the effective *negative current sheet* on the core-crust boundary in order to exclude the magnetic field from the crustal toroidal current (see Fig. 5 in Bonazzola & Gourgoulhon 1996).

A.3.2 Model II

Model II is crustal current model, but it does not have current sheet on the core-crust boundary. Therefore the solution is below:

$$\Psi(r,\theta) = \begin{cases} \dfrac{4\pi S_0 n_0}{3}\sin^2\theta\left[\dfrac{1}{2}r_s^2 r^2 - \dfrac{1}{2}r_{in}^2 r^2\right] & (0 \le r \le r_{in}) \\ \dfrac{4\pi S_0 n_0}{3}\sin^2\theta\left[\left(\dfrac{1}{5}r^4 - \dfrac{1}{5}\dfrac{r_{in}^5}{r}\right) + \left(\dfrac{1}{2}r_s^2 r^2 - \dfrac{1}{2}r^4\right)\right] & (r_{in} \le r \le r_s) \\ \dfrac{4\pi S_0 n_0}{3}\sin^2\theta\left[\left(\dfrac{1}{5}\dfrac{r_s^5}{r} - \dfrac{1}{5}\dfrac{r_{in}^5}{r}\right)\right] & (r_s \le r) \end{cases} . \quad \text{(A.51)}$$

A.3.3 Model III & IV

These models have both core current and crustal current. Therefore the solutions are described by the sum of the core current magnetic field Ψ_{co} and the crustal current magnetic field Ψ_{cr}. The crustal current magnetic field Ψ_{cr} is equal with the model II solution. We can also obtain the profile of Ψ_{co} easily. The solution is as follow:

$$\Psi_{co}(r,\theta) = \begin{cases} \dfrac{4\pi\mu_0\rho_0}{3}\sin^2\theta\left[\left(\dfrac{1}{5}r^4\right) + \left(\dfrac{1}{2}r_{in}^2 r^2 - \dfrac{1}{2}r^4\right)\right] & (0 \le r < r_{in}) \\ \dfrac{4\pi\mu_0\rho_0}{3}\sin^2\theta\left[\left(\dfrac{1}{5}\dfrac{r_{in}^5}{r}\right)\right] & (r_{in} \le r) \end{cases} . \quad \text{(A.52)}$$

As a result, the general solutions of the model III and IV are as below:

$$\Psi(r,\theta) = \begin{cases} \dfrac{4\pi}{3}\sin^2\theta\left[\mu_0\rho_0\left\{\left(\dfrac{1}{5}r^4\right) + \left(\dfrac{1}{2}r_{in}^2 r^2 - \dfrac{1}{2}r^4\right)\right\} + S_0 n_0\left\{\dfrac{1}{2}r_s^2 r^2 - \dfrac{1}{2}r_{in}^2 r^2\right\}\right] + j_s r^2\sin^2\theta & (0 \le r < r_{in}) \\ \dfrac{4\pi}{3}\sin^2\theta\left[\mu_0\rho_0\left(\dfrac{1}{5}\dfrac{r_{in}^5}{r}\right) + S_0 n_0\left\{\left(\dfrac{1}{5}r^4 - \dfrac{1}{5}\dfrac{r_{in}^5}{r}\right) + \left(\dfrac{1}{2}r_s^2 r^2 - \dfrac{1}{2}r^4\right)\right\}\right] + j_s r_{in}^3 r^{-1}\sin^2\theta & (r_{in} \le r \le r_s) \\ \dfrac{4\pi}{3}\sin^2\theta\left[\mu_0\rho_0\left(\dfrac{1}{5}\dfrac{r_{in}^5}{r}\right) + S_0 n_0\left\{\dfrac{1}{5}\dfrac{r_s^5}{r} - \dfrac{1}{5}\dfrac{r_{in}^5}{r}\right\}\right] + j_s r_{in}^3 r^{-1}\sin^2\theta & (r_s \le r) \end{cases} , \quad \text{(A.53)}$$

where $\mu_0 S_0 > 0$ (model III) and $\mu_0 S_0 < 0$ (model IV). Especially noted, model III and IV can have arbitrary current sheet on the core-crust boundary. The last term represents the contribution from the dipole current sheet (see Fujisawa & Eriguchi 2013). The j_s denotes a magnitude of the current sheet.

A.3.4 The magnetic field configurations of each model

We show some graphs of the analytical solutions. We set $r_s = 1$ and $r_{in} = 0.75$. The functional parameters are $5S_0 n_0 = \mu_0\rho_0$ (model III) and $-5S_0 n_0 = \mu_0\rho_0$ (model IV). We have showed the distributions of Ψ in Fig.5.1. Fig.A.1 displays profiles of Ψ on the equatorial plane normalized its surface value. As seen form these figures, the model I is a pure crustal open magnetic model,

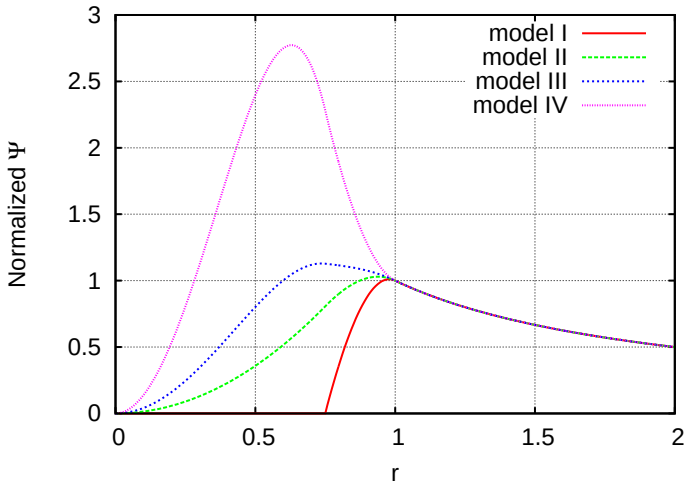

Figure A.1: The Ψ profiles of each model on the equatorial plane. They are normalized by value of $\Psi(r_s, \pi/2)$.

the model II is a strong crustal magnetic model, the model III is a strong core magnetic model and the model IV is a very strong core magnetic model respectively.

I would rather be first in a little Iberian village than
second in Rome.
(Gaius Julius Caesar)

B

Details of numerical method

B.1 Dimensionless quantities

In chapters 2, 3 and 6 of this thesis, physical quantities are used in their dimensionless forms for numerical computations, because we have calculated the matter equation self-consistently using normalized radius (chapter 2) as

$$\hat{r} \equiv \frac{r}{r_e} = \frac{r}{\sqrt{\frac{1}{\beta}\frac{p_{\max}}{4\pi G\rho_{\max}^2}}} , \tag{B.1}$$

for polytropic configurations and

$$\hat{r} \equiv \frac{r}{r_e} = \frac{r}{\sqrt{\frac{1}{\beta}\frac{8a}{b}\frac{1}{4\pi G\rho_{\max}^2}}} , \tag{B.2}$$

for the Fermi gas models, and

$$\hat{\rho} \equiv \frac{\rho}{\rho_{\max}} . \tag{B.3}$$

Their explicit forms of other physical quantities are

$$\hat{\phi}_g \equiv \frac{\phi_g}{4\pi G r_e^2 \rho_{\max}} , \tag{B.4}$$

$$\hat{\Omega} \equiv \frac{\Omega}{\sqrt{4\pi G\rho_{\max}}} , \tag{B.5}$$

$$\hat{\boldsymbol{v}} \equiv \frac{\boldsymbol{v}}{\sqrt{4\pi G\rho_{\max}}r_e}\,, \tag{B.6}$$

$$\hat{Q} \equiv \frac{Q}{\sqrt{4\pi G\rho_{\max}^3}r_e^3}\,, \tag{B.7}$$

$$\hat{\mu} \equiv \frac{\mu}{\sqrt{4\pi G}/r_e}\,, \tag{B.8}$$

$$\hat{B}_{suffix} \equiv \frac{B_{suffix}}{\sqrt{4\pi G}r_e\rho_{\max}}\,, \tag{B.9}$$

$$\hat{A}_{\varphi} \equiv \frac{A_{\varphi}}{\sqrt{4\pi G}r_e^2\rho_{\max}}\,, \tag{B.10}$$

$$\hat{\Psi} \equiv \frac{\Psi}{\sqrt{4\pi G}r_e^3\rho_{\max}}\,, \tag{B.11}$$

$$\hat{K} \equiv \frac{K}{4\pi G r_e^6\rho_{\max}^2}\,, \tag{B.12}$$

$$\hat{j}_{\varphi} \equiv \frac{j_{\varphi}}{\sqrt{4\pi G\rho_{\max}}c}\,, \tag{B.13}$$

$$\hat{C} \equiv \frac{C}{4\pi G r_e^2\rho_{\max}}\,. \tag{B.14}$$

Here B_{suffix} is the component of the magnetic field where $suffix$ may be c (center), sur (surface), p (*poloidal*) and t (*toroidal*). Similarly we define normalized global quantities as follows:

$$\hat{M} = \frac{M}{r_e^3\rho_{\max}}\,, \tag{B.15}$$

$$\hat{W} = \frac{W}{4\pi G r_e^5\rho_{\max}^2}\,, \tag{B.16}$$

$$\hat{T} = \frac{T}{4\pi G r_e^5\rho_{\max}^2}\,, \tag{B.17}$$

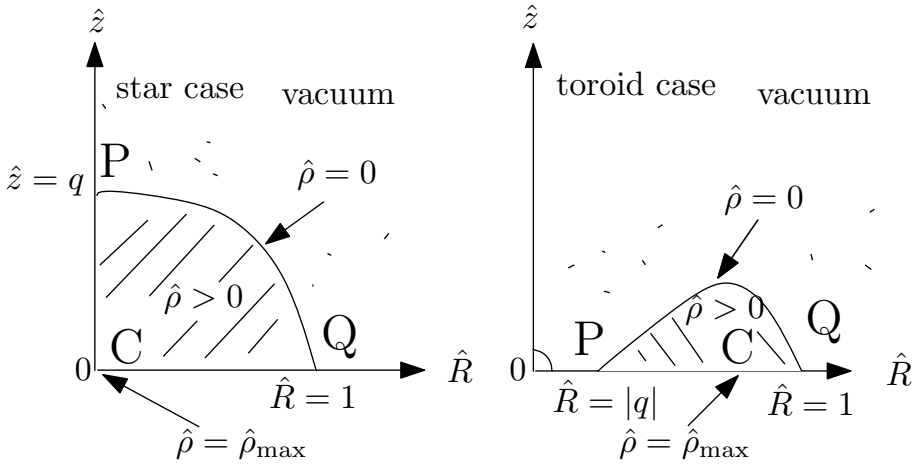

Figure B.1: Three points used HSCF scheme in case of the star (left) and in case of the toroid (right).

$$\hat{\Pi} = \frac{\Pi}{4\pi G r_e^5 \rho_{\max}^2}\,, \tag{B.18}$$

$$\hat{U} = \frac{U}{4\pi G r_e^5 \rho_{\max}^2}\,, \tag{B.19}$$

$$\hat{\mathcal{M}} = \frac{\mathcal{M}}{4\pi G r_e^5 \rho_{\max}^2}\,. \tag{B.20}$$

We obtain dimensionless equations using these dimensionless quantities as follows;

$$\frac{1}{4\pi G r_e^2 \rho_{\max}} \int \frac{dp}{\rho} = -\hat{\phi}_g - \frac{1}{2}|\hat{\boldsymbol{v}}|^2 + \int_{\hat{\Psi}} \hat{\mu}(\hat{\Psi})\, d\hat{\Psi} + \hat{r}\sin\theta \hat{v}_\varphi \hat{\Omega}(\hat{\Psi}) + \hat{C}, \tag{B.21}$$

in case of the magnetized star and

$$\frac{1}{4\pi G r_e^2 \rho_{\max}} \int \frac{dp}{\rho} = -\hat{\phi}_g + \frac{\hat{M}_c}{4\pi\hat{r}} - \frac{1}{2}|\hat{\boldsymbol{v}}|^2 + \int_{\hat{\Psi}} \hat{\mu}(\hat{\Psi})\, d\hat{\Psi} + \hat{r}\sin\theta \hat{v}_\varphi \hat{\Omega}(\hat{\Psi}) + \hat{C}, \tag{B.22}$$

in case of the magnetized toroids. We change the left side of Eq. (B.21) using polytrope relation,

$$\frac{1}{4\pi G r_e^2 \rho_{\max}} \int \frac{dp}{\rho} = \beta(N+1)\hat{\rho}^{1/N}, \tag{B.23}$$

or using Fermi gas,

$$\frac{1}{4\pi G r_e^2 \rho_{\max}} \int \frac{dp}{\rho} = \beta\left[1 + \left(\frac{\rho_0}{b}\right)^{\frac{2}{3}}\right]^{\frac{1}{2}}. \tag{B.24}$$

B.2 Numerical Scheme

In our numerical studies, the generalized iteration scheme known as Hachisu's Self-Consistent-Field method, HSCF method (Hachisu 1986a,b). is adopted in order to solve the non-linear system of equations for equilibrium stars. In this generalized HSCF method, the density, the gravitational potential and the vector potential are iteratively solved (Tomimura & Eriguchi 2005). We assume the equatorial symmetry in this section and use the functional forms of $\hat{\mu}$ and $\hat{\Omega}$ as follow:

$$\hat{\mu}(\hat{\Psi}) = \hat{\mu}_0(\hat{\Psi} + \epsilon)^m, \tag{B.25}$$

$$\hat{\Omega}(\hat{\Psi}) = \hat{\Omega}_0(\hat{\Psi}^2 + d^2)^\alpha. \tag{B.26}$$

We start our computation by assuming initial guesses for the mass density and the magnetic field distribution. Using a trial density and a magnetic field distribution, the gravitational potential $\hat{\phi}_g$ and the vector potential $\hat{A}_\varphi$ are computed by expanding the potentials as

$$\hat{\phi}_g(\hat{r},\theta) = -\sum_{n=0}^{n_{\max}} P_{2n}(\cos\theta) \int_0^\infty \hat{r}'^2 f_{2n}(\hat{r},\hat{r}')d\hat{r}' \int_0^{\pi/2} P_{2n}(\cos\theta')\sin\theta' d\theta' \times \hat{\rho}(\hat{r}',\theta'), \tag{B.27}$$

$$\begin{aligned}\hat{A}_\varphi(\hat{r},\theta) =& \sum_{n=1}^{\ell_{\max}} \frac{P^1_{2n-1}(\cos\theta)}{2n(2n-1)} \int_0^\infty \hat{r}'^2 f_{2n}(\hat{r},\hat{r}')d\hat{r}' \int_0^{\pi/2} P_{2n}(\cos\theta')\sin\theta' d\theta' \times \hat{j_\varphi}(\hat{r}',\theta') \\ &+ \sum_{n=1}^{\infty} \left(a_{2n-1} r^{2n-1} P^1_{2n-1}(\cos\theta) + b_{2n-1} r^{-2n} P^1_{2n-1}(\cos\theta) \right),\end{aligned} \tag{B.28}$$

$$f_{2n}(\hat{r},\hat{r}') = \begin{cases} \hat{r}'^{2n}/\hat{r}^{2n+1}, & (\hat{r} \geq \hat{r}') \\ \hat{r}^{2n}/\hat{r}'^{2n+1}, & (\hat{r} \leq \hat{r}') \end{cases}, \tag{B.29}$$

where P_n are the Legendre polynomials of degree n and P^1_n are the associated Legendre functions of order one. In the actual computations, we take $n_{\max} \geq 20$, $\ell_{\max} \geq 20$.

In our formulation there appear some more constants, i.e. a length scale factor β and an integration constant $\hat{C}$. These two constants are not free parameters which should be specified to solve the problem, but are unknown parameters which should be solved for. After the two potentials are obtained, these two constants as well as the model parameter i.e. $\hat{\Omega}_0$ or $\hat{\mu}_0$, are solved by imposing the following three conditions at three special grid points.

B.2.1 The case of polytropic stars

First, we describe the case of the magnetized polytropic stars. (left panel in Fig. B.1). At the polar surface (point P), i.e. at $\hat{r} = q$ and $\theta = 0$, and at the equatorial surface (point Q), i.e. at $\hat{r} = 1$ and $\theta = \pi/2$, the density must vanish. At the point where the density takes its maximum value (point C), i.e. at $\hat{r} = \hat{r}_{\max}$ and $\theta = \theta_{\max}$, the dimensionless density must be unity. These

three conditions are expressed as follows:

$$0 = -\hat{\phi}_g|_P - \frac{1}{2}(\hat{v}_r|_P^2 + \hat{v}_\theta|_P^2 + \hat{v}_\varphi|_P^2) + \frac{\hat{\mu}_0}{m+1}(\hat{\Psi}|_P + \epsilon)^{m+1} + \hat{r}\sin\theta\hat{v}_\varphi\hat{\Omega}_0(\hat{\Psi}^2 + d^2)^\alpha|_P + \hat{C}\,, \tag{B.30}$$

$$0 = -\hat{\phi}_g|_Q - \frac{1}{2}(\hat{v}_r|_Q^2 + \hat{v}_\theta|_Q^2 + \hat{v}_\varphi|_Q^2) + \frac{\hat{\mu}_0}{m+1}(\hat{\Psi}|_Q + \epsilon)^{m+1} + \hat{r}\sin\theta\hat{v}_\varphi\hat{\Omega}_0(\hat{\Psi}^2 + d^2)^\alpha|_Q + \hat{C}\,, \tag{B.31}$$

$$\beta(1+N) = -\hat{\phi}_g|_C - \frac{1}{2}(\hat{v}_r|_C^2 + \hat{v}_\theta|_C^2 + \hat{v}_\varphi|_C^2) + \frac{\hat{\mu}_0}{m+1}(\hat{\Psi}|_C + \epsilon)^{m+1} + \hat{r}\sin\theta\hat{v}_\varphi\hat{\Omega}_0(\hat{\Psi}^2 + d^2)^\alpha|_C + \hat{C}\,. \tag{B.32}$$

From these equations we obtain three constants β, $\hat{C}$ and $\hat{\Omega}_0$ or $\hat{\mu}_0$. Using the three constants and the two potentials, we solve the first integral of equation of motion for the matter density:

$$\beta(1+N)\hat{\rho}^{\frac{1}{N}} = -\hat{\phi}_g - \frac{1}{2}(\hat{v}_r^2 + \hat{v}_\theta^2 + \hat{v}_\varphi^2) + \frac{\hat{\mu}_0}{m+1}(\hat{\Psi} + \epsilon)^{m+1} + \hat{r}\sin\theta\hat{v}_\varphi\hat{\Omega}_0(\hat{\Psi}^2 + d^2)^\alpha + \hat{C}\,. \tag{B.33}$$

B.2.2 The case of Fermi gas

Second, we describe the case of magnetized white dwarfs. Three points of the star (point P, Q and C) are the same as in the case of neutron stars, but the terms on the left-hand side of Eqs. (B.30), (B.31), (B.32) are different. We use the right-hand side of the Eq. (B.24) and express as follows:

$$\beta = -\hat{\phi}_g|_P - \frac{1}{2}(\hat{v}_r|_P^2 + \hat{v}_\theta|_P^2 + \hat{v}_\varphi|_P^2) + \frac{\hat{\mu}_0}{m+1}(\hat{\Psi}|_P + \epsilon)^{m+1} + \hat{r}\sin\theta\hat{v}_\varphi\hat{\Omega}_0(\hat{\Psi}^2 + d^2)^\alpha|_P + \hat{C}\,, \tag{B.34}$$

$$\beta = -\hat{\phi}_g|_Q - \frac{1}{2}(\hat{v}_r|_Q^2 + \hat{v}_\theta|_Q^2 + \hat{v}_\varphi|_Q^2) + \frac{\hat{\mu}_0}{m+1}(\hat{\Psi}|_Q + \epsilon)^{m+1} + \hat{r}\sin\theta\hat{v}_\varphi\hat{\Omega}_0(\hat{\Psi}^2 + d^2)^\alpha|_Q + \hat{C}\,, \tag{B.35}$$

$$\beta\left[1 + \left(\frac{\rho_0}{b}\right)^{\frac{2}{3}}\right]^{\frac{1}{2}} = -\hat{\phi}_g|_C - \frac{1}{2}(\hat{v}_r|_C^2 + \hat{v}_\theta|_C^2 + \hat{v}_\varphi|_C^2) + \frac{\hat{\mu}_0}{m+1}(\hat{\Psi}|_C + \epsilon)^{m+1} + \hat{r}\sin\theta\hat{v}_\varphi\hat{\Omega}_0(\hat{\Psi}^2 + d^2)^\alpha|_C + \hat{C}\,. \tag{B.36}$$

From these equations we obtain three constants β, $\hat{C}$ and $\hat{\Omega}_0$ or $\hat{\mu}_0$. Using the three constants and the two potentials, we solve the first integral of equation of motion for the matter density:

$$\beta\left[1 + \left(\frac{\hat{\rho}\rho_0}{b}\right)^{\frac{2}{3}}\right]^{\frac{1}{2}} = -\hat{\phi}_g - \frac{1}{2}(\hat{v}_r^2 + \hat{v}_\theta^2 + \hat{v}_\varphi^2) + \frac{\hat{\mu}_0}{m+1}(\hat{\Psi} + \epsilon)^{m+1} + \hat{r}\sin\theta\hat{v}_\varphi\hat{\Omega}_0(\hat{\Psi}^2 + d^2)^\alpha + \hat{C}\,. \tag{B.37}$$

B.2.3 The case of toroids

Finally, we describe the case of the magnetized toroids (right panel in Fig. B.1). We consider the gravitational potential from the central star $\left(\hat{M}_c/4\pi\hat{r}\right)$ in this case. At the inner surface (point P), i.e. at $\hat{r} = q$ and $\theta = \pi/2$, and at the outer surface (point Q), i.e. at $\hat{r} = 1$ and $\theta = \pi/2$, the density must vanish. At the point where the density takes its maximum value (point C), i.e. at $\hat{r} = \hat{r}_{\max}$ and $\theta = \theta_{\max}$, the dimensionless density must be unity. These three

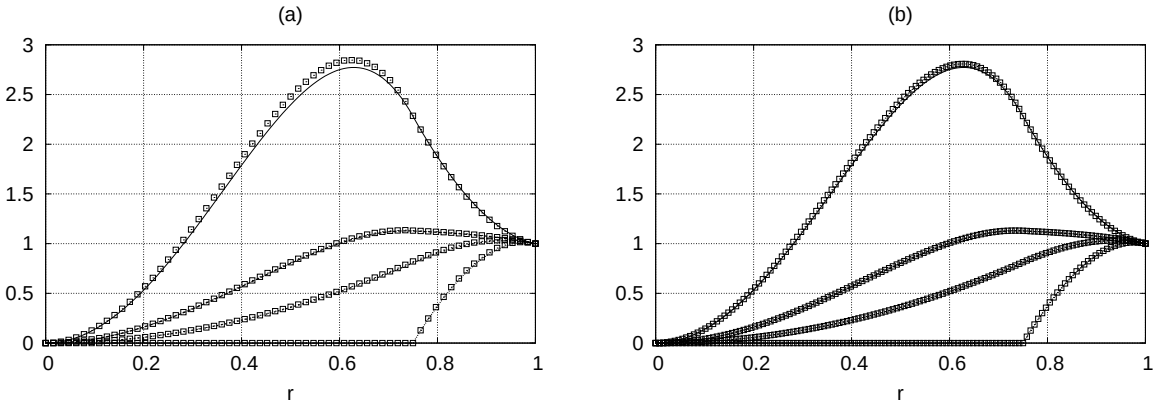

Figure B.2: Numerical (points) and analytical (lines) solutions of each model. Left panel(a): $N_{r1} = 65$ ($r = [0:1]$), $N_\theta = 257$ ($\theta = [0:\pi]$) solutions. Right panel(b): $N_{r1} = 129$, $N_\theta = 257$ solutions. The solutions in (b) represent the analytical solutions very well.

conditions are expressed as follows,

$$0 = -\hat{\phi}_g|_P + \frac{\hat{M}_c}{4\pi\hat{r}}\Big|_P - \frac{1}{2}(\hat{v}_r|_P^2 + \hat{v}_\theta|_P^2 + \hat{v}_\varphi|_P^2) + \frac{\hat{\mu}_0}{m+1}(\hat{\Psi}|_P + \epsilon)^{m+1} + \hat{r}\sin\theta\hat{v}_\varphi\hat{\Omega}_0(\hat{\Psi}^2 + d^2)^\alpha|_P + \hat{C}\,, \quad \text{(B.38)}$$

$$0 = -\hat{\phi}_g|_Q + \frac{\hat{M}_c}{4\pi\hat{r}}\Big|_Q - \frac{1}{2}(\hat{v}_r|_Q^2 + \hat{v}_\theta|_Q^2 + \hat{v}_\varphi|_Q^2) + \frac{\hat{\mu}_0}{m+1}(\hat{\Psi}|_Q + \epsilon)^{m+1} + \hat{r}\sin\theta\hat{v}_\varphi\hat{\Omega}_0(\hat{\Psi}^2 + d^2)^\alpha|_Q + \hat{C}\,, \quad \text{(B.39)}$$

$$\beta(1+N) = -\hat{\phi}_g|_C + \frac{\hat{M}_c}{4\pi\hat{r}} - \frac{1}{2}(\hat{v}_r|_C^2 + \hat{v}_\theta|_C^2 + \hat{v}_\varphi|_C^2) + \frac{\hat{\mu}_0}{m+1}(\hat{\Psi}|_C + \epsilon)^{m+1} + \hat{r}\sin\theta\hat{v}_\varphi\hat{\Omega}_0(\hat{\Psi}^2 + d^2)^\alpha|_C + \hat{C}\,, \quad \text{(B.40)}$$

From these equations we obtain three constants β, $\hat{C}$ and $\hat{\Omega}_0$ or $\hat{\mu}_0$. Using the three constants and the two potentials, we solve the first integral of equation of motion for the matter density:

$$\beta(1+N)\hat{\rho}^{\frac{1}{N}} = -\hat{\phi}_g + \frac{\hat{M}_c}{4\pi\hat{r}} - \frac{1}{2}(\hat{v}_r^2 + \hat{v}_\theta^2 + \hat{v}_\varphi^2) + \frac{\hat{\mu}_0}{m+1}(\hat{\Psi} + \epsilon)^{m+1} + \hat{r}\sin\theta\hat{v}_\varphi\hat{\Omega}_0(\hat{\Psi}^2 + d^2)^\alpha + \hat{C}\,. \quad \text{(B.41)}$$

The newly obtained density and other quantities are used as a new guess for the next iteration cycle. We carry out this iteration procedure until the relative changes of all physical quantities between two iteration cycles becomes less than some prescribed small number, $10^{-4} \sim 10^{-6}$.

B.3 Accuracy check for numerical computations in chapter 5

We have seen the convergence of numerical solutions in order to check the numerical accuracy in chapter 5. We see the differences between the analytical solution (App. A.3) and numerical solution changing the mesh numbers (a: $N_{r1} = 65$, b: $N_{r1} = 129$ in Fig. B.2), where N_{r1} means the mesh numbers within the stellar region (r = [0:1]). We display the four numerical and analytical solutions (model I, II, III and IV) in Fig. B.2. As seen from the Fig. B.2, the solutions in (b) represent the analytical solutions very well.

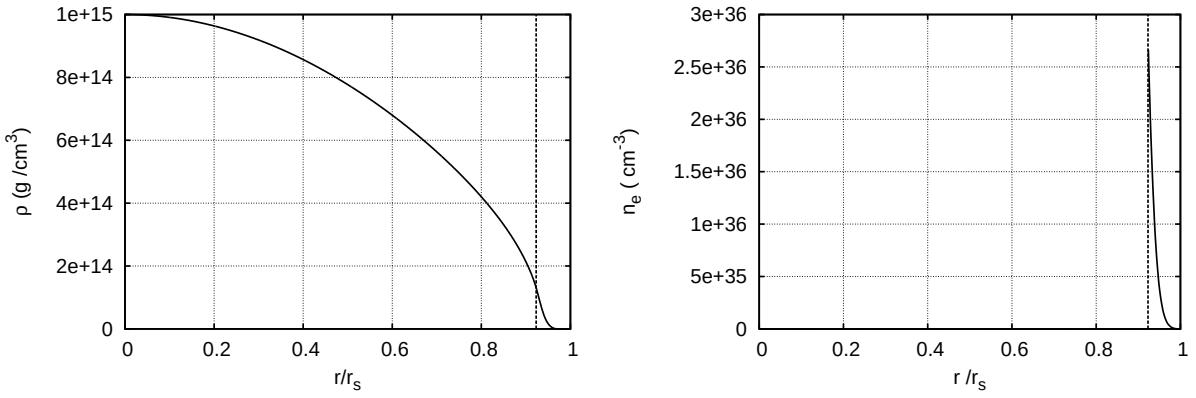

Figure B.3: Mass density profile (left) and electron number density profile within the crust (right) are displayed. The horizontal axis is normalized by the stellar radius r_s. Dashed lines correspond to the crust-core interface.

	κ_0	S_0	μ_0	model	$\mathcal{M}cr_t/\mathcal{M}cr$	$\mathcal{M}co_t/\mathcal{M}co$	$\mathcal{M}cr/\mathcal{M}$	$\mathcal{M}co/\mathcal{M}$	j_s
(App-a)	800	1	0	I	1.23E-4	0.0	0.98	0.00	-
(App-b)	250	1	0	II	1.40E-2	0.0	0.08	0.67	-
(App-c)	30	1	1	III	7.38E-2	3.71E-3	0.07	0.70	1.0
(App-d)	30	1	1	III	1.14E-1	2.41E-2	0.07	0.74	0.0
(App-e)	30	1	1	III	1.21E-1	2.92E-2	0.08	0.74	-0.05
(App-f)	10	-1	0.1	IV	4.09E-3	6.11E-2	0.08	0.83	0.1
(App-g)	10	-1	0.1	IV	1.62E-2	3.37E-1	0.02	0.96	-1.0
(App-h)	10	-1	0.1	IV	7.73E-3	2.68E-1	0.02	0.95	0.0

Table B.1: Parameters and numerical solutions of models with core magnetic fields. j_s denotes the strength of the current sheet on the core-crust boundary.

B.4 Hall equilibria with realistic equation of state

In this section, we employ SLy equation of state (Douchin & Haensel 2001) as a realistic equation of state in order to treat core and crust simultaneously. The maximum mass reaches $2.05M_\odot$ and can explain $\sim 2M_\odot$ neutron stars (Antoniadis et al. 2013; Demorest et al. 2010). We obtain both mass density and number density distributions using the SLy equation of state.

We fix the maximum density $\rho_{\max} = 1.0 \times 10^{15}\mathrm{g/cm^3}$ and calculate mass density and electron number density distributions (Fig. B.3). The stellar radius and the mass of the model are $M \sim 1.4M_\odot$ and $r_s \sim 1.3 \times 10^6\mathrm{cm}$ respectively. The electron number density at the base of the crust is $n_e \sim 2.67 \times 10^{36}\mathrm{cm^{-3}}$ in this model. We calculated 8 models using these mass density and number density distributions. Numerical results are displayed in Table B.1 and Fig. B.4.

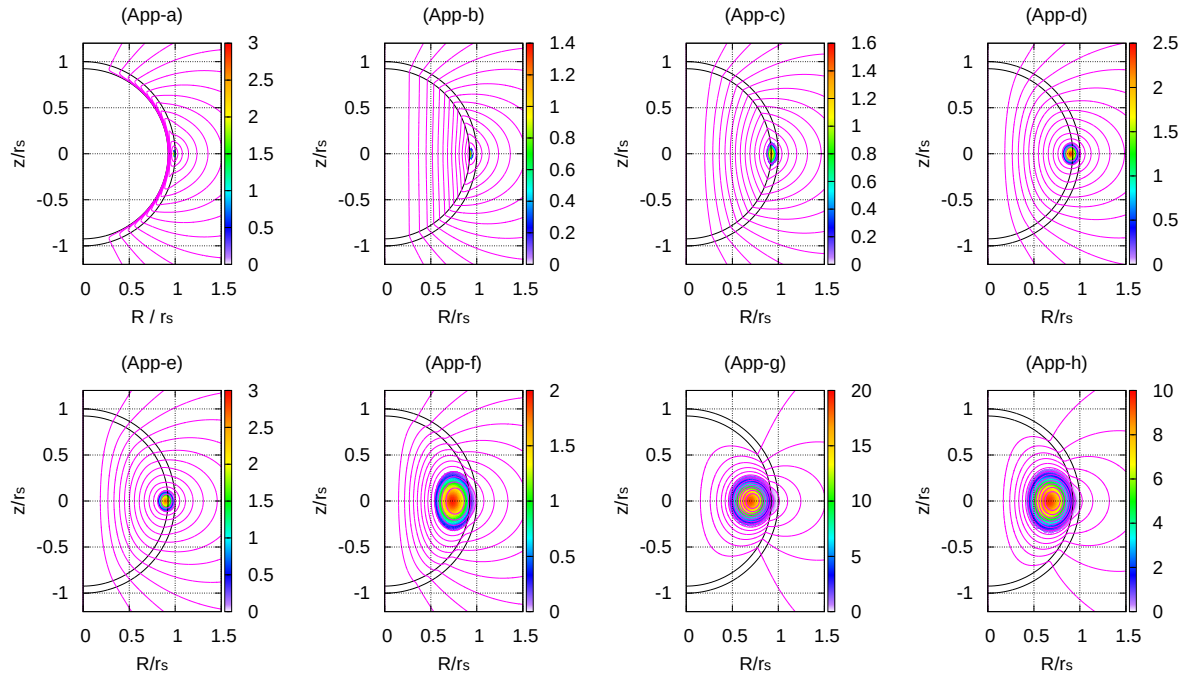

Figure B.4: The contours of Ψ in each model (solid line). The inner curve and the outer curve denote the core-crust interface and the stellar surface respectively. The colour maps denote the magnitude of the toroidal magnetic field B_φ normalized by the strength of the dipole component of poloidal magnetic field at the north pole.

Bibliography

Antoniadis J., Freire P. C. C., Wex N., Tauris T. M., Lynch R. S., van Kerkwijk M. H., Kramer M., Bassa C., Dhillon V. S., Driebe T., Hessels J. W. T., Kaspi V. M., Kondratiev V. I., Langer N., Marsh T. R., McLaughlin M. A., Pennucci T. T., Ransom S. M., Stairs I. H., van Leeuwen J., Verbiest J. P. W., Whelan D. G., 2013, Science, 340, 448

Armstrong J., Kuhn J. R., 1999, ApJ, 525, 533

Babcock H. W., 1947, ApJ, 105, 105

Banerjee D., Bhatt J. R., Das A. C., Prasanna A. R., 1995, ApJ, 449, 789

Baureis P., Ebert R., Schmitz F., 1989, A&A, 225, 405

Beloborodov A. M., Thompson C., 2007, ApJ, 657, 967

Birkl R., Stergioulas N., Müller E., 2011, Phys. Rev. D, 84, 023003

Bisnovatyi-Kogan G. S., Blinnikov S. I., 1972, Ap&SS, 19, 119

Bisnovatyi-Kogan G. S., Seidov Z. F., 1985, Ap&SS, 115, 275

Bocquet M., Bonazzola S., Gourgoulhon E., Novak J., 1995, A&A, 301, 757

Bonanno A., Urpin V., 2008, A&A, 477, 35

Bonazzola S., Gourgoulhon E., 1996, A&A, 312, 675

Braithwaite J., 2006, A&A, 453, 687

—, 2007, A&A, 469, 275

—, 2008, MNRAS, 386, 1947

—, 2009, MNRAS, 397, 763

Braithwaite J., Nordlund Å., 2006, A&A, 450, 1077

Braithwaite J., Spruit H. C., 2004, Nature, 431, 819

—, 2006, A&A, 450, 1097

Broderick A. E., Narayan R., 2008, MNRAS, 383, 943

Brun A. S., Browning M. K., Toomre J., 2005, ApJ, 629, 461

Chandrasekhar S., 1939, An introduction to the study of stellar structure, Chandrasekhar, S., ed.

—, 1956a, ApJ, 124, 232

—, 1956b, Proceedings of the National Academy of Science, 42, 1

—, 1956c, Proceedings of the National Academy of Science, 42, 1

Chandrasekhar S., Fermi E., 1953, ApJ, 118, 116

Chandrasekhar S., Prendergast K. H., 1956, Proceedings of the National Academy of Science, 42, 5

Charbonneau P., MacGregor K. B., 2001, ApJ, 559, 1094

Ciolfi R., Ferrari V., Gualtieri L., 2010, MNRAS, 406, 2540

Ciolfi R., Ferrari V., Gualtieri L., Pons J. A., 2009, MNRAS, 397, 913

Ciolfi R., Lander S. K., Manca G. M., Rezzolla L., 2011, ApJ, 736, L6

Ciolfi R., Rezzolla L., 2012, ApJ, 760, 1

—, 2013, MNRAS, 435, L43

Colaiuda A., Ferrari V., Gualtieri L., Pons J. A., 2008, MNRAS, 385, 2080

Cumming A., Arras P., Zweibel E., 2004, ApJ, 609, 999

Cutler C., 2002, Phys. Rev. D, 66, 084025

Demorest P. B., Pennucci T., Ransom S. M., Roberts M. S. E., Hessels J. W. T., 2010, Nature, 467, 1081

Douchin F., Haensel P., 2001, A&A, 380, 151

Duez M. D., Liu Y. T., Shapiro S. L., Shibata M., Stephens B. C., 2006, Phys. Rev. D, 73, 104015

Duez V., Braithwaite J., Mathis S., 2010, ApJ, 724, L34

Duez V., Mathis S., 2010, A&A, 517, A58+

Duncan R. C., Thompson C., 1992, ApJ, 392, L9

—, 1996, in American Institute of Physics Conference Series, Vol. 366, High Velocity Neutron Stars, R. E. Rothschild & R. E. Lingenfelter, ed., pp. 111–117

Eddington A. S., 1925, The Observatory, 48, 73

Enoto T., Nakagawa Y. E., Rea N., Esposito P., Götz D., Hurley K., Israel G. L., Kokubun M., Makishima K., Mereghetti S., Murakami H., Nakazawa K., Sakamoto T., Stella L., Tiengo A., Turolla R., Yamada S., Yamaoka K., Yoshida A., Zane S., 2009, ApJ, 693, L122

Enoto T., Nakazawa K., Makishima K., Nakagawa Y. E., Sakamoto T., Ohno M., Takahashi T., Terada Y., Yamaoka K., Murakami T., Takahashi H., 2010, PASJ, 62, 475

Eriguchi Y., Mueller E., Hachisu I., 1986, A&A, 168, 130

Esposito P., Burgay M., Possenti A., Turolla R., S. Z., Dw Luca A., Tiengo A., Israel G. L., Mattana F., Mereghetti S., Bailes M., Romano P., Götz D., Rea N., 2009, MNRAS, 399, L44

Ferraro V. C. A., 1954, ApJ, 119, 407

Flowers E., Ruderman M. A., 1977, ApJ, 215, 302

Fujisawa K., Eriguchi Y., 2013, MNRAS, 432, 1245

—, 2014, MNRAS, 438, L61

Fujisawa K., Takahashi R., Yoshida S., Eriguchi Y., 2013, MNRAS, 431, 1453

Fujisawa K., Yoshida S., Eriguchi Y., 2012, MNRAS, 422, 434

Geppert U., Rheinhardt M., 2002, A&A, 392, 1015

—, 2006, A&A, 456, 639

Ghanbari J., Abbassi S., 2004, MNRAS, 350, 1437

Gjellestad G., 1954, ApJ, 119, 14

Glampedakis K., Andersson N., Lander S. K., 2012, MNRAS, 420, 1263

Glampedakis K., Lander S. K., Andersson N., 2014, MNRAS, 437, 2

Goldreich P., Julian W. H., 1969, ApJ, 157, 869

Goldreich P., Reisenegger A., 1992, ApJ, 395, 250

Gough D., 2012, Science, 337, 1611

Gourgoulhon E., Markakis C., Uryū K., Eriguchi Y., 2011, Phys. Rev. D, 83, 104007

Gourgouliatos K. N., Cumming A., 2014, MNRAS, 438, 1618

Gourgouliatos K. N., Cumming A., Reisenegger A., Armaza C., Lyutikov M., Valdivia J. A., 2013, MNRAS, 434, 2480

Gourgouliatos K. N., Lynden-Bell D., 2008, MNRAS, 391, 268

Hachisu I., 1986a, ApJS, 61, 479

—, 1986b, ApJS, 62, 461

Harding A. K., Lai D., 2006, Reports on Progress in Physics, 69, 2631

Haskell B., Samuelsson L., Glampedakis K., Andersson N., 2008, MNRAS, 385, 531

Hollerbach R., Rüdiger G., 2002, MNRAS, 337, 216

—, 2004, MNRAS, 347, 1273

Hotokezaka K., Kyutoku K., Okawa H., Shibata M., Kiuchi K., 2011, Phys. Rev. D, 83, 124008

Ioka K., Sasaki M., 2004, ApJ, 600, 296

Jones P. B., 1988, MNRAS, 233, 875

Jordan S., Schmelcher P., Becken W., Schweizer W., 1998, A&A, 336, L33

Kiuchi K., Kotake K., 2008, MNRAS, 385, 1327

Kiuchi K., Sekiguchi Y., Shibata M., Taniguchi K., 2009, Phys. Rev. D, 80, 064037

Kiuchi K., Yoshida S., 2008, Phys. Rev. D, 78, 044045

Kiuchi K., Yoshida S., Shibata M., 2011, A&A, 532, A30

Kluźniak W., Ruderman M. A., 1998, ApJ, 505, L113

Kojima Y., Kisaka S., 2012, MNRAS, 421, 2722

Konno K., Obata T., Kojima Y., 1999, A&A, 352, 211

Kouveliotou C., Dieters S., Strohmayer T., van Paradijs J., Fishman G. J., Meegan C. A., Hurley K., Kommers J., Smith I., Frail D., Murakami T., 1998, Nature, 393, 235

Kouveliotou C., Strohmayer T., Hurley K., van Paradijs J., Finger M. H., Dieters S., Woods P., Thompson C., Duncan R. C., 1999, ApJ, 510, L115

Kuhn J. R., Bush R., Emilio M., Scholl I. F., 2012, Science, 337, 1638

Kyutoku K., Okawa H., Shibata M., Taniguchi K., 2011, Phys. Rev. D, 84, 064018

Kyutoku K., Shibata M., Taniguchi K., 2010, Phys. Rev. D, 82, 044049

Lander S. K., 2013, Physical Review Letters, 110, 071101

—, 2014, MNRAS, 437, 424

Lander S. K., Andersson N., Glampedakis K., 2012, MNRAS, 419, 732

Lander S. K., Jones D. I., 2009, MNRAS, 395, 2162

Lasky P. D., Zink B., Kokkotas K. D., Glampedakis K., 2011, ApJ, 735, L20

Latter W. B., Schmidt G. D., Green R. F., 1987, ApJ, 320, 308

Li Z.-Y., Shu F. H., 1996, ApJ, 472, 211

Lovelace R. V. E., Mehanian C., Mobarry C. M., Sulkanen M. E., 1986, ApJS, 62, 1

Lüst R., Schlüter A., 1954, ZAp, 34, 263

Makishima K., Enoto T., Hiraga J. S., Nakano T., Nakazawa K., Sakurai S., Sasano M., Murakami H., 2014, ArXiv e-prints

Markey P., Tayler R. J., 1973, MNRAS, 163, 77

—, 1974, MNRAS, 168, 505

Masada Y., Nagataki S., Shibata K., Terasawa T., 2010, PASJ, 62, 1093

Mastrano A., Melatos A., Reisenegger A., Akgün T., 2011, MNRAS, 417, 2288

Matsumoto J., Masada Y., Asano E., Shibata K., 2011, ApJ, 733, 18

Mereghetti S., 2008, Astron Astrophys Rev, 15, 225

Miesch M. S., 2005, Living Reviews in Solar Physics, 2, 1

Miketinac M. J., 1973, Ap&SS, 22, 413

—, 1975, Ap&SS, 35, 349

Moss D., 1994, in IAU Symposium, Vol. 162, Pulsation; Rotation; and Mass Loss in Early-Type Stars, L. A. Balona, H. F. Henrichs, & J. M. Le Contel, ed., pp. 173–+

Murakami T., Kubo S., Shibazaki N., Takeshima T., Yoshida A., Kawai N., 1999, ApJ, 510, L119

Naito T., Kojima Y., 1994, MNRAS, 266, 597

Narayan R., Piran T., Kumar P., 2001, ApJ, 557, 949

Nordlund Å., Stein R. F., Asplund M., 2009, Living Reviews in Solar Physics, 6, 2

Okada R., Fukue J., Matsumoto R., 1989, PASJ, 41, 133

Ostriker J., 1964, ApJ, 140, 1067

Ostriker J. P., Hartwick F. D. A., 1968, ApJ, 153, 797

Otani J., Takahashi R., Eriguchi Y., 2009, MNRAS, 396, 2152

Parfrey K., Beloborodov A. M., Hui L., 2013, ApJ, 774, 92

Perna R., Pons J. A., 2011, ApJ, 727, L51

Pons J. A., Geppert U., 2007, A&A, 470, 303

Pons J. A., Link B., Miralles J. A., Geppert U., 2007, Physical Review Letters, 98, 071101

Prendergast K. H., 1956, ApJ, 123, 498

Rea N., Esposito P., Turolla R., Israel G. L., Zane S., Stella L., Mereghetti S., Tiengo A., Götz D., Göğüş E., Kouveliotou C., 2010, Science, 330, 944

Rea N., Israel G. L., Esposito P., Pons J. A., Camero-Arranz A., Mignani R. P., Turolla R., Zane S., Burgay M., Possenti A., Campana S., Enoto T., Gehrels N., Göğüş E., Götz D., Kouveliotou C., Makishima K., Mereghetti S., Oates S. R., Palmer D. M., Perna R., Stella L., Tiengo A., 2012, ApJ, 754, 27

Rea N., Israel G. L., Turolla R., Esposito P., Mereghetti S., Götz D., Zane S., Tiengo A., Hurley K., Feroci M., Still M., Yershov V., Winkler C., Perna R., Bernardini F., Ubertini P., Stella L., Campana S., van der Klis M., Woods P., 2009, MNRAS, 396, 2419

Reisenegger A., Benguria R., Prieto J. P., Araya P. A., Lai D., 2007, A&A, 472, 233

Rheinhardt M., Geppert U., 2002, Physical Review Letters, 88, 101103

Rheinhardt M., Konenkov D., Geppert U., 2004, A&A, 420, 631

Roberts P. H., 1955, ApJ, 122, 508

Roxburgh I. W., 1974, Ap&SS, 27, 425

Schmidt G. D., Stockman H. S., Grandi S. A., 1986, ApJ, 300, 804

Sekiguchi Y., Shibata M., 2004, Phys. Rev. D, 70, 084005

—, 2007, Progress of Theoretical Physics, 117, 1029

—, 2011, ApJ, 737, 6

Shalybkov D. A., Urpin V. A., 1997, A&A, 321, 685

Shibata M., 2000, Progress of Theoretical Physics, 104, 325

—, 2003, ApJ, 595, 992

Shibata M., Sekiguchi Y., 2005, Phys. Rev. D, 72, 044014

Shibata M., Sekiguchi Y., Takahashi R., 2007, Progress of Theoretical Physics, 118, 257

Shibata M., Shapiro S. L., 2002, ApJ, 572, L39

Shibata M., Taniguchi K., 2008, Phys. Rev. D, 77, 084015

Shibata M., Taniguchi K., Uryū K., 2003, Phys. Rev. D, 68, 084020

—, 2005, Phys. Rev. D, 71, 084021

Shibata M., Uryū K., 2006, Phys. Rev. D, 74, 121503

Shibata M., Uryū K. ō., 2000, Phys. Rev. D, 61, 064001

Shibata M., Uryu K., 2007, Classical and Quantum Gravity, 24, 125

Spruit H. C., 1999, A&A, 349, 189

—, 2009, in Proceedings IAU Symposium, Vol. 259, Cosmic Magnetic Fields: From Planets, to Stars and Galaxies, K. G. Strassmeier, A. G. Kosovichev & J. E. Beckman, ed., pp. 61–73

Sykes J., 1957, ApJ, 125, 615

Takahashi H. R., Asano E., Matsumoto R., 2009, MNRAS, 394, 547

—, 2011, MNRAS, 414, 2069

Tayler R. J., 1973, MNRAS, 161, 365

—, 1980, MNRAS, 191, 151

Thompson C., Duncan R. C., 1995, MNRAS, 275, 255

—, 2001, ApJ, 561, 980

Thompson C., Lyutikov M., Kulkarni S. R., 2002, ApJ, 574, 332

Tomimura Y., Eriguchi Y., 2005, MNRAS, 359, 1117

Urpin V. A., Shalybkov D. A., 1995, A&A, 294, 117

Viganò D., Pons J. A., 2012, MNRAS, 425, 2487

Viganò D., Pons J. A., Miralles J. A., 2011, A&A, 533, A125

—, 2012, Computer Physics Communications, 183, 2042

Viganò D., Rea N., Pons J. A., Perna R., Aguilera D. N., Miralles J. A., 2013, MNRAS, 434, 123

Wada T., Shibata S., 2007, MNRAS, 376, 1460

—, 2011, MNRAS, 418, 612

Wade G. A., Alecian E., Bohlender D. A., Bouret J.-C., Cohen D. H., Duez V., Gagné M., Grunhut J. H., Henrichs H. F., Hill N. R., Kochukhov O., Mathis S., Neiner C., Oksala M. E., Owocki S., Petit V., Shultz M., Rivinius T., Townsend R. H. D., Vink J. S., Vink, 2011, in IAU Symposium, Vol. 272, IAU Symposium, Neiner C., Wade G., Meynet G., Peters G., eds., pp. 118–123

Wentzel D. G., 1961, ApJ, 133, 170

Wickramasinghe D. T., Ferrario L., 2000, PASP, 112, 873

Woltjer L., 1959a, ApJ, 130, 400

—, 1959b, ApJ, 130, 405

—, 1960, ApJ, 131, 227

Wong C.-Y., 1974, ApJ, 190, 675

Woods P. M., Thompson C., 2006, in Astrophysics Series, Vol. 39, Compact Stellar X-ray Sources, W. Lewin, & M. van der Klis, ed., pp. 547–586

Wright G. A. E., 1973, MNRAS, 162, 339

Yoshida S., Eriguchi Y., 2006, ApJ, 164, 156

Yoshida S., Kiuchi K., Shibata M., 2012, Phys. Rev. D, 86, 044012

Yoshida S., Yoshida S., Eriguchi Y., 2006, ApJ, 651, 462

Zhao J., Nagashima K., Bogart R. S., Kosovichev A. G., Duvall Jr. T. L., 2012, ApJ, 749, L5